UNIVERSITA' DEGLI STUDI DI MODENA E REGGIO EMILIA

PhD SCHOOL

in

HIGH MECHANICS AND AUTOMOTIVE DESIGN & TECHNOLOGY

Cycle XXV

Dean: Prof. Ing. Antonio Strozzi

Scientific disciplinary sector: ING–IND/21 (Metallurgy)

STRUCTURAL FEATURES AND PLASTIC BEHAVIOR OF HEAT RESISTANT ALPHA TITANIUM ALLOYS

Author:

Ing. SILVIA GAIANI

Tutor:

Prof. Ing. Paolo Veronesi

Co-Tutor:

Chiar.mo Prof. Giorgio Poli

Modena, 22nd March 2013

Dissertation Presented in Partial Fulfillment of the Requirements for the Degree Doctor of Philosophy in the Graduate School of the University of Modena and Reggio Emilia

Ringraziamenti

Nella vita di ognuno di noi c'è un prima ed un dopo. Il mio dopo è iniziato il 14 Luglio 2004, ed è stato un percorso doloroso e sconosciuto che mi ha condotto lontano da casa. Spesso, partendo per un viaggio, la meta finale e gli incontri che ci attendono lungo il cammino non sono noti a priori. Quando cinque anni fa decisi di trasferirmi a Ljubljana non avrei mai pensato che questa scelta avrebbe cambiato così radicalmente il corso degli eventi, portandomi a vivere nuove esperienze, facendomi conoscere persone ed una cultura diversa dalla mia, permettendomi un arricchimento personale e professionale che mai avrei creduto realizzabile.

Pertanto, il primo ringraziamento va alla persona che ha inizialmente reso possibile tutto questo, Igor Akrapovič, che ha creduto nelle mie capacità dandomi un'occasione che per me ha sempre rappresentato molto più che un semplice impiego. Voglio inoltre ringraziare tutti i colleghi dell'azienda Akrapovič, ed in particolar modo Robert Tisu, che delle prove di caratterizzazione illustrate in questa tesi conosce ogni dettaglio, Sebastijan Jurendič, mago indiscusso delle simulazioni FEM, e Albin Mohar, con il quale in questi anni ho diviso non solo la scrivania ma anche i successi, le sconfitte e tutte le piccole e grandi battaglie del quotidiano.

Sul versante sloveno, la mia riconoscenza va anche alla Dr.ssa Irena Pribošič dell'Institut Jožef Štefan, per l'aiuto datomi nell'eseguire le analisi di tessitura con tecnica EBSD, e al Dr. Uroš Bohinc dell'Istituto ZAG (Zavod za Gradbenistvo Slovenije) che mi ha supportato nell'esecuzione delle misure ottiche di deformazione.

Tornando su suolo italico, vorrei ringraziare il Prof. Paolo Veronesi, perché in fondo se sono arrivata a conseguire il Dottorato di ricerca è soltanto colpa sua.

Grazie alla mia famiglia, per il supporto e l'amore incondizionato che mi ha sempre dimostrato in qualsiasi circostanza, e ovviamente grazie a Paolo, perché anche dopo nove anni quello che abbiamo condiviso insieme è sempre vivo e presente e costituisce un grande stimolo per cercare di vivere una vita piena.

Infine, grazie a Cristiana, per la sua presenza e sensibilità, per i consigli preziosi, la mano sempre tesa verso il prossimo e per essere semplicemente la persona straordinaria che è.

Table of Contents

Abstract

The research activity was mainly focused on two titanium alpha alloys for heat resistant applications named Ti-Fe-Si-O and Ti-Al-Si-Nb. The aforementioned materials are commonly used in automotive industry for manufacturing of exhaust systems subjected to service temperature up to 850 °C.

Cold formability of these alloys is extremely limited due to the anisotropic behavior ascribable to their peculiar crystallographic configuration. Understanding the deformation mechanisms of these materials constitutes a fundamental issue to be deepened for understanding the process parameters to be used during operations of deep drawing, bending and hydroforming as well as to understand the component's geometries which can be achieved using these technologies.

At the beginning, a thorough characterization campaign on the two alloys has been made, with the aim of highlighting their basic mechanical properties. Particular attention has been paid in studying the parameters which can provide specific informations about anisotropy, like the plastic strain ratio values.

Subsequently, the experimental results were used as input data for simulating the plastic response of the materials using a finite elements code. For this specific application, the Barlat & Lian 1989 criterion has been chosen. This model is specifically intended for describing the behavior of orthotropic metal sheets exhibiting planar anisotropy and subjected to plane stress conditions. Many efforts have been made in optimizing the quality of the experimental input data used by the program, in order to describe the yield locus function as accurately as possible.

The requirement of having an accurate and reliable predictive model which can be profitably used for industrial applications, brings out the needs to study these alpha titanium alloys using experimental approaches aimed to highlight in detail their intrinsic deformation mechanisms. In this regard, the use of optic measuring methods allows achieving significant progresses in understanding the plastic behavior of these materials as well as in refining the quality of FEA output. In parallel, studying the preferential crystallographic orientation (texture) and its evolution during a predefined uniaxial deformation allows correlating macroscopic deformation with microstructural properties of the material.

Finally, this research activity allowed achieving multiple targets. In detail:

- Developing and establishing a characterization procedure dedicated to anisotropic materials which can be profitably used for comparative analyses of different alloys and also for assessing their compliance in purchasing of raw materials

- Validating the effectiveness of Barlat & Lian 1989 criterion in predicting the plane stress anisotropic plastic flow for material presenting hcp crystal lattice as well as refining the input experimental data. The extensive use of finite element analyses for predicting the plastic response of this family of materials has enabled to understand how their response during deformation is strongly influenced not only by its initial characteristics, but also by the nature and direction of the loading conditions. In consideration to that, is understandable how FEA simulation is an essential method to be used if components with difficult geometries subjected to complex stress state need to be studied
- Correlating the crystallographic orientation of the material with its plastic response by performing texture analyses allows obtaining a better understanding of its behavior during deformation. This approach is doubly interesting, because in a near future it could be used as an experimental basis for implementing modeling techniques capable of modeling the plastic response of material simulating the texture development during the deformation process of hcp titanium alloys

KEYWORDS: titanium, texture, anisotropy, plasticity, FEA

Sintesi Analitica

L'attività di ricerca ha riguardato prevalentemente due leghe di titanio alfa per impieghi a caldo denominate Ti-Fe-Si-O e Ti-Al-Si-Nb. I suddetti materiali sono impiegati nell'industria automotive per la costruzione di impianti di scarico sottoposti in esercizio a temperature fino a 850 °C.

La formabilità a freddo di queste leghe, che risulta estremamente limitata dal comportamento anisotropo imputabile alla peculiare configurazione cristallografica che le contraddistingue, costituisce una tematica fondamentale da approfondire qualora si vogliano comprendere a fondo i parametri di processo da impiegare durante operazioni di imbutitura, piegatura, idroformatura nonché stabilire le geometrie dei componenti ottenibili utilizzando queste tecnologie.

Si è proceduto inizialmente alla caratterizzazione approfondita delle leghe studiate, con la finalità di evidenziare le loro caratteristiche meccaniche di base, prestando particolare attenzione ai parametri indicatori di anisotropia, come il parametro di Lankford.

In seguito, i risultati sperimentali sono stati utilizzati come dati di ingresso per la simulazione della risposta plastica del materiale attraverso l'utilizzo di un codice ad elementi finiti. Per questa applicazione specifica è stato scelto il criterio di Barlat e Lian 1989, specificatamente sviluppato per lo studio di lamiere ortotrope soggette a sollecitazioni biassiali. L'ottimizzazione della qualità dei dati sperimentali di ingresso impiegati dal programma di simulazione ha permesso di descrivere la superficie limite del dominio elastico nella maniera più accurata possibile.

Proprio l'esigenza di realizzare modelli predittivi precisi e sfruttabili per applicazioni industriali ha fatto emergere la necessità di studiare queste leghe utilizzando approcci sperimentali mirati ad evidenziare in dettaglio i loro meccanismi intrinseci di deformazione. A questo proposito, l'impiego di tecniche di misura ottiche ha permesso di compiere efficaci progressi nella comprensione dei limiti di plasticità nonché nell'affinamento dei modelli matematici. Parallelamente, lo studio dell'orientamento cristallografico preferenziale (tessitura) e della sua evoluzione durante l'esplicarsi di una deformazione monoassiale nota ha permesso di correlare le proprietà macroscopiche di deformabilità con quelle microscopiche proprie della microstruttura del materiale.

In conclusione, l'attività di ricerca ha permesso di raggiungere i seguenti obiettivi:

- Sviluppare e consolidare una procedura di caratterizzazione dei materiali anisotropi che può essere impiegata per l'analisi comparativa di diverse leghe e per il loro controllo di conformità in fase di acquisizione della materia prima.

- Validare l'efficacia del criterio di Barlat 1989 per lo studio predittivo del comportamento plastico di materiali anisotropi con cella elementare e.c. sottoposti a sollecitazioni biassiali, nonché approfondire la tecnica di affinamento dei dati sperimentali di input. L'utilizzo di tecniche di simulazione predittive del comportamento plastico di materiali anisotropi ha permesso di comprendere come la risposta del materiale sia fortemente influenzata non solo dalle sue caratteristiche intrinseche, ma anche da natura ed orientamento della sollecitazione esterna applicata. Da questa considerazione si può intuire come l'impiego di codici FEA sia indispensabile quando si studiano particolari di geometria difficoltosa sottoposti a stati tensionali complessi.
- Correlare l'orientamento cristallografico del materiale con la sua risposta plastica attraverso lo studio della tessitura permette di ottenere una migliore comprensione del suo comportamento durante la deformazione. La metodologia di analisi risulta interessante poiché in futuro potrà essere utilizzata come base sperimentale per codici di calcolo in grado di modellare la formabilità del materiale attraverso la simulazione dell'evoluzione microstrutturale della lega.

PAROLE CHIAVE: titanio, tessitura, anisotropia, plasticità, FEA

Povzetek

Raziskovalna dejavnost je bila osredotočena na dve temperaturno odporni titanovi alfa zlitini ki se imenujejo Ti-Fe-Si-O in Ti-Al-Si-Nb. Materiala se pogosto uporabljata v avtomobilski industriji za izdelavo izpušnih sistemov s predvidenim temperaturnim območjem uporabe do 850 °C.

Hladno preoblikovanje teh zlitin je zelo omejeno zaradi anizotropnih lastnosti, ki so posledica njihove kristalografske zgradbe. Razumevanje mehanizma deformacije teh materialov je ključnega pomena za določitev pravilnih procesnih parametrov, potrebnih za globoki vlek, krivljenje in hidro-oblikovanje, kot tudi razumevanja geometrij, ki se lahko dosegajo s takšnimi procesi preoblikovanja.

Najprej je bila izvedena karakterizacija materialov, kjer smo določili njihove osnovne mehanske lastnosti ter lastnosti, ki določajo anizotropijo teh materialov: Lankfordov koeficient in koeficient utrjevanja.

Pridobljeni eksperimentalni rezultati so bili uporabljeni kot vhodni podatki pri simulaciji plastičnega odziva materiala z metodo končnih elementov pri čemer je bil uporabljen Barlat-Lianov 1989 kriterij. Ta model se najpogosteje uporablja pri opisu obnašanja pločevin z ortotropnimi materialnimi lastnosti, ki so podvržene ravninskemu napetostnemu stanju. Velik poudarek je bil na kvaliteti pridobljenih eksperimentalnih vhodnih podatkov z namenom, da bi da bi bilo modeliranje mejne krivulje tečenja čim bolj zanesljivo.

V praksi potrebujemo kar najbolj natančen simulacijski model. Zato je preučevanje titanovih zlitin s poudarkom na določitvi njihovih notranjih deformacijskih mehanizmov ključnega pomena. Uporaba optičnih merilnih metod znatno pripomore k boljšemu razumevanju plastičnega obnašanja materialov ter k boljše razumevanju rezultatov računalniških analiz. Preučevanje glavnih kristalnih orientacij in njihovega razvoja med enoosno deformacijo, nam omogoča primerjavo deformacij na makro nivoju z mikrostrukturnimi spremembami zlitin.

Izvedena raziskovalna dejavnost je pripomogla k doseganju naslednjih ciljev:

- Izdelavi standardnega postopka karakterizacije anizotropnih materialov, uporabnega za medsebojno primerjavo različnih vrst zlitin in vhodno kontrolo materialov.

- Vrednotenju učinkovitosti Barlat-Lianovega kriterija za napoved ravninskih napetosti anizotropnega plastičnega toka za material s heksagonalno kristalno rešetko in optimizacijo vhodnih eksperimentalnih podatkov. Široka uporaba analize z metodo končnih elementov za napovedovanje plastičnega odziva te družine materialov nam pomaga razumeti, da je njihovo obnašanje med deformacijo močno odvisno tako od začetnih karakteristik kot tudi od zunanjih obremenitev. Ob upoštevanju tega je razumljivo, da je uporaba FEA simulacije bistvena v primeru, ko so predmet raziskav komponente s kompleksno geometrijo, ki so izpostavljene zahtevnim obremenitvam.

- Primerjava kristalne orientacije s plastičnim odzivom materiala na ta način, da se izvede analizo tekstur omogoča boljše razumevanje mehanizmov deformacije med postopki preoblikovanja. Ta pristop je izjemno zanimiv, saj bo lahko v prihodnje uporabljen kot eksperimentalna baza za uvedbo tehnik modeliranja, ki bi lahko simulirale obnašanje tekstur pri postopku preoblikovanja v povezavi z anizotropnim obnašanjem materialov s heksagonalno kristalno rešetko (v smislu napetosti in deformacij).

KLJUČNE BESEDE: titan, tekstur, anizotropija, plastičnost, FEA

CHAPTER 1
INTRODUCTION

Titanium and its alloys are widely used in several demanding applications due to their low density–strength ratio, high biocompatibility and high corrosion and oxidation resistance at elevated temperature[1]. Modern titanium alloys have different structures and properties, depending on the specific field of use and requested characteristic of final components. Specifically, a considerable research work has been carried out during the last two decades to develop high temperature resistant titanium alloys with excellent creep properties as well as good oxidation resistance, which can be used mainly for industrial and automotive applications. This family of alloys present alpha based microstructure.

For alpha based titanium alloys, crystallographic texture and mechanical fibering as results of raw material production processes or thermomechanical treatments play a crucial role on the physical and mechanical properties of materials. This fact has especially become more important for these materials with hexagonal close–packed (HCP) structure owing to their inherent anisotropy and specific type of deformation modes based on a combination of slip and twinning[2]. The activation of such modes depends on their relative critical stresses, and hence on the orientation of the crystals with respect to the loading direction.

The very pronounced texture in cold rolled titanium sheets gives raise to strong anisotropic mechanical behavior, and has a detrimental influence on other properties such as fatigue, creep but especially on plastic formability at room temperature[3]. The major factors which influence the degree of deformation that can be achieved during different plastic processes without failure are:

- Material features (microstructure, heat treatments, texture orientation, defects, …)
- External process variables (stress, strain rate, temperature, friction coefficient, …)

In order to optimize titanium deep drawing processes performed at room temperature and, in parallel, achieving an improved design of the components which can allow exploiting all the characteristic of the material, a complete understanding of both the aforementioned factors must be achieved.

---

[1] Dawne S. Hickton - Global Commercial Aerospace – Proceeding of the 25th ITA Conference, Orlando (FL, USA) - October 3-6, 2010

[2] S. L. Semiatin, T. R. Bieler - Effect of Texture and Slip Mode on the Anisotropy of Plastic Flow and Flow Softening during Hot Working of Ti-6Al-4V - Metallurgical and materials transactions - Volume 32a, July 2001— pp. 1787

[3] R. Penelle, T.Baudin, C. Quesne - Relationships between Texture, Microstructure and Properties in Titanium and some Titanium Alloys - Proceedings of the 10th World Conference on Titanium - Hamburg, Germany July 13-18, 2003

The material properties and the mechanical and physical behavior of these alpha titanium alloys are essential for processing and application, but the available knowledge is currently limited. Systematic and comprehensive investigations are needed to thoroughly characterize these new materials for optimizing and controlling their processing like sheet metal forming. In particular this applies to deep drawing as a kind of plastic forming that often requires numerical simulation via Finite Element Analysis (FEA) to predict, analyze and optimize the process behavior. The simulation requires the input of suitable material models describing the mechanical properties.

In present work, two different titanium alloys for heat resistant applications have been specifically chosen for establishing a unified path model for characterization and comparison of plastic behavior: Ti-Fe-Si-O and Ti-Al-Si-Nb. Once the behavior of a material was 'mapped' by means of a reliable characterization scheme, the next step was developing anisotropic formulations at a macroscopic level which can be easily implemented in FEA codes, and thus can be applied routinely for detailed analysis of complex forming processes.

1.1 Aim of the thesis

The final aim of this research is developing a finite element calculation method which allows simulating in a fast and reliable way the plastic behavior of anisotropic metallic materials subjected to cold forming operations, such as deep drawing. This target is very important, in order to realize feasibility studies of deep-drawn components, as well as a leaner and cheaper tool design. In this specific case, the object of present study are the two aforementioned alpha titanium alloys manufactured by cold-rolling and intended for elevated temperatures applications. These materials exhibit marked anisotropic behavior and consequently considerable difficulties during plastic deformation processes.

In order to achieve this result, a commercial FE software (LS-Dyna) and the Lian & Barlat 1989 yield criterion were used. A crucial aspect for generating a predictive model as close as possible to the real plastic behavior of the material is using experimental values as input data.

To this end, a wide mechanical characterization campaign has been performed on the two alloys by using traditional laboratory techniques (based on clip-on extensometers) and also new experimental approaches based on optical methods of measurement. The latter, due to the possibility of detecting a complete stress / strain distribution on the entire specimen's surface, has been a particularly effective method for mathematical model refining and for highlighting the triaxial stress state which occurs during necking. In addition to that, with optical measurements on Ti-Fe-Si-O alloy also some peculiar deformation mechanisms in the yielding region have been outlined for the first time.

Finally, for better understanding the plastic behavior of the two titanium alloys, a study focused on their preferential crystallographic orientation (texture) was performed with the aim of analyzing the intrinsic deformation mechanisms on a microscopic scale.

1.2 General Outline

With the premises discussed in previous paragraph as a background, the following tasks have been accomplished in this work:

- In Chapter 2 an overview of titanium characteristics and different families of alloys is presented, with a specific focus on the class of heat resistant titanium alloys. In addition to that, in this section are explained the basic deformation mechanisms on crystallographic scale occurring in HCP metals and the tendency of these materials to give rise to a preferential crystallographic orientation (texture).

- In Chapter 3 the results of a wide range of tensile testing is presented and discussed. This characterization campaign has been done with the aim of identifying the basic properties of the materials. Tension tests have been made on strip specimens cut from textured sheets at different angles to the reference (rolling and transverse) directions. The purpose was to check the anisotropic plasticity theory of Hill, which makes predictions about the angular variation of yield stress and, strain ratio.

- In Chapter 4 the experimental data obtained from mechanical testing have been used as input for FEA simulation of plastic response. For this purpose the Barlat & Lian 1989 method has been chosen. This model has been developed with the aim of predicting the behavior of orthotropic sheet metals (specifically cold rolled sheets) subjected to plane stresses. The analytical procedures adopted for optimizing the quality of the input data and consequently of the plastic response are explained and commented in detail.

- In Chapter 5 different approaches using optic measurements methods have been used with the aim to optimize the output results of FEA simulation. In detail, the procedures adopted are the following:
    i. Nakazima test in order to determinate the characteristic Forming Limit Diagram (FLD) for both alloys. The forming limit curve for sheet metal represents a limit up to which the material can be formed before the cracks on the specimen occur. The knowledge of this diagram is very important for ultimately determine the feasibility of a given deformation process
    ii. Bulge test, which is a standard method used for studying the behaviour of the material loaded in a biaxial condition where the principal stresses are symmetric ($\sigma_1 = \sigma_2$). Having these experimental data allow validate the reliability of the elliptical yielding locus domain obtained by FEA simulation
    iii. Tensile testing in longitudinal and transverse direction run using a optic system for determination of plastic strain. With this method, an accurate study of the yielding

mechanism and of the triaxial stresses state during necking can be made. The results obtained with this procedure can be used for FE simulation refining

iv. Experimental determination of friction coefficients with different lubricant and surface's contact condition for achieving better approximation during FE simulations

- In Chapter 6 with the aim of understanding the influence of crystallographic orientation on mechanical properties, several texture measurements have been performed using different techniques (X-Ray Diffraction and Electron Back Scattered Diffraction). The approach used for this series of measurement is double: at first the characterization of the two alloys in as rolled condition, and secondarily several acquisitions performed on specimens subjected to different levels of strain, in order to analyze texture evolution

- Finally, in Chapter 7 the results obtained in previous chapter have been discussed and analyzed

CHAPTER 2
TITANIUM BACKGROUND

2.1 Titanium basic properties

Titanium has been recognized as an element (symbol Ti; atomic number 22; and atomic weight 47.9) for at least 200 years. However, commercial production of titanium and its alloys did not begin until the 1950's[4]. They are extremely attractive materials for engineering applications in many different fields, because they have a high strength to weight ratio, high elevated temperature properties, and excellent corrosion resistance.

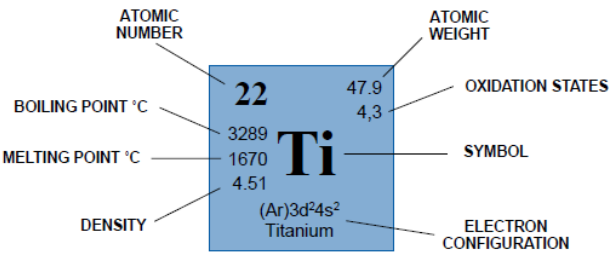

hcp Crystal Structure		Heat of Vaporization	9.83 MJ/kg
Lattice Parameters	c=0.468 nm	Specific Heat	518 J/kg °K
	a=0.295 nm	Magnetic Susceptibility	3.17 x 10^{-6} cm^3/g
Atomic Volume	10.64 cm^3/mol	Magnetic Permeability	1.00005
Covalent Radius	1.32Å	Modulus of Elasticity	100 GPa
Color	Dark Grey	Poisson's Ratio	0.32
Hardness	70 to 74 BHN	Solidus/Liquidus Temp.	1725°C
Coefficient of Thermal Expansion	8.4 x 10^{-6}/°C	Beta Transus Temp.	882°C
Electrical Resistivity	42 µohm-cm	Thermal Neutron Absorption Cross Section	5.6 Barnes
Thermal Conductivity	20 W/m-°K	Electronegativity	1.5 Pauling's
Heat of Fusion	292 kJ/kg		

Fig. 2-1 – Properties of pure elemental Ti at room temperature[4]

Despite of common thinking, titanium is not an '*exotic*' metal; in fact it is the fourth most abundant structural metal in the earth's crust[5], and the ninth industrial metal in terms of use worldwide. Today, titanium alloys are common, readily available engineered metals that compete directly with stainless and specialty steels, copper alloys, nickel based alloys and composites. Its greatest disadvantage is the high cost compared to competing materials which frequently offset's titanium's engineering advantages and restrings the market for titanium applications.

[4] VV.AA. - Titanium alloy Guide – RMI International Company – pp. 3
[5] Eylon D. - Titanium for Energy and Industrial Applications - *Metallurgical Society AIME* (1987)

Due to its unique set of properties nowadays, titanium and its alloys have been widely used throughout the aerospace industry for most types of structural components, including airframes and engine components, as well as in many non-aerospace applications. Just to mention a few, as a metal, cars, sports equipment such as racing yacht parts, golf clubs, tennis racquets and bike frames, wrist watches, underwater craft, and general industrial equipment. Its non-toxicity also makes it useful for surgical implants such as pacemakers, artificial joints and bone pins. Pure titanium has also excellent resistance to corrosion, and due to this property is used widely in the chemical industries[6].

The crystal structure of titanium at room temperature and pressure is close-packed hexagonal, and it is known as "*α phase*"; the c/a ratio of the hexagonal Ti lattice is equal to 1,587. At about 890°C, the titanium undergoes an allotropic transformation to a body-centered cubic phase, called "β phase", which remains stable to the melting temperature.

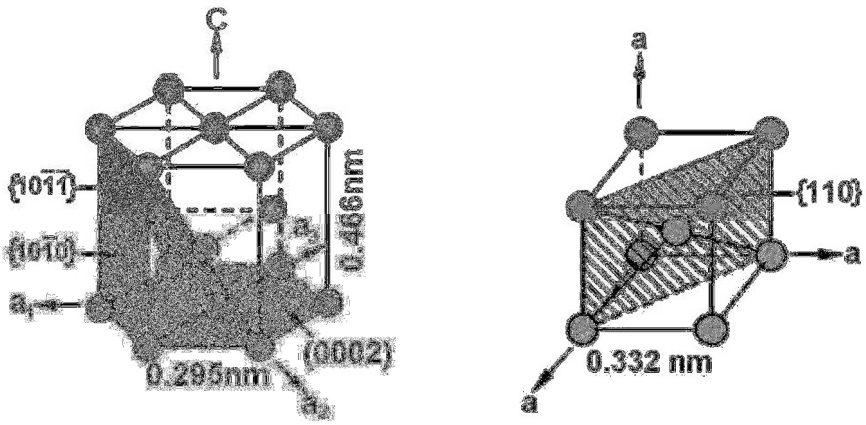

Fig. 2-2 – Unit cells of alpha and beta phases
(source: http://web-o-rama.net/titanium/1properties.html)

Titanium and other metals with hexagonal closed packed crystal structure could develop sharp deformation textures that lead to a pronounced plastic anisotropy of the final material[7]. Various factors can cause anisotropy in metals, among them are: cold/hot rolling process parameters, alloying elements (especially substitutional), grain morphology, final re-crystallization treatments.

In this scenario it becomes evident that an understanding on how the production processes affects the final properties of a semi-finished or finished material is of major significance. Moreover, considering that the cost associated with the testing and development of a product is somehow enormous and time consuming, availability of experimental characterization techniques and computational tools capable of providing reliable data leading to the prediction of "optimal" processing paths linking the commercially available "raw material" to its semi-finished or finished forms, is of strategic importance.

[6] VV.AA. - Titanium, the infinite choice – Brochure published from International Titanium Association Education Committee
[7] Hill R., 1952 - The elastic behavior of a crystalline aggregate - Proc. Phys. Soc. A 65, pp 349-354.

2.2 Titanium basic metallurgy

2.2.1 History of the process – Sponge production

Titanium production requires complicated processes that are capital and energy intensive. Refining the ore to titanium metal requires multistep, high-temperature batch processes. At the temperatures required for its reduction, titanium cannot be exposed to the atmosphere because of its great affinity for oxygen, nitrogen, carbon, and hydrogen which would make the metal brittle. Therefore, either vacuum or inert gas metallurgy techniques are necessary to reduce and process the metal.

The first production process on industrial scale which has been used for obtaining metallic titanium is named "Hunter process", from his inventor Matthew Hunter who developed it in 1910 at Rensselaer Polytechnic Institute (Troy, N.Y., U.S.A.) in cooperation with the General Electric Company[8]. The Hunter process begins by preparing a mixture of rutile with chlorine and coke. The coke serves as a source of carbon which reacts with oxygen in the TiO_2 when extreme heat is applied, producing titanium tetrachloride and carbon dioxide. The titanium tetrachloride is reduced with sodium to form pure metallic titanium by heating $TiCl_4$ with Na in a steel bomb at 700–800 °C.

In 1932 William J. Kroll from Luxembourg produced significant quantities of ductile titanium by combining $TiCl_4$ with calcium. The process developed by Kroll is basically a carbo-chlorination process, which starts by using ores with TiO2 content greater than 90% and lead to the production of porous titanium material called "*sponge*"[9]. Only natural rutile meets the requirements of purity requested from Kroll process, but ilmenite can be upgraded through combinations of pyrometallurgical and hydrometallurgical techniques to produce a synthetic rutile of 90 to 93 percent TiO_2.

In the first step of this process, the oxide ores are reacted with chlorine in a fluidized bed of petroleum coke. Oxygen combines with carbon in the coke to produce carbon monoxide and carbon dioxide, while the titanium and chlorine react to form a gaseous $TiCl_4$

The raw $TiCl_4$ is cleaned of fine particles of entrained coke and titanium ore, and then it is liquefied and passed through a distillation column to remove volatile impurities of both high and low boiling points. Afterwards, $TiCl_4$ is reduced using magnesium; this reduction reaction take place in sealed steel vessels at approximately 800 – 1.000° C in an inert argon atmosphere to avoid contamination of the final product by air or moisture. Kroll process produces titanium in form of sponge, with the salts NaCl or $MgCl_2$ entrapped in the pores. The sponge is crushed, and the metal and salts are separated by either a dilute acid leach or by high-temperature vacuum distillation. The salts are recycled through electrolytic cells to produce sodium or magnesium for reuse in metal reduction and chlorine for reuse in chlorination of the ore.

[8] VV.AA. - History of Titanium - Titanium Industries, Inc. – Internet web site
[9] VV.AA. - Titanium Processing – Encyclopedia Britannica On Line

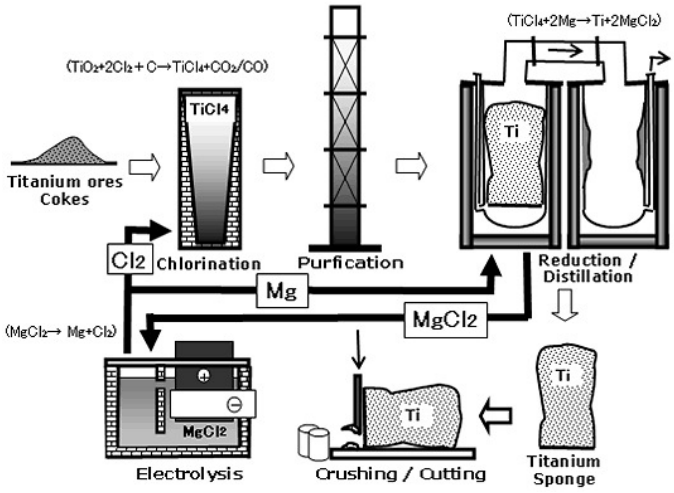

Fig. 2-3 – Titanium Sponge Production (I*mage courtesy of Toho Titanium Co, LTD, Japan)*

While Kroll's work demonstrated a method for titanium production on a laboratory scale, it took nearly a decade more before it could be adapted for large-scale production. This work was conducted by the United States Bureau of Mines from 1938 to 1947. In 1948, DuPont opened the first large scale manufacturing operation[10].

Also if with many optimizations, the method developed and patented by Kroll is still the most used industrial process for production of titanium sponge[11].

2.2.2 Sponge conversion into ingots

The conversion of purified titanium sponge to a form useful for structural purposes involves several steps. Consolidation into titanium ingot is performed in a vacuum or argon environment, and the most used technique for fulfilling this operation is the process named "Vacuum Arc Melting". In this process, sponge, alloying elements, and in some cases recycled scrap are first mechanically compacted and then welded into a long, cylindrical electrode. The electrode is melted vertically into a water-cooled copper crucible by passing an electric current through it. To ensure uniform distribution of alloying elements, this primary ingot is remelted at least twice in a similar manner. Double melting is considered necessary for all application to ensure an acceptable degree of homogeneity in the resulting product. Final ingots produced with this method can weigh between 4 and 10 tons.

VAR has many advantages, including high purity, good control and repeatability in product. However, the process is operated in vertical position, which can cause gravity induced segregations[12].

With the aim of achieving a defects reduction and better microstructural control, during the 1990s many efforts have been devoted to improve titanium melting technology. The latest development in this field is the so called "*Cold Heart Melting Furnace*". This method utilizes a water cooled copper vessel (the hearth) which contains the molten titanium. In this specific case, the heat input from the

[10] Freemantle, M. - Titanium Extracted Directly from TiO2 - *Chemical and Engineering News,* 25 September 2000.
[11] F.H. Froes – How to market titanium: lower the costs – Journal of metals (2004), Vol. 56, N°1, pp. 39
[12] Matthew J. Donachie, Jr. – Titanium: a technical guide 2nd Ed. - ASM International 2000, pp. 27-28

heat source is balanced against the rate of heat extraction from the water-cooled copper hearth. This maintains a thin layer of solid titanium alloy (called the "skull") in contact with the hearth, so the molten titanium alloy only contacts the solid titanium alloy.

There are two types of cold hearth melting furnaces in use today. One uses plasma arc melting (PAM) technology and the other uses electron beam melting (EBM) technology. These furnaces obviously differ in heat source (plasma torches vs. electron beam guns). Also, electron beam melting furnaces operate in vacuum, whereas plasma arc melting furnaces operate in a partial pressure of argon. Apart from these differences, the remaining physical arrangements of these furnaces are very similar[13]. The main advantages of CHM are the possibility of producing non axisymmetric shape, such as slabs or bars, and also the feasibility in using all forms of reverts.

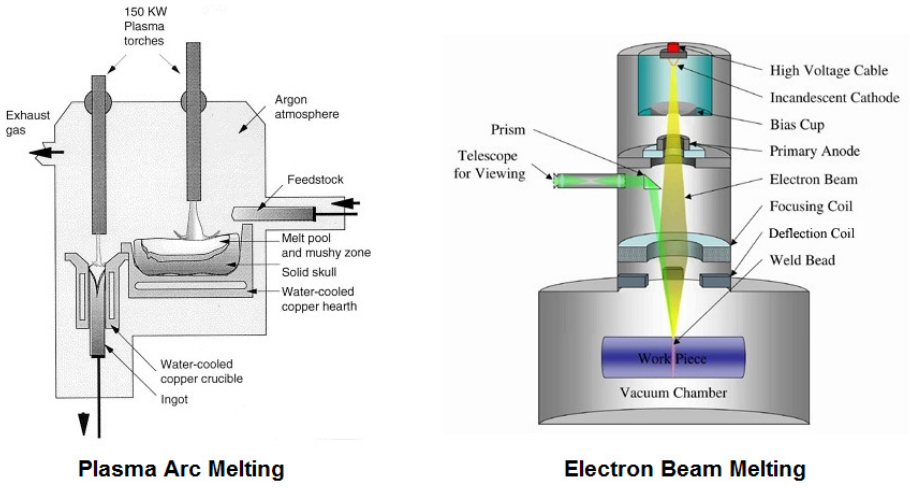

Fig. 2-4 – Schematic representation of PAM and EBM techniques

Consolidated ingots produced with different technologies are then processed into mill products such as bar, billet, wire, tubing, plate, and sheet by traditional steel facilities; currently, plate and sheet comprise 40% of titanium mill products[14]. The starting material for plate and sheet is a forged bloom that is an intermediate product of the ingot conversion process. The bloom is hot rolled into a slab, which then receives further hot reductions. For plate, this final hot reduction stops at the desired thickness. The plate is then given an annealing treatment before it is surface conditioned by grinding and/or pickling. These hot rolled plates could be also the starting product for manufacturing of cold rolled sheet metal. Usually, the cold rolled titanium flat products are produced in a multi-stand mill, such as a Steckel or a Sendzimir mill. These mills use several rolls to back a pair of very small diameter work rolls to ensure flatness of the thin, cold rolled product. After cold rolling, the strip is annealed again and coiled for shipment. Because of the unidirectional working of strip, it always has a significant degree of texture, but because most of the material that is produced as strip is CP titanium, this typically is not a limitation.

[13] G. Lutjering, J. C. Williams - Titanium 2nd Edition – Ed. Springer (2007), pp. 65-66
[14] G. Lutjering, J. C. Williams - Titanium 2nd Edition – Ed. Springer (2007), pp. 76

2.2.3 Titanium production costs analysis

Summarizing the contents presented in previous paragraphs, the processing of titanium ductile metal occurs in four major steps:

1) Reduction of titanium ore into "sponge" by using of Kroll process (see Fig. 2-3)

2) Melting of sponge (or sponge plus a master alloy) to form an ingot by using VAR, EBM or PAM process

3) Primary fabrication by hot processing, where an ingot is converted into general mill products such as billets, bars, plates or sheet

4) Secondary fabrication by hot or cold processing for obtaining final shapes from mill products

In fact 95% of titanium ores dug on yearly base are used as the oxide for pigments and paints production. Only 5% is turned into ingot, and afterwards into metallic titanium semi-finished products.

Titanium is expensive to refine, process, and fabricate. In terms of the processing cost of materials per cubic inch, titanium is five times more expensive to refine than aluminum, and more than ten times more expensive than aluminum to form ingots and fabricate finished products[15].

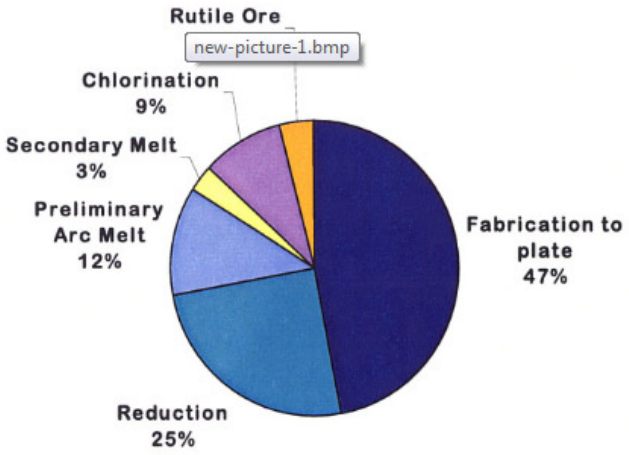

Fig. 2-5 – Impact of single production phases on the final cost of hot rolled titanium plate[16]

Of all the stages of production, fabrication is the most costly, followed by extracting sponge from ore. Assuming that the Kroll process is used for sponge production and VAR is used for ingot production, Kraft (2004) [16]calculated the cost composition of the conventional mill processing of a one inch thick titanium alloy plate. Fabrication is the largest cost factor, accounting for 47% of the mill product cost. Sponge production is the second largest cost, accounting for about one third of the total. The ingot melting process makes up approximately 12% of the production cost, while rutile ore accounts for 4 %[17].

[15] P.C.Turner and J.S.Hansen - An Assessment of Existing Titanium Technologies - Albany Research Center, Department of Energy, July 28, 1999

[16] Kraft, E. - Summary of Emerging Titanium Cost Reduction Technologies - 2004, EHK Technologies for ORNL: Vancouver, WA. p. 1-59.

[17] S. Seong, O. Younossi, , B. W. Goldsmith - Titanium: Industrial base, price trends, and technology initiatives – Rand Corporation (2009) – pp. 15 - 16

2.3 Classification of Ti alloys

Like iron, pure titanium can exist in two crystalline forms: hexagonal close-packed (HCP) below 883° C and body-centered cubic (BCC) at higher temperatures up to its melting point, which is 1668 °C. Because its atomic diameter is similar to many common metals such as aluminum, iron, tin, and vanadium, titanium can easily be alloyed to improve its properties. This transformation temperature, known as the beta transus temperature, can be raised or lowered depending on the type and amount of impurities or alloying additions.The allotropic behavior and the capacity to alloy with many elements result in titanium alloys that have a wide range of mechanical and corrosion-resistant properties.

Generally speaking, all the alloying elements presenting an atomic radius within the range 0,85 – 1,15 of the atomic radius of Ti (which is equal to 176 pm) are combining with the base metal by substitutional mechanism. Rather, elements with an atomic radius less than 0.59 that of Ti occupy interstitial sites, and also have substantial solubility (e.g. H, N, O, C)[18]. The ease with which solutes dissolve in titanium makes it difficult to design precipitation–hardened alloys.

The alloying elements can be categorized according to their effect on the stabilities of α and β phases (Fig. 2-6).

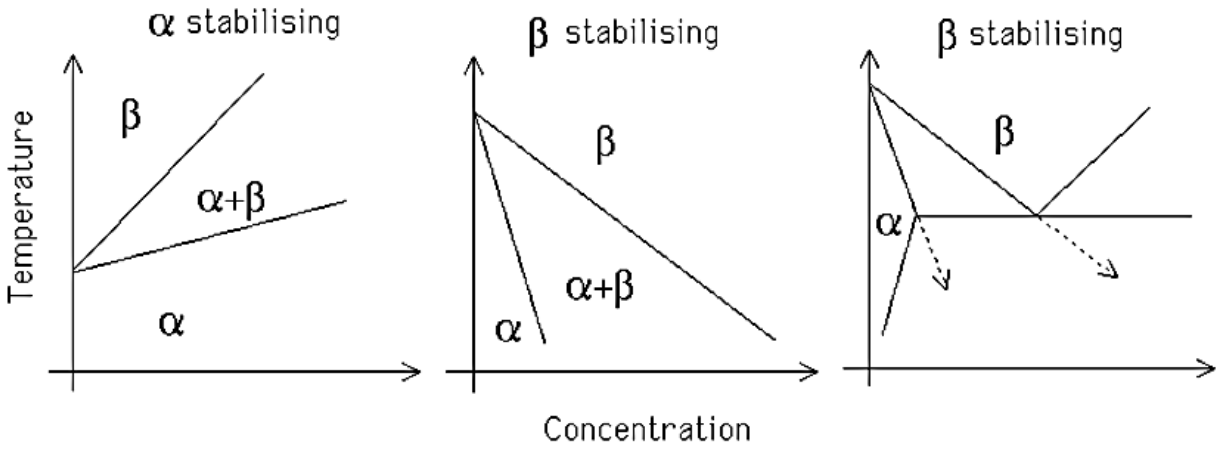

Fig. 2-6 – Effects of alloying elements in phase diagram modification[18]

In the following paragraphs, the effects of the major alloying elements will be evaluated and presented in detail, also considering their impact on the basic properties of the final materials. Knowing the basic microstructure of a Ti alloy is extremely important, because these alloys are classified according to the amount of alpha and beta retained in their structures at room temperature. Classifications include commercially pure, alpha, alpha-beta, and metastable beta alloys.

[18] H. K. D. H. Bhadeshia - Titanium & its Alloys - Materials Science & Metallurgy Part II, Course C9 – pp. 4-5

2.3.1 Commercially pure alloys

Commercially pure titanium alloys are used primarily for applications where a good corrosion resistance is required. They are also useful in applications requiring high ductility for fabrication but relatively low strength in service. Yield strengths range goes from 170 to 520 MPa.

According to ASTM standards, there are four different commercially pure titanium grades; the main difference between them is the oxygen and the iron content, which is determining the strength levels and the ductility of commercially pure titanium. In detail, the oxygen content varies between 0,18 – 0,40 %, while the iron content is between 0,2 – 0,5%; usually the material is supplied in mill annealed condition[19].

Grade 1 titanium is the softest and most ductile of these pure titanium grades. It possesses the greatest formability, excellent corrosion resistance and high impact toughness. Grade 2 is the most popular of the commercially pure titanium industry, thanks to its varied usability and wide availability.

In the higher-strength grades, Grade 3 and 4, oxygen and iron are intentionally added to the residual amounts already in the sponge to provide extra strength and higher mechanical properties.

The CP grades show good formability and weldability, excellent corrosion resistance and can be used in for application in temperature up to 400 °C. Common applications of CP alloys are tubing, tanks and fittings for chemical industries and desalination plants

2.3.2 Alpha Ti Alloys

Alpha stabilizers are those elements that increase the beta transus temperature by stabilizing the alpha phase. In this group are included aluminum, oxygen, nitrogen, and carbon. Aluminum, the main alpha stabilizer, increases also tensile strength, creep strength, and elastic modulus.

Titanium alpha alloys have good fracture toughness and creep resistance combined with moderate mechanical strength, which is retained at increased temperatures up to 600ºC[20]. These alloys can be easily welded, but their workability in cold state is difficult due to anisotropic behavior which will be analyzed in detail in paragraph 2.4.3.

Alpha alloys cannot be heat treated to develop higher mechanical properties because they are single-phase alloys.

The main application fields for these alloys are steam turbine blades, autoclaves and other process equipment vessels, high pressure cryogenic vessels, aircraft engine compressor blades, missile fuel tanks and structural parts, operating for short times up to 600ºC, airframe and jet-engine parts, welded stator assemblies and hollow compressor blades[21].

[19] Titanium alloys guide – RMI Titanium Company
[20] H. K. D. H. Bhadeshia - Titanium & its Alloys - Materials Science & Metallurgy - Part II Course C9 pp.7
[21] Flake. C. Campbell – Elements of metallurgy and engineering alloys – Ed. ASM international (2008) pp. 530

2.3.3 Beta Ti Alloys

The class of titanium alloys generically referred to as "beta alloys" is a family of materials containing enough beta stabilizer alloying elements to retain 100% beta microstructure after quenching. The most used beta stabilizer elements used for creating these alloys are molybdenum, vanadium, iron, niobium, chrome and silicon.

Since they offer the highest strength-to-weight ratio and deepest hardenability of all Ti alloys, one might expect them to compete favorably for a variety of aerospace applications. To the contrary, however, with the exception of few successful applications, the beta alloys have remained a very small segment of the industry (just approximately 1% of the total USA titanium market for mill products)[22].

Referring to Fig. 2-7, alloys which lie between the critical level of beta stabilizer content β_C and the point β_S are still in the two phase region and belong to the family of beta metastable titanium alloys. These alloys can achieve beta 100% beta structure after quenching, but being this phase metastable, it will precipitate a secondary phase (normally alpha) upon aging.

Alloys to the right of the point β_S are considered beta stable alloys, and so no secondary re-precipitation can occur; this mean that beta stable alloys cannot be hardened by ageing.

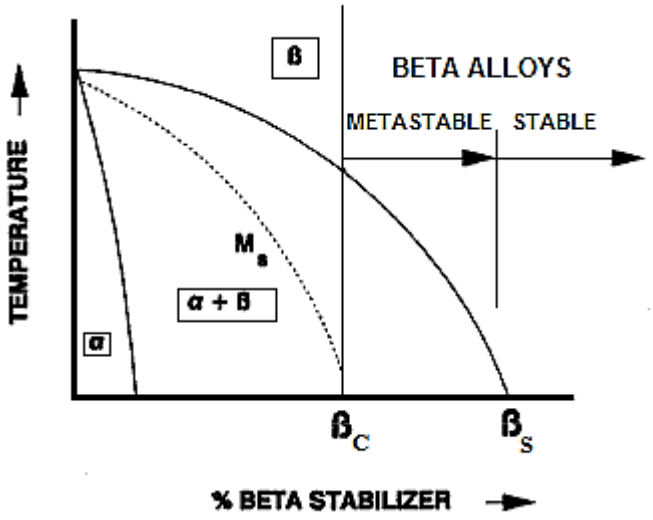

Fig. 2-7 – Binary phase diagram of titanium and Beta stabilizer[22]

There is a common practice for determining the beta stability of an alloy presenting several alloying elements. By arbitrarily using molybdenum as a baseline, we can define the parameter *Moly Equivalent* as follow:

$$Mo\ Eq. = Mo\% + 0{,}67\ V\% + 0{,}44\ V\% + 0{,}28\ Nb + 1{,}6\ Cr - Al\% \qquad (1.1)$$

[22] Paul J. Bania - Beta Titanium Alloys and Their Role in the Titanium Industry – Journal Of Material, July 1994, Vol. 46, Issue 7, pp. 16-19

In general, a Mo Eq. value above about 10.0 is required to stabilize beta upon quenching. It is not clear what Mo Eq. is required to produce a truly stable beta alloy, since even alloys with Mo Eq. = 30 are unstable at elevated temperatures under applied stress.

As with most alloy systems, beta alloys offer advantages and disadvantages. Beta alloys typically exhibit outstanding cold formability. However, their low modulus and high strength can often result in a high springback, which must be accounted for in tooling design

Because of the high degree of stability of the beta phase, a water quench is often not required for solution treating; air cooling greatly reduces distortion, as does the low solution temperature. However, beta alloys are notorious for surface oxygen contamination, even in supposed "vacuum" heat treatments, so care is needed to remove such contamination, usually by pickling.

While beta alloys usually exhibit excellent fill characteristics during casting, segregation may limit the utility of some alloys.

2.3.4 Alpha/Beta Ti Alloys

Titanium alpha+beta alloys are materials presenting a biphasic mixed structure at room temperature. The mutual quantity of the two phases is depending on the content of alpha stabilizer or beta stabilizer elements.

A wide variety of microstructures can be generated in alpha+beta alloys by adjusting not only the chemical composition, but also the thermomechanical process parameters[23]. In fact this family of alloys can be submitted to a large variety of heat treatments, which allow obtaining many different types of microstructures and mechanical characteristics. The most common heat treatment is solution treating (with heating at a temperature near to β transus) followed by an ageing cycle which allow having a re-precipitation hardening of different composites in the titanium matrix.

The most commonly used titanium alloy is Grade 5 (Ti-6Al-4V), capable of withstanding temperatures up to 450°C and used in aircraft ducts, airframes and landing gear as well as in space vehicles[24]. Grade 23 (Ti-6Al-4V ELI), developed from Grade 5 reducing the content of interstitial elements as oxygen and hydrogen, offers improved ductility for cryogenic service and is used on airframes, space vehicles and medical applications. Grades 5 and 23 are examples of alpha-beta alloys, which offer a good compromise between the virtues of alpha alloys (lighter weight, higher creep resistance) and those of beta alloys (higher strength, lower creep resistance); their use account more that 50% of all titanium tonnage in the world.

[23] L. Meekisho, X. Yao, G. E. Totten - Quenching Theory and Technology, Second Edition – Ed. Taylor and Francis Group LLC – pp. 86-87
[24] VV.AA. – Welding Titanium: a designers and users handbook – Titanium Information Group (1999) pp.2

2.3.5 Heat resistant titanium alloys

Titanium-based alloys represent competitive and attractive materials for the aerospace and automotive industry due to their superior strength-to-weight ratio and their corrosion resistance. However, due to the rapid oxidation of these alloys occurring at temperatures above 600 °C, their use in applications where higher operating temperatures are request (i.e. compressor blades and other structural parts of jet engines) is limited[25]. As a matter of fact, at these temperatures the titanium alloys, and particularly those presenting α/β mixed structure, are susceptible of rapid oxidation in air as well as α-case formation. Alpha case is an oxygen-rich Ti hexagonal solid solution caused by diffusion of the interstitial element into the base metal which modifies the original structure near the surface. These modifications due to the inward diffusion of oxygen and particularly the preferential stabilization of the more brittle alpha-case considerably reduce the mechanical properties of titanium alloys above 500 °C by the increased tendency of crack formation under stress[26].

The manufacturers of these components designed for elevated temperature applications, are obviously searching for methods and new alloy for reducing the high temperature oxidation rate, because this would allow for a higher operating temperature limit.

It has been found that the oxidation behavior of Ti, dominated by scale formation and cracking, can be improved by additions of appropriate alloying elements, such as Al, Si, Nb, Ta, Zr, Sn, or Cr. The beneficial role of these elements can be explained by several mechanisms:

- reduction of oxygen diffusion and solubility in the metallic matrix
- decreasing inward diffusion of oxygen through the scale
- formation of a protective-oxide barrier of the alloying element
- modification of the mechanical properties and improving oxide–scale adherence

The protective nature of these elements depends on the temperature, atmosphere, and their concentration. The most diffused titanium alloys specifically meant for heat resistant application are mainly alpha or near alpha based.

The first generation of these alloys, put on the market during 1990s, uses aluminum as mail alloying element. Anyway, the Al content must be maintained below at a certain level, due to the fact that its diffusion coefficient phase is lower than the Ti α-phase more than two orders of magnitude. Generally it is observed that the creep properties and oxidation resistance of the alloy increases with the increasing of Al content, while its plastic deformation ability is reduced[27]. Therefore, in order to avoid precipitation of brittle intermetallic alloy compounds Ti_3Al, a coefficient known as "*aluminum equivalent*" can be determinate as follow:

$$Al\ Eq. = Al\% + \frac{1}{3}\,Sn\% + \frac{1}{6}\,Zr\% + 10\,(O\% + C + 2N\%) \qquad (1.2)$$

[25] D. Vojtěch, M. Mort'aniková, P. Novák - Kinetic and Thermodynamic Aspects of High-Temperature Oxidation of Selected Ti-Based Alloys – Defect and Diffusion Forum, Vol. 263, pp. 123-128 (2006)
[26] A. M. Chaze, C. Codett - Journal of Less Common Metals - Vol. 157, pp. 55 (1990)
[27] T.R. Bieler, R.M. Trevino, L. Zeng – Alloys: Titanium – Encyclopedia of Condensed Matter Physics (2005) – pp. 67-69

It has been shown by many authors that the addition of an appropriate amount of silicon to titanium effectively increases the high temperature oxidation resistance, just like the wear and creep resistance.

The role of silicon in the high-temperature oxidation of Ti–Si alloys is not known completely, but it is generally believed that Si[28]:

- reduces the depth of oxygen penetration into a metallic substrate
- reduces the diffusion rate of oxygen in the scales,
- slows down the rate of rutile recrystallization and stratification, thus reducing the fraction of porosity in the scales.

In the traditional titanium alloys specifically developed for working at elevated temperatures, the silicon content is limited due to 0.3 – 0.55 in mass, due its limited solubility in α-titanium.

Another element which is often used in heat resistant titanium alloy formulation is Nb. The primary scope of its addition is preventing the grain size growth during long periods of exposure at elevated temperature, and also helping the formation of a more compact and adherent scale[29].

Generally speaking, all the beta stabilizer elements Mo, Nb and V can be used for to improving the alloys creep resistance by segregating around dislocations and thereby blocking the mechanism of slip movements.

2.3.5.1 Ti-Fe-Si-O alloy

The application of titanium and its alloys to original-equipment manufacturers (OEM) automotive and motorcycle parts has grown dramatically in the last ten years. Exhaust system applications, including mufflers and exhaust pipes, have been a prime target for titanium in automobiles and motorcycles. In addition to weight savings, the appearance of titanium appeals to certain motorcycle customers. Price, and in some instances, temperature capability, are apparent obstacles to the application of titanium in automotive exhaust systems.

Ti-Fe-Si-O is a highly formable titanium alloy designed specifically for automotive exhaust sheet and tube materials. This material is a Ti-Fe-Si-O alloy, in which the maximum content of iron is 0.5%, silicon, 0.6%, and oxygen, 0.15% (in weight percent)[30]. The cold rolled sheet metal coils are produced starting from a slab melted using the electron-beam single-melt process (EBSM). The material is using as main alloying elements silicon, with the aim of enhancing oxidation resistance, together with oxygen and iron for increasing mechanical properties.

---

[28] D. Vojtěch, T.Kubatík, H. Čížová - Application of Silicon for a Protection of Titanium against High-Temperature Oxidation - Materials Science Forum, Vol. 482, pp. 243 – 246

[29] P. Perez, V. A. C. Haanappel, M. F. Stroosnijder - The Effect of Niobium on the Oxidation Behavior of Titanium in Ar/20% O2 Atmospheres - *Oxidation of Metals, Vol. 53, Nos. 5/6, 2000*

[30] Yoji Kosaka, Stephen P. Fox, and Kurt Faller - Newly Developed Titanium Alloy Sheets for the Exhaust Systems of Motorcycles and Automobiles – Journal of Materials, November 2004

Compared with CP Ti Grade 2, Ti-Fe-Si-O demonstrates improved oxidation resistance, higher strength and reduced deterioration after exposure at elevated temperatures, yet with similar forming and welding characteristics.

The microstructures for selected alloys after exposure at 700 °C for 100 h are given in Figure 2-8 and 2-9. It is important to note that the addition of silicon in Ti-Fe-Si-O alloy allows maintaining a fine grain structure with a limited amount of scale formation after the exposure.

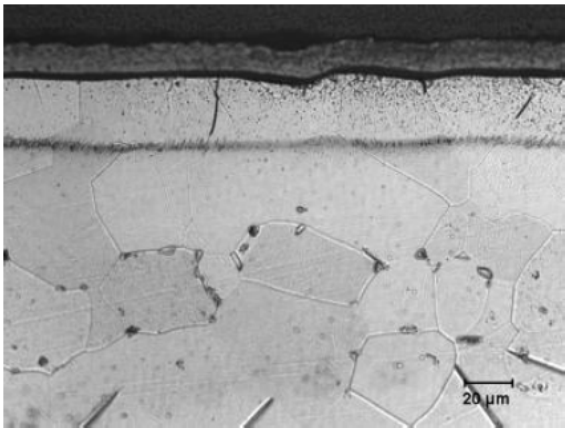

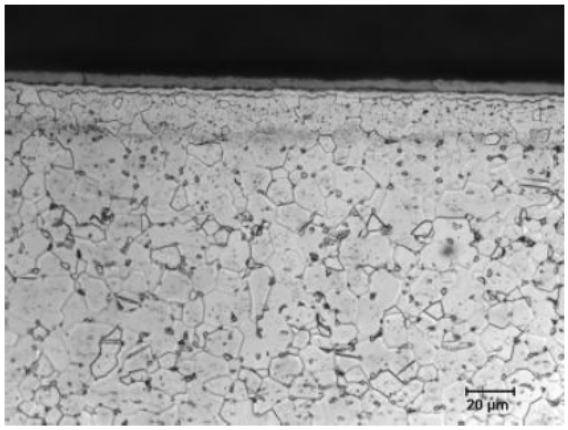

Fig. 2-8 and 2-9 – Microstructures of Gr. 2 and Ti-Fe-Si-O after exposure @700 °C for 100 hours (I*mage courtesy of Timet Titanium Corp., USA)*

The strength of Ti-Fe-Si-O alloy at room temperature is significantly higher than titanium Grade 2, which is primarily coming from the addition of iron; its superior strength over CP titanium extends to elevated temperatures. Parameters that are critical to formability such as n-value or R-value are similar to those for Grade 2. The alloy is delivered in annealed condition (annealing temperature equal to 780 °C for 7 minutes).

A complete characterization of the material in terms of mechanical and plastic properties is shown in Chapter 3 of present work.

2.3.5.2 Ti-Al-Si-Nb alloy

Ti-Al-Si-Nb alloy is one of the best-performing alloys for exhaust systems applications, and is basically obtained by improving the original formulation of the standard alloy Grade 37 (Ti 1,5 Al) with the addition of specific alloying elements as silicon and niobium.

This alloy presents also very good plastic properties significantly improved in comparison with Grade 37 and fully aligned with the one of the most formable pure grade 2. The addition of silicon has a big impact in enhancing the oxidation resistance, while the presence of niobium is helpful for controlling the grain growth during long periods of exposure at elevated temperature. Lower content of aluminum also reduces descaling problems after long exposures.

The behavior of Ti-Al-Si-Nb alloy at different level of temperature for 200 hours of exposure, compared with pure Grade 2 and Grade 37 alloy, is shown is Fig. 2-10.

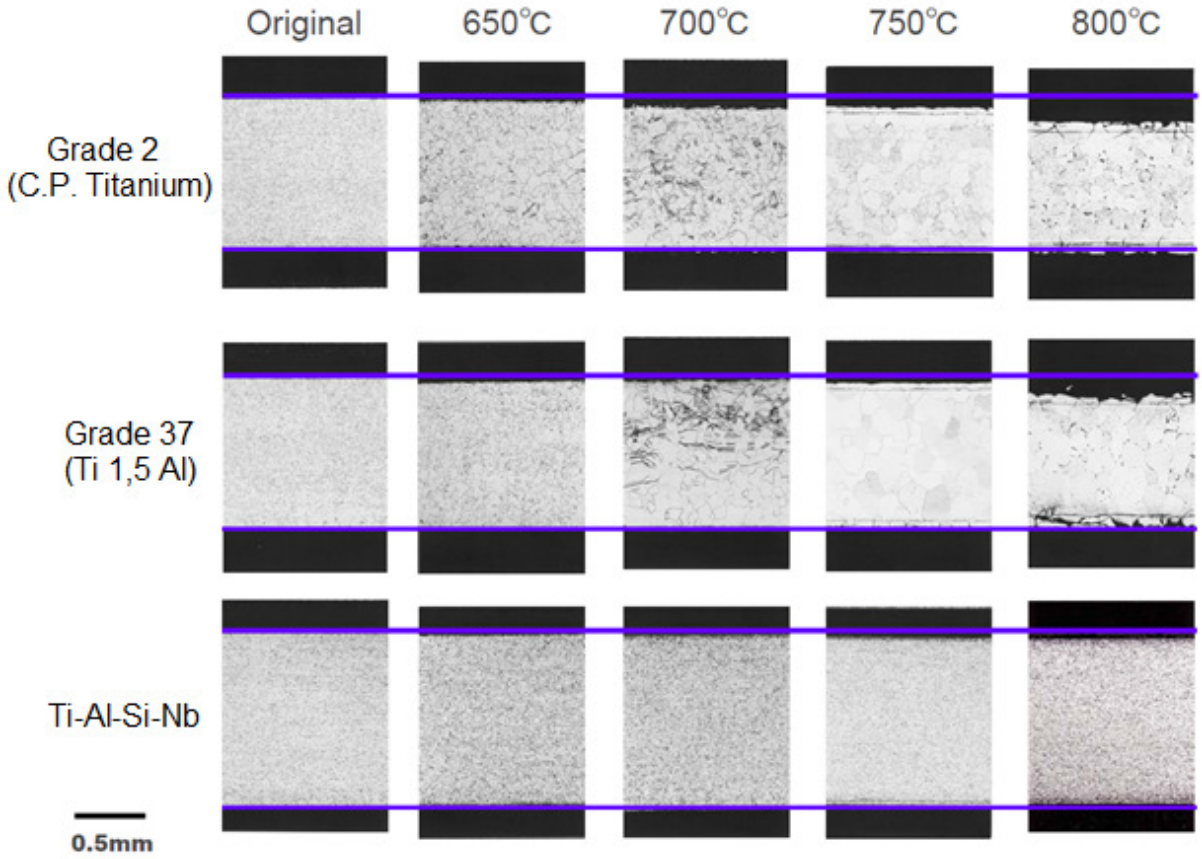

Fig. 2-10 – Grain growth and thickness reduction after 200h exposure

(*Image courtesy of Kobe Steel Corporation LTD, Japan*)

The strength of Ti-Al-Si-Nb at room temperature is approximately 50% higher than titanium Grade 2. Is also interesting pointing out that β transus temperature is raised 22 °C versus the one of commercially pure Grade 2. The alloy is delivered in annealed condition (annealing temperature equal to 850 °C for 3 minutes).

A complete characterization of the material in terms of mechanical and plastic properties is shown in Chapter 3 of present work.

This specific alloy was used for the production of OEM Toyota Lexus LF-A muffler. Lexus LF-A is the most expensive supercar ever produced in Japan; it went on the market in 2010 and was produced in just 500 pieces[31].

[31] K. Tada, Y. Itsumi - Characteristics of Low-cost Heat-resistant Titanium Alloy for Automobile Exhaust Systems, KS Ti-0.9SA - Kobe Steel Engineering Reports, Vol. 60 No. 2, Aug. 2010

2.4 Deformation mechanisms in HCP metals: slip & twinning

The specific deformation mechanisms in metals with a hexagonal close packed (hcp) crystal structure are less well understood than those in cubic metals which usually have a large number of independent slip systems. An important role in hcp metals is played by the dimensions of the crystal lattice and especially from the c/a ratio. Generally speaking, the deviation of the material from the ideal c/a ratio, which is 1.633, determines the dominant slip plane. This simple rule is based on the observation that slip occurs more easily on the family of planes with the largest interplanar spacing, which obviously depends on the c/a ratio. A material with c/a ratio greater than ideal is thought to deform primarily on basal planes, whereas one with a c/a ratio less than ideal is thought to deform primarily on prismatic planes.

In pure titanium c/a ratio is equal to 1,587; the reduced c/a ratio of alpha based titanium leads to a larger space between prismatic planes. This causes the packing density of this specific slip planes to increase compared to the density of basal planes and thus enhancing slip on prismatic planes rather than basal[32] via the activation of dislocations with $\langle a \rangle$ type Burgers vector.

Prismatic and basal planes present three slip systems each; however, only two are independent of each other, resulting in only four independent slip systems. Slip on pyramidal planes does not increase the number further, since this glide is composed of a prismatic and a basal component, and therefore cannot be considered an independent slip system. However, according to the Von Mises criterion, at least five independent slip systems are required for accommodating a homogeneous plastic deformation of polycrystalline materials. This means that, in order to accomplish Von Mises criterion, a fifth slip system presenting a so called "non basal Burger vector" must be activated. Generally the slip plane presenting the $\langle c + a \rangle$ type Burger vector is the pyramidal first order with slip direction <1123>; however this slip plane can be activated only with high resolved shear stress.

A summary of the various slip systems active in alpha titanium is provided in Fig. 2-11.

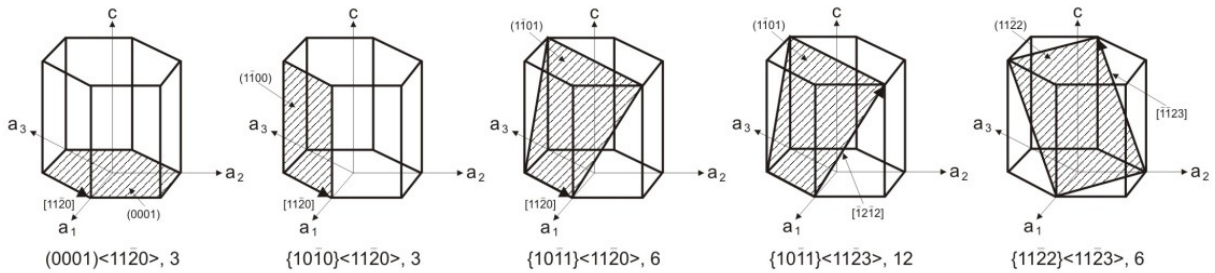

Fig. 2-11 – Slip system in Ti alloys (source www.interchopen.com)

Predicting the anisotropy of polycrystals involves modeling of single crystals and execution of a physically correct averaging technique for combining single crystal properties into polycrystal

[32] C. Leyens, M. Peters - Titanium and Titanium Alloys – Ed. DLR (German Aerospace Center), pp.6

behavior. Plastic yielding of single crystals generally occurs by shearing on selected crystallographic slip systems according to Schmid law[33]. Experiments showed that slip occurs when the shear stress acting in the slip direction on the slip plane reaches some critical value called "Critical Resolved Shear Stress" (CRSS). This critical shear stress is related to the stress required to move dislocations across the slip plane. Referring to Figure 2-12, the resolved shear stress acting parallel to the slip direction of the considered slip plane can be defined as follow:

$$RSS = \frac{F \cdot \cos\lambda}{A/\cos\phi} = \sigma \cdot cos\lambda \cdot \cos\phi \qquad \text{"Schmid Law"} \qquad (1.3)$$

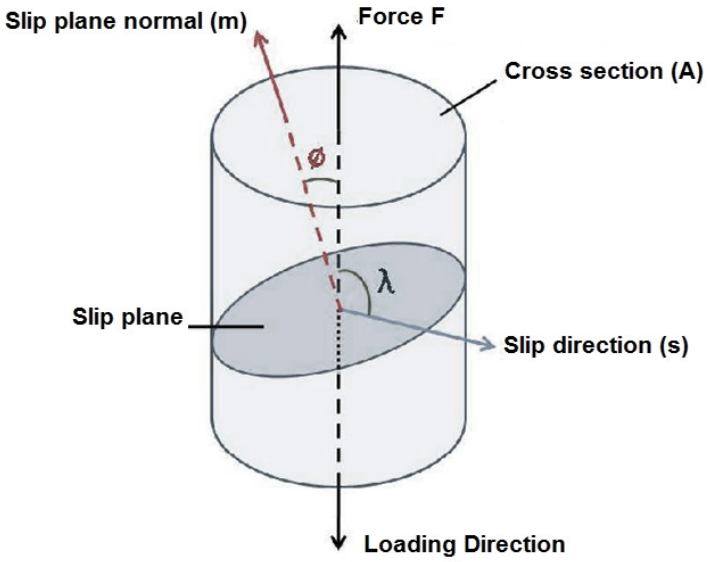

Fig. 2-12 – Schematic representation of Schmid Law[33]

In case of materials presenting HCP crystallographic structure, it is very important to consider the case of load applied parallel to c axis direction. With this specific configuration, basal slip system present angles ϕ=0° and λ=90°, while prismatic slip systems present ϕ=90° and λ=0°: it's easy to conclude that in both cases the resolved shear stresses are equal to zero and dislocation movements cannot be activated.

Considering the pyramidal slip system {1011}where dislocation with $\langle c + a \rangle$ Burger vector can move, both the angles ϕ and λ are approximately equal to 45°: in this condition deformation is difficult to activate at room temperature, since it shows a high value of CRSS.

The absolute value of CRSS is strongly dependent on type of alloys and temperature at which the deformation is taking place.

[33] A. Tuncer - The role of texture evolution and strain hardening on the anisotropic response of polycrystalline metals - Master's Thesis, 2009, pp. 3-4 - Master of Science (M.S.)

The aforementioned considerations about only four independent slip systems and the fact that activation of dislocation movement is strongly connected to loading direction leads to the conclusion that a different mechanism than slip must be activated in order to accomplish Von Mises criterion. This specific mechanism is twinning, a deformation mechanism where a part of the atomic lattice is deformed so that it forms a mirror image of the undeformed part near to it[34]. The crystal plane of symmetry between deformed and undeformed part is called "*twin plane*". Twinning, like slip, occurs along specific directions, called "*twin directions*". The mechanism is similar to slip mechanism and results in the elongation of the crystal in the direction of load application; again twinning can occur when shear stress surpasses a critical value.

The basic differences between the crystallographic slip and deformation twinning are the following[35]:

- In slip mechanism the atoms on one side of the slip plane all move of the same distance, while in twinning atoms move of a distance which is proportional to their distance from the twin plane
- For slip, the crystallographic orientation above and below the slip plane is the same both before and after the deformation; for twinning, there will be a reorientation across the twin plane
- On a twinning plane deformation can happen in one direction only. This limitation does not exist in the case of slip, where on a slip plane shear can happen in two opposite directions
- While deformation twinning changes the lattice orientation of the material abruptly, the change in the lattice orientation of the material caused by slip is gradual

Consequently, it can be stated that in titanium alloys presenting hcp crystal structures always both slip and twinning mechanisms are occurring simultaneously during plastic deformation.

In hexagonal close packed metals, presenting low number of independent slip planes, deformation twinning is an important phenomenon because it can re-orient the slip plane original position into one more favorable in terms of plastic deformation. Consequently, it can be deduced that twinning preferentially operates when the position of the slip planes are unfavorable with respect to the external loading. However twinning propensity, frequency, density and morphology can vary among grains of the same orientation and under the same loading conditions. These characteristics appear to be highly sensitive to both microstructure (grain size, orientation, dislocation density, alloy content) and applied loading conditions (strain rate, temperature and stress level)[36].

Although there are no doubts regarding the occurrence of deformation twining in alpha titanium alloys in a wide range of temperature and strain rate conditions, there exist several gaps in current

[34] Mechanism of Twinning in Metals - *Nature* 123, 262-263 (16 February 1929)
[35] M. Tisza Physical Metallurgy for Engineers - *Ed. ASM International, 2nd Edition (2002)* – pp. 142
[36] I. J. Beyerlein, C. N. Tomé - Probabilistic twin nucleation model for HCP polycrystalline metals - *Proc. R. Soc. A* (2010) pp. 2517–2544

literature in our understanding of the role played by deformation twins in the plastic and strain hardening response exhibited by this metal. This is due to the fact that for a single crystal of a given orientation with respect to a uniaxially applied stress, some twin systems will only be activated in tension, while others will only be activated in compression. Specifically, in alpha bases titanium alloys can be identified four preferential twinning systems which can contribute to deformation: two tensile ({1012 } and {1121}) and two compressive ({1122} and {1011}) twinning modes[37]; these systems are shown in Figure 2-13.

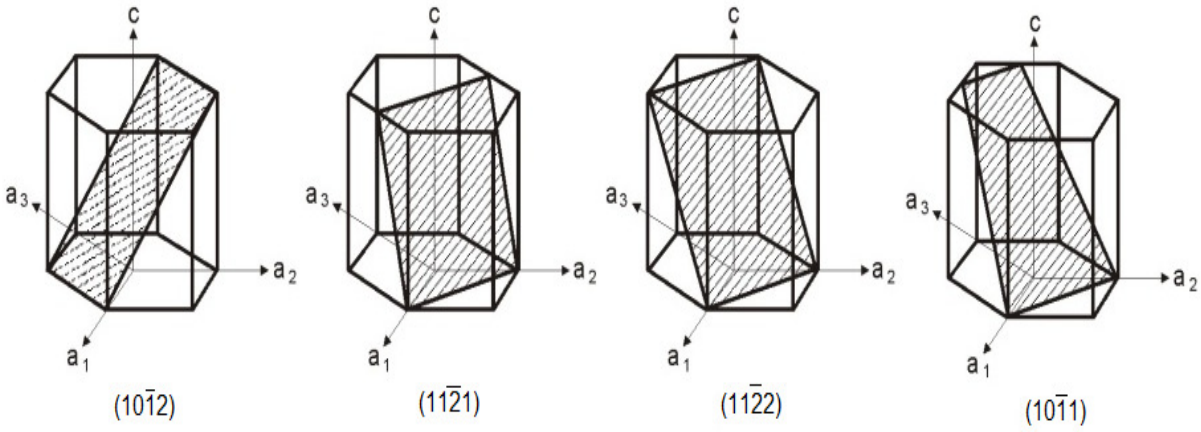

Fig. 2-13 – Twin deformation planes in HCP titanium (source www.interchopen.com)

At room temperature, deformation twinning has a lower CRSS than the pyramidal $\langle c + a \rangle$ slip system, and it can provide the fifth independent plastic deformation mechanism to satisfy the Von Mises criterion, allowing the plastic deformation also in case of loading direction parallel to *c* axis. At elevated temperature, the CRSS of pyramidal $\langle c + a \rangle$ slip and other non-basal slip systems decreases, and they can provide the fifth independent plastic deformation mechanism.

The great variety of the possible deformation modes represents a significant difficulty in the determination of the nature and the physical characteristics of the deformation mechanisms for a given alpha titanium alloy. The first problem is the identification of the operating slip and twinning system families. Another problem arises when the activity of more than one deformation mode (i.e. more than one slip system family, or twinning family) is detected. Namely, the relative strengths of these deformation modes are strongly connected with CRSS values. The knowledge of the CRSS values is indispensable in the calculation of any mechanical parameter related to plastic deformation (Lankford parameter, yield surface, texture development, etc.). In table 2-I an overview of CRSS values for different slip and twinning mechanism is presented.

[37] S.L. Semiatin, S.V. Shevchenko, O.M. Ivasishin, M.G. Glavicic, Y.B. Chun, S.K. Hwang - Modeling and simulation of texture evolution during the thermomechanical processing of titanium alloys - ASM Handbook, Vol. 22–Modeling and Simulation: Processing of Metallic Materials

System	$\{hkil\}\langle uvw\rangle$	crss	Twinning shear
Slip			
Prismatic	$\{10\bar{1}0\}\langle\bar{1}2\bar{1}0\rangle$	1	
Basal	$\{0001\}\langle2\bar{1}\bar{1}0\rangle$	2.5	
Pyramidal $\langle c+a\rangle$	$\{10\bar{1}1\}\langle\bar{1}\bar{1}23\rangle$	2.5	
Twinning			
Tensile	$\{10\bar{1}2\}\langle\bar{1}011\rangle$	1.2	0.167
Compressive	$\{2\bar{1}\bar{1}2\}\langle2\bar{1}\bar{1}3\rangle$	1.7	0.225

Tab. 2-I – RCSS for slip and twin modes in Ti single crystal[41]

The addition of iron (substitutional element) does not lessen the twinning ratio, despite the grain size reduction caused by this alloying element. As opposed to this, increasing concentrations of solute atoms in alpha titanium, such as oxygen or aluminum, suppress the occurrence of twinning. Therefore, twinning as a deformation mode to allow shape changes parallel to the c-axis only plays a major role in pure titanium or in CP titanium with low oxygen concentrations[38].

Generally, has been also observed in different papers[39,40] that in alpha titanium twinning becomes a more dominant mode of plastic deformation as the temperature is decreased. If the stress required for twinning rises less rapidly with decreasing temperature than the flow stress for slip, a transition to twinning will be expected. There is low mobility of lattice dislocations at low temperatures, which inhibits slip. However, the stress required for twinning varies slowly with temperature which means that twinning is not a thermally activated process.

Concluding, the occurrence of deformation twins has been correlated also to major changes in both the strain hardening response[41] and the crystallographic texture[42] evolution in titanium alloy.

2.5 Preferred crystallographic orientation in HCP metals

Metals are usually crystalline in the solid state. In a polycrystalline aggregate each grain is an individual crystal differing from its neighboring grains in lattice orientation. At any stage of the manufacturing process, the crystals are seldom oriented completely at random. However, during subsequent plastic deformation, the crystals rotate toward certain stable orientations. Upon recrystallization, new crystals form and grow preferentially at the expense of the deformed matrix crystal. All these processes lead to the development of non-randomness of the grain orientations in a polycrystalline aggregate, known as preferred orientations, or “texture”.

[38] G. Lutjering, J.C. Williams – Titanium 2nd Edition – Ed. Springer – pp. 22
[39] Su Leen Wong - Deformation Twinning: Mechanisms and Their Role in Crystal Plasticity Models -
[40] J. W. Christian, S. Mahajan - Deformation Twinning. Progress in Materials Science 39, 1-157
[41] A. A. Salem, S. R. Kalidindi, R. D. Doherty, and S.L. Semiatin - Strain Hardening Due to Deformation Twinning in α-Titanium: Mechanisms - Metallurgical and materials transactions - volume 37a, January 2006— pp. 259
[42] M. J. Philippe, C. Eslingt, B. Hocheid - Role of Twinning in Texture Development and in Plastic Deformation of Hexagonal Materials - *Textures and Microstructures* – 1988, Vol. 7, pp. 265-301

A large number of polycrystalline materials display preferred orientation of crystallites. Such alignment has a profound effect on anisotropy of physical properties. Preferred orientation or texture forms during growth or plastic deformation and is modified during recrystallization or phase transformations.

Texture development in hexagonal metals has received a lot of attention because of the application of zirconium alloys in the nuclear industry and titanium alloys as structural materials in aerospace. In titanium alloys where the hexagonal phase predominates, the textures which develop are usually described in terms of the orientation of the basal plane (0001). The basal textures which develop in titanium alloys during deformation operations can be broadly classified as those in which the basal planes are parallel to the rolling plane and those in which the basal planes are normal to the rolling plane (Figure 2-14).

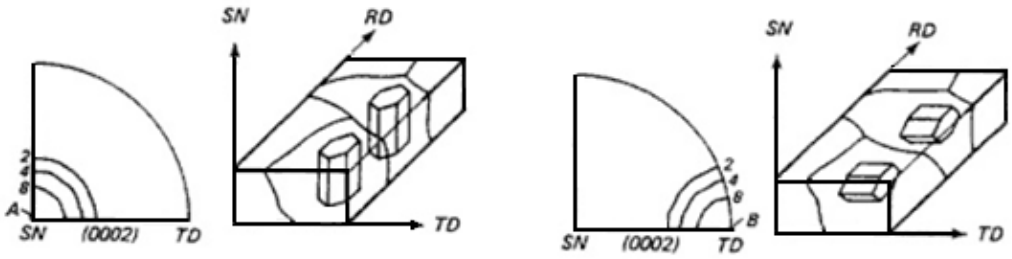

Fig. 2-14 – Example of hcp lattice basic orientations

The nature of the texture developed in a particular specimen depends from several factors; the ones who play the most important roles are the following[43]:

- Type and number of phases present in the alloy
- Type and quantity of alloying elements and impurities
- Type of manufacturing process (extrusion, rolling, casting, …)
- Process parameters (rolling ratio, rolling speed, …)
- Thermal treatments

All the aforementioned aspects are important in determining the final texture configuration of the material.

Generally, a textured material usually exhibits strong anisotropic properties. Depending on the nature of the texture and the intended use of the material, anisotropy may or may not be a desirable feature from the practical point of view. To fully utilize the anisotropy for one's own purpose, it is often necessary to "tailor-make" a texture for a particular purpose.

[43] U. F. Kocks, C. N. Tome, H. R. Wenk: *Texture and Anisotropy - Preferred Orientations in Polycrystals and their Effect on Materials Properties* - Cambridge University Press, (UK 1998) - pp. 203-204

2.5.1 Fiber texture

Wire and rod produced by drawing, swaging, rod rolling, or extrusion (constrained tensile deformation) usually develop preferred orientations that are uniaxial or fibrous. One or two specific crystallographic directions are oriented parallel to the wire or rod axis, whereas other crystallographic directions are distributed more or less at random around this axis (fiber texture). Frequently, a preferred orientation may also develop in the radial direction. In general, the texture is more diffuse and complex at the surface than in the interior. This usually arises from frictional forces at the surface during forming operations. The nature of the texture depends essentially on the crystal structure and on material and processing variables.

In hcp metals, there is an indication that the fiber texture of extruded rods or drawn wires depends on the c/a ratio. In those metals having c/a < 1.633 (ideal close-packing), such as Zr, Ti, and Be, the fiber axis is {1010}. For zinc (c/a > 1.633), the c axis is either parallel or nearly perpendicular to the rod or wire axis. In the latter case, there is no preferred alignment of the directions in the basal plane with the rod or wire axis. The axial ratio of Mg is very close to that of the ideal close-packing. Its fiber-texture characteristics are intermediate between those of Zn and Zr, Ti, or Be.

2.5.2 Rolling texture

Once again, the textures of cold-rolled hexagonal metals and alloys can be categorized into three groups according to their *c/a* ratios, namely materials with *c/a* ratios greater than, approximately equal to, and less than the ideal value of 1.633.

Metals and alloys with *c/a* ratios approximately equal to the ideal *c/a* ratio of 1.633, such as Mg, tend to form basal fiber textures (as in Fig. 2-15-a) during rolling. The origin of such textures may be understood in terms of the slip systems operating on basal planes.

Metals and alloys with *c/a* ratios above the ideal, such as Zn (1.856) and Cd (1.885), tend to exhibit textures with basal poles tilted ±15–25◦ away from the normal direction toward the rolling direction, the {1120} poles aligned with the rolling direction, and the {1010} directions pointed parallel to the transverse direction (Fig. 2-15-b). Such textures are due to the combination of basal slip and large-scale twinning. It should be noted that twining in HCP materials can be classified into two groups based on the critical *c/a* ratio of $\sqrt{3}$ *(*=1.732*)*, below or above this value the twin will form upon compression or tension, respectively[44].

Finally, the metals and alloys, possessing *c/a* ratio less than 1.633 such as Zr (1.589) and Ti (1.587), tend to form textures with basal poles tilted ±20–40◦ away from the normal direction toward the transverse direction, the {1010} poles aligned with the rolling direction, and the {1120} directions pointed parallel to the transverse direction[45]. In the latter case, slip on prismatic planes is largely

[44] *Y.N. Wang, J.C. Huang* - Texture analysis in hexagonal materials - *Materials Chemistry and Physics 81 (2003) 11–26*
[45] *Hsun Hu - Texture Of Metals*- Texture, 1974, Vol. 1, pp. 233-258.

responsible for textures of these types with basal pole spreading. In general, the *c/a* ratio reflects the activation of the different slip systems, as explained previously in Paragraph 2.4.

The rolling texture can be affected changing the process parameters, especially the rolling ratio plays a fundamental role; generally the tilting angle of basal plane towards normal direction is increasing with the increase of thickness reduction.

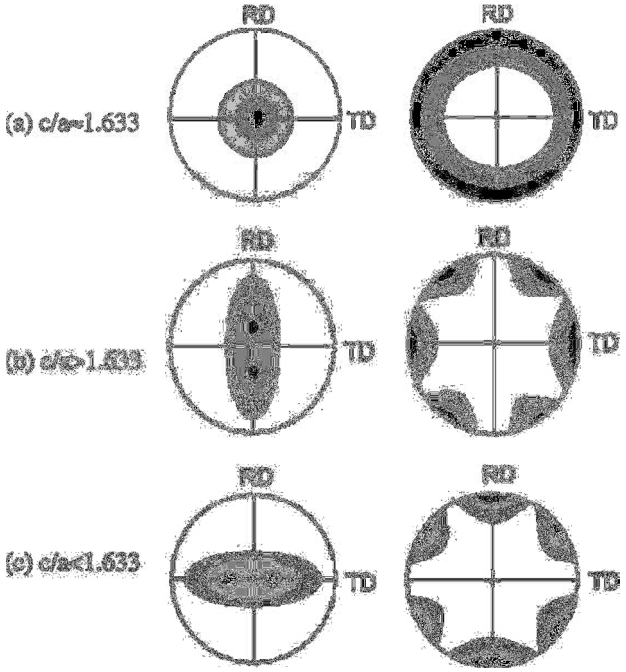

Fig. 2-15 – Influence of c/a ratio on rolling texture configuration[44]

2.5.3 Recrystallization texture

HCP metals and alloys exhibit a wider variety of recrystallization textures, which are strongly related to the initial deformation textures, annealing temperature and compositions. However, for titanium sheet metal cold rolled with conventional rolling ratios, the basal pole figures of recrystallized HCP metals are often essentially similar to those of rolling textures. The main basal texture components can be explained by the ~30° rotation about (0001) which makes orientation change between rolled and annealed textures[46]. In fact, closer examination frequently reveals other types of textural changes upon annealing.

This kind of change of texture during primary recrystallization process is called the continuous recrystallization or recrystallization in situ, and often occurs in highly deformed metals. Such continuous recrystallization is mainly contributed by the formation of subgrains via dislocation rearrangement and the growth and coarsening of cells and subgrains. The occurrence of continuous recrystallization or extended recovery is consistent with the high level of stacking fault energy in

[46]Z. S. Zhu, J. L. Cu., N. P. Chen - On the texture controlling methods and mechanical property anisotropy in commercially pure titanium sheet - Materials for Mechanical Engineering, 1994, 18(6): 8−1

titanium. It is well established that the extent of recovery is higher in metals or alloys with high stacking fault energy.

With increasing annealing time or temperature, the texture undergoes continuous changes. However, these textural changes, attributable mainly to normal grain growth, cannot be related to the parent texture by simple rotations[47]. Based on the microstructural changes and the mechanical softening observed during the annealing treatment, it has been suggested that the observed textural evolution is probably a result of extensive overlapping of the various stages (recovery, polygonization, recrystallization and grain growth) occurring during the annealing process.

[47] N. Bozzolo, N. Dewobroto, F. Wagner – Recrystallization in cold rolled titanium: mechanism of texture and microstructure evolution - Materials Science Forum Vol. 467 – pp. 453-558

CHAPTER 3
MECHANICAL CHARACTERIZATION: EXPERIMENTAL PROCEDURES & RESULTS

3.1 Materials

3.1.1 Chemical Composition

For chemical composition determination, a sample for every investigated alloy has been extracted from a cold rolled sheet metal. The chemical composition analysis has been performed using a spark optical emission spectrometer SpectroMaxx specifically calibrated for titanium alloys inspection.

The results obtained as average value of five different discharges are summarized In Tab. 3-I.

	Al (%)	**Si** (%)	**Nb** (%)	**Fe** (%)	**C** (%)	**Cr** (%)	**Ni** (%)	**Cu** (%)	**Ti**
Ti-Fe-Si-O	0,012	0,442	0,0040	0,190	0,100	0,0086	0,0095	0,0036	balance
Ti-Al-Si-Nb	0,498	0,368	0,184	0,039	0,014	0,0041	0,0060	0,0074	balance

Tab. 3-I – Chemical content of the alloys

The two alloys Ti-Fe-Si-O and TI-AL-SI-NB-EX are patented materials; the nominal composition declared from the producer is reported in Tab. 3- II & 3-III.

	Si (%)	**Fe** (%)	**C** (%)	**O** (%)	**H** (%)	**N** (%)	**Ti**
Ti-Fe-Si-O	0,10–0,60	0,50 max	0,1 max	0,02–0,15	0,015 max	0,03 max	balance

Tab. 3-II – Nominal chemical composition of Ti-Fe-Si-O alloy

	Al (%)	**Si** (%)	**Nb** (%)	**Fe** (%)	**C** (%)	**O** (%)	**H** (%)	**N** (%)	**Ti**
Ti-Al-Si-Nb	0,4–0,6	0,35–0,55	0,1–0,3	0,50	0,08	0,25	0,015	0,03	Bal.

Tab. 3-III – Nominal chemical composition of Ti-Al-Si-Nb alloy

Comparing the chemical composition obtained by spectrometer analyses with the nominal compositions prescribed from the producer it can be stated that both the alloys are compliant with the specifications.

3.1.2 Gas content determination

The gas content analyses have been performed on small samples (mass <1 gram) extracted from a cold rolled sheet metal. The test has been carried out using an Eltra O-N-H 2000 equipment and following the requirements of standards ASTM E1409[48] and ASTM E1417[49]. This instrument can

[48] ASTM E1409 - 08 Standard Test Method for Determination of Oxygen and Nitrogen in Titanium and Titanium Alloys by the Inert Gas Fusion Technique

alternatively operate as simultaneous oxygen/hydrogen or as simultaneous oxygen/nitrogen detector. Nitrogen and hydrogen are detected with a dual range thermal conductivity cell, while oxygen is measured by using an infrared cell. In this case, oxygen and nitrogen have been detected simultaneously and at the later stage hydrogen has been measured on a separate sample.

The results obtained as average value of three measurements are summarized In Tab. 3-IV.

	O (%)	**N** (ppm)	**H** (ppm)
Ti-Fe-Si-O	0,1318	54,6	11,8
Ti-Al-Si-Nb	0,078	38,4	29,6

Tab. 3-IV – Interstitial elements content

The content of interstitial elements is accomplishing the prescription of the alloy's producers.

3.1.3 Microstructural analysis

The samples for microstructural analysis with optic microscope Zeiss Axiovert have been encompassed in samples of epoxy resin and later grinded for flattening the surface. The samples preparation has been realized in three steps:

a) SiC grinding papers with P 320 grain density for 8 minutes
b) Diamond abrasive particles (3 μm) on cloth surface for 8 minutes
c) Colloidal Silica (0.05 μm) on cloth surface for 8 min

For etching the surface, a Kroll's reagent (92 ml H_2O + 6 ml HNO_3 + 2 ml HF) has been used; sample's etching was done by immersion for 20 seconds at room temperature. The microstructures of the two alloys are shown in Fig. 3-1 and 3-2.

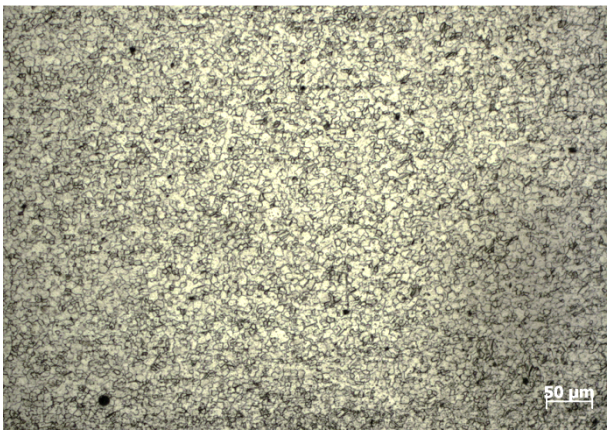

Fig. 3-1 – Microstructure of Ti-Al-Si-Nb alloy

Fig. 3-2 – Microstructure of Ti-Fe-Si-O alloy

From the microstructural analysis it can be seen that both the alloys present very fine equiaxial grains of alpha phase. The matrix is fully alpha; this type microstructure is typical for materials which have undergone an annealing treatment.

[49] ASTM E1447 - 09 Standard Test Method for Determination of Hydrogen in Titanium and Titanium Alloys by the Inert Gas Fusion Thermal Conductivity/Infrared Detection Method

3.2 Mechanical Characterization

3.2.1 Tensile Testing Procedure

The tensile tests were performed according with recommendations of international standard for uniaxial tensile test at room temperature EN ISO 6892-1[50], Annex B (Types of test pieces to be used for thin products: sheets, strips and flats between 0,1 mm and 3 mm thickness).

The equipment used for the tests is a universal tensile machine Instron 8032 with a maximum capacity of 100 kN; the elongation (strain 1) is measured by an extensometer with gauge length 80 mm, while the width reduction (strain) 2 is measured by a second extensometer with gauge length 15 mm. The specimens were extracted from production coils along three main directions: rolling direction (longitudinal), perpendicular to rolling direction (transverse) and 45° with respect to the rolling direction (diagonal).

The specimen's dimensions, according to the aforementioned standard, are:

- Initial gauge length L_0 = 80 mm
- Parallel sides length L_c = 120 mm
- Initial width b_0 = 20 mm
- Sheet thickness t_0 = 0,9 mm

Fig. 3-3 – Specimens orientation

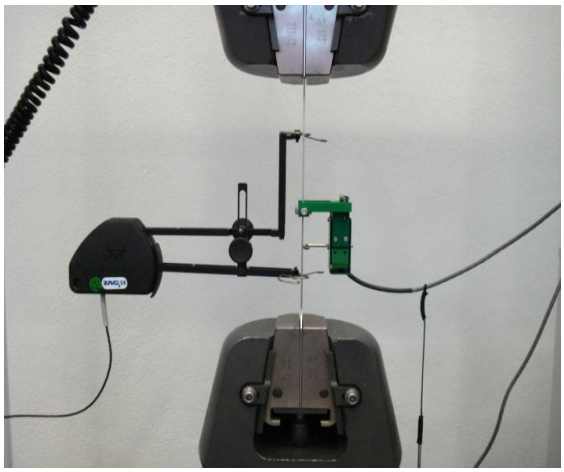

Fig. 3-4 – Specimen with strain gauges

The test conditions in terms of speed and type of machine's control are shown in Table 3-V.

Material	Elastic field	Plastic field
Ti-Al-Si-Nb	Type of control = Constant strain rate Speed = 0,00012 1/s up to 1% elong.	Type of control = Constant strain rate Speed = 0,0017 1/s after 1% elong. Transition time = 5 sec
Ti-Fe-Si-O	Type of control = Crosshead speed Speed = 0,3 mm/s up to 3,5% elong.	Type of control = Constant strain rate Speed = 0,001 1/s after 3,5% elong. Transition time = 2 sec

Tab. 3-V – Tensile testing conditions

The testing speed is different depending on the alloy, because in both cases the target was having a constant stress rate equal to 12 MPa/s in the elastic field and < 2 MPa/s in the plastic field.

[50] EN ISO 6892-1 (2009) - Metallic materials - Tensile testing - Part 1: Method of test at room temperature

3.2.1.1 Experimental results

The results obtained from the tensile tests outlined in previous paragraph are presented in Table 3-VI and Table 3-VII.

	R_p (MPa)	R_{EH} (MPa)	R_{EL} (MPa)	R_m (MPa)	A_g (-)	A_{80} (-)	R_{EH}/R_m (-)
L1	522,0	522,7	508,4	592,7	12,5	24,5	88,2
L2	521,4	521,6	508,8	593,6	12,6	25,1	87,9
L3	510,7	514,5	505,8	590,3	11,9	23,9	87,2
Av.	**518,0**	**519,6**	**507,7**	**592,2**	**12,3**	**24,5**	**87,7**
D1	526,1	537,4	517,6	561,4	9,3	25,2	95,7
D2	521,7	543,6	517,6	563,2	9,3	24,6	96,5
D3	522,0	549,6	518,9	564,0	9,3	25,5	97,4
Av.	**523,2**	**543,5**	**518,0**	**562,8**	**9,3**	**25,1**	**96,6**
T1	559,7	581,0	559,3	576,3	5,4	26,2	100,8
T2	552,1	576,1	543,2	573,5	6,2	24,5	100,5
T3	558,9	584,7	539,9	574,7	6,6	22,3	101,7
Av.	**556,9**	**580,6**	**547,5**	**574,8**	**6,1**	**24,3**	**101,0**

R_p = Yield point at 0,2%

R_{eh} = Upper yield point

R_{el} = Lower yield point

R_m = Tensile Strength

A_g = Non–proportional elongation at maximum force

A_{80} = Non proportional elongation at break (for specimens with L_0 = 80mm)

Tab. 3-VI – Tensile test results for Ti-Fe-Si-O alloy

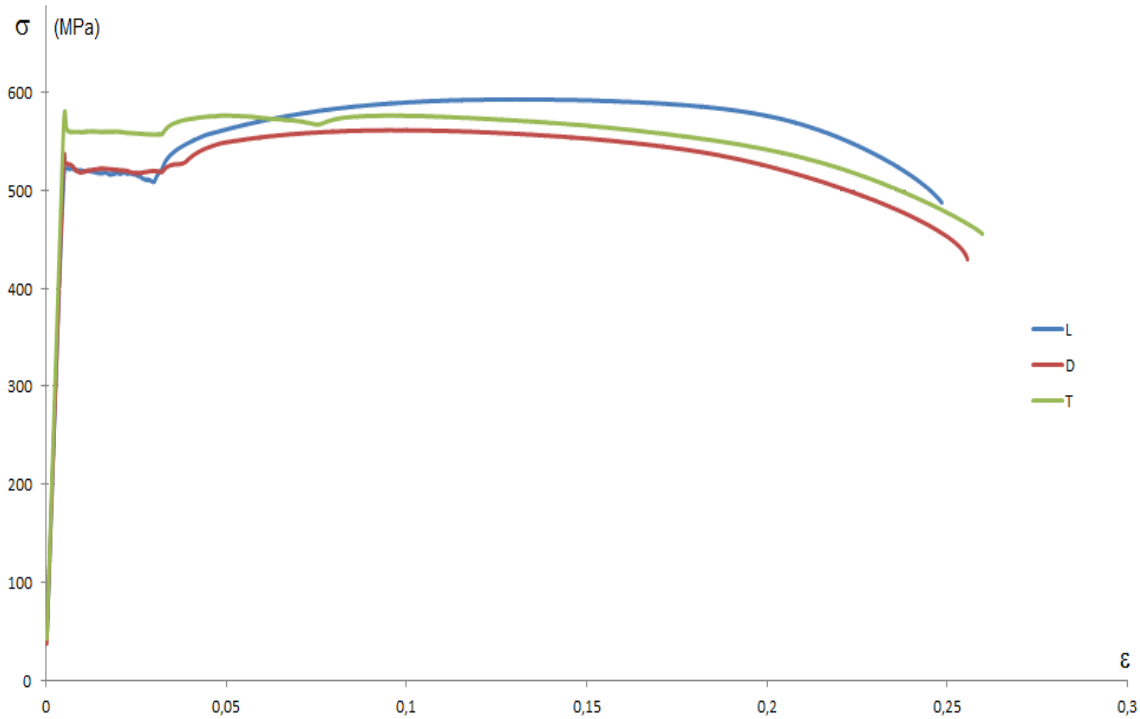

Fig. 3-5 – Stress / Strain curve for Ti-Fe-Si-O alloy in different directions

	R_p (MPa)	R_m (MPa)	A_g (-)	A_{80} (-)	R_{EH}/R_m (-)
L1	308,1	445,3	14,2	24,5	69,2
L2	304,3	445,7	14,4	27,7	68,2
L3	305,9	447,8	15,0	28,9	68,3
Av.	**306,1**	**446,3**	**14,5**	**27,0**	**68,6**
D1	339,8	410,1	9,3	30,3	82,9
D2	339,7	410,5	9,4	30,7	82,7
D3	340,1	410,7	9,5	29,9	82,8
Av.	**339,9**	**410,4**	**9,4**	**30,3**	**82,8**
T1	379,0	431,1	5,9	29,4	87,9
T2	377,2	431,3	5,9	29,1	87,5
T3	381,0	432,2	5,9	28,2	88,1
Av.	**379,1**	**431,6**	**5,9**	**28,9**	**87,8**

R_p = Yield point at 0,2%

R_m = Tensile Strength

A_g = Non–proportional elongation at maximum force

A_{80} = Non proportional elongation at break (for specimens with L_0 = 80mm)

Tab. 3-VII – Tensile test results for Ti-Al-Si-Nb alloy

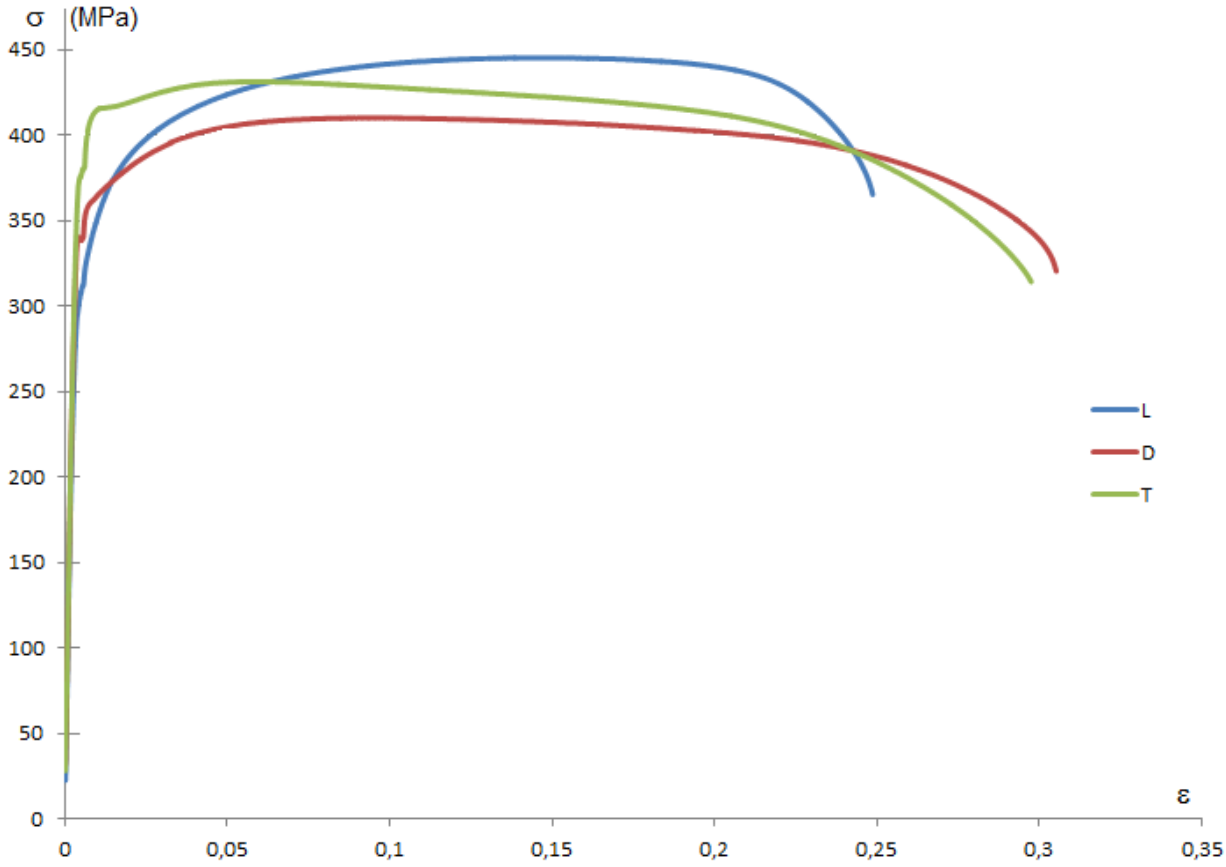

Fig. 3-6 - Stress / Strain curve for Ti-Al-Si-Nb alloy in different directions

3.2.1.2 Yielding Behavior

Observing the stress – strain curve of Ti-Fe-Si-O, it can be seen that the alloy exhibits after yielding repeated stress drops followed by periods of reloading. In detail, the behavior of this alloy is characterized by an initially high yield stress followed immediately by a sudden drop in stress. With continued straining, the stress stays nearly constant for several percent strain (3,5% in longitudinal direction, 6% in transverse direction, see Fig. 3-7) before normal strain hardening begins normally.

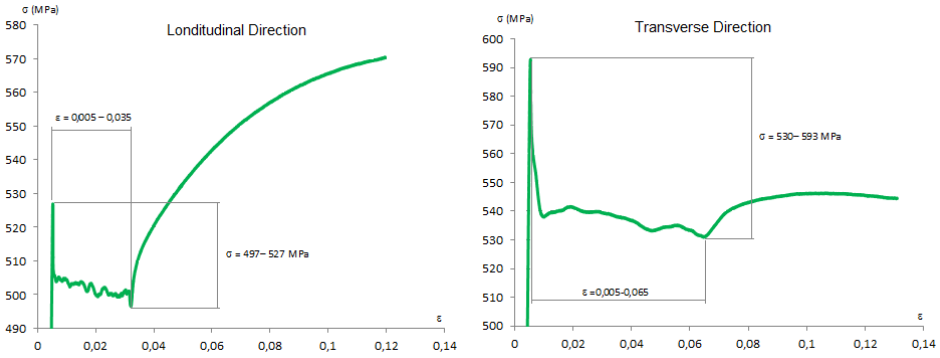

Fig. 3-7 – Yielding behavior of Ti-Fe-Si-O alloy in longitudinal and transverse direction

This phenomenon, also known as Portevin – Le Chatelier effect (PLC), is often observed in ductile steel or Al-Mg alloys, but is almost unknown for titanium alpha alloys. PLC occurs when dislocation meets obstacles, like forest dislocations, and are temporary stopped for a certain time. During this time solutes, such as interstitial particles, diffuse around the dislocations further strengthening the obstacles held on the dislocations. Eventually these dislocations will overcome these obstacles with sufficient stress and will quickly move to the next obstacle where they are stopped and the process can repeat again.[51]

The physical manifestation of PLC effect is the formation of Lüders bands (or shear bands), i.e. localized bands of plastic deformation that spontaneously appear at different locations when stress reaches a critical level. Continuing with strain, the bands then widen; at this stage the number of dislocation remains constant and thus the material does not harden.

A full explanation of this behavior involves a discussion of the density and velocity of dislocations, how dislocations break free of the solute atoms, and how this results in a localized process which produces the Lüders bands which in turn propagate until they cover the whole specimen. An optical approach for studying this phenomenon will be analyzed in paragraph 5.3.

Conversely, the stress-strain curve of the alloy Ti-Al-Si-Nb shows a perfectly monotonic trend, without any presence of discontinuities or oscillatory effects in the proximity of the yielding. Certainly, this type of trend is indicative of a more homogenous and stable behavior during plastic deformation.

[51] Mesarovic S. – Dynamic Strain Aging and Plastic Instabilities – Journal of Mechanical Physic of Solids 43:671-701 No. 5

3.2.2 Elastic Modulus Determination

The value of elastic modulus (or "*Young's modulus*") is a material property useful in design for calculating compliance of structural materials that follow Hooke's law when subjected to uniaxial loading (that is, the strain is proportional to the applied force)[52]. From a practical point of view, it represents the stiffness of the material. For determining the elastic modulus, a test specimen is loaded uniaxially and load and strain are measured. The value is obtained from the stress-strain curve, evaluating the slope of the graph within the elastic field of material.

Precise determination of Young's modulus requires due regard for the numerous variables that may affect such determinations. These include:

- Characteristics of the specimen (orientation of grains relative to the direction of the stress, grain size, residual stress, previous strain history, dimensions …)
- Testing conditions (alignment of the specimen, speed of testing, temperature, condition of test equipment, error in extension and/or load measurements, …)
- Interpretation of data and calculation method

With reference to the latter point, according to standard, there are different techniques which can be used for Young's modulus determination. In detail:

1) Automatic Young Modulus Method

This method takes as starting value the point at 2% of maximum load and as ending value the yielding point. Within this range, the data on the stress axis between the start and end values are divided into six equal regions (not overlapped) and for all the regions a least square fit algorithm is applied for calculating their own slope. Subsequently, the pair of consecutive regions that has the highest slope sum is determined; from this pair, is found which region has the highest slope and the elastic modulus is the slope of that region.

2) Cord Method

This calculation determines the slope of the stress/strain curve between two specific points chosen on the curve. It constructs a straight line between the lower and upper bounds that previously specified.

3) E–Modulus Method

This calculation is performed in accordance with the ISO 6892-1[50] and ASTM E8[53] standards. It determines the elastic modulus of the material by using a standard linear regression technique. The portion of the curve to be used for the calculation is chosen automatically and excludes the initial and final portions of the elastic deformation where the stress-strain curve is non-linear.

[52] ASTM E111 - 04(2010) - Standard Test Method for Young's Modulus, Tangent Modulus, and Chord Modulus
[53] ASTM E8 - 11 Standard Test Methods for Tension Testing of Metallic Materials

4) Tangent Method

This calculation finds the slope of the stress/strain curve in a specific point on the curve. It constructs a modulus line at a tangent to the point that you specify.

The results obtained by using various calculation methods can lead to different results (see the example shown in Fig. 3-8, where the output of tangent and cord methods are compared).

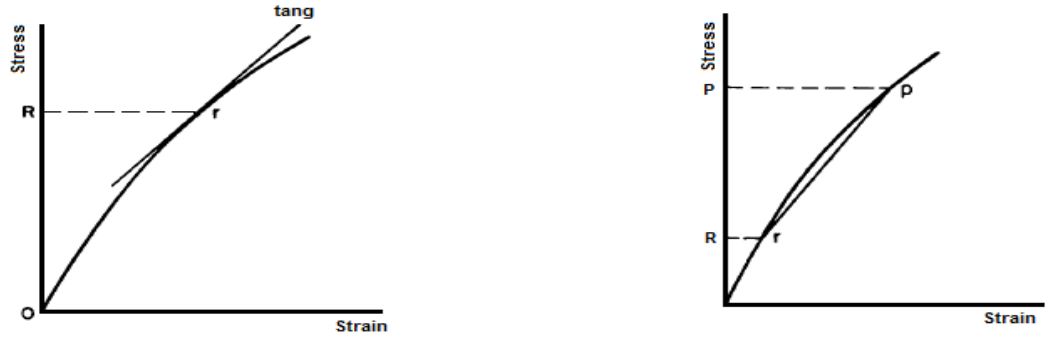

Fig. 3-8 – Graphic representation of tangent and cord methods

Considering that the value of elastic modulus is extensively used for determination of plasticity parameters, is understandable that the choice of which technique will be used for its calculation plays an important role. Due to this reason, in the following paragraph the Young's modulus values obtained using different techniques will be shown and compared.

3.2.2.1 Experimental results

For both materials an analysis of elastic field has been made, with the aim of identifying the portion of the σ-ε curve which is showing a good linearity.

Ti-Fe-Si-O shows a very good proportional trend, so for E modulus calculation with cord and linear regression methods the portion of diagram included between 100 – 400 MPa has been chosen. Conversely, Ti-Al-Si-Nb presents an elastic field with a mediocre linearity, and due to this reason a limited portion of diagram included between 75 – 175 MPa has been chosen for the aforementioned calculation methods.

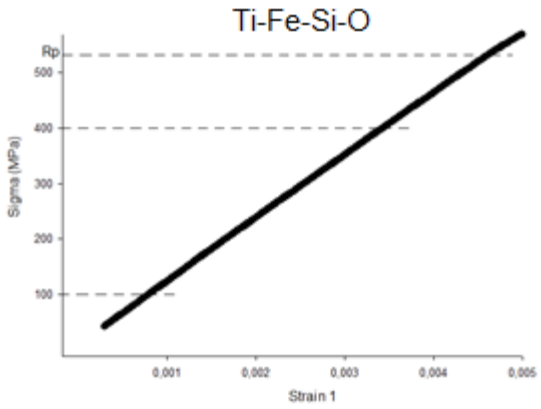

Fig. 3-9 – Ti-Fe-Si-O boundaries for E calculation

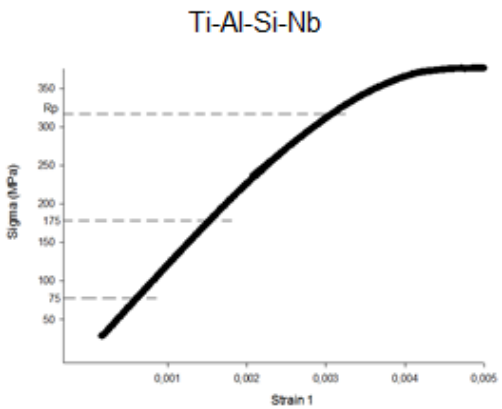

Fig. 3-10 – Ti-Al-Si-Nb boundaries for E calculation

Concerning the tangent calculation method, a specific point needs to be chosen for performing the E modulus determination. In this case, for both the material the point ε=0,25% has been selected for the calculation, because it is located approximately in the middle of the elastic field.

The results obtained by using the calculation methods previously discussed are summarized in Tables 3-VIII and 3-IX.

	E_{AUTO} (MPa)	E_{CORD} (MPa)	E_{LR} (MPa)	E_{TANG} (MPa)
L1	104.766	104.136	104.505	108.644
L2	103.664	104.219	104.685	107.727
L3	101.858	101.821	101.815	104.607
Av.	**103.429**	**103.982**	**103.668**	**106.922**
D1	106.291	105.606	105.320	110.119
D2	108.232	107.915	107.834	110.022
D3	108.389	107.987	107.940	110.576
Av.	**107.637**	**107.169**	**107.031**	**110.239**
T1	114.605	114.011	113.917	118.973
T2	110.816	111.166	110.911	112.565
T3	114.189	114.150	114.002	114.648
Av.	**113.203**	**113.109**	**112.943**	**115.395**

Tab. 3-VIII – Elastic modulus for Ti-Fe-Si-O alloy

	E_{AUTO} (MPa)	E_{CORD} (MPa)	E_{LR} (MPa)	E_{TANG} (MPa)
L1	100.515	101.008	102.215	109.464
L2	106.486	100.110	100.584	112.219
L3	102.211	98.192	99.938	197.881
Av.	**103.063**	**99.770**	**100.912**	**109.854**
D1	109.845	108.863	109.032	117.858
D2	106.697	108.344	108.484	115.099
D3	105.913	108.587	108.025	114.810
Av.	**107.567**	**108.598**	**108.513**	**115.922**
T1	110.304	109.769	109.444	120.150
T2	111.133	111.255	110.562	125.611
T3	108.738	114.873	114.468	121.077
Av.	**110.058**	**111.965**	**111.491**	**122.279**

Tab. 3-IX – Elastic modulus for Ti-Al-Si-Nb alloy

3.2.3 Poisson's Ratio

Poisson's Ratio is the absolute value of the ratio of transverse strain to the corresponding axial strain resulting from uniformly distributed axial stress below the proportional limit of the material. In detail:

$$\nu = \frac{\varepsilon_w}{\varepsilon_l} \qquad (3.1)$$

Transverse strain ε_w is measured in a direction perpendicular to the applied load while axial strain ε_l is measured in a direction of the applied load. In case of homogeneous and isotropic solid, in the elastic field, the lateral strain bears a constant relationship to the axial strain. This constant, called Poisson's ratio, is an intrinsic material property just like Young's modulus and Shear modulus.

Also in this case, the standard[54] allows different calculation methods, such as:

1) Cord Method

This calculation determines the slope of the transverse strain/tensile strain curve between two specific points chosen on the curve. It constructs a straight line between the lower and upper bounds that previously specified.

2) Linear Regression Method

This calculation determines the slope of the transverse strain/tensile strain curve between two specific points using least squares fit on test data.

3.2.3.1 Experimental results

In Table 3-X the Poisson's ratio values obtained using different methods are summarized.

	Ti-Fe-Si-O		TI-AL-SI-NB-EX	
	ν_{CORD} (--)	ν_{LR} (--)	ν_{CORD} (--)	ν_{LR} (--)
L1	0,3760	0,3781	0,4343	0,4383
L2	0,3819	0,3851	0,4101	0,4024
L3	0,3559	0,3587	0,3846	0,3863
Av.	**0,3713**	**0,3740**	**0,4097**	**0,4090**
D1	0,3979	0,4014	0,4022	0,4055
D2	0,4101	0,4114	0,4111	0,4102
D3	0,4100	0,4101	0,4021	0,3953
Av.	**0,4060**	**0,4076**	**0,4051**	**0,4036**
T1	0,4030	0,4353	0,4286	0,4269
T2	0,4111	0,4105	0,4666	0,4795
T3	0,4334	0,4366	0,4687	0,4751
Av.	**0,4158**	**0,4276**	**0,4546**	**0,4605**

Tab. 3-X – Poisson ratio for Ti-Fe-Si-O and Ti-Al-Si-Nb alloys

[54] ASTM E132 - 04(2010) Standard Test Method for Poisson's Ratio at Room Temperature

3.2.4 Plastic Strain Ratio

According to International Standard ISO 10113[55], the plastic strain ratio (also known as *R-value* or *Lankford coefficient*) is defined as the ratio of the true width strain to the true thickness strain in a tensile test, or:

$$R = \frac{\varepsilon_w}{\varepsilon_t} \tag{3.2}$$

This coefficient is a term commonly used for describing the resistance to thinning of sheet metal during forming, and is generally linked to deep drawability of the materials. Materials with higher *R*-value are desirable for forming due to their resistance to thinning, while materials with lower *R*-value will thin earlier causing possible ruptures during forming. The resistance to thinning contributes to the forming of shapes, such as cylindrical flat-bottom cups, by the deep-drawing process. The *R*-value, therefore, is considered a measure of sheet metal drawability. It is particularly useful for evaluating materials intended for parts where a substantial portion of the blank must be drawn from beneath the blank holder into the die opening.

Plastic strain ratio is also an indicator of plastic anisotropy, and is strongly related to the preferred crystallographic orientations within a polycrystalline metal[56]. In fact, materials usually show different R-values when tested in different orientations relative to the rolling direction. The angle of sampling of the individual test coupon is noted by a subscript. Thus, for a test specimen whose length is aligned parallel to the rolling direction, the R-value would be reported as r_0. If, in addition, the measurement is made at 20 % elongation and it is deemed necessary to note the percent strain at which the value was measured, the value would be reported as $r_{0° - 20\%}$[57].

Plastic strain ratio is also a convenient and meaningful way to represent anisotropy occurring during plastic deformation in general sense, without specific implication toward deep drawing performance. *R*-values have shown significance in yielding theories and material models since before the correlation between *R*-value and drawability was made (e.g., Hill's 1948 Yield Function). In some more recently developed and widely applied material models, like Barlat criterion, *R* values are not explicit to the mathematical formulation. However, experimentally determined *R*-values may be used to determine the explicitly defined coefficients of plastic anisotropy of a particular material model (see Par. 4.6).

According to standard requirements, for determining the plastic strain ratio, the width and thickness true strains ε_w and ε_t are needed. As the thickness strain is difficult to measure with precision during a tensile test of a thin sheet specimen, the plastic deformation volume constancy assumption is typically used:

[55] ISO 10113 (2006) - Metallic materials — Sheet and strip — Determination of plastic strain ratio
[56] B.M. Hance - Influence of Discontinuous Yielding on Normal Anisotropy (R-Value) Measurements - Journal of Materials Engineering and Performance - Volume 14(5) October 2005 – pp. 616-622
[57] ASTM E517 - 00(2010) Standard Test Method for Plastic Strain Ratio r for Sheet Metal

$$\varepsilon_l + \varepsilon_w + \varepsilon_t = 0 \rightarrow \varepsilon_t = -\varepsilon_l - \varepsilon_w \rightarrow R = \frac{\varepsilon_w}{-(\varepsilon_l + \varepsilon_w)} \qquad (3.3)$$

Where:

ε_l = true length strain

Thus, only the width strain and the length strain are measured while the thickness strain is a calculated value.

From strain experimental data, such as those obtained in this study, two different definitions of R-value can be used for calculation. The first method derives simply from the application of the R-value definition expressed in Eq. 3.2, and consists of the ratio of the accumulated width to thickness true strain, normally given at a specified elongation (for steel is usually taken at 15%). In the second method, however the one prescribed from ISO 10113, the true plastic width strain should be plotted as a function of true plastic length strain and a linear regression fit through the data on the range of interest. The plastic strain ratio is calculated as follows from the slope of the linear regression m:

$$R = -\frac{m}{1+m} \qquad (3.4)$$

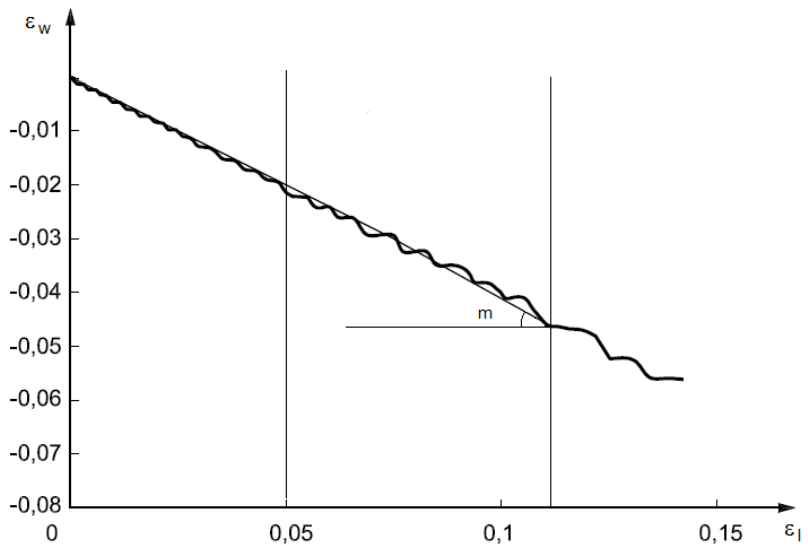

Fig. 3-11 – Example of linear regression[56]

The major distinction between these two calculation methods is their different dependences on the strain. The plastic strain ratio obtained applying the conventional equation is a punctual value and it varies with elongation. By contrast, the R value calculated using a linear regression is constant by definition within a specific elongation range, which makes it attractive for characterizing the drawability. Figure 3-12 illustrates the differences between these two definitions.

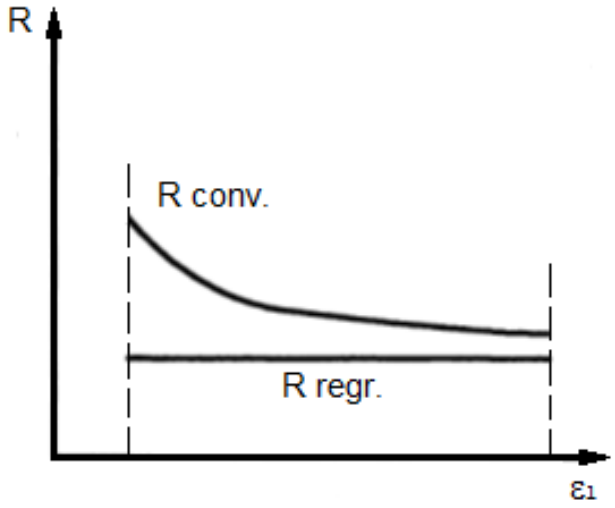

Fig. 3-12 – Difference between R value calculated punctually or by using linear regression method

3.2.4.1 True Plastic Strains Calculation: effect of elastic field

According to ISO 10113, for more accurate calculation of plastic strain ratio, the portion of strain occurred in elastic field (before yielding) should be deducted when the true plastic strains in longitudinal and transverse direction are calculated. With this assumption, the equations for determining the two aforementioned strains are:

$$\varepsilon_l = \ln\left(\left(\frac{\Delta L + L_0}{L_0}\right) - \left(\frac{F}{S_0 \cdot E}\right)\right) = \ln(1 + \bar{\varepsilon}_l - \frac{\bar{\sigma}}{E}) \qquad (3.5)$$

And

$$\varepsilon_w = \ln\left(\left(\frac{b_0 - \Delta b}{b_0}\right) + \left(\frac{\nu \cdot F}{S_0 \cdot E}\right)\right) = \ln(1 - \overline{\varepsilon_w} + \frac{\nu \cdot \bar{\sigma}}{E}) \qquad (3.6)$$

Where:

$\bar{\varepsilon}_l$= engineering strain along longitudinal direction

$\bar{\varepsilon}_w$= engineering strain along transverse direction

$\bar{\sigma}$= engineering stress

E = Young's modulus

ν = Poisson coefficient

In paragraph 3.2.4.3 the plastic strain ratio values will be calculated using both the approaches (with and without elastic strain portion). The E modulus and the Poisson ratio needed for the determination of true plastic strains are also experimental data obtained using the linear regression method.

3.2.4.2 Normal & Planar Anisotropy

Experiments show that R depends on the in-plane direction. The average of the R-values obtained usually for three different directions (rolling 0°, diagonal 45°, and transverse 90°) in the plane of sheet represents the coefficient of normal anisotropy and can be determined from the following equation:

$$\bar{R} = \frac{r_{0^\circ} + 2 \cdot r_{45^\circ} + r_{90^\circ}}{4} \qquad (3.7)$$

A measure of the variation of normal anisotropy with the angle to the rolling direction is known as "planar anisotropy" and can be obtained from equation:

$$\Delta R = \frac{r_{0^\circ} - 2 \cdot r_{45^\circ} + r_{90^\circ}}{2} \qquad (3.8)$$

The planar anisotropy is thought to be a measure of the tendency to form ears during plastic deformation operations, especially deep drawing. The correlation between planar anisotropy and the ears formation is outlined in Fig. 3-13.

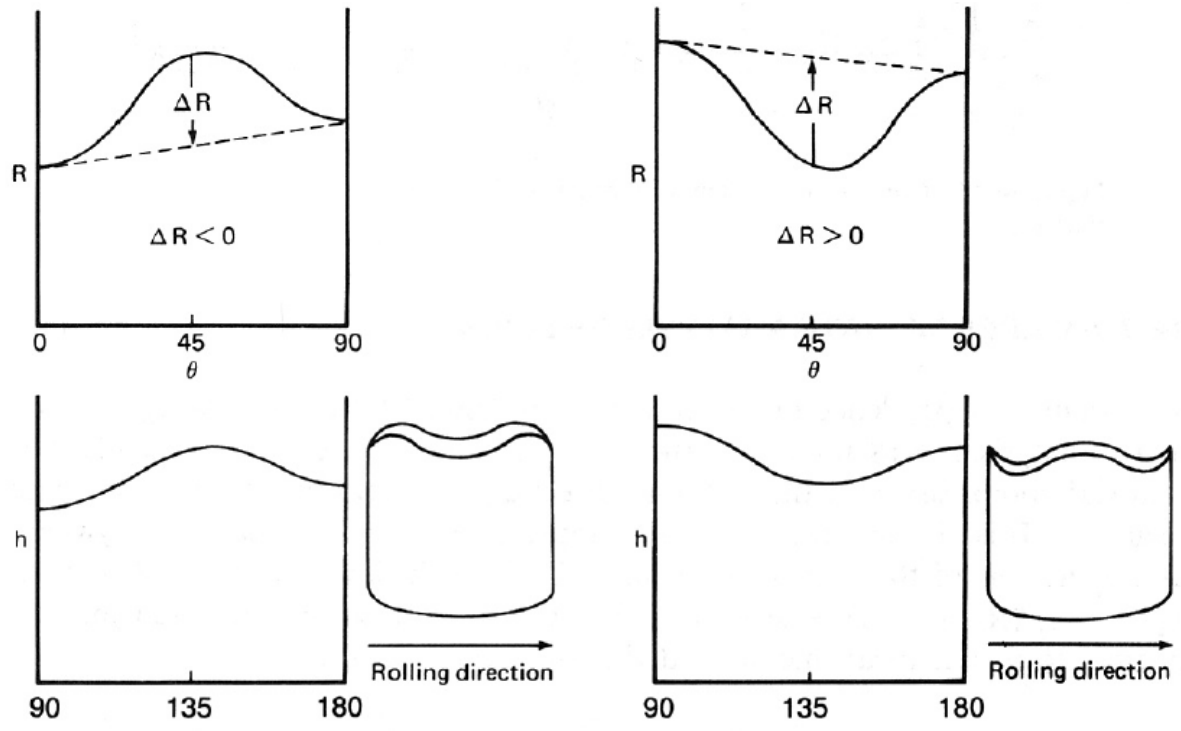

Fig. 3-13 – Correlation between earring and angular variation of R

In paragraph 3.2.4.3 the normal and planar anisotropy values will be calculated using the average values of plastic strain ratio in three directions (0° - 45° - 90°) obtained using the linear regression method according to ISO 10113 standard.

3.2.4.3 Experimental results

The plastic strain ratio values have been determined using the experimental data obtained from tensile tests shown in paragraph 3.2.1. The raw data exported from the software of the universal tensile machine have been reworked in order to perform the plastic stain ratio calculation according to the method prescribed from standard ISO 10113.

Ti-Al-Si-Nb		Conventional (punctual values)				Linear Regression (ISO method)			
		$R_{1\%}$ (--)	$R_{5\%}$ (--)	$R_{10\%}$ (--)	$R_{15\%}$ (--)	$R_{1\%-5\%}$ (--)	$R_{5\%-10\%}$ (--)	$R_{10\%-15\%}$ (--)	R_{tot} (--)
L1	Elastic +	1,237	1,431	1,381	1,432	1,498	1,320	1,529	1,395
	Plastic	1,599	1,619	1,632	1,842	1,618	1,625	2,330	1,955
L2	Elastic +	1,137	1,397	1,362	1,301	1,479	1,332	1,205	1,319
	Plastic	1,493	1,591	1,614	1,648	1,614	1,640	1,702	1,645
L3	Elastic +	1,156	1,397	1,353	1,304	1,356	1,309	1,209	1,309
	Plastic	1,647	1,610	1,610	1,644	1,608	1,610	1,709	1,629
Av.	Elastic +	**1,177**	**1,408**	**1,365**	**1,346**	**1,444**	**1,320**	**1,314**	**1,341**
	Plastic	**1,580**	**1,607**	**1,619**	**1,711**	**1,613**	**1,610**	**1,913**	**1,743**
D1	Elastic +	1,983	2,361	2,343	2,186	2,541	2,167	-	2,418
	Plastic	3,947	2,999	3,225	3,349	2,966	2,420	-	3,184
D2	Elastic +	2,181	2,349	2,202	2,018	2,543	2,391	-	2,197
	Plastic	4,666	2,968	2,956	2,966	2,771	2,940	-	2,852
D3	Elastic +	2,028	2,357	2,309	2,018	2,461	2,354	-	2,418
	Plastic	4,227	3,000	3,164	2,971	2,862	3,115	-	3,111
Av.	Elastic +	**2,064**	**2,356**	**2,285**	**2,074**	**2,515**	**2,355**	-	**2,344**
	Plastic	**4,280**	**2,989**	**3,115**	**3,095**	**2,866**	**2,990**	-	**3,382**
T1	Elastic +	3,059	3,299	3,307	-	3,230	3,297	-	3,243
	Plastic	11,757	4,718	5,390	-	3,933	6,087	-	4,865
T2	Elastic +	2,906	3,227	3,085	-	3,184	2,937	-	3,510
	Plastic	9,409	4,417	4,737	-	3,852	5,016	-	4,373
T3	Elastic +	3,213	3,321	3,158	-	3,203	3,003	-	3,062
	Plastic	13,148	4,585	4,910	-	3,892	5,219	-	4,482
Av.	Elastic +	**3,059**	**3,249**	**3,183**	-	**3,205**	**3,079**	-	**3,272**
	Plastic	**11,438**	**4,573**	**5,012**	-	**3,892**	**5,440**	-	**4,573**

Tab. 3-XI – Ti-Al-Si-Nb alloy plastic strain ratio (punctual values and ISO method)

Ti-Al-Si-Nb	Normal Anisotropy $\bar{R}$			Planar Anisotropy ΔR		
	$R_{1\%-5\%}$ (--)	$R_{5\%-10\%}$ (--)	R_{tot} (--)	$R_{1\%-5\%}$ (--)	$R_{5\%-10\%}$ (--)	R_{tot} (--)
Elastic + Plastic	2,383	2,328	2,303	-0,2635	-0,054	-0,082
Plastic	2,863	3,041	3,379	-0,007	0,101	-0,045

Tab. 3-XII – Ti-Al-Si-Nb alloy normal and planar anisotropy values

Ti-Fe-Si-O		Conventional (punctual values)				Linear Regression (ISO method)			
		$R_{2\%-5\%}$ (--)	$R_{5\%-8\%}$ (--)	$R_{8\%-11\%}$ (--)	R_{tot} (--)	$R_{2\%-5\%}$ (--)	$R_{5\%-8\%}$ (--)	$R_{8\%-11\%}$ (--)	R_{tot} (--)
L1	Elastic +	2,636	1,459	1,457	1,435	1,270	1,445	1,378	1,510
	Plastic	2,327	1,722	1,731	1,759	2,008	1,671	1,799	1,766
L2	Elastic +	1,576	1,470	1,467	1,441	1,207	1,458	1,371	1,351
	Plastic	2,163	1,730	1,746	1,767	1,602	1,767	1,817	1,917
L3	Elastic +	2,143	1,498	1,482	1,446	1,324	1,453	1,360	1,578
	Plastic	2,449	1,819	1,798	1,797	1,563	1,771	1,802	2,198
Av.	Elastic +	**2,118**	**1,476**	**1,487**	**1,441**	**1,267**	**1,452**	**1,369**	**1,479**
	Plastic	**2,313**	**1,757**	**1,758**	**1,774**	**1,724**	**1,736**	**1,806**	**1,961**
D1	Elastic +	1,249	2,233	2,630	2,643	1,464	2,570	2,656	4,382
	Plastic	1,254	2,938	3,744	4,052	1,719	3,919	4,956	6,740
D2	Elastic +	1,133	2,273	2,624	2,658	1,115	2,684	2,733	4,506
	Plastic	1,324	2,986	3,707	4,067	1,269	3,595	5,196	7,354
D3	Elastic +	1,125	2,162	2,504	2,466	1,069	2,799	2,850	4,977
	Plastic	1,316	2,793	3,473	3,632	1,348	3,323	3,724	7,576
Av.	Elastic +	**1,169**	**2,223**	**2,586**	**2,589**	**1,216**	**2,684**	**2,746**	**4,622**
	Plastic	**1,298**	**2,905**	**3,641**	**3,917**	**1,445**	**3,612**	**4,426**	**7,223**
T1	Elastic +	1,138	18,877	3,801	3,416	1,058	3,013	3,391	5,618
	Plastic	1,020	20,124	6,488	6,094	1,284	4,128	5,793	8,115
T2	Elastic +	1,163	17,721	3,715	4,613	1,592	2,831	4,659	5,566
	Plastic	1,055	20,082	6,367	6,669	1,759	3,972	8,746	10,54
T3	Elastic +	1,170	17,440	3,944	3,889	1,036	2,477	2,922	6,739
	Plastic	1,053	19,210	6,317	6,582	1,271	3,610	4,725	8,276
Av.	Elastic +	**1,157**	**18,021**	**3,820**	**3,972**	**1,228**	**2,773**	**3,657**	**5,974**
	Plastic	**1,042**	**19,805**	**6,390**	**6,448**	**1,438**	**3,903**	**4,458**	**8,979**

Tab. 3-XIII – Ti-Fe-Si-O alloy plastic strain ratio (punctual values and ISO method)

Ti-Fe-Si-O	Normal Anisotropy $\bar{R}$				Planar Anisotropy ΔR			
	$R_{2\%-5\%}$ (--)	$R_{5\%-8\%}$ (--)	$R_{8\%-11\%}$ (--)	R_{tot} (--)	$R_{2\%-5\%}$ (--)	$R_{5\%-8\%}$ (--)	$R_{8\%-11\%}$ (--)	R_{tot} (--)
Elastic + Plastic	1,232	2,399	2,630	4,174	0,031	-0,571	-0,233	-0,513
Plastic	1,346	3,216	3,779	6,346	0,136	-0,792	-1,294	-1,753

Tab. 3-XIV– Ti-Fe-Si-O alloy normal and planar anisotropy values

3.2.5 Strain Hardening

Plastic deformation takes place combining three different mechanisms: diffusional processes, twinning and dislocation motion. The contribution of diffusional processes is important at elevated temperatures, ($T > 0.6\ T_m$), and twinning might account for up to a few per cent strain. Dislocation processes are, generally speaking, the dominant deformation mechanism of plastic deformation at room temperature. Considering only the contribution due to dislocation processes, a shear stress acting parallel to the slip plane causes these dislocations to move through the lattice. As they move, they may encounter obstacles such as solute atoms, particles, grain boundaries and other dislocations, effectively impeding their motions until the stress is increased enough to allow the dislocation to overcome the obstacle. As the dislocations glide, climb and cross-slip through the lattice additional dislocations are being generated and start moving through the lattice (Frank Read mechanism)[58]. With this ever increasing dislocation density the distance between them decreases, they encounter each other more often, and it becomes increasingly difficult to deform the material. This process is called "strain hardening".

There is a well-known equation that depicts the strain hardening phenomenon called "Hollomon equation". This describes strain hardening as a power law function of stress and strain after yielding. Hollomon's equation is:

$$\sigma = \varepsilon_l \cdot K^n \tag{3.9}$$

Where symbols have the following meaning:

σ = True Stress (MPa)

ε_l = Longitudinal true strain

n = Strain hardening exponent

K = Strength coefficient (MPa)

The strain hardening exponent "n" and the strength coefficient "K" can be evaluated by following the method explained in International Standard ISO 10275[59] and using the experimental data collected during uniaxial tensile testing. This method allows determining the strain hardening exponent over the entire plastic stress-strain curve or for any specific portion(s) of the stress-strain curve previously specified. The true stress and true strain values can be calculated using the experimental data as follow:

$$\sigma = \bar{\sigma}\cdot(1 + \bar{\varepsilon}_l) \tag{3.10}$$

$$\varepsilon_l = \ln(1 + \bar{\varepsilon}_l) \tag{3.11}$$

[58] Mike L. Meier, Amiya K. Mukherjee - The onset of tensile instability - Department of Chemical Engineering and Materials Science University of California

[59] ISO 10275:2007 - Metallic materials -- Sheet and strip -- Determination of tensile strain hardening exponent

Where:

$\bar{\varepsilon}_l$= engineering strain

$\bar{\sigma}$ = engineering stress

The choice of using true stress and true strain values is done because engineering stress and strain values are based entirely on the unstrained dimensions of the specimen, thus they cannot provide true indications of the plastic behavior during deformation. Using true values based on instantaneous measurements allows obtaining a flow curve, also called "true stress-true strain curve", which represents the basic plastic-flow characteristics of the material. The true stress – true strain curve is basically valid between yield strength limit and ultimate tensile strength. Fig. 3-14 shows the behavior of true stress and engineering stress for the considered titanium alloy.

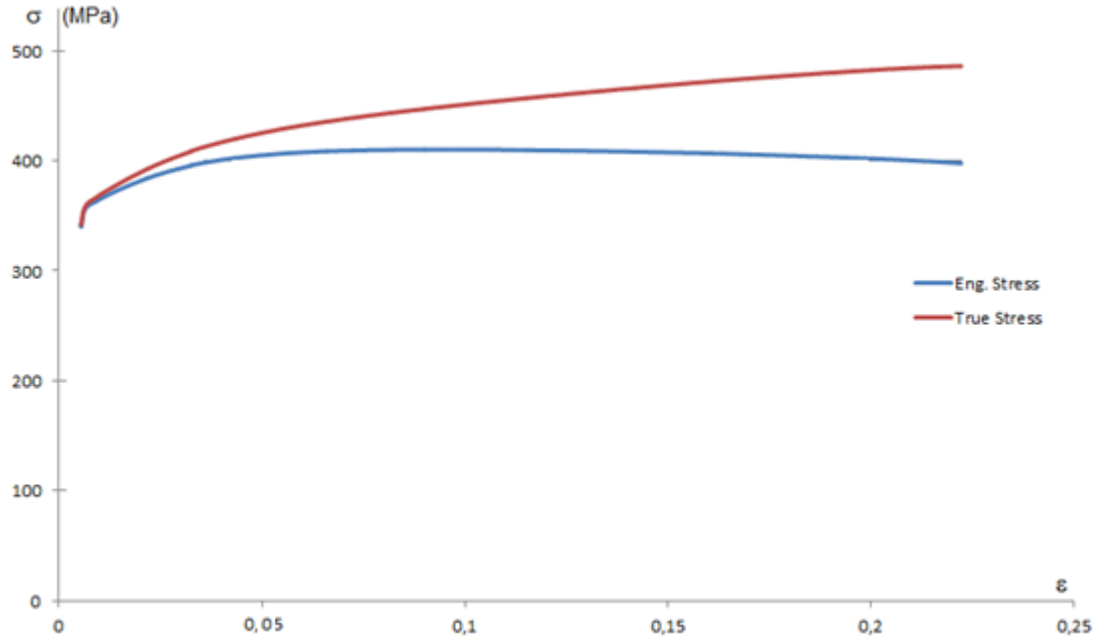

Fig. 3-14 – Difference between true stress –true strain curve and engineering stress – engineering strain curve

In the plastic field, the Hollomon equation can be written in logarithmic form as follow:

$$\ln \sigma = lnK + n \ln \varepsilon \qquad (3.12)$$

The *n*-value is determined from a linear regression of the logarithm of true stress vs. the logarithm of true plastic strain. The interval for the regression shall be expressed as plastic strains, with a minimum range of 2 %. It is possible to determine *n*-values over different intervals based on the same test. The range(s) of uniform strain over which the tensile strain hardening exponent was determined must be added in the exponent notation (examples $n_{2\%-4\%}$).

3.2.5.1 Experimental Results

The strain hardening exponents and the strength coefficients have been determined using the experimental data obtained from tensile tests shown in paragraph 3.2.1. The raw data exported from the software of the universal tensile machine has been reworked in order to perform the calculation according to the method prescribed from standard ISO 10275.

The obtained results are summarized in Tab.3-XV and 3-XVI.

	2% - 4%		4% - 6%		6% - 8%		2% - 8%	
	n	**K** (MPa)	**n**	**K** (MPa)	**n**	**K** (MPa)	**n**	**K** (MPa)
L1	0,129	658,081	0,129	657,262	0,131	660,983	0,141	678,174
L2	0,129	659,055	0,128	656,601	0,132	663,367	0,138	675,000
L3	0,129	658,815	0,129	659,118	0,133	666,470	0,139	678,166
Av.	**0,129**	**658,650**	**0,129**	**657,660**	**0,132**	**663,607**	**0,139**	**677,113**
D1	0,102	579,614	0,087	552,611	0,092	560,700	0,091	559,654
D2	0,098	573,473	0,087	553,562	0,092	561,244	0,090	557,862
D3	0,100	575,809	0,088	554,828	0,093	563,452	0,091	559,870
Av.	**0,100**	**576,298**	**0,087**	**553,667**	**0,092**	**561,799**	**0,091**	**559,129**
T1	0,064	548,926	0,060	542,759	0,057	537,071	0,060	542,001
T2	0,064	548,543	0,060	542,192	0,057	537,542	0,059	541,413
T3	0,063	549,105	0,059	542,316	0,057	538,300	0,059	541,518
Av.	**0,064**	**548,858**	**0,060**	**542,422**	**0,057**	**537,638**	**0,059**	**541,644**

Tab. 3-XV – Strain hardening exponent and strength coefficient for Ti-Al-Si-Nb alloy

	4% - 6%		6% - 8%		4% - 8%	
	n	**K**	**n**	**K**	**n**	**K**
L1	0,138	896,149	0,144	910,023	0,149	920,382
L2	0,138	896,028	0,143	909,499	0,147	917,543
L3	0,138	893,206	0,143	907,855	0,146	911,850
Av.	**0,138**	**895,128**	**0,143**	**909,125**	**0,147**	**916,592**
D1	0,114	813,056	0,105	791,773	0,113	807,863
D2	0,114	814,234	0,106	795,701	0,114	813,799
D3	0,112	812,055	0,106	798,236	0,118	826,375
Av.	**0,113**	**813,115**	**0,106**	**795,237**	**0,115**	**816,012**
T1	0,061	723,864	0,087	784,625	0,114	859,030
T2	0,066	738,924	0,096	791,028	0,101	802,855
T3	0,065	736,758	0,101	810,028	0,107	817,425
Av.	**0,064**	**733,182**	**0,095**	**795,227**	**0,107**	**826,437**

Tab. 3-XVI – Strain hardening exponent and strength coefficient for Ti-Fe-Si-O alloy

3.2.6 Relation between sample orientation and plastic strain ratio

A series of sheet tensile specimens were laser cut at 10 degrees increments from the rolling to the transverse direction. The specimen orientation is defined by the angle θ that the specimen axis makes with the rolling direction, as shown in Figure 3-15.

The longitudinal specimens would then be marked 0° degrees and the transverse 90° degrees. The test procedure and setup is essentially the same as that employed in previous investigations explained in paragraph 3.2.1. The geometry of the sheet tensile specimens is again according to the prescription of standard EN ISO 6892-1.

The only relevant difference compared to the tensile test previously carried out is related to speed control. In fact, in this specific case, in order to avoid discontinuities in the stress-strain curve, the trials have been performed keeping the deformation speed constant and equal to 0,00020 1/s.

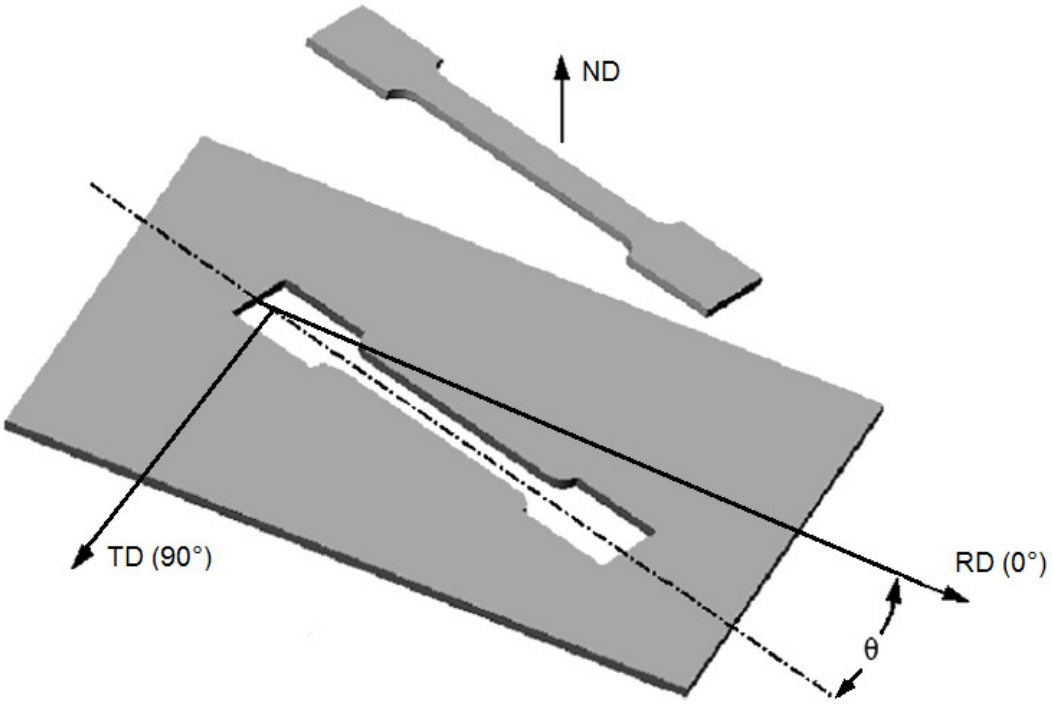

Fig. 3-15 - Example of specimen extraction and orientation

The target which should be achieved examining the effect of loading orientation on the mechanical response is the capability to predict the material's properties variations (especially yield stress and plastic strain ratio) in the plane of the sheet metal. This variation is a very important element characterizing the geometry of the yield locus, and its knowledge can be very helpful for choosing the correct yielding criterion to be used for formability simulation (see paragraph 4.1).

Another interesting aspect is trying to identify a connection between the initial texture of the alloys and the mechanical properties along different sample orientation.

The results achieve with this series of tests are outlined in the following paragraphs.

3.2.6.1 Experimental results

A) Young's Modulus

An understanding of the effect of texture upon Young's modulus is facilitated by the knowledge of single-crystal elastic properties[60]. Research has shown that for hexagonal single crystals, Young's modulus is sensitive to the angle that the applied stress makes with the basal pole and is symmetrical about this pole[61]. Sonic measurements of Young's modulus in single crystals of titanium have shown that Young's modulus is the lowest (~145.000 MPa) when the stress axis lies in the basal plane and the highest (~210.000 MPa) when the stress axis coincides with the basal pole[62]. It can be seen that a variation of about 50 percent in modulus is observed in titanium single crystals. It would be expected that, for certain preferred orientations, a variation in Young's modulus will appear in polycrystalline titanium sheet. This discussion applies to the alpha or hexagonal phase but a similar one could be presented for the beta or body-centered cubic phase.

	E modulus (MPa)										
	0°	10°	20°	30°	40°	45°	50°	60°	70°	80°	90°
Ti-Al-Si-Nb	102.469	104.794	109.198	110.420	111.043	112.354	115.125	116.765	115.061	119.994	121.429
Ti-Fe-Si-O	101.858	101.904	103.803	103.115	105.144	106.882	106.263	107.656	109.756	111.848	113.304

Tab. 3-XVII – E modulus, values between 0° – 90°

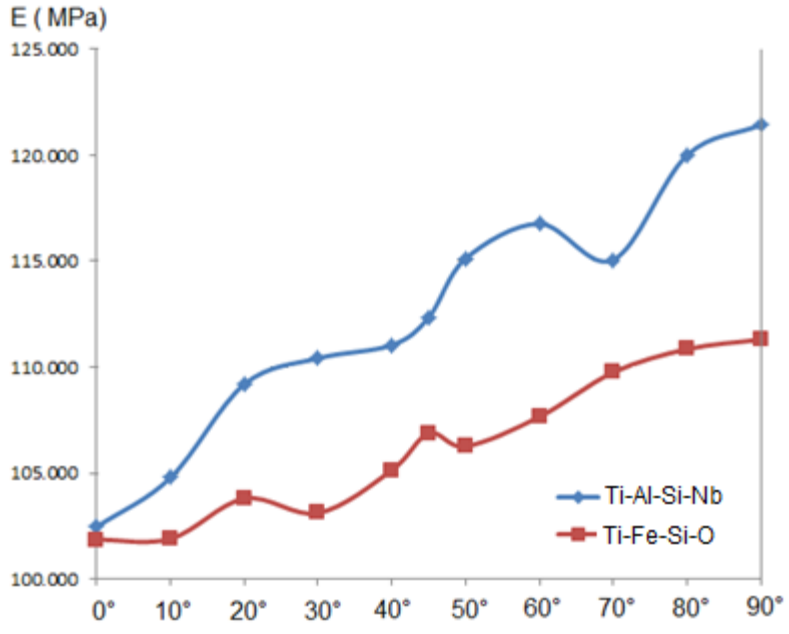

Fig. 3-16 – E Modulus trend between 0° – 90°

[60] Hearmon, R. F. S. – An Introduction to Applied Anisotropic Elasticity – *Acta Crystallographica* (1962) – Vol. 15, pp. 625-626

[61] Fisher, E. S., and Renken, C. J. *Single-Crystal Elastic Moduli and the hcp-bcc Transformation in Ti, Zr, and Hf* - The Physical Review, v. 135,no. 2A, July 1964, p. A482-A494.

[62] J. W. Flowers, K. C. O'Brien Jr., P. C. Mc Eleney – Elastic Constant of Alpha Titanium Single Crystals at 25°C - *Journal of Less Common Metals* – Vol. 7, no. 5, November 1964, pp. 393-395

B) Yield Strength

It is also demonstrated that the yield strength of single crystals is a function of orientation. It appears that the yield strength should also vary with specimen orientation depending upon texture type. For the alpha deformation type, the variation will be small when the basal poles are near the sheet normal and large when they are near the transverse direction.

		Yield Strength $R_{p0,2}$ (MPa)										
		0°	**10°**	**20°**	**30°**	**40°**	**45°**	**50°**	**60°**	**70°**	**80°**	**90°**
Ti-Al-Si-Nb		317,7	328,1	331,7	343,4	352,1	359,0	363,2	376,1	385,5	390,0	393,8
Ti-Fe-Si-	R_p	504,3	505,5	507,8	506,3	508,3	509,6	509,4	528,9	541,3	549,3	555,3
	R_E	526,9	531,6	535,9	540,7	542,7	547,7	552,0	571,7	583,3	593,3	592,9

Tab. 3-XVIII – Yield strength, values between 0° – 90°

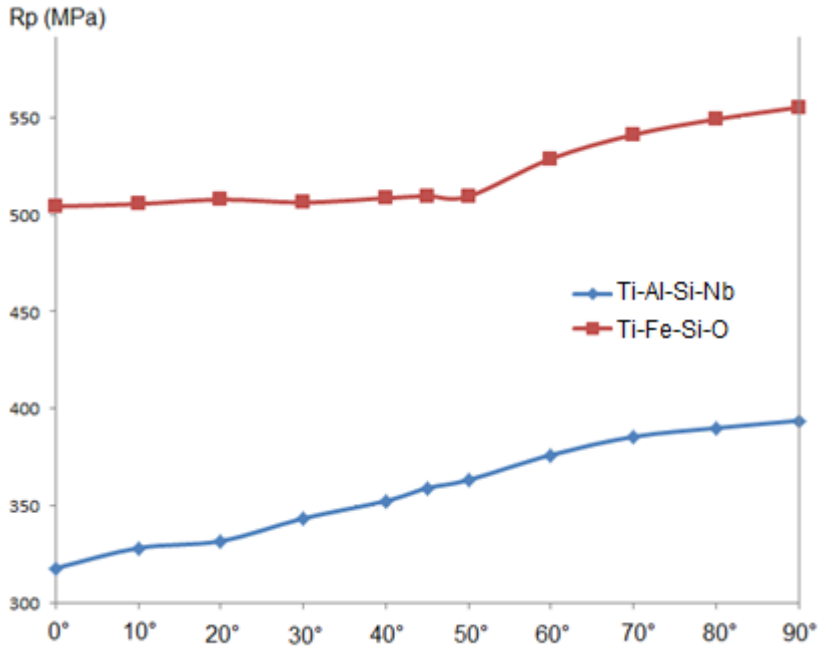

Fig. 3-17 – Yield strength trend between 0° – 90°

C) Tensile Strength

The variation in tensile strength with specimen orientation depends upon two things:

1) The yield strength value
2) The rate of strain hardening

In our specific case, both the alloys present yielding values which are increasing moving to longitudinal to transverse direction, while the trend of the strain hardening exponent is opposite. The sum of these behaviors is, for both the alloys, a tensile strength curve "U shaped" which is showing minimum values at about 45° orientation.

	Tensile Strength R_m (MPa)										
	0°	**10°**	**20°**	**30°**	**40°**	**45°**	**50°**	**60°**	**70°**	**80°**	**90°**
Ti-Al-Si-Nb	456,5	462,2	450,2	441,9	432,9	432,8	431,0	437,9	443,9	446,6	449,5
Ti-Fe-Si-O	573,7	574,1	561,7	547,8	532,4	528,6	527,1	532,8	542,5	545,1	546,1

Tab. 3-IXX – Tensile strength, values between 0° – 90°

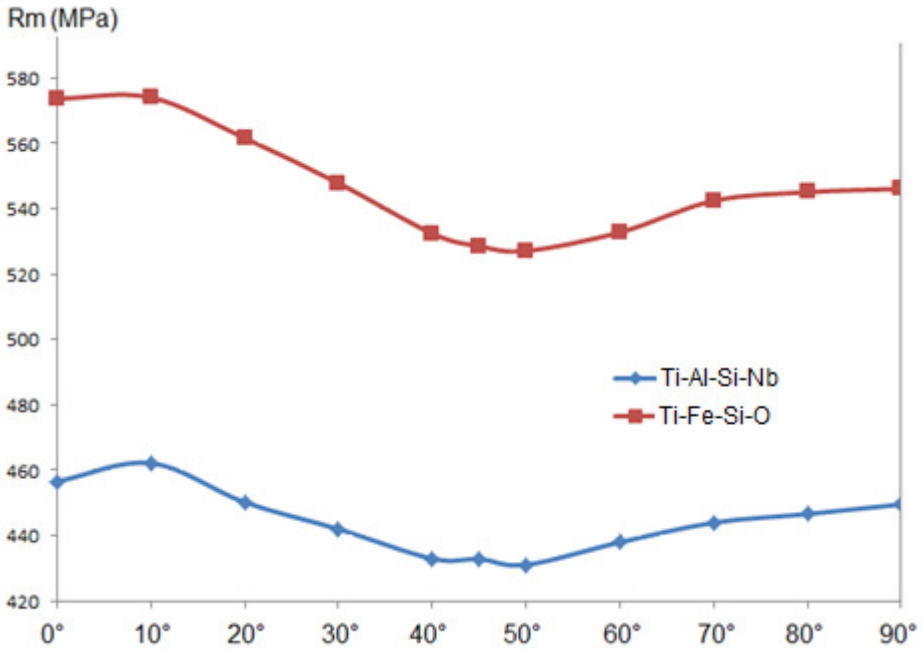

Fig. 3-18 – Tensile strength trend between 0° – 90°

D) Elongation at break

It appears that relatively little can be said about the variation in percent elongation and its connection with texture. In some cases it seems there is a mild tendency for the elongation to peak at an angle of about 45 degrees.

	Elongation at break A_{80} (%)										
	0°	**10°**	**20°**	**30°**	**40°**	**45°**	**50°**	**60°**	**70°**	**80°**	**90°**
Ti-Al-Si-Nb	30,29	31,16	32,17	32,35	33,29	33,15	33,36	32,25	31,94	31,81	31,47
Ti-Fe-Si-O	32,90	32,66	32,75	35,32	35,15	35,02	31,45	29,72	30,41	31,34	33,64

Tab. 3-XX – Elongation at break, values between 0° – 90°

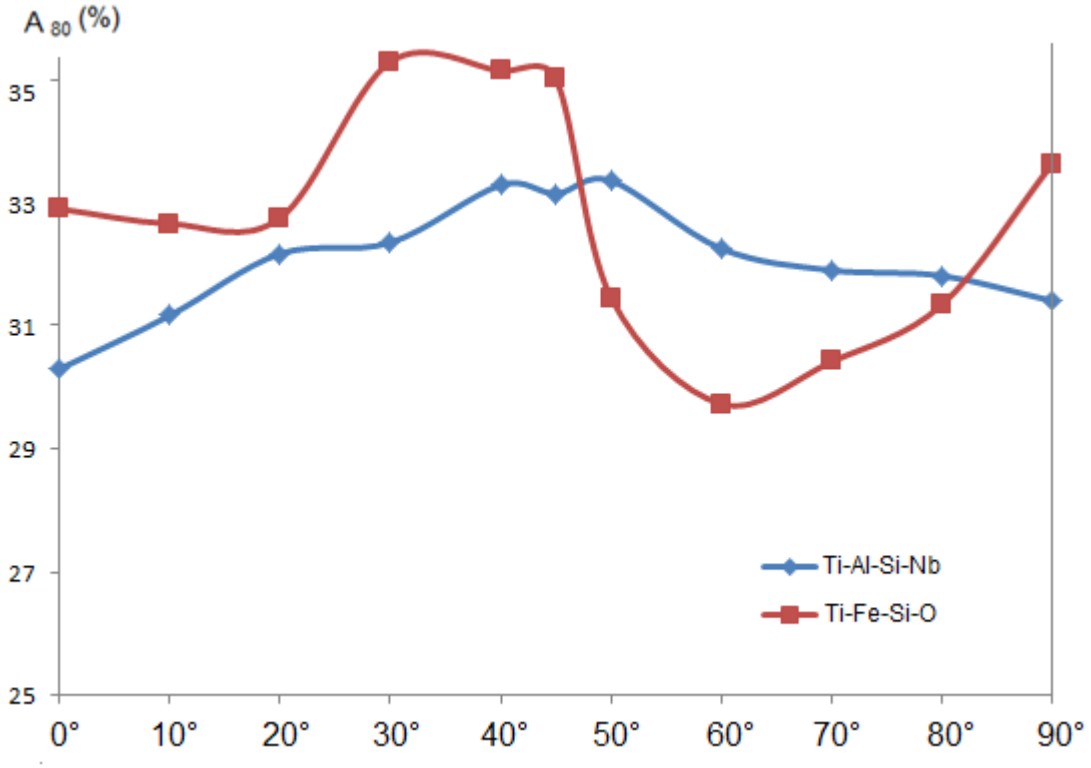

Fig. 3-19 – Elongation at break trend between 0° – 90°

E) Elongation at maximum strength

	Elongation at maximum strength A_{gt} (%)										
	0°	**10°**	**20°**	**30°**	**40°**	**45°**	**50°**	**60°**	**70°**	**80°**	**90°**
Ti-Al-Si-Nb	14,46	14,49	13,85	13,52	11,25	9,61	8,49	7,06	6,65	6,41	6,33
Ti-Fe-Si-O	15,72	15,65	15,73	15,23	13,2	13,87	10,53	10,27	9,73	9,94	9,71

Tab. 3-XXI – Elongation at maximum strength, values between 0° – 90°

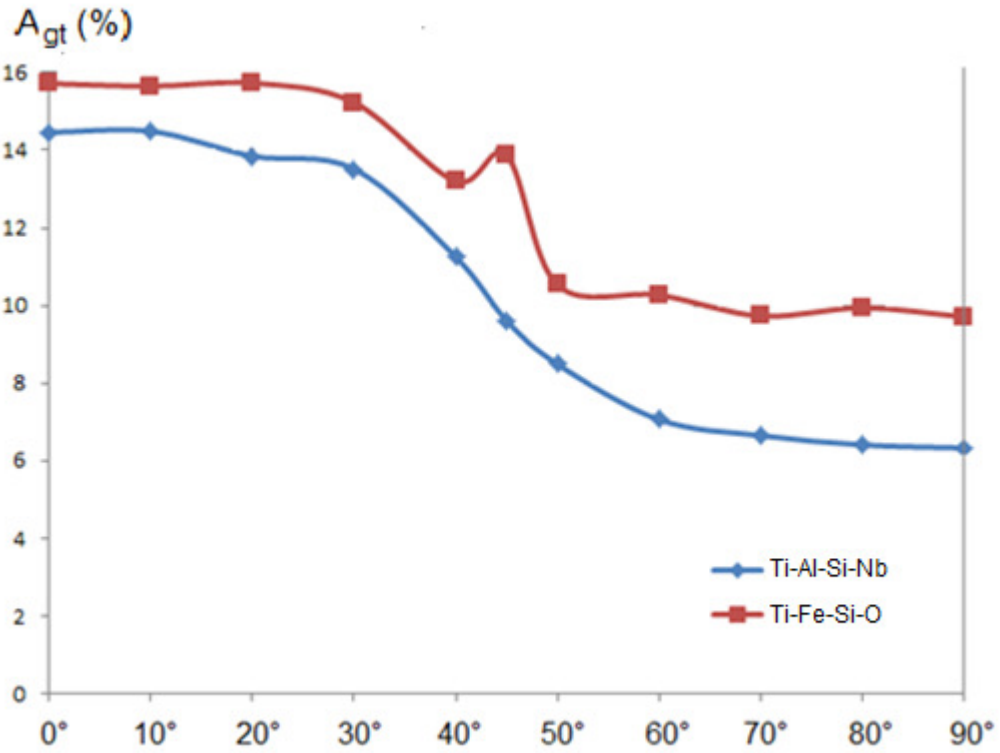

Fig. 3-20 – Elongation at maximum strength trend between 0° – 90°

F) Strain hardening exponent and coefficient

		Strain Hardening Exponent and Coefficient (--, MPa)										
		0°	**10°**	**20°**	**30°**	**40°**	**45°**	**50°**	**60°**	**70°**	**80°**	**90°**
Ti-Al-Si-Nb	**n**	0,138	0,135	0,133	0,129	0,120	0,107	0,101	0,095	0,084	0,078	0,074
	K	677,3	685,2	691,4	669,5	647,1	618,4	609,1	599,3	591,3	589,3	586,3
Ti-Fe-Si-O	**n**	0,148	0,151	0,147	0,137	0,115	0,118	0,109	0,079	0,067	0,068	0,704
	K	933,2	927,5	904,5	864,8	793,13	817,8	790,3	736,5	728,7	739,8	749,9

Tab. 3- XXII – Strain hardening coefficient and exponent, values between 0° – 90°

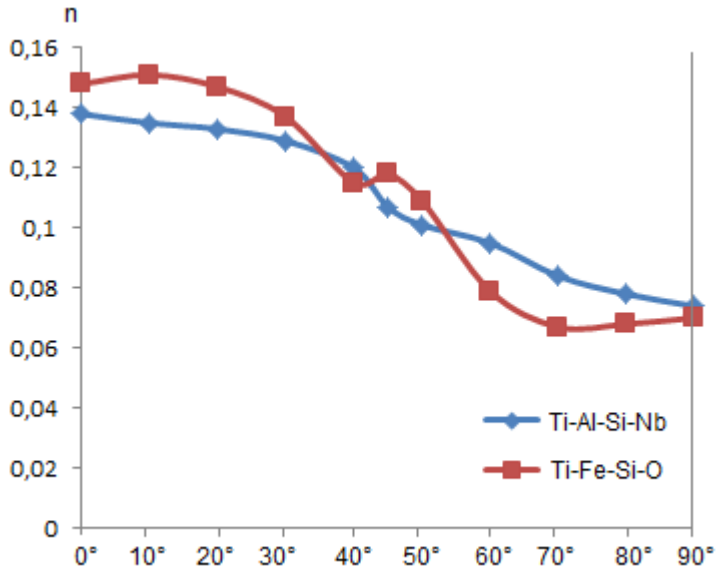

Fig. 3-21 – Strain hardening exponent trend between 0° – 90°

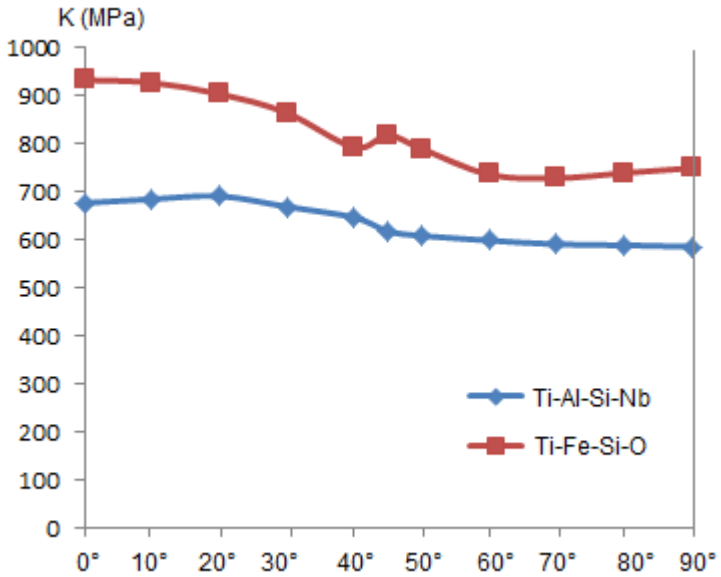

Fig. 3-22 – Strain hardening coefficient trend between 0° – 90°

E) Plastic Strain Ratio

In order to study the behavior of plastic strain ratio, a different approach has been chosen compared to the method prescribed from standard ISO 10113. Considering all the specimens oriented between 0°and 90°, the plastic strain ratio has been calculated for every single value of longitudinal strain included between 0,01 and 0,15. Two different approaches have been applied:

- Calculation of R values by direct application of Eq. 3.3; in this case the strains in longitudinal, transverse and thickness direction are determined as follow:

$$\varepsilon_l = \ln(1 + \bar{\varepsilon}_l)$$
$$\varepsilon_w = -\ln(1 + \bar{\varepsilon}_w)$$
$$\varepsilon_t = -(\varepsilon_l + \varepsilon_w)$$

Where $\bar{\varepsilon}_l$ and $\bar{\varepsilon}_w$ are the strains red by the two extensometer during the test

- Calculation of true plastic strain ratio values using Equations 3.5 and 3.6. In this way, the portion of strain occurred in elastic field (before yielding) is deducted when the true plastic strains in longitudinal and transverse direction are calculated.

In Fig. 3-23 and 3-24 are shown the R(ε_l) diagrams for every Ti-Fe-Si-O specimens extracted from the sheet metal with variable orientation between 0°and 90° to rolling direction.

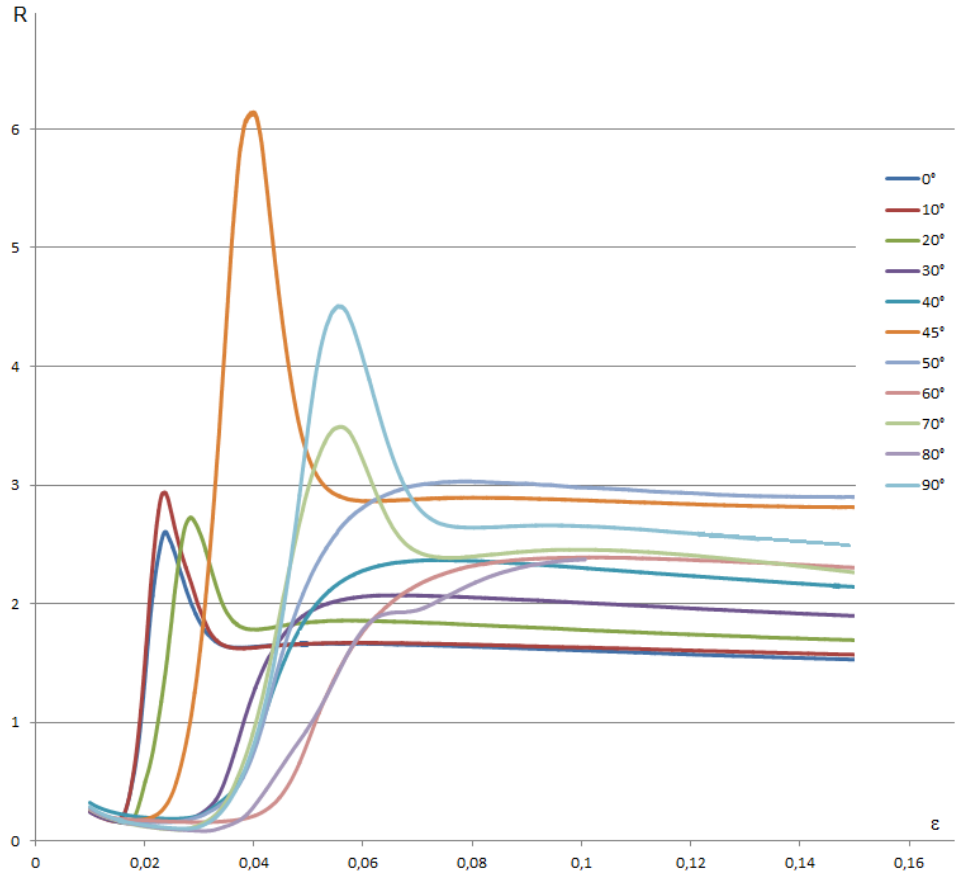

Fig. 3-23 – Plastic strain ratio (elastic + plastic) trend for different specimen orientation (Ti-Fe-Si-O alloy)

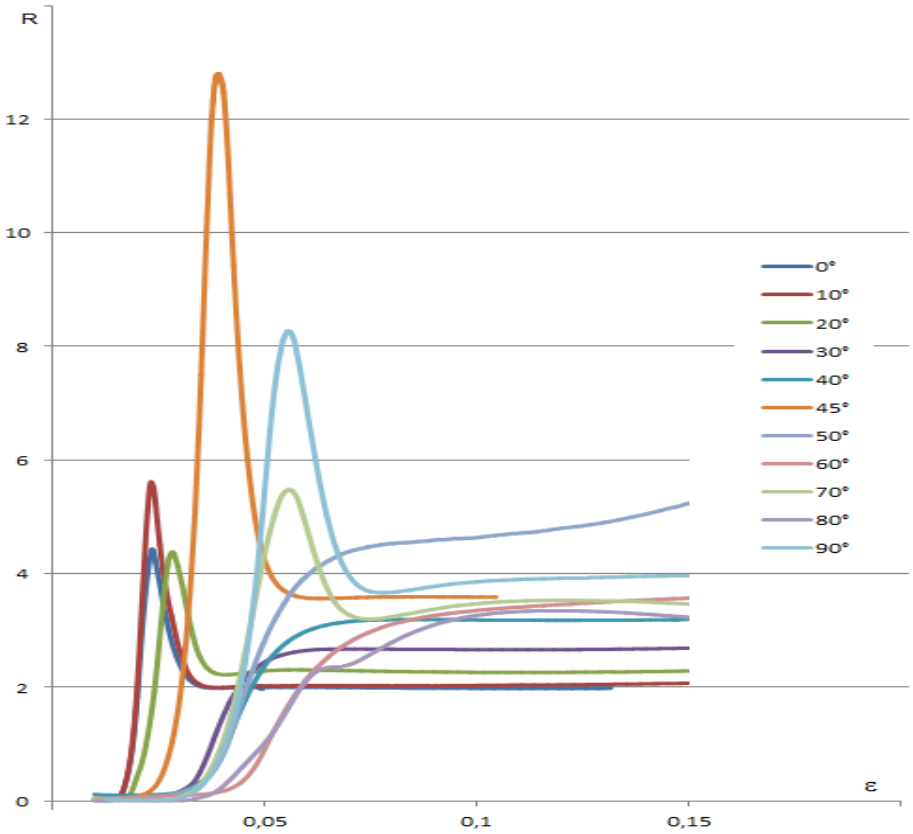

Fig. 3-24 – True plastic strain ratio trend for different specimen orientations (Ti-Fe-Si-O alloy)

Ti-Fe-Si-O alloy presents a peculiar trend of plastic strain ratio values in the area situated in the proximity of its discontinuous yielding region. If the plastic ratio diagrams are overlapped with the σ – ε curve (see Fig. 3.25), it is possible to notice that the position of the peak is always located in the second half of discontinuous yielding region. Considering that the end of yielding in diagonal and transverse direction is respectively 5% and 6,5% is understandable that with the conventional R value determination performed according to ISO 10113 standard the calculated values present a tendency to be overestimated due to the presence of the local peak. It is also very important highlighting that, when the discontinuous yielding is ended, the plastic strain ratio becomes almost a constant value, also for deformation levels belonging to the necking region.

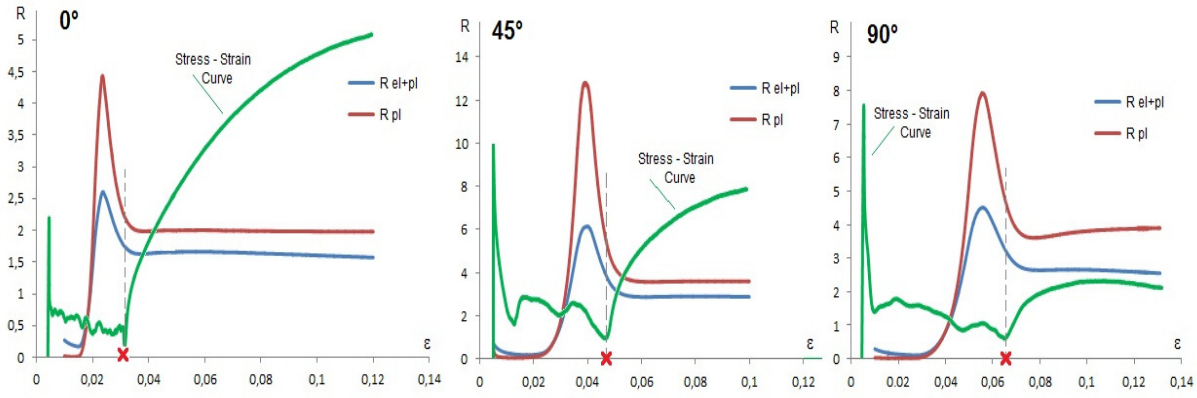

Fig. 3-25 – Plastic strain ratio peaks in correspondence of yielding zone (Ti-Fe-Si-O alloy)

In Fig. 3-26 and 3-27 are shown the R(ε_l) diagrams for Ti-Al-Si-Nb specimens extracted from the sheet metal with variable orientation between 0°and 90° to rolling direction.

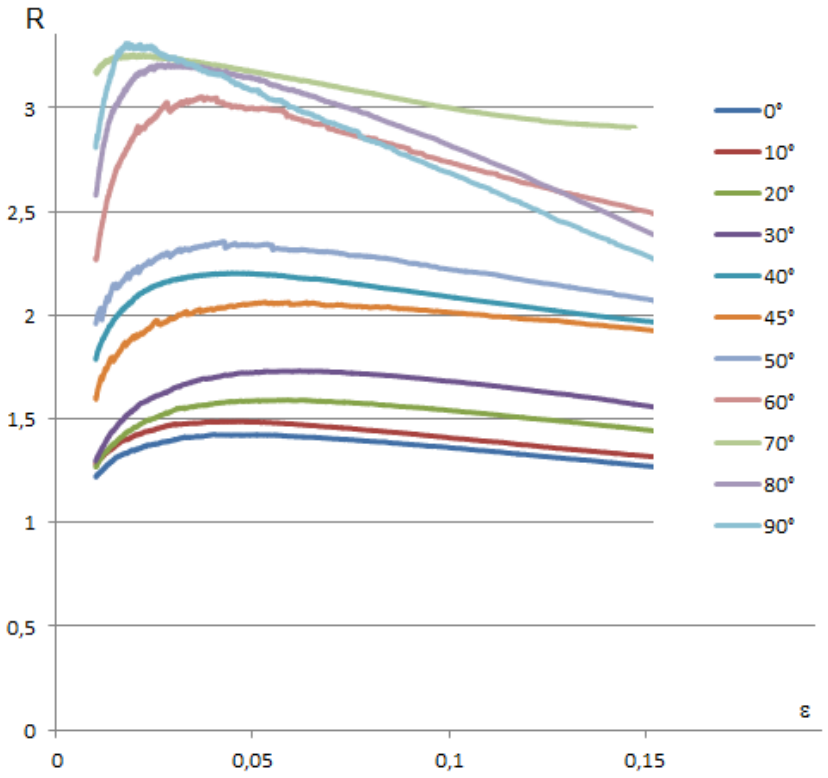

Fig. 3-26 – Plastic strain ratio (elastic + plastic) trend for different specimen orientation (Ti-Al-Si-Nb alloy)

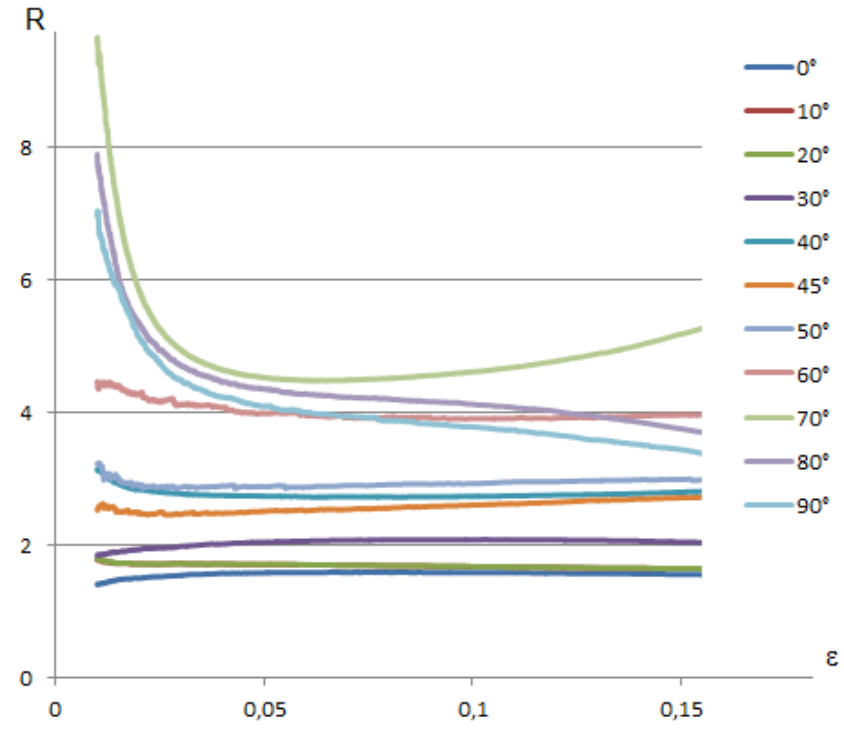

Fig. 3-27 – True plastic strain ratio trend for different specimen orientations (Ti-Al-Si-Nb alloy)

3.2.7 Erichsen cupping test

The Erichsen cupping test is a ductility test, which is employed to evaluate the ability of sheet metal to undergo plastic deformation in stretch forming. The test consists of forming an indentation by pressing a punch with a spherical end against a test piece clamped between a blank holder and a die, until a through crack appears. The depth of the cup is then measured; the deformation eight is also called *"Erichsen Index"* (E.I.). The specifications for performing this test, as well as the tool geometry are summarized in standard ISO 20482[63].

In this specific case, the trials have been performed using a standard tool produced from Instron; the geometry of this tool is in accordance with the prescription of the aforementioned international standard (see Fig. 3-29).

The specimens were squares dimensions 95 x 95 mm extracted from the same coil used for tensile test; even if the loading conditions are supposed to be axial symmetric, the blanks have been cut in longitudinal and transverse direction in order to evaluate some asymmetric behavior of the materials. According to standard, the specimens have been slightly lubricated with a graphite based lubricant on the side of the punch. The trials have been performed controlling the punch displacement; during the test, the speed of the crosshead has been kept constant and equal to 8 mm/min. The torque applied to the two screws positioned on the blank holder for locking the specimen in the correct position on the tool was 15 N·m, in order to obtain a uniform holding load equal to 10 KN.

Fig. 3-29 – Erichsen test tooling

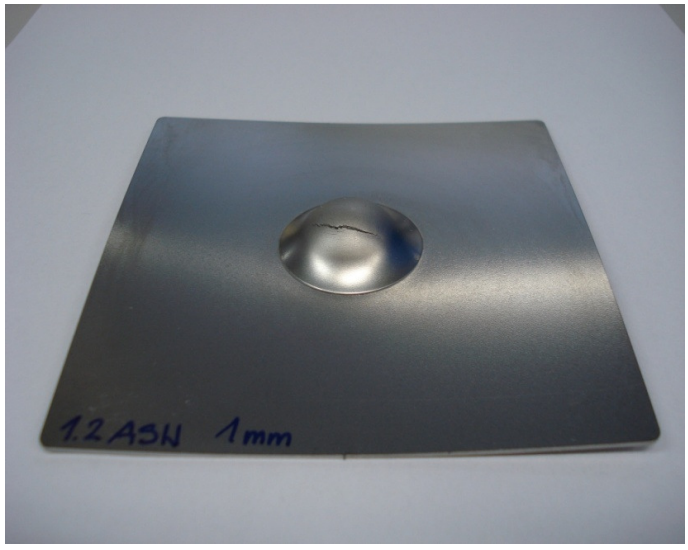

Fig. 3-30 - Deformed blank after the test

[63] ISO 20482:2003 - Metallic materials -Sheet and strip - Erichsen cupping test

3.2.7.1 Experimental results

The experimental data obtained by performing the Erichsen cupping test on Ti-Fe-Si-O and Ti-Al-Si-Nb alloys are listed in Tab. 3-XXIII.

Material	Direction	Force at break (N)	Erichsen Index (mm)
Ti-Fe-Si-O	L1	25.898	9,062
	L2	26.067	9,118
	L3	25.851	9,101
	Average	**25.938**	**9,094**
	T1	26.186	9,229
	T2	26.553	9,314
	T3	26.275	9,208
	Average	**26.338**	**9,250**
Ti-Al-Si-Nb	L1	24.357,53	8,721
	L2	24.091,91	8,654
	L3	23.847,36	8,461
	Average	**24.098,93**	**8,612**
	T1	24.905,97	8,914
	T2	24.886,16	8,881
	T3	24.864,89	8,881
	Average	**24.885,67**	**8,892**

Tab. 3-XXIII – Erichsen cupping test results

CHAPTER 4
SIMULATING TITANIUM PLASTIC RESPONSE USING FINITE ELEMENTS ANALYSIS

In order to improve the design of industrial products in terms of costs and time, several numerical simulation techniques able to predict the formability of metallic materials are more and more used by the mechanical component manufacturers. These simulations allow, on one hand, a better understanding of the phenomena taking place during the forming process and on the other hand, a better control of the quality of the products. On the top of that, they also provide valuable informations in terms of tools design and forming process development.

However, the usefulness of numerical simulation in designing sheet metal forming processes requires good criteria and a solid base of experimental data for predicting in a correct way the material's behavior and for identifying its modes of failure such as tearing, wrinkling and geometry deviation due to springback. From this point of view, titanium alpha alloys, because of their peculiar structure presenting preferential crystallographic orientation and twinning deformation mode, present strong anisotropic behavior and a yield surface which significantly changes its shape with accumulated plastic deformation.

Despite anisotropy has been studied in great detail by researchers over the past many decades, phenomenological modeling of hcp materials deformation is less developed. Due to the lack of availability of hcp phenomenological models in commercial FE code, hcp sheet forming simulations are still performed using classic anisotropic formulations for cubic metals such as Hill's 1948 criterion[64]. The major difficulty encountered in formulating analytic expressions for the yield functions of hcp metals is related to the description of the strength differential effect[65] (tension vs. compression asymmetry due to twinning).

Many yield functions have been defined in order to represent the elastic limit and subsequent plastic deformation for different anisotropic sheet metals. The quadratic Hill_48 model was successfully applied for steel sheet over a long period and is still widely used. The parameters, used in the plane stress version of the Hill_48 model are usually determined by uniaxial tensile tests at 0°, 45° and 90° with respect to the rolling direction. This anisotropic model was primarily based on the

[64] R Hill - A theory of the yielding and plastic flow of anisotropic metals - Proceedings of the Royal Society of London 193, pp. 281–297.(1948)
[65] B. Plunkett, R.A. Lebensohn, O. Cazacu, F. Barlat - Anisotropic yield function of hexagonal materials taking into account texture development and anisotropic hardening - Acta Materialia 54 (2006) 4159–4169

generalization of the von-Mises yield criterion. Although this model has been useful because of its simplicity, it was not able to capture together the observed anisotropy in yield stress and the R-ratios[66]

At a later stage, Hosford[67] modified Hill's anisotropic criterion to account for strength differential effects and developed the first real equation which could be used specifically for HCP metals.

In recent years, a series of comprehensive studies conducted on a variety of metallic materials (especially Al alloys) from Barlat and co-workers[68] [69] [70] have not only described the procedures and methodologies to study the influence of plastic deformation, texture and precipitation behavior on the anisotropy or on the yield locus, but also strongly proposed several relations between nature of yielding and its anisotropy on the yield locus.

In the following paragraphs will be shown how a wide range of experimental data has been use for generating a predictive mathematical model of titanium plastic response by using LS-Dyna finite elements program. Obviously, the objective of this study is creating a valid material model, so that the difference between experimental and numerical results is minimal.

4.1 Barlat & Lian 1989 anisotropic yield function

The practical choice of a yielding criterion for performing plastic deformation simulations need to take into account the following two factors:

- the type of anisotropy it has to describe
- the stress state to which it must be applied

The most general yielding criteria are able to describe orthotropic plasticity under full plane stress states (two normal stresses and one shear stress). Orthotropic materials have three mutually perpendicular planes of symmetry. This type of anisotropy is often assumed for metal sheets fabricated by cold rolling. The orthotropic directions are: the rolling direction (RD), the direction transverse to the rolling direction in the plane of the plate (TD), and the direction perpendicular to the plate (ND).

In 1989, Barlat and Lian proposed a plane stress yield function for orthotropic material which can be considered as a generalization of Hosford 1972 yield criteria. In this study this criterion has been chosen for simulating the plastic response of Ti-Fe-Si-O and Ti-Al-Si-Nb alloys by using LS-DYNA software (material model #36).

This model has been chosen because its input parameters can be derived from the standard tensile test and has a well-defined physical relevance.

[66] O. G. Lademo, O. Hopperstad, M. Langseth - An evaluation of yield criteria and flow rules for aluminum alloys – Int. Journakl of Plasticity Vol. 15 (1999) – pp. 191-208
[67] Hosford W F. A generalized isotropic yield criterion. Journal of Applied Mechanics, 1972, 39: 607–609
[68] F. Barlat, K. Lian - Plastic behavior and stretchability of sheet metals. Part I: A yield function for orthotropic sheets under plane stress conditions – Int. Journal of Plasticity Vol.5 (1989) – pp. 51-66
[69] F. Barlat, J. Liu - Precipitate-induced anisotropy in binary Al-Cu alloys - Materials Science A, 257(1), *1998*, pp. 47-61.
[70] O. Cazacu, F. Barlat, B. Plunket - Anisotropic yield function of hexagonal materials taking into account texture development and anisotropic hardening - Acta Materialia 54 (2006) 4159–4169

The anisotropic plane yield criterion Φ can be defined by the following equation[71]:

$$\Phi = a \cdot |K_1 + K_2|^m + a \cdot |K_1 - K_2|^m + c \cdot |2K_2|^m = 2\sigma_y{}^m \quad (4.1)$$

Where:

- σ_y = yield stress
- m = flow potential exponent (or Barlat coefficient)

And the tensor invariants K_1 and K_2 are defined as:

$$K_1 = \frac{\sigma_x + h\sigma_y}{2} \quad (4.2)$$

$$K_2 = \sqrt{\left(\frac{\sigma_x - h\sigma_y}{2}\right) + p^2\tau_{xy}{}^2} \quad (4.3)$$

σ_x and σ_y are the stresses in the local x and y directions, and a, c, h, p are material parameters:

$$a = 2 - 2\sqrt{\frac{R_{0°}}{1+R_{0°}} \cdot \frac{R_{90°}}{1+R_{90°}}} \quad (4.4)$$

$$h = \sqrt{\frac{R_{0°}}{1+R_{0°}} \cdot \frac{1+R_{90°}}{R_{90°}}} \quad (4.5)$$

If the flow stress of monotonic tension σ_x (rolling direction) is considered as a reference state, the following relation can be written:

$$c = 2 - a \quad (4.6)$$

The *p* parameter cannot be calculated analytically; however, if *a*, *c*, and *h* are known values, a mathematical relation between the R value in an arbitrary direction ϕ and p does exist. This relation is a monotonic function, and can be obtained by subsequent iteration. In order to calculate the plastic stain ratio R in an arbitrary direction, the following equation could be used (ϕ=45° has been used):

$$R_\varphi = \frac{2m \cdot \sigma_Y{}^m}{\left(\frac{\partial\Phi}{\partial\sigma_x} + \frac{\partial\Phi}{\partial\sigma_y}\right)\sigma_\varphi} - 1 \quad (4.7)$$

For these simulations, an exponential hardening law has been chosen:

$$\sigma_y = k \cdot (\varepsilon_0 + \varepsilon_p)^n \quad (4.8)$$

Where:

- k = strain coefficient
- ε_0 = strain at yielding
- ε_p = plastic strain
- n = strain hardening exponent

[71] V.V.A.A.– Ansys LS-Dyna user's guide – *Ansys Inc., Release 12.0, April 2009, pp. 77*

As can be easily seen form equation 4.4, 4.5 and 4.6, the three parameters *a*, *c*, *h* are normally identified by plastic strain ratio values. Later, it will be shown how, using as input initial data the anisotropy coefficient $R_{0°}$, $R_{45°}$, $R_{90°}$ as a function of plastic strain R(ε), and how the evolution of the yield locus can be determinated starting from these functions.

The flow potential exponent m determines the base shape of the yield surface. This exponent is m=6 for BBC materials[72] and m=8 for FCC materials[73] respectively; unfortunately no literature data are available for hcp titanium alloys and later in this study the flow potential will be obtained by using an iteration procedure. The main drawback of this material model is that it cannot consider yield asymmetry in any way; however, it will be demonstrated that it still gives adequate results for predominantly tensile load paths.

4.2 First attempt: constant input data

The first attempt for building the material model using Barlat and Lian 1989 yield function was done inserting as input data constant values of material properties obtained from the mechanical characterization described in chapter 3.

In detail, for building the material model, LS-Dyna requires the following input data[74]:

- Elastic Modulus E (GPa)
- Density ρ (g/cm^3)
- Poisson's Ratio ν (–)
- Hardening rule type (1=linear or 2=exponential, in our case exponential law)
- Strength Coefficient k (MPa)
- Strain hardening exponent n (–)
- Yielding stress R_p (MPa)
- Flow potential exponent m (–)
- Plastic strain ratio in rolling, transverse and diagonal direction $R_{0°}$, $R_{90°}$, $R_{45°}$ (–)
- Orthotropic material axes definition (0=standard orientation, 2=local coordinate system inputted by the user by choosing specific nodes of the 3D meshed model)

The experimental data for Ti-Fe-Si-O and Ti-Al-Si-Nb are summarized in Tab. 4-I. All the aforementioned material properties, with the exception of plastic strain ratio values, are referred to specimens extracted along longitudinal direction (0°).

[72] A. V. Hershey - The plasticity of an isotropic aggregate of anisotropic face centered cubic crystals – Journal Of Applied Mechanics, (1954) Vol. 21, pp.241– 249

[73] R. W. Logan, W. F. Hosford – Upper bound anisotropic yield locus calculations assuming pencil glide – Int. Journal of Mech. Science, (1980)Vol. 22, pp. 419– 430

[74] VV.AA. – Ansys LS-Dyna user's guide – *Ansys Inc., Release 12.0, April 2009* – pp. 78

Material Properties	Sym.	Ti-Fe-Si-O	Ti-Al-Si-Nb
Elastic Modulus	E	104 GPa	100 GPa
Density	ρ	4,51 g/cm^3	4,54 g/cm^3
Poisson's Ratio	ν	0,374	0,409
Strength Coefficient	k	916 MPa	677 MPa
Strain Hardening Exponent	n	0,147	0,139
Yielding Stress	R_p	518 MPa	306 MPa
Flow Potential Exponent	m	2	2
Plastic strain ratio longitudinal dir.	$R_{0°}$	1,961	1,743
Plastic strain ratio transverse dir.	$R_{90°}$	7,223	4,573
Plastic strain ratio diagonal dir.	$R_{45°}$	8,979	3,382

Tab. 4-I – Alloys constant input data

Initially the Hollomon equation $\sigma = K \cdot \varepsilon^n$ was used as the yield stress function, however the fit at higher strains is poor. In contrast to steel, titanium exhibits substantial additional elongation past R_m, with a fairly gradual onset of localization, which is in line with the properties expected from its crystal structure. This property becomes even more pronounced in the diagonal and transverse direction where the peak force occurs at very low strains yet the material still achieves a moderate strain at fracture. The assumption follows that quite some useful deformation occurs after the onset of localization in metal forming applications. This property cannot be reasonably captured by any of the traditional hardening laws, and since the simulation software enables the use of an arbitrary curve for the material hardening property, there is no need to develop a new functional approximation.

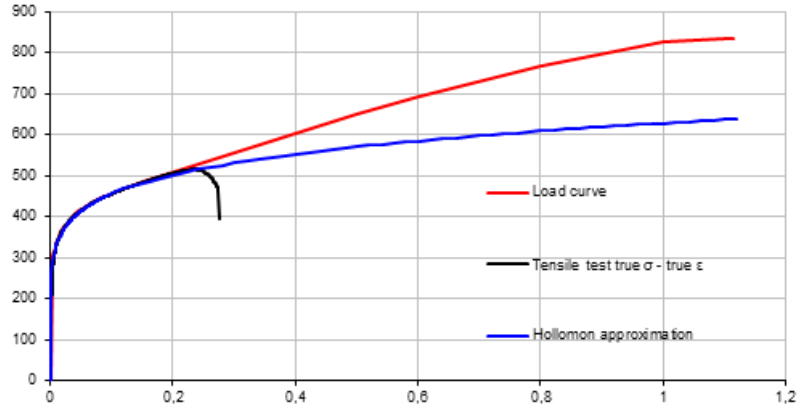

Fig. 4-1 – Comparison between true σ-ε curve and Hollomon approximation (Ti-Al-Si-Nb alloy)

The final load curve for the material is shown in Fig. 4-1 along with the measured true σ – true ε curve and the functional approximation using the Hollomon power law. Compared to the Hollomon approximation it is somewhat steeper to support the extensive post-R_m deformation. Also note how far past the global strain at breaking the curve extends, this offers some insight into the materials behavior in the necking region after the onset of localized deformation.

4.3 Yield curve as input data

The yield curve obtained performing a standard uniaxial tensile test provides reliable data for describing the material's behavior only in a mild plastic strain range, more precisely up to the onset of necking. This is due to the fact that, after this specific point, the uniaxial stress state changes to complex triaxial one; hence it is physically inappropriate to determine the yield curve by the standard analytical procedure. In addition to this, the two titanium alloys under investigation exhibit a tendency in continuing the deformation under nearly constant load also after the ultimate tensile strength point has been reached. This behavior is particularly marked in case of tensile test performed in diagonal and transverse direction, where the peak force occurs at very low strains (8 – 11%) while the elongation at break remains comparable with the value obtained in the rolling direction (26 – 30%).

When FE simulations of deep drawn parts are made, the strains developed during forming can be locally very high, and the yield curve defined in the above manner is not representative after the onset of necking. A method for coping with this problem is using engineering stress and strain values, as previously mentioned in paragraph 3.2.5.

Among many commonly accepted exponential hardening laws, the one used by LS-Dyna for creating the material model is the Hollomon – Ludwig equation, in accordance with Eq. 4.8.

However, the experimental n and k values used as inputs as basic material data are obtained performing a linear regression of the logarithm of the true stress – true strain values within a specific limited strain range, and so extending this value to high deformation levels can lead to wrong results. Moreover, as far as the end point of the yield curve calculated with Eq. 4.8 is not known, the function can be extended beyond reasonable limits which can lead, when used in numerical simulations, to unreliable results.

As shown in paragraph 4.2, the results obtained by simulating the plastic response by using constant values and the exponential hardening law were unsatisfactory. In order to improve the model's response, a mixed experimental – numerical method will be introduced in the following paragraph.

4.3.1 Inverse Procedure

According to the inverse procedure developed by Kocand and Štok[75] [76], a yield curve to be used as input data for the material model is obtained by running numerical simulations of the tensile test and modifying iteratively the parameters until the result of the simulation and the corresponding experimental data are matching. The quantitative measure of closeness of the two responses is named cost function, and it is a scalar function containing a number of components equal to the material parameters which can be tuned for adjusting the output results. In this method the true strain ε is taken

[75] P. Koc, B. Štok - Computer-aided identification of the yield curve of a sheet metal after onset of necking - Computational Materials Science 31 (2004) 155–168

[76] P. Koc, B. Štok - Usage of the yield curve in numerical simulations - Journal of Mechanical Engineering, 54 (2008), p. 821-829

as the independent variable and the yield curve is sectioned in a number "*t*" of intervals; the intervals boundaries remain constant during all the iteration process. With this assumption, the value of the yield function $\sigma(\varepsilon)$ at a specific strain $\varepsilon \in (\varepsilon_{i-1}, \varepsilon_i)$ can be expressed as follows:

$$\sigma(\varepsilon) = \sigma^{i-1} + \frac{\sigma^i - \sigma^{i-1}}{\varepsilon_i - \varepsilon_{i-1}}(\varepsilon - \varepsilon_{i-1}) \qquad \text{i=1, …, t} \qquad (4.9)$$

where coefficients σ^{i-1} and σ^i are the values of function $\sigma(\varepsilon)$ corresponding to the edges of the i^{th} interval. The material parameters which can be manipulated for iterating the functions are written in a vectorial form:

$$p^T = [p_0, p_1, \ldots, p_n] \qquad (4.10)$$

In principle, the greater the number of material parameters incorporated in the yield curve approximation, the greater the physical objectivity of the identified material behavior. However, not always the strategy of increasing the number of material parameters during the inverse determination of the yield curve is assuring a more precise material characterization. In the considered case the identification procedure starts with a single identification parameter p_1 active, and identification is performed by considering a single subinterval in the necking region ($\varepsilon \in$ [XX – YY]). After finding a local minimum of the cost function, an additional parameter (p_2) is added to the parameter vector, and a new local minimum with both parameters p_1 and p_2 subject to identification over the aforementioned interval is searched.

The inverse identification procedure requires as input the experimental data obtained by a uniaxial tensile test in longitudinal direction; a single test for both alloys, which seems to be representative in average of the materials behavior, has been chosen for the yield curve identification. For the simulation, a ¼ symmetry model of the parallel section of the tensile specimen was modeled using shell elements. An element size of approximately 0.8 mm was adopted, as it is representative of the element sizes typically used in later forming simulations. Mass scaling was used to maintain a time step of $5 \cdot 10^{-7}$ and the deformation rate was scaled by an order of 10^3, as this was found to yield satisfactory results[77]

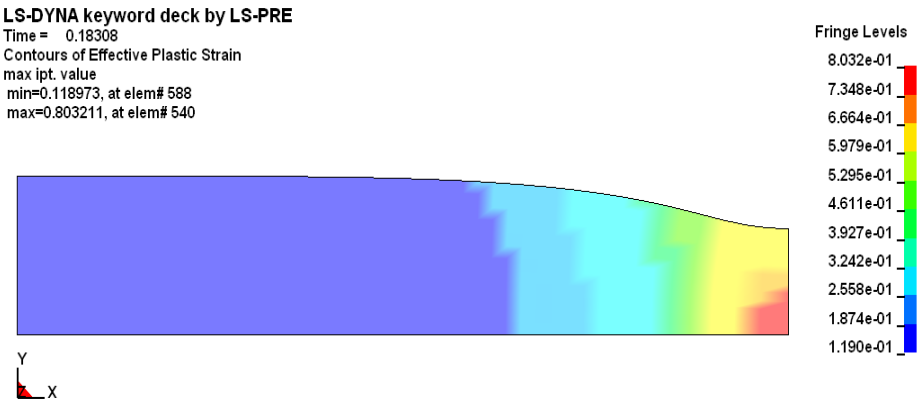

Fig. 4-2 – Uniaxial tensile test simulation

[77] S. Jurendič, S. Gaiani - Deep drawing simulation of α-titanium alloys using LS-Dyna – Proceedings of 8th European LS-Dyna Conference (2011)

As example of the inverse procedure method, the final stage of true stress – true strain curve through for Ti-Al-Si-Nb alloy is shown in Fig. 4-3. This diagram is compared with one experimental true stress-true strain curve and the functional approximation using the exponential hardening law. It can be asserted that the discrepancy between the calculated curve and the experimental target curve is smaller than mutual discrepancies between other measured curves.

The curves result well overlapped also in the necking region, which is always the most critical area for the mathematical model approximation.

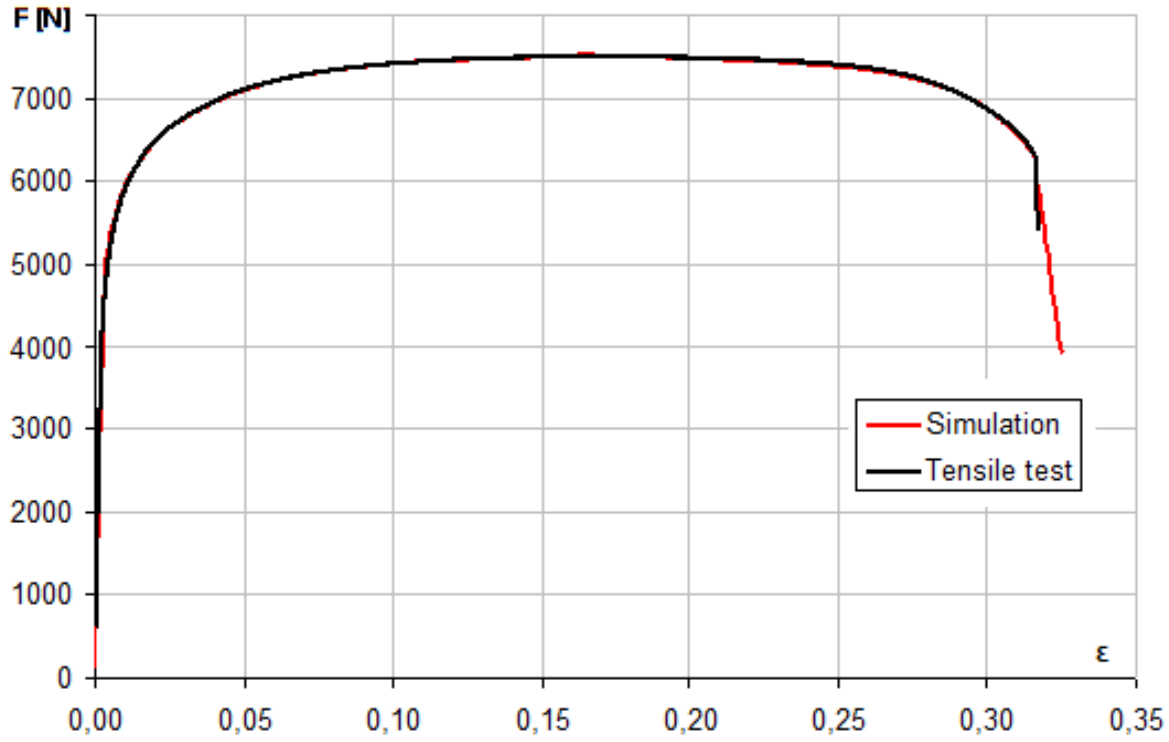

Fig. 4-3 – Comparison between experimental σ-ε curve and simulated one

4.4 Plastic strain ratios as functions of strain

The plastic strain ratio input values $R_{0°}$, $R_{45°}$, $R_{90°}$ have been calculated according to standard ISO 10130 specifications using the experimental data of the tensile testing. The results achieved with this method are a constant numeric values obtained realizing a linear regression within a specific strain interval, and due to this reason they represent averaged quantities. Moreover, the experimental results previously presented show how Ti-Fe-Si-O alloy presents a tendency to modify the plastic strain ratio with the progress of deformation, especially along diagonal and transverse directions.

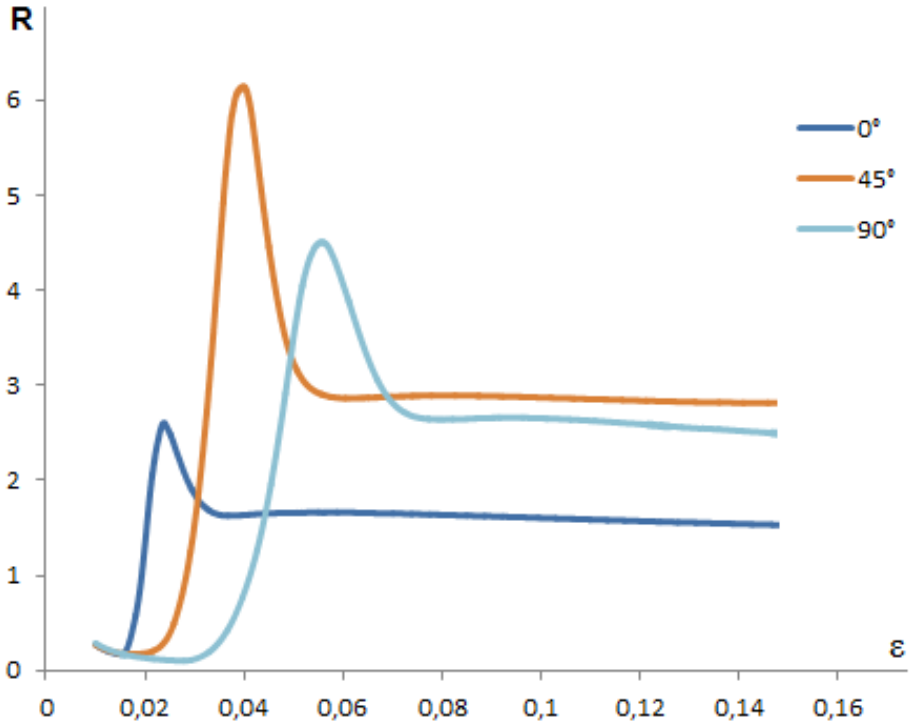

Fig. 4-4 – Plastic strain ratios trend for Ti-Fe-Si-O alloy

Another aspect which needs to be taken into consideration is that the signal of width contraction acquired from the clip-on transvers extensometer is referred to a specific section, and after the onset of necking its readings are basically incorrect (unless the extensometer clips are placed exactly where the necking will occur). In fact, as can be seen in Fig. 4-5, during the test its signal is stopped for elongation >17%.

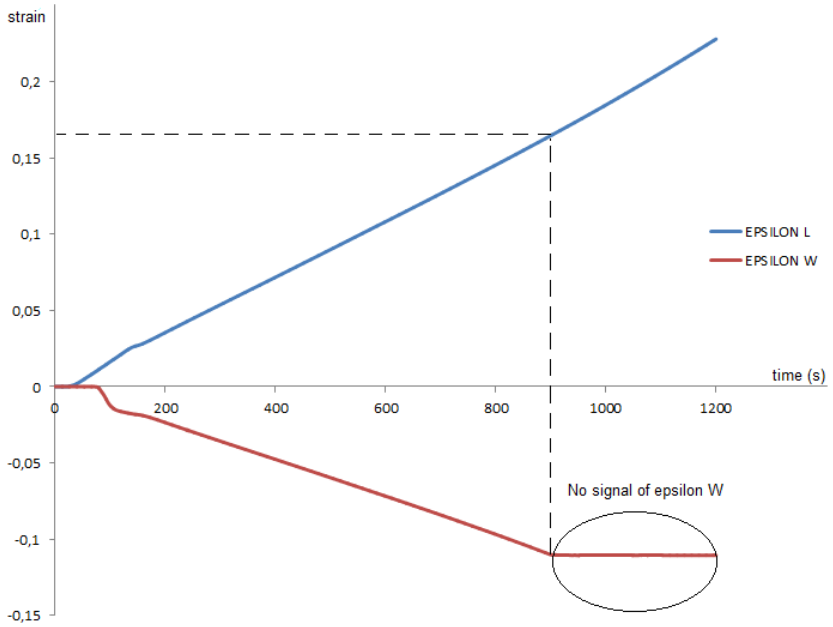

Fig. 4-5 – Longitudinal and transverse strain behavior during tensile test

To be able to accurately define the R values has great relevance, since it is not only the formability parameter, but also the crucial anisotropy parameter in software for simulation of the plastic forming process[78].

In order to minimize inaccuracy during simulation, the plastic strain ratios are determined using ISO procedure in intervals of 0,5% from initial yield to the onset of localized necking on the specimen. After the point of maximum load, in the field of large strains, the curves are extrapolated using an exponential function. Fig. 4-6 shows the variation of the plastic strain ratio with increasing of plastic strain. The variation in the longitudinal direction is nearly negligible, while in the diagonal and transverse directions there is a significant variation in the initial plastic region before the values stabilizes. The completed curves are converted into a discreet function to be used as input values in the model.

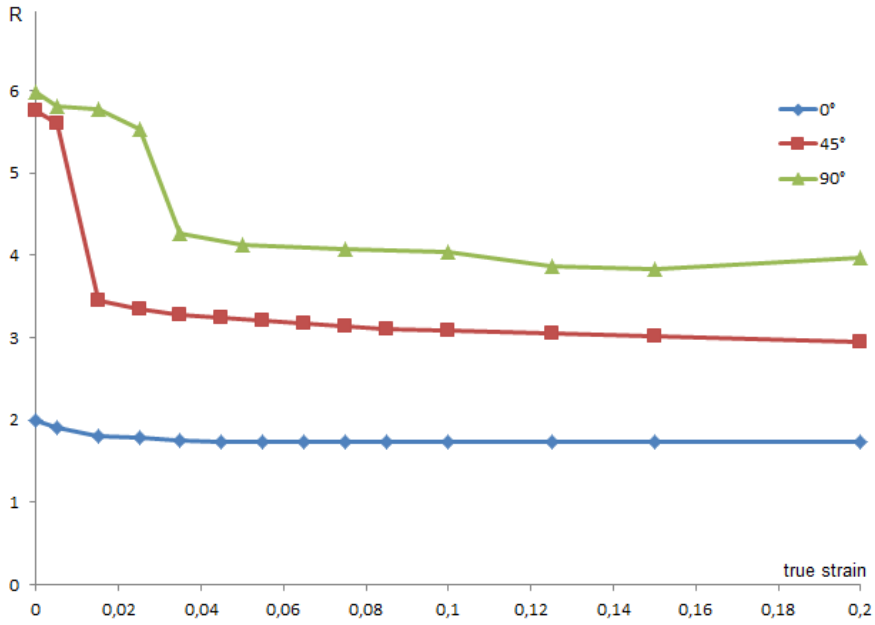

Fig. 4-6 – Example of plastic strain ratio input function for Ti-Fe-Si-O alloy

4.5 Flow exponent determination

The flow potential exponent *m* (also known as Barlat coefficient) is a parameter which plays a significant role in defining the shape of the yield locus. As can be seen in Fig. 4-7, this exponent influences especially the elongation of the curve in the upper quadrant of the yield locus. The convexity conditions necessary for defining the yield function impose that *m* has a constant value greater than the unit[79].

The *m* exponent is a specific material's characteristic and is strongly influenced by the geometry of crystal lattice. The authors of the model specify recommended values for face centered cubic (m=8)

[78] S. Aleksandrović, M. Stefanović, D. Adamović, V. Lazić – Variation of Normal Anisotropy Ratio "*r*" during Plastic Forming – Strojniški vestnik - Journal of Mechanical Engineering Vol. 55(2009) pp. 392-399
[79] H.J. Bunge, K. Pöhlandt, A.E. Tekkaya D,. Banabic - Formability of Metallic Materials: Plastic Anisotropy, Formability Testing, Forming Limits – Ed. Springer, pp.144

and body centered cubic materials (m=6), however very few references can be found in literature regarding HCP materials. Because of this reason, a separate numerical evaluation of the Barlat coefficient has been carried out.

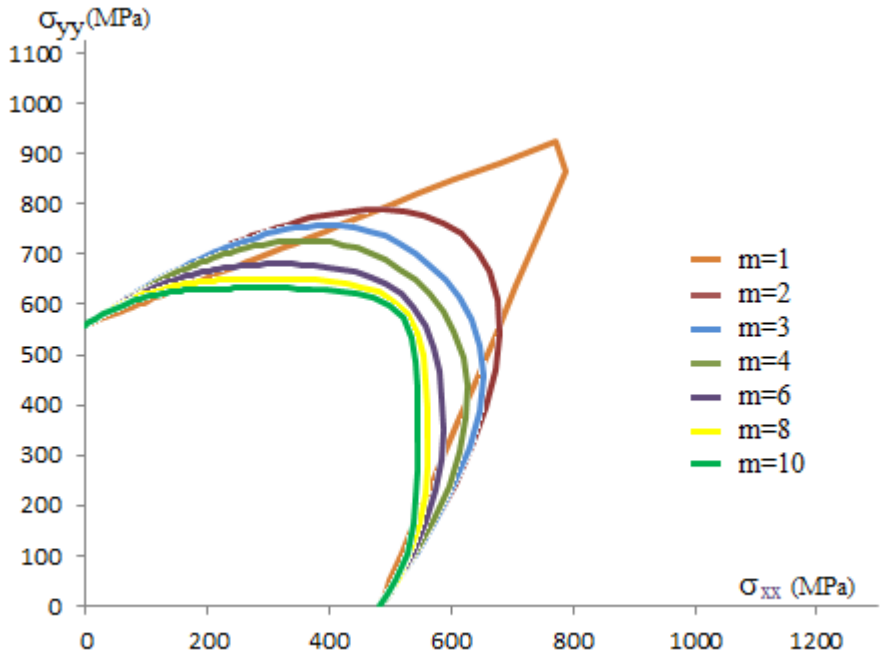

Fig. 4-7 – Influence of the flow exponent m on the yield locus shape

The *m* parameter controls the shape of the yield locus, thus a biaxial test should be used to determine the proper value. The Erichsen cupping test (see. Par. 3.2.7) was chosen because is a standard test which can be performed using a simple tool on a universal testing machine. This test evaluates the ability of the metallic sheets to undergo plastic deformation in stretch forming inducing an equal biaxial stress state. For this particular type of loading conditions, which are located in the quadrant of the yield locus mainly influenced by the *m* exponent, the choice of simulating the Erichsen cupping test has been made.

Similarly to the yield curve identification, several numerical simulations were run for different values of *m* exponent, which was the only variable parameter; the results so obtained were compared to the experimental ones previously presented.

The numerical model used for running the simulations is constituted of three and four node shell elements. We assume that there is no drawing of the material from under the blank holder, thus only the free portion on the blank is modelled and fixed around its perimeter in all degrees of freedom, avoiding the need to model the blank holder. The die and punch are modelled using rigid materials (Material model #20 in LS-Dyna) and friction contacts are prescribed between the tools and the blank (f=0,2). Mass and time scaling are used to cut calculation time, adaptive re-meshing was found to not provide a significant time saving in this case, thus a denser mesh was used for the entire simulation.

The results obtained by the simulation are summarized in Fig. 4-8; it is shown how, for both titanium alloys under investigation, the best results in terms of matching the experimental diagram

were obtained with *m*=2. This will be the value which will be used for subsequent FE simulations of plastic formed titanium components realized with Ti-Fe-Si-O and Ti-Al-Si-Nb alloys.

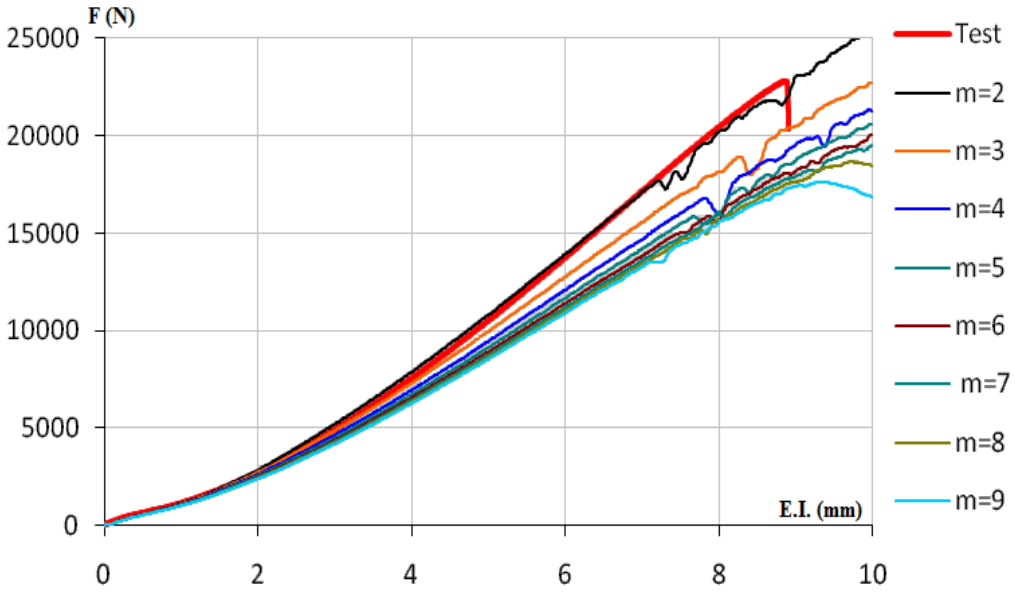

Fig. 4-8 – Impact of different flow exponent on loading curve for Erichsen cupping test

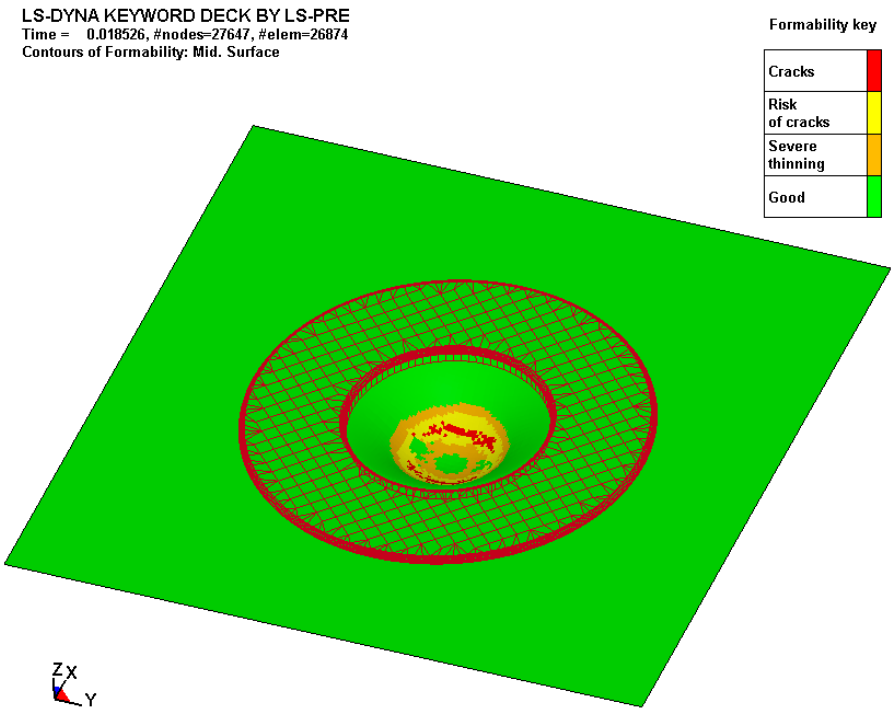

Fig. 4-9 – FE simulation of Erichsen cupping test

4.6 Example of FE analysis of a deep drawn titanium component: influence of material type on final results

A motorcycle exhaust end-cap, shown in Fig. 4-11, was selected for this activity of FE simulation. The part is manufactured by deep drawing, and the final shape is obtained with subsequent steps; the phase object of the FE analysis is the first deformation stage, because in this case the depth of the cap is considerably high, the radius at the top is small and the sides are tapering. Because of these reasons, this exhaust system component presents several problems of plastic forming and is considered as a significant case study for exploring the formability limits of deep drawing technology applied to alpha titanium alloys.

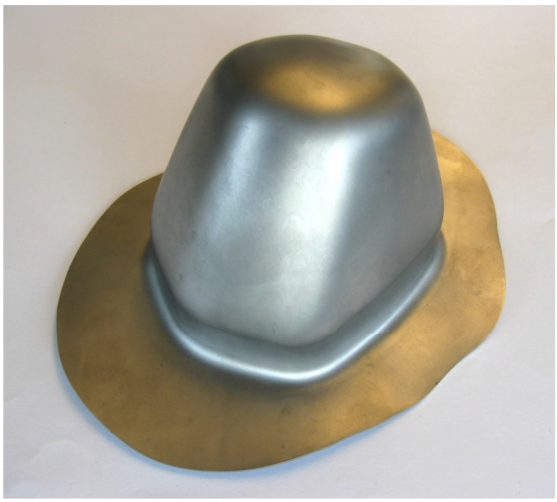

Fig. 4-10 – First deformation stage

Fig. 4-11 – Final shape of the component

In order to evaluate the feasibility of this part by deep drawing, and performing a study about the possibility of using an existing tool, the simulations have been carried out considering two titanium alpha alloys for heat resistant applications. In addition to Ti-Al-Si-Nb alloy, main object of present work, also the alloy Grade 37 (Ti 1,5 Al), has been chosen for simulation trials.

Even though Grade 37 alloy is a standard material included in ASTM B265[80], a complete characterization equal to the one presented in Chapter 3 has been performed also on this material, in order to collect experimental data to be used as input for FE analyses.

The simulations performed on this motorcycle component show that the part can be successfully drawn only with Grade 37 alloy, while with Ti-Al-Si-Nb the final shape cannot be obtained completely without the onset of cracks appearing at the leading edge of the punch. In order to show the type of informations which can be derived from FE simulation, the results obtained with the aforementioned alloys will be presented and discussed in the following paragraphs.

[80] ASTM B265 (2006) - Standard Specification for Titanium and Titanium Alloy Strip, Sheet, and Plate

4.6.1 Material model

The experimental data inputted for building the material model are:

- Yield curve σ(ε) function in rolling direction 0°
- Plastic strain ratio R(ε) functions in three direction 0°, 45°, 90°
- Flow exponent m=2

4.6.2 Numerical model

Fig. 4-12 shows the numerical model of the end-cap deep drawing process. The model is comprised of three and four node shell elements. The tool components are considered rigid, and friction contacts are prescribed between the tools and the blank. Mass and time scaling, as well as adaptive re-meshing, were used to cut calculation time.

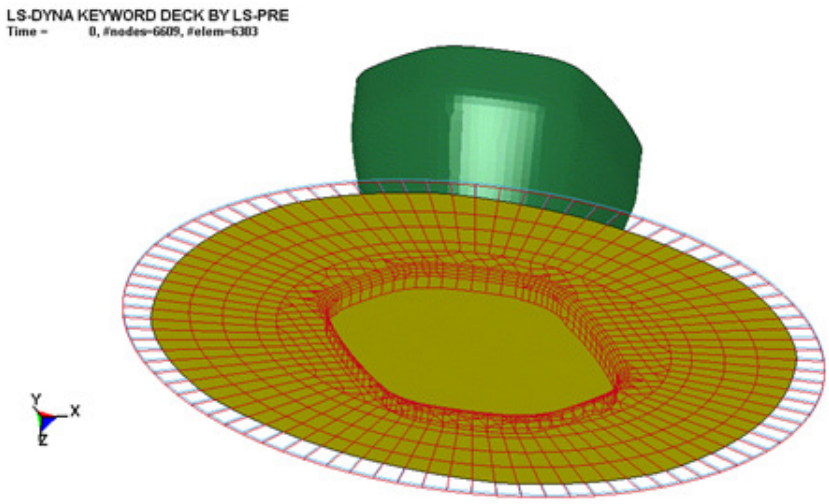

Fig. 4-12 – Numerical model of deep drawing process

A series of simulation of deep drawing were carried out with the aforementioned Ti alloys with a sheet thickness of 0,9 mm. Longitudinal and transverse orientations of the material rolling direction with regard to the longer axis of the end-cap were tested and compared.

In detail, the simulation conditions were:

- Blank mesh: 2D shell elements with Belytschko – Tsay formulation and five integration points
- Blank Orientation: rolling direction parallel and perpendicular to the maximum length of the end cap section
- Tool mesh: idealized rigid 2D shell (LS Dyna material model #20)
- Punch movement: constant speed of 65 mm/min up to 90 mm
- Blank holder: constant holding force of 100 kN

The different tool's components are considered rigid and penalty frictional interfaces are prescribed between the tools and the blank. Friction coefficients of 0.2 are used for the lubricated contacts (die-blank, holder-blank), and 0.3 for the unlubricated contact (punch-blank). The die is fixed in all degrees of freedom while the punch and blank holder are free to move only in the z direction (perpendicularly to the blank surface).

4.6.3 Results of the simulation

The results of the simulations correspond well to the deep drawing tests performed on a production press with a complete tooling set. The endcap could be drawn using Grade 37 alloy, but is supposed to break at a depth of 47 mm if it is manufactured using Ti-Al-Si-Nb alloy (see Fig.4-22). Similarly, the simulations exhibit various indicators of material failure for Ti-Al-Si-Nb alloy, while no problems are encountered while using the material parameters for Grade 37 alloy.

The following aspects of the simulation were evaluated when processing the results:

- Stress distribution and maximum achievable load during deformation
- Mayor-minor strains plotted on the FLD diagram
- Thickness distribution

4.6.3.1 Stress distributions & force displacements

The simulation performed using Ti-Al-Si-Nb alloy shows strong stress localization around the leading edge of the punch (see Fig. 4-13). At approximately 40 mm of displacement, the force peak is reached and afterthat an excessive stretching of the blank is starting until the material failure occurs. This result is also confirmed with the force-displacement plot, where the degradation of the blank at around 40 mm displacement is clearly visible.

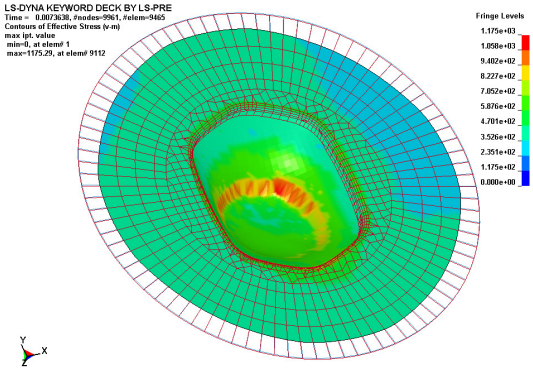

Fig. 4-13 – Stress distribution on Ti-Al-Si-Nb endcap

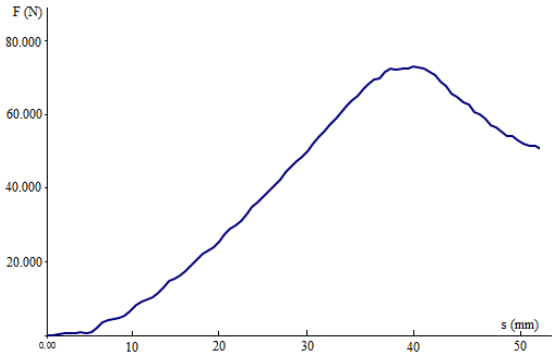

Fig. 4-14 – Force displacement on Ti-Al-Si-Nb endcap

The result of a practical deep drawing operation is shown in Fig. 4-15, the area where the break occurs correlates well to the failure predicted by the simulation.

Fig. 4-15 – Deep drawing test on Ti-Al-Si-Nb

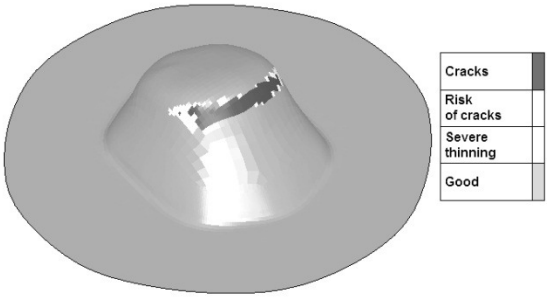

Fig. 4-16 – Deep drawing simulation on Ti-Al-Si-Nb

The simulation performed using Grade 37 alloy indicates more uniform stress and strain distributions compared to the one performed on Ti-Al-Si-Nb alloy. During the deformation, the peak stresses move from the leading edge of the punch to the inner edge of the die. There is no excessive stretching of the blank that would indicate possible failure during deep drawing.

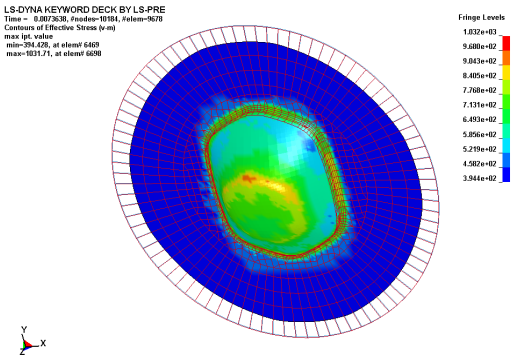

Fig. 4-17 – Stress distribution on Grade 37 endcap

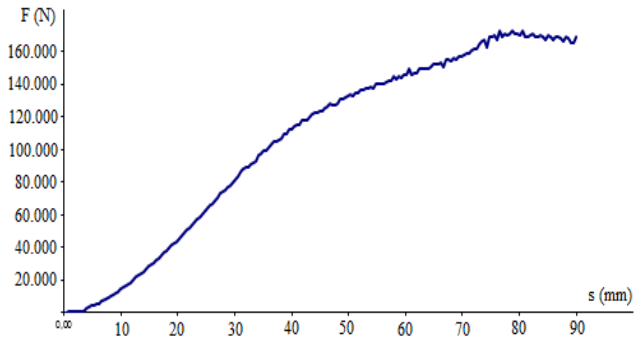

Fig. 4-18 – Force displacement on Grade 37 endcap

It's also important to notice that in this case the force-displacement plot doesn't show any irregularities; the deep drawing process can be completed without concerns.

4.6.3.2 FLC representation

For both the considered alloys, the strain distribution characteristics of every node of the mesh at the end of the forming process were plotted on the mayor-minor strain domain and compared with FLCs plot (for detailed explanation of this diagram see Paragraph 5.1.1). In Fig. 4-19 and 4-20 are represented the Forming Limit Curves characteristic for Ti-Al-Si-Nb and Grade 37 alloys; the red line represents the fracture limit of the material, while the yellow one represents the necking limit. If the strains conditions are so to exceed the red line, is a clear indication that the material will breaks; the area between the yellow and the red lines is a zone with demanding deformation levels but the parts can be still shaped.

To this end, it can be stated that in Fig. 4-19 is clearly shown the localized deformation which exceeds the forming limit curve in case of Ti-Al-Si-Nb alloy: those red points coincide with the excessive deformation at the leading edge of the punch. Likewise, it can be also noticed in Fig. 4-20

that for Grade 37 alloy, in comparison to Ti-Al-Si-Nb alloy, the strains are much more condensed on the FLD, providing a sufficient safety margin which allows obtaining the final shape of the deep drawn endcap.

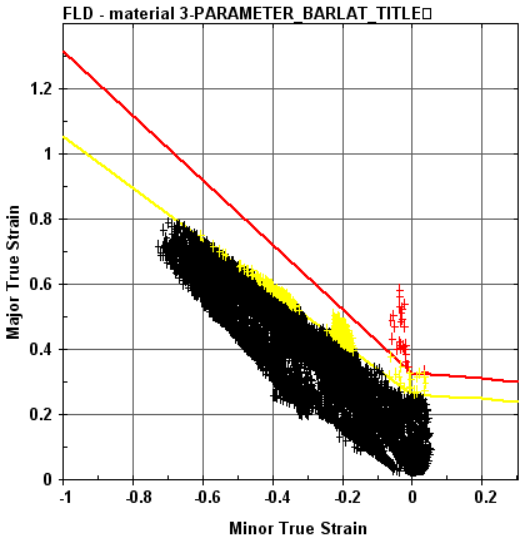

Fig. 4-19 – Strains distribution for Ti-Al-Si-Nb

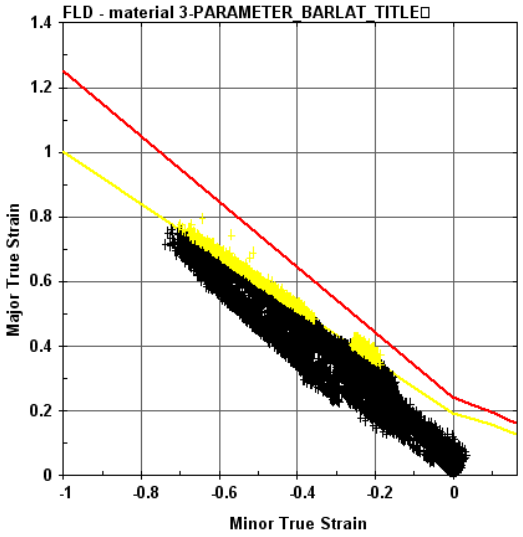

Fig. 4-20 – Strains distribution for Grade 37 alloy

4.6.3.3 Thickness distribution

The simulated thickness distributions with both blank orientations at the maximum safe drawing depth (equal to 47 mm) were compared to the experimental thickness distributions measured on the real parts deep drawn up to the same height. The zero point on the horizontal axis corresponds to the die shoulder, with the distance measured along the surface of the part.

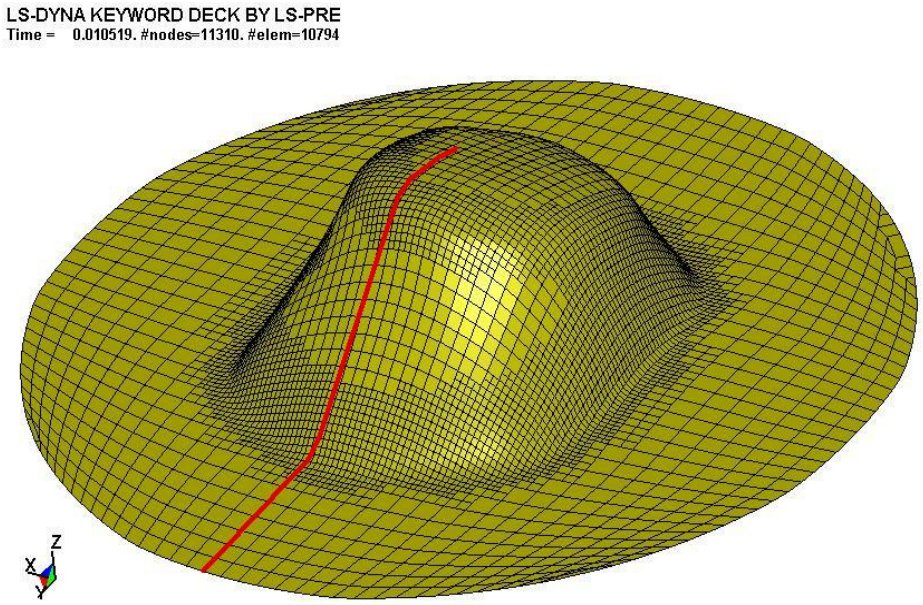

Fig. 4-21 – Thickness distribution section

The experimental thickness measurements and the results obtained from the simulation performed on Ti-Al-Si-Nb alloy are compared in Fig. 4-22. It can be easily seen that the numerical results

compare fairly well to the measurements; the severe discrepancy in the longitudinal direction is due to the simulation predicting a break in the rosette before this depth is achieved.

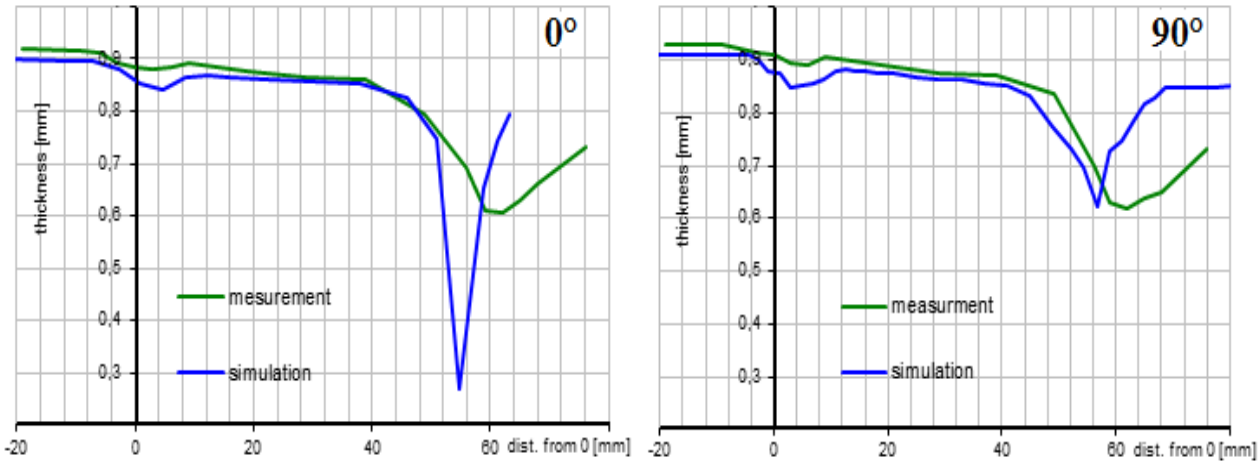

Fig. 4-22 – Comparison of thickness distribution (measured and simulated) on Ti-Al-Si-Nb in L and T direction

The diagrams represented in Fig. 4-23, clearly show that Grade 37 alloy exhibits considerably less thinning in the critical region than Ti-Al-Si-Nb alloy. Although the thickness distribution does vary with blank orientation, longitudinal orientation giving a smoother transition into thinning and thus a more uniform thickness distribution than transverse, the minimal thickness in the critical region is quite similar for both materials.

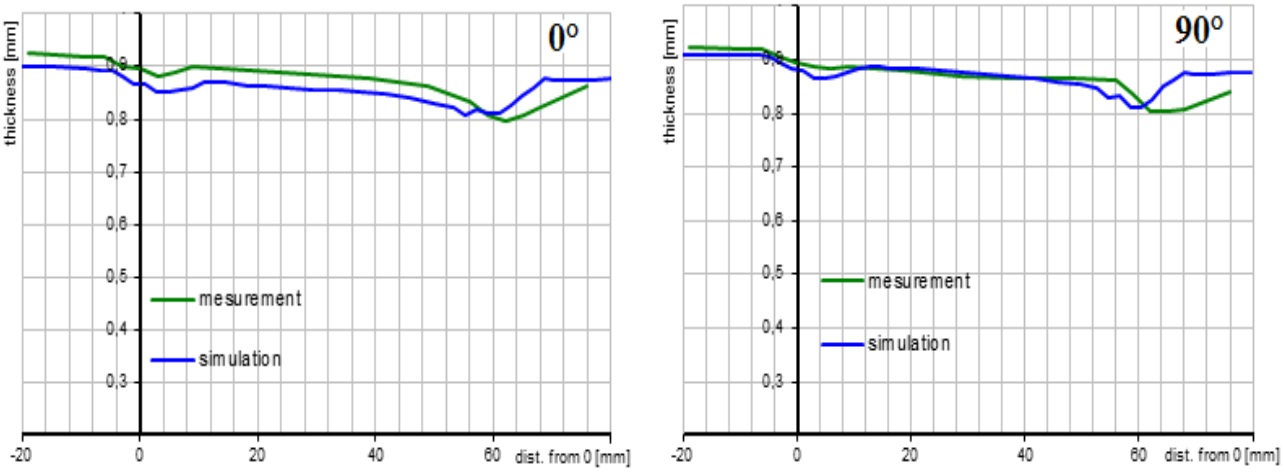

Fig. 4-23 – Comparison of thickness distribution (measured and simulated) on Grade 37 in L and T direction

CHAPTER 5
MATHEMATICAL MODEL REFINING

5.1 Formability Limits

A reliable numerical simulation for predicting the plastic behavior of the material doesn't constitutes the only necessary factor needed for an exhaustive analysis and design of a deep drawing or stamping process. In order to possess a comprehensive knowledge of the limits of the process, in terms of maximum applicable deformation on the blank, a formability analysis has also to be performed.

Different methodologies have been proposed throughout time in order to evaluate formability. These comprise different levels of completeness, which is usually achieved at the increase test complexity, and range from the analysis of simple uniaxial tensile tests, to more comprehensive tests such as cupping and bulging, to even more complex procedures such as Nakajima and Marciniak tests[81].

Uniaxial tensile tests are able to evaluate the values of stress and strains that bring the specimen to failure for a single strain condition. However, they can't consider complex stress states and therefore can only be used for preliminary analyses. Cupping and bulging tests uses a punch, in the case of the cupping test, or a pressurized fluid, in the case of the bulging test, in order to apply a more complex stress state on the sheet. The stress state obtained through these tests is close to the plane stress case. The results are given in terms of maximum punch displacement and load or maximum pressure before failure. They are relatively simple and fast but, even if they consider a strain condition more similar to those achieved in areal stamping process, they are also limited, due to the fact that only a generic evaluation of material formability can be achieved[82].

Some of the most important tests in order to correctly analyze the formability of sheet metals are those that enable to draw the FLC (*Forming Limit Curve*) of the material. This diagram represents the formability limit for different strain paths for a given material, describing the area and therefore the couples of principal strains that are likely to conduct to the onset of instability.

In the following paragraphs, some basic informations about the meaning of FLC diagrams will be given, together with a detailed explanation regarding the methods which can be used for plotting them. Finally, the experimental data obtained for Ti-Fe-Si-O and Ti-Al-Si-Nb alloys will be presented and discussed.

[81] Goodwin G. - Application of strain analysis to sheet metal forming problems - Metallurgia Italiana 60 (1968), pp. 767-771
[82] Keller S. - Circular grid system: a valuable aid for evaluation sheet forming - Sheet Metal Industries Journal 45 (1969), pp. 633-640

5.1.1 Basic understandings concerning the Forming Limit Curves

Forming Limit Curves (FLCs) are mostly used as a parameter in finite element analysis to control where the material exceeds the level of formability. They are also used in workshops to analyze actual and potential problems of sheet forming or to compare the formability of different materials.

FLCs represent the formability limits in the coordinate system of major (ε_1) and minor (ε_2) principal strains as shown in Fig. 5-1.

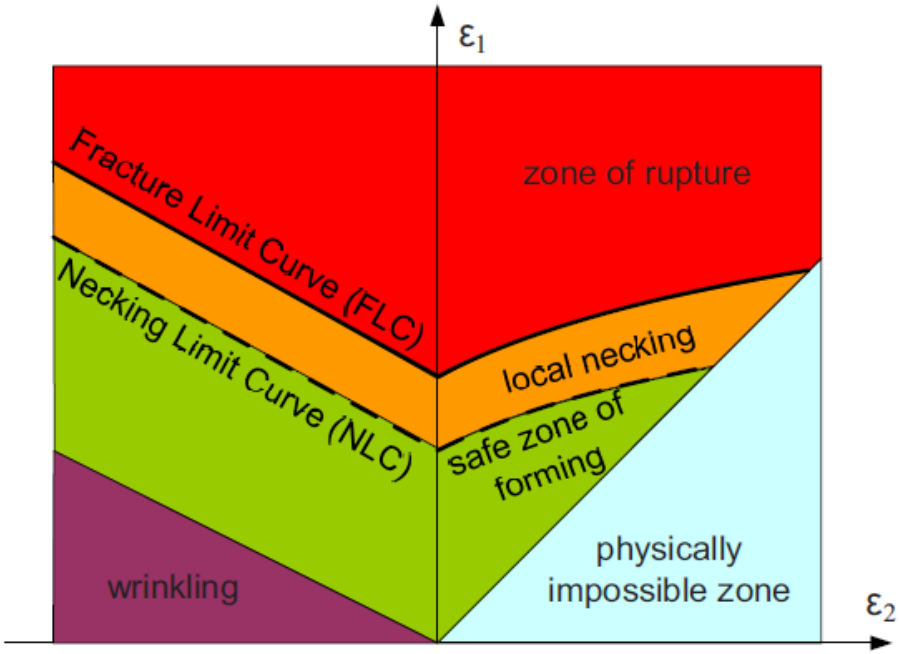

Fig. 5-1 – Characteristic limit curves and zones of FLC diagram

The formability limit is usually characterized by the failure (rupture) and this is called as "Fracture Limit Curve". While to observe the onset of fracture is quite easy, however to determine the principal strain values at the onset of rupture is rather complicated. Anyway, in the last decade, due to the development of modern optical strain measuring equipments, several steps forward have been made for experimental determination of the strains distribution during deformation. These technical progresses allow obtaining more accurate FLCs diagram, improving both the scientific research and the industrial applications in the field of formability.

However, it is evident that in normal production conditions even the local necking cannot be permitted: neither from the point of view of aesthetic appearance nor the functional operation of the part. This is the reason why further limit curves are determined besides the rupture for the limit of necking as well[83]. The "Necking Limit Curve" (*NLC*) represents the onset of local necking. Though the exact measurement of principal strain components at the limit state of necking is at least as difficult as it is for the onset of fracture, but this limit is more acceptable for real industrial parts, since

[83] M. Tisza, Z. P. Kovács - New methods for predicting the formability of sheet metals - *Production Processes and Systems, Volume 5. No. 1 (2012) pp. 45-54*

at this stage still there is no any undesirable local necking. The zone between the fracture and the necking limit curve is called as the range of local necking.

At certain level of compressive stresses a local instability of sheet can also occur: this phenomenon is referred as wrinkling. It is also evident that besides rupture and local necking, wrinkling should also be avoided. Below the local necking zone, the green zone indicates the safe region of normal forming conditions.

5.1.2 Nakazima & Marciniak Test

The testing procedures which are most commonly used in order to plot FLC diagrams are the Nakazima[84] and the Marciniak[85] methods.

In both cases, the standard evaluation procedure to be used for experimental determination of FLC diagram for a given material is usually performed using specimens presenting different geometries and dimensions, with the aim of creating different combinations (couples) of major and minor strain values.

The basic difference between the aforementioned methods is the use of punch presenting different geometry (hemispherical for Nakazima and cylindrical for Marciniak). A schematic representation of the two methods is given in Fig. 5-2.

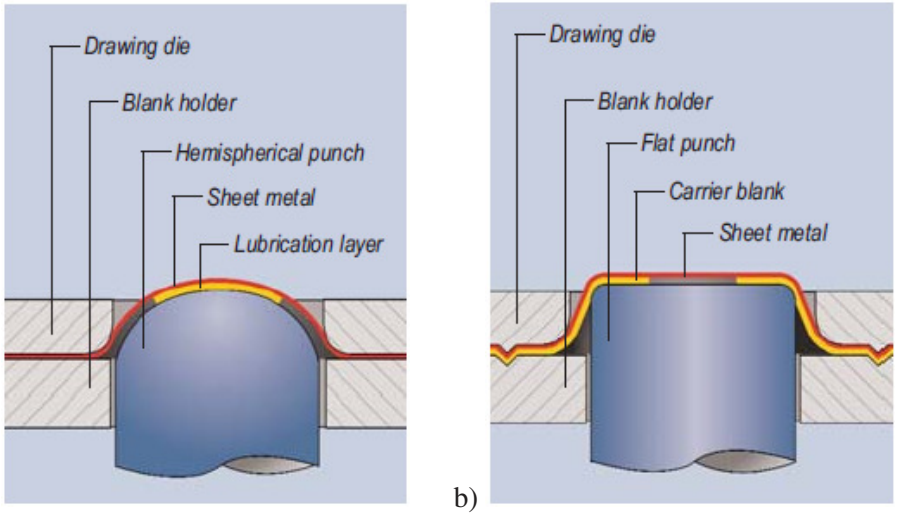

Fig. 5-2 – Schematic representations of a) Nakajima test and b) Marciniak test

As can be seen from the schematic representation, in these tests the specimens are fixed on clamping equipment with a blank holder, and in this configuration a punch moving at a constant speed deforms the specimen until it fractures. During the test, the strains on specific sections of the specimen's surface are evaluated so that values of major and minor strain ε_1 and ε_2 can be determinated. These two values define a strain conditions which brings the sheet to failure. Then, in

[84] Nakazima K., Kikuma T., Asaku K. - Study on formability of steel sheet - Yawata Technical report 264 (1968)
[85] Marciniak Z., Kuczynzky K. - Limit strains in the process of stretch- forming sheet metal - International Journal of Mechanical Sciences 9 (1967), pages 609-620

accordance to standard ISO 12004-2[86], both major and minor strain values obtained along these sections are selected and fitted with inverse parabolas in order to evaluate the strains that brought to failure avoiding considering post-necking deformations.

Using different specimen geometries, different strain fields could be imposed on the specimen, thus obtaining several sets of major and minor values that describe the Forming Limit Curve of the given material. An example of standard specimens used for FLC determination is shown in Fig. 5-3.

Fig. 5-3 – Example of fractured Nakajima formability test specimens

Since the obtained values of major and minor strains depend on the punch-sheet interaction it is very important for obtaining accurate values that sheet deformation is as close as possible to a free forming case. Therefore, particular attention has to be given to lowering as much as possible the friction at the punch-sheet interface and usually very low punch speeds are also adopted. More than this, since slipping of the specimen in the clamping equipment has to be absolutely avoided in order not to alter the material flow during testing, the blank holders usually features specifically designed draw beads.

Concerning the sample preparation, an option is etching on its surface a repeating pattern of geometrical features with known dimensions, an example of which is illustrated in Figure 5-4.

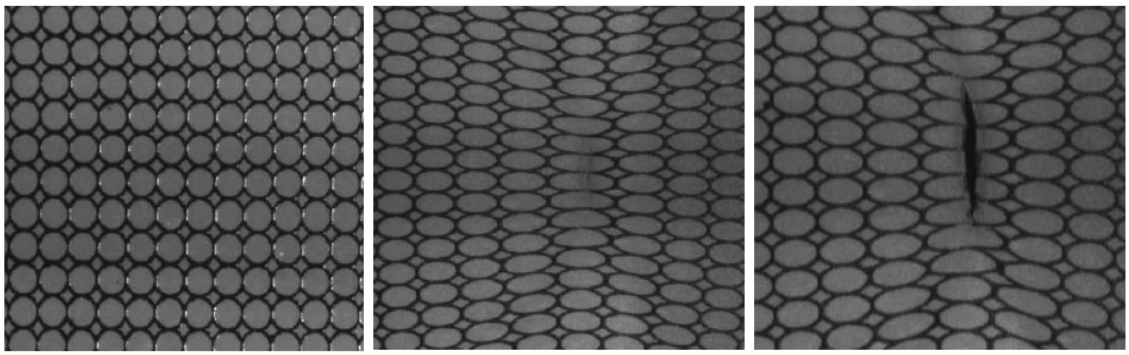

Fig. 5-4 – Example of etched pattern (before and after deformation) on sample's surface

[86] ISO 12004-2:2008 - Metallic materials -- Sheet and strip -- Determination of forming-limit curves -- Part 2: Determination of forming-limit curves in the laboratory

After the test, it will be measured how these features changed shape along three parallel sections normal to fracture direction. This procedure is consolidated since long time, however it results extremely time consuming since every single feature has to be measured singularly by an operator. More than this, the resolution of the strain profile depends on feature dimensions which in turn affects the quality of the evaluations: an higher number of points means that their analysis can be performed with a greater accuracy, but the dimensions of a single feature would diminish as well, lowering the accuracy of the single strain measurement.

Optical measuring systems are therefore being employed with increasing frequency. These enable an inline evaluation of the strain profiles along the whole surface of the specimen, with increased accuracy and on a large number of points. This type of equipment uses two cameras, in order to obtain a stereoscopic view of the test area and therefore evaluate the displacements in all three dimensions. A stochastic pattern has to be sprayed on specimen's surface: first a neutral white layer and subsequently black painting random dots (see Fig. 5-5).

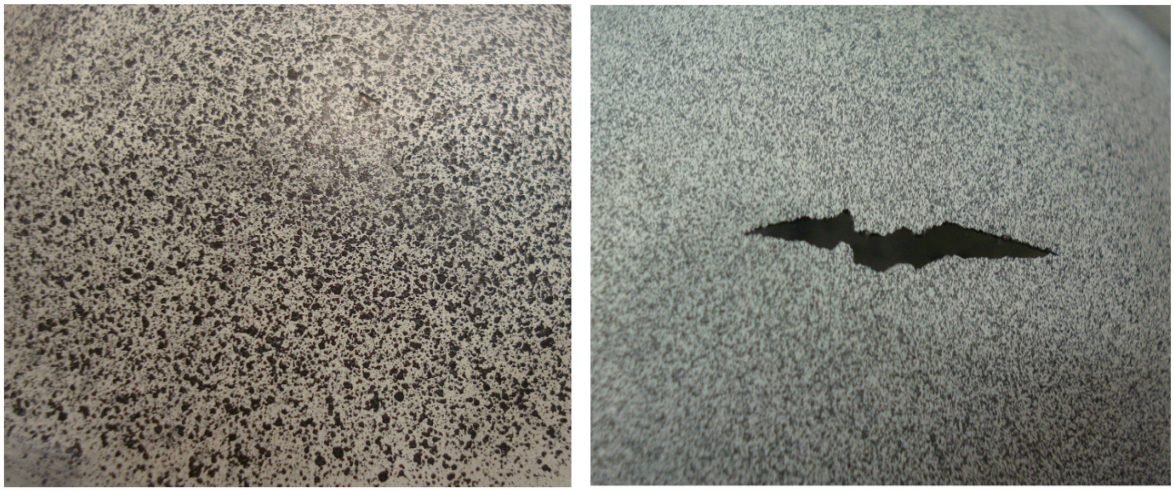

Fig. 5-5 – Example of stochastic sprayed pattern (before and after deformation) on sample's surface

By using the optic measuring system, recording of the etched patterns is replaced by the allocation of stochastic patterns. Thus, the number of measuring points is considerably increased. In addition, minor blurs and defects in the pattern are compensated such that numerous reliable measuring values are created.

5.1.3 Testing Procedure

The determination of Forming Limit Curves for the alloys Ti-Fe-Si-O and Ti-Al-Si-Nb have been performed at Erlangen University (Nurnberg, Germany) in the department of Manufacturing Technologies. The choice to outsource these trials has been made due to the specific equipment owned from this department for performing the Nakazima test. The testing machine and the optic measuring system Aramis can be seen in Fig. 5-6.

Fig. 5-6 – Testing equipment for Nakazima (or bulge) test

Aramis system, produced by GOM, is a 3D optical deformation analyzer which uses two high resolution CCD cameras and can provide complete stereoscopic 3D surface determination, displacement and strain results in real time. This equipment is visible in Fig. 5-6, mounted on the top of the hydraulic machine.

For the determination of FLC diagrams, seven different specimens have been used; the basic geometry of these specimens and of the punch can be seen in Fig. 5-7 and Fig. 5-8.

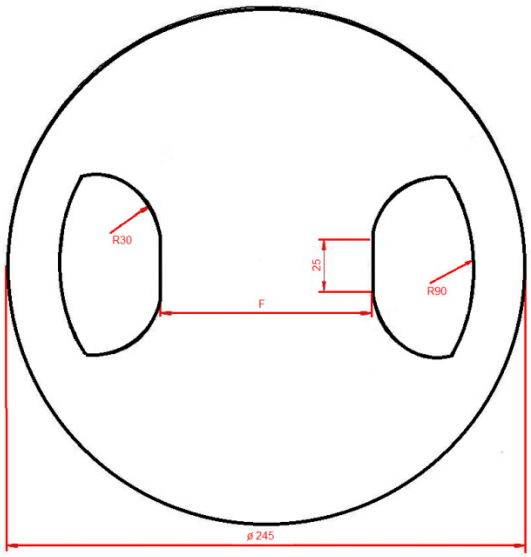

Fig. 5-7 – Specimens basic geometry

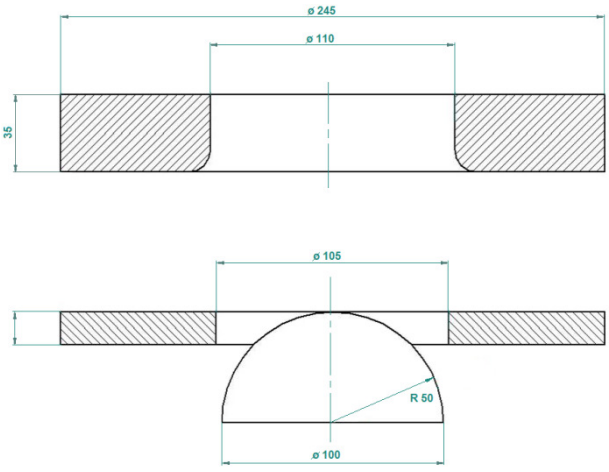

Fig. 5-8 – Punch basic geometry

The series of specimens chosen for the test, presents the same outer diameter equal to ϕ 245 mm and variable values for the dimension marked with "F" in Fig. 5-7. Specifically, the selected "F" dimensions were: 0 (full disc), 50, 70, 80, 100, 110, 125 mm.

Fig. 5-9 – Nakazima specimens after testing

For all the seven values of dimension "F" mentioned above, three specimens have been tested in longitudinal direction and the same has been done along transverse direction; in total, for FLC diagram determination, 42 Nakazima specimens have been used. For both the alloys the thickness of the sheets under testing was 0,9 mm; this data is very important in case of FLC determination, because thinner is the material, the more reduced are the deformation boundaries.

During testing, the punch speed was equal to 90 mm/min; in order to reduce the friction between samples and tool, a multiple layer of lubricant has been used between the two surfaces. In detail, both specimen and punch have been oiled with wool grease, and between them a PTFE foil and a Mipolan rubber sheet (also lubricated) were interposed. This ploy allows having a more accurate distribution of the load during testing, and also it increases the chance that the break will occur in the center of the deformed dome.

According to standard ISO 12004-2, the point chosen for evaluation of the principal strains ε_1 and ε_2 is the one identified 0,1 s before the crack initiation. The use of the optic system allow selecting the precise frame before the fracture occurs; on this frame, where load and deformation parameters can be visualized, five parallel sections are chosen and the software automatically calculates and exports the couple of values ε_1 and ε_2. The measuring points (major and minor strains), characteristics for every different specimen geometries, are then connected and thus allow designing the FLC diagram of the tested material.

The experimental data obtained by performing the Nakazima test on Ti-Fe-Si-O and Ti-Al-Si-Nb alloys are summarized in the following paragraph.

5.1.3.1 Experimental Results

The experimental results obtained performing the Nakazima tests on the two alloys are summarized in Tab. 5-I and Tab. 5-II.

Specim.		Longitudinal (0°)		Transverse (90°)	
		Major Strain ε_1	Minor Strain ε_2	Major Strain ε_1	Minor Strain ε_2
0	1	0,325	0,269	0,270	0,269
	2	0,388	0,328	0,322	0,328
	3	0,399	0,349	0,331	0,349
S125	1	0,361	-0,001	0,464	-0,085
	2	0,348	-0,007	0,465	-0,078
	3	0,343	-0,001	0,467	-0,088
S110	1	0,467	-0,058	0,391	-0,818
	2	0,436	-0,058	0,385	-0,858
	3	0,464	-0,061	0,408	-0,871
S100	1	0,488	-0,094	0,546	-1,875
	2	0,486	-0,090	0,552	-1,929
	3	0,492	-0,090	0,549	-1,919
S80	1	0,552	-0,170	0,701	-0,447
	2	0,567	-0,173	0,738	-0,477
	3	0,563	-0,173	0,738	-0,467
S70	1	0,598	-0,212	0,794	-0,536
	2	0,611	-0,216	0,782	-0,548
	3	0,567	-0,201	0,790	-0,561
S50	1	0,700	-0,304	1,000	-0,620
	2	0,724	-0,314	0,995	-0,620
	3	0,648	-0,286	0,987	-0,613

Tab. 5-I – FLC experimental data for Ti-Al-Si-Nb alloy*

**The experimental data shown in Tab. 5-I have been normalized by diving them for a constant value*

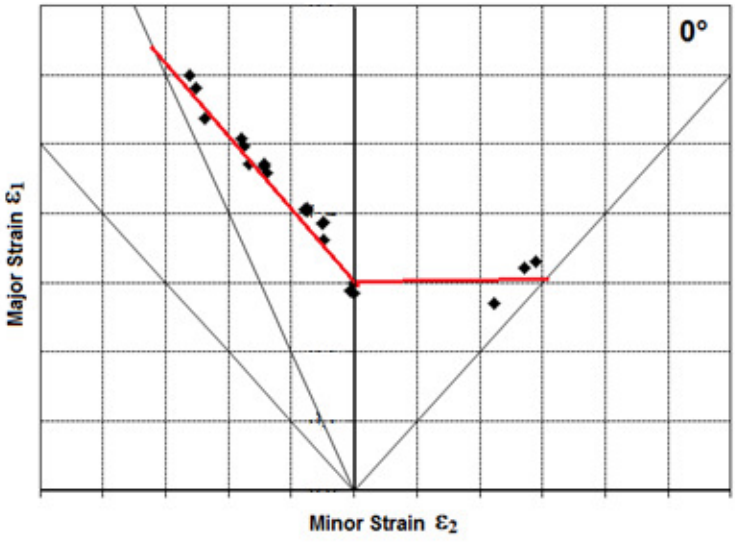

Fig. 5-10 – FLC for Ti-Al-Si-Nb alloy in longitudinal direction**

*** The FLD diagram shown in Fig. 5-10 is represented without scale on ε_1- ε_2 plane, in order to preserve the property informations related to this chart*

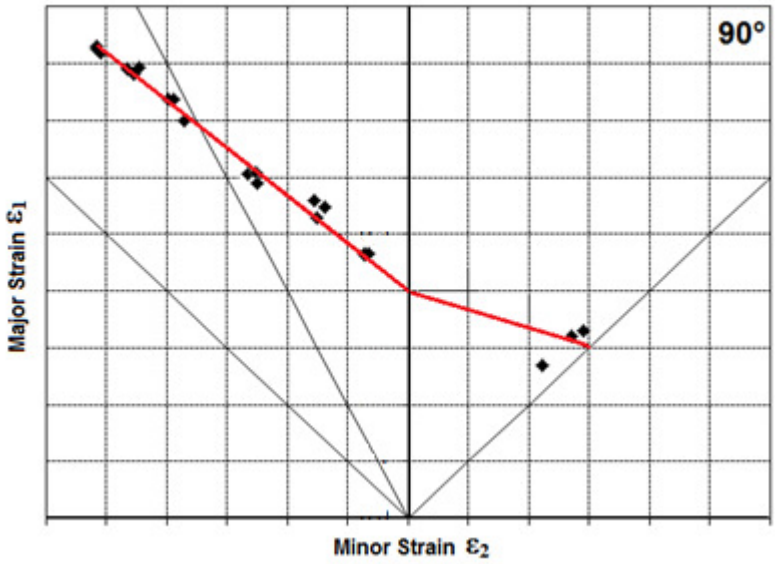

Fig. 5-11 – FLC for Ti-Al-Si-Nb alloy in transverse direction**

*** The FLD diagram shown in Fig. 5-11 is represented without scale on ε_1- ε_2 plane, in order to preserve the property informations related to this chart*

Specim.		Longitudinal (0°)		Transverse (90°)	
		Major Strain ε_1	Minor Strain ε_2	Major Strain ε_1	Minor Strain ε_2
0	1	0,333	0,275	0,333	0,275
	2	0,315	0,256	0,315	0,256
	3	0,331	0,260	0,331	0,260
S125	1	0,325	-0,012	0,539	-0,078
	2	0,311	-0,010	0,531	-0,068
	3	0,302	-0,006	0,532	-0,069
S110	1	0,396	-0,062	0,697	-0,268
	2	0,384	-0,063	0,724	-0,273
	3	0,359	-0,075	0,764	-0,295
S100	1	0,428	-0,091	0,787	-0,363
	2	0,438	-0,103	0,790	-0,369
	3	0,434	-0,100	0,782	-0,361
S80	1	0,488	-0,163	0,884	-0,494
	2	0,491	-0,161	0,928	-0,528
	3	0,493	-0,153	0,892	-0,506
S70	1	0,532	-0,205	0,913	-0,542
	2	0,521	-0,200	0,935	-0,542
	3	0,557	-0,215	0,916	-0,534
S50	1	0,611	-0,295	0,967	-0,615
	2	0,587	-0,286	1,000	-0,648
	3	0,641	-0,311	0,969	-0,627

Tab. 5-II – FLC experimental data for Ti-Fe-Si-O alloy*

**The experimental data shown in Tab. 5-I have been normalized by diving them for a constant value*

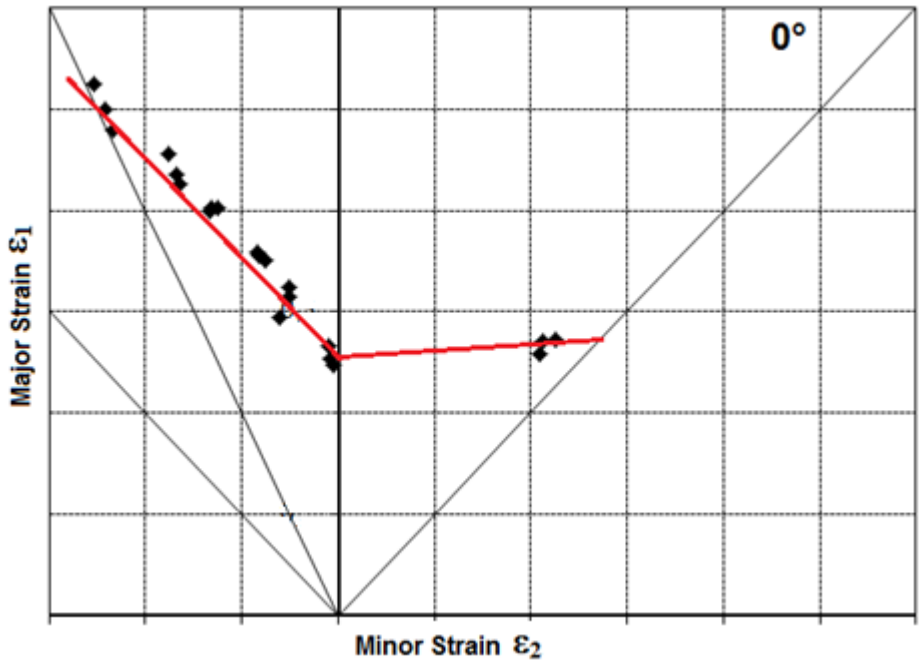

Fig. 5-12 – FLC for Ti-Fe-Si-O in longitudinal direction

*** The FLD diagram shown in Fig. 5-12 is represented without scale on ε_1- ε_2 plane, in order to preserve the property informations related to this chart*

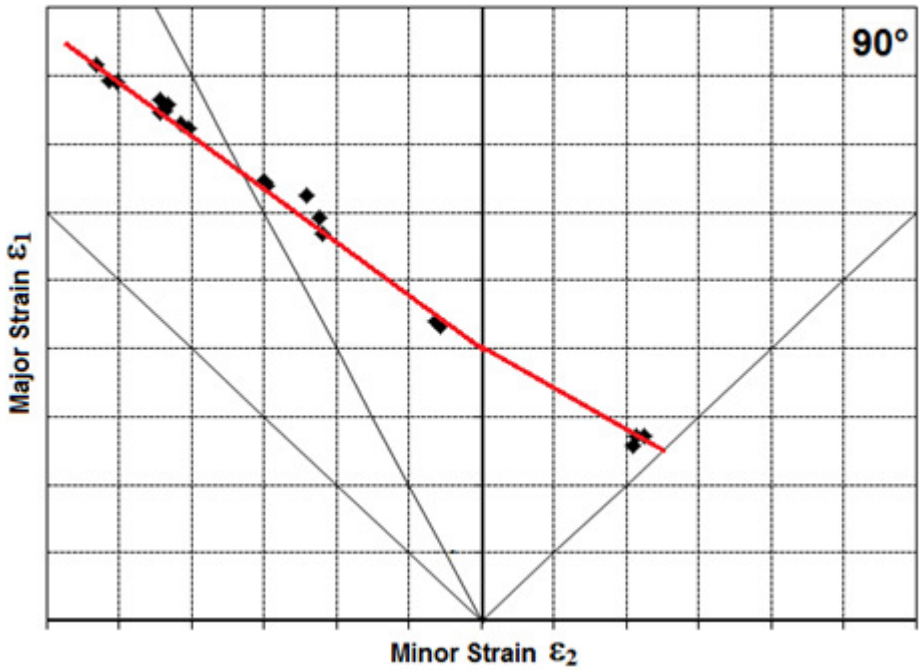

Fig. 5-13 – FLD for Ti-Fe-Si-O in transverse direction

*** The FLD diagram shown in Fig. 5-13 is represented without scale on ε_1- ε_2 plane, in order to preserve the property informations related to this chart*

5.1.4 Example of application of Forming Limit Curve during FE simulation

When a formability simulation of a sheet metal component is performed by using LS-Dyna (see Par. 4.6.3.2), the strains conditions of every single node of the mesh can be represented on the major – minor principal strains domain ($\varepsilon_1 - \varepsilon_2$). In this case, if the experimental Forming Limit Curve of the material is known, it can be plotted on the same plane $\varepsilon_1 - \varepsilon_2$ together with the principal strains distribution of the parts under investigation.

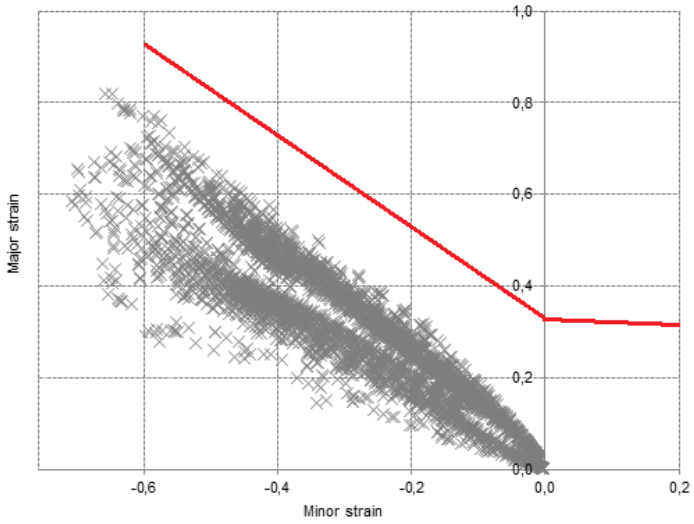

Fig. 5-14 – Strains distribution during plastic forming represented on FLC (no failure)

With this technique, an immediate overview regarding the possibility of achieving a successful plastic deformation can be obtained. In fact, if all the predicted strains are located below the FLC as show in Fig. 5-14, it means that the shape of the component under investigation can be reached without failures or cracks occurring on the sheet metal. Conversely, if some points present strains level positioned above the FLC, the failure of the material is predicted during the simulation (see Fig. 5-15).

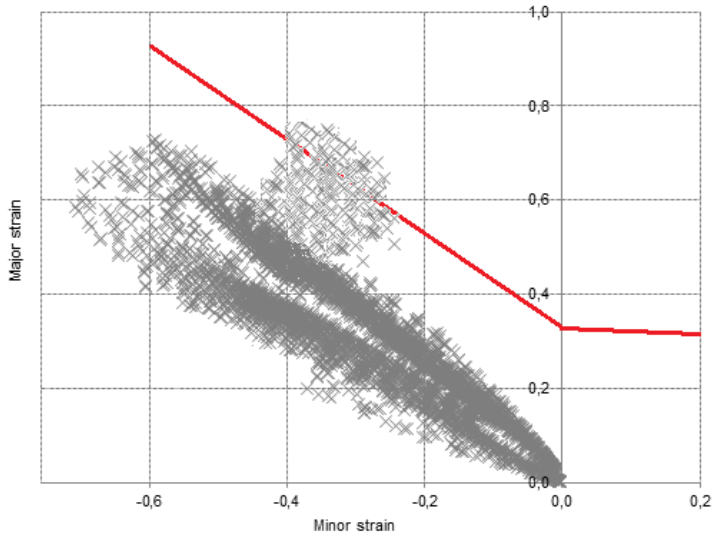

Fig. 5-15 – Strains distribution during plastic forming represented on FLC (failure)

Observing the component's positions where the nodes show deformations localized in the rupture area, few considerations regarding the possibility of implementing tool's modifications can be made.

5.2 Hydraulic Bulge Test

The successful implementation of the finite element simulations in the design phase of sheet metal forming processes depends on the accuracy of the material characteristics. The standard uniaxial tensile test is a widely accepted method to obtain relevant properties of sheet metal materials. However, the range of strain obtained from tensile test is limited compared to higher strain/deformation and biaxial state of stress that occur in practical stamping operations[87]. Therefore if further informations on material behavior are needed, extrapolation of tensile data is performed by using the hardening law, which is used for defining the relationship between the flow stress and the plastic strain.

The bulge test is an alternative to obtain ranges of deformation higher than tensile test, thus being possible to obtain non-extrapolated data for material behavior[88]. The main problem of using this technique for the determination the stress-strain relationship is the measurement of the bulge radius and polar thickness of the specimen. This data is required to calculate the stress based on the membrane theory[89].

Several methods may be used to obtain stress-strain data from bulge test, but a common concept is behind them, which needs the measurement of bulge pressure, curvature of bulge specimen, its thickness at the pole and the application of membrane theory.

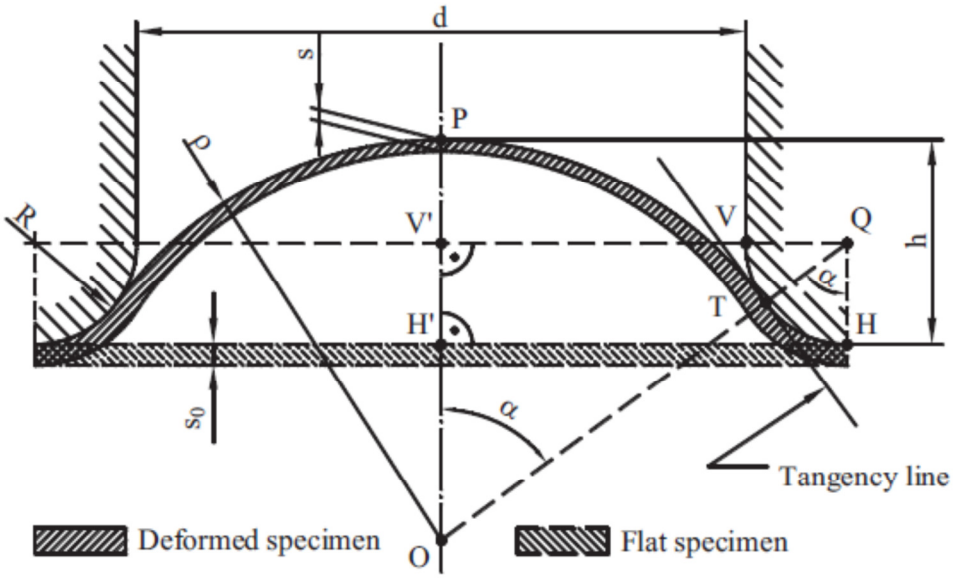

Fig. 5-16 – Schematic representation of the sheet specimen subjected to hydraulic bulging

The membrane theory neglects bending stresses. Thus, it is only applicable for thin sheets and gives for the bulge test the following relationship between stresses, sheet geometry and bulge pressure:

[87] T. Altan, H. Palaniswamy, P. Bortot, M. Mirtsch, W. Heidl - Determination of sheet material properties using biaxial bulge tests - Proceedings of the 2nd Int. Conference on Accuracy in Forming Technology, Nov. 13-15, 2006, Chemnitz, Germany

[88] A. D. Santos, P. Teixeira, A. Barata da Rocha, F. Barlat - On the Determination of Flow Stress Using Bulge Test and Mechanical Measurement - Proceedings of the 10th International Conference on Numerical Methods in Industrial Forming Processes, pp. 845-852

[89] L. Lazarescu, D. S. Comsa, D. Banabic - Determination of stress-strain curves of sheet metals by hydraulic bulge test - Journal of Materials Process Technologies 115, 83-86 (2001)

$$\frac{\sigma_1}{R_1} + \frac{\sigma_2}{R_2} = \frac{p}{s} \qquad (5.1)$$

Where:

σ_1 and σ_2 = principal stresses on the sheet surface

R_1 and R_2 = corresponding radii of the curved surface

p = hydraulic pressure

s = instantaneous sheet thickness on the top of the dome

Considering that bulge test is using a fluid in pressure which is generating a spherical dome on the material sheet under testing, the equation 5.1 can be simplified as follow:

$$\sigma = \frac{p \cdot \rho}{2s} \qquad (5.2)$$

Where:

ρ = instantaneous radius of the dome surface

The corresponding thickness strain (the so-called biaxial strain ε_s) can be evaluated as follows:

$$\varepsilon_s = \ln \frac{s_0}{s} \qquad (5.3)$$

Equations (5.2) and (5.3) can be used to obtain a biaxial stress − strain diagram only if the quantities p, ρ and s are either measured or derived from other experimental data. The pressure p can be easily measured using a sensor connected to the hydraulic chamber of the experimental device. The other process variables, namely the curvature radius ρ and the polar thickness *s* are less accessible to the direct determination. It is more convenient to obtain their values in an indirect manner, using approximate formulas that involve the current value of the polar height h or the basic dimension of the tool used for performing the bulge test. With reference to Fig. 5-16, the most common mathematical equations used for determining the thickness distribution at the top of the dome are:

$$s = s_0 \cdot \left(\frac{\sin \alpha}{\alpha}\right)^2 \quad \text{“Enikeev - Kruglov[90]”} \qquad (5.4)$$

$$s = s_0 \cdot \left(\frac{\left(\frac{d}{2}\right)^2}{\left(\frac{d}{2}\right)^2 + h^2}\right)^2 \quad \text{“Marciniak[91]”} \qquad (5.5)$$

In this specific case, an optical measuring method has been chosen. With this system, the curvature radius is obtained by a parabolic interpolation of the measured area, while the sheet thickness at the pole is determined by the values of major and minor strain assuming volume constancy.

[90] A.A. Kruglov , F.U. Enikeev, R.Ya. Lutfullin - Superplastic forming of a spherical shell out a welded envelope - Materials Science and Engineering A323 (2002) 416–426

[91] J. Slota, E. Spi{ák: Comparison of the Forming Limit Diagram (FLD) Models for Drawing Quality (DQ) Steel Sheets. Metallurgy 44 (2005) 4, 249 - 253.

5.2.1 Testing Procedure

The hydraulic bulge tests on Ti-Fe-Si-O and Ti-Al-Si-Nb alloys have been performed at Erlangen University (Nurnberg, Germany) in the department of Manufacturing Technologies. For this trial, the hydraulic machine and the optic measuring system were the same used for Nakazima tests outlined in previous paragraphs (see Fig. 5-6).

Unfortunately, the hydraulic bulge test is not standardized by any international organization; due to this reason, the dimensions of the die are mainly defined from the power and capacity of the hydraulic machine. In this specific case, the die opening was equal to 110 mm, while the fillet radius was 10 mm. Other relevant specifications of the testing are the capacity of the hydraulic pump, equal to 25 MPa, and the measuring range of the pressure sensor, going from 0 to 100 bar.

During the test, the specimen is bulged into the die opening by continuously increasing fluid pressure, causing material flow in the whole bulged area. For the determination of the flow curves the instantaneous pressure, as well as the major and minor strains in plane direction, have been measured. The pressure is recorded using sensors at the oil feed, while the strains were determined using the optical measurement system Aramis. As previously explained, the system recognizes a stochastical pattern applied to the specimen surface by recording the bulging process via two CCD cameras. The optical strain measurement system allocates coordinates to every pixel in the image and by referring all data of the recorded pictures to the initial state picture it provides the requested information on the curvature radius ρ and major and minor strains distribution.

The curvature radius is calculated analyzing the recorded data and using a parabolic approximation which fit all the reference points situated in the neighboring regions of the top of the dome. The sheet thickness at the pole is determined by the values of major and minor strain and assuming volume constancy.

An important parameter that must be taken into account when performing the hydraulic bulge test is the pressure increase rate, which is determining the speed of deformation of material. Modifying the speed of the oil piston the rate of pressure increase is defined and the strain rate of the material can be varied.

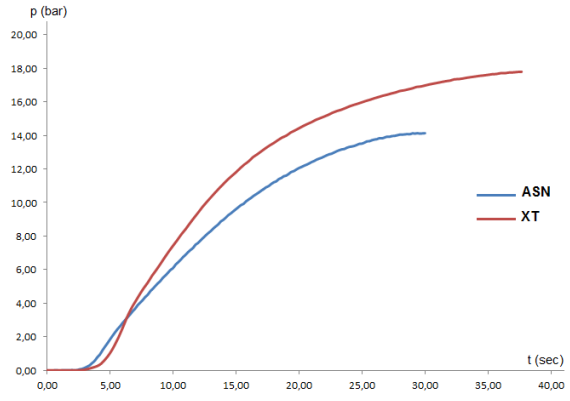

Fig. 5-17 – Pressure increase during test

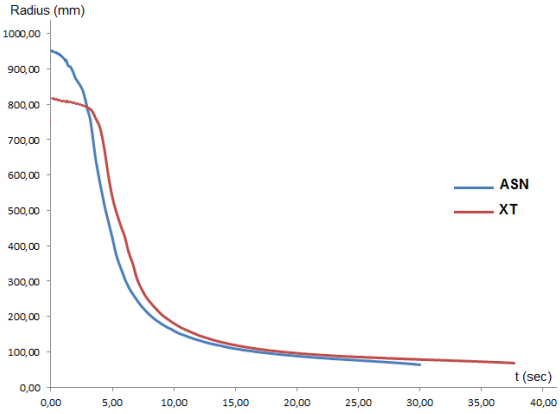

Fig. 5-18 – Radius modification during test

5.2.1.1 Experimental Results

For every alloy, on three different specimens the hydraulic bulge test has been performed. The data recorded at break are summarized in Tab. 5-III.

Material		**Pressure** (bar)	**Radius** (mm)	ε_1 (--)	ε_2 (--)	ε_s (--)	σ (MPa)
Ti-Fe-Si-O	1	17,80	68,21	0,27	0,26	0,53	1.133,26
	2	17,52	68,83	0,26	0,25	0,51	1.116,94
	3	17,71	68,52	0,26	0,25	0,51	1.132,12
Ti-Al-Si-Nb	1	14,14	63,49	0,30	0,29	0,59	898,15
	2	14,10	65,98	0,28	0,27	0,55	881,40
	3	14,16	64,22	0,28	0,30	0,58	898,76

Tab. 5-III – Hydraulic bulge test: results at break

Examples of the flow stress curve obtained performing the hydraulic bulge test on Ti-Fe-Si-O and Ti-Al-Si-Nb alloys are shown in Fig. 5-19 and Fig. 5-20.

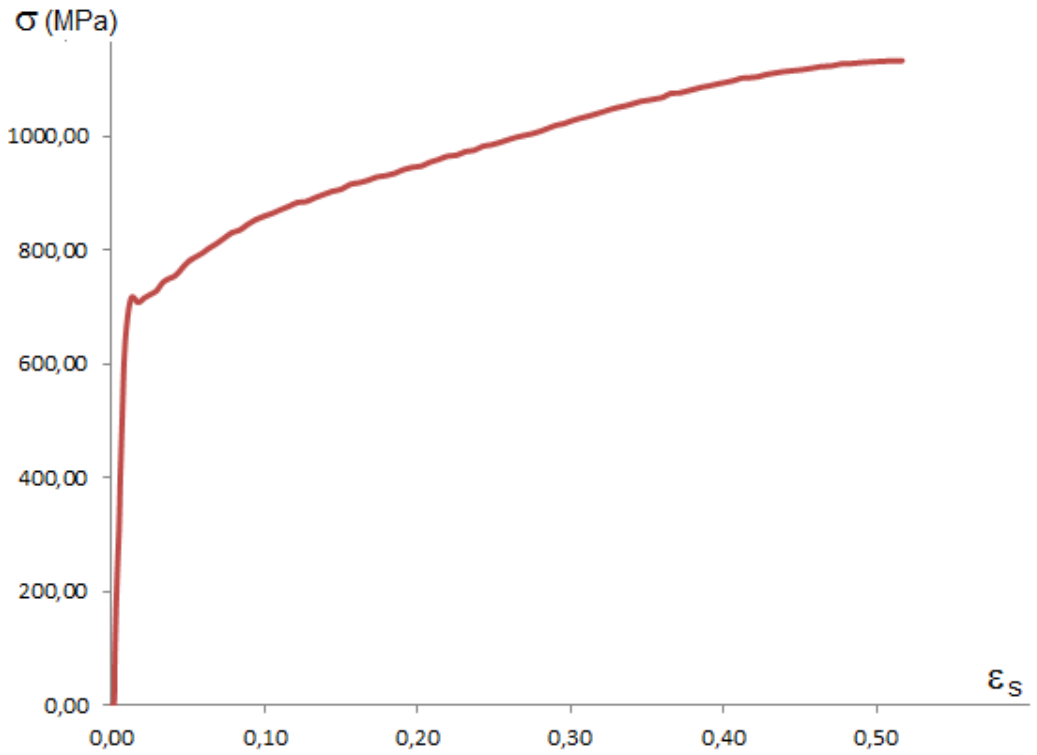

Fig. 5-19 – Flow stress curve for Ti-Fe-Si-O alloy

Looking the σ–ε_s diagram of Ti-Fe-Si-O alloy, it can be easily seen that the discontinuous yielding behavior shown from this material during tensile test is visible also in the flow stress curve obtained by the hydraulic bulge test. Vice versa, the flow stress curve for Ti-Al-Si-Nb alloy looks regular and is not presenting any discontinuities.

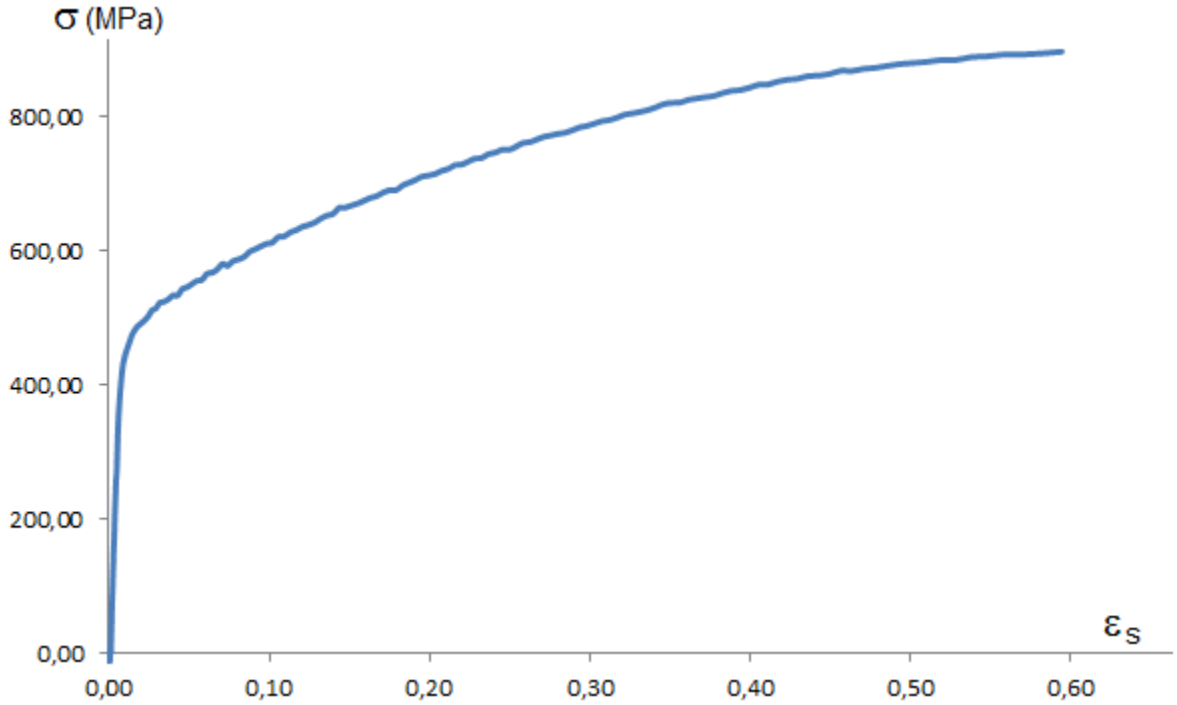

Fig. 5-20 – Flow stress curve for Ti-Al-Si-Nb alloy

5.2.2 Experimental Yielding Locus

In Fig. 5-21 is shown how the experimental data obtained from uniaxial tensile tests in longitudinal and transverse direction and from bulge test can be represented on the σ_1 - σ_2 plane. Obviously the yield locus can be drawn as an ellipse crossing these three experimental points.

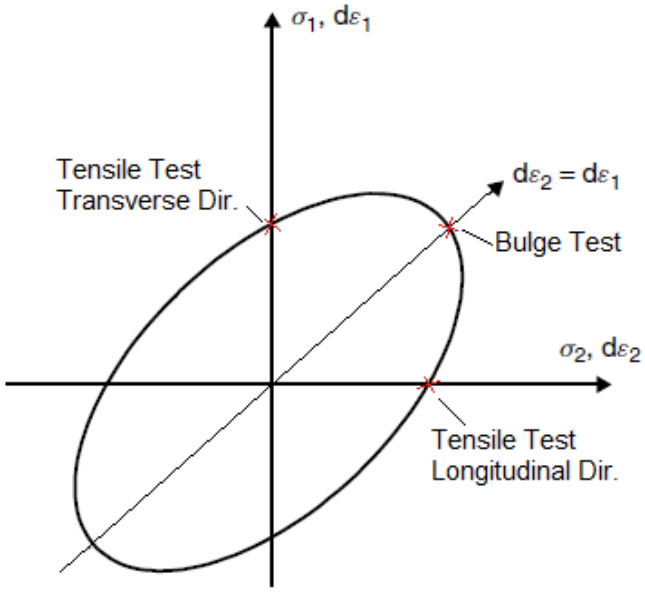

Fig. 5-21 – Representation of experimental data for uniaxial tensile tests and bulge test on the yield locus

From this observation, it can be easily understood that the ellipse built by crossing the experimental data can be compared with the yield locus obtained resolving equation 4.1 characteristic for Barlat & Lian yield criterion.

As example of the procedure comparison between simulated and experimental results, the data for Ti-Al-Si-Nb alloy have been taken into account. In this specific case, as yielding values $R_{p0,2}$ in longitudinal and transverse direction the average values of three uniaxial tensile test have been chosen (see Tab. IX). Concerning the bulge test, the corresponding $R_{p0,2}$ value has been obtained interpolating on the true stress – true strain diagram the condition $\varepsilon_{xx} = \varepsilon_{yy} = 0{,}002$. The point represented on the $\sigma_{xx} = \sigma_{yy}$ plane is the average values obtained interpolating the experimental of three bulge test ($\sigma_{0,2bulge}$ = 473,13 MPa).

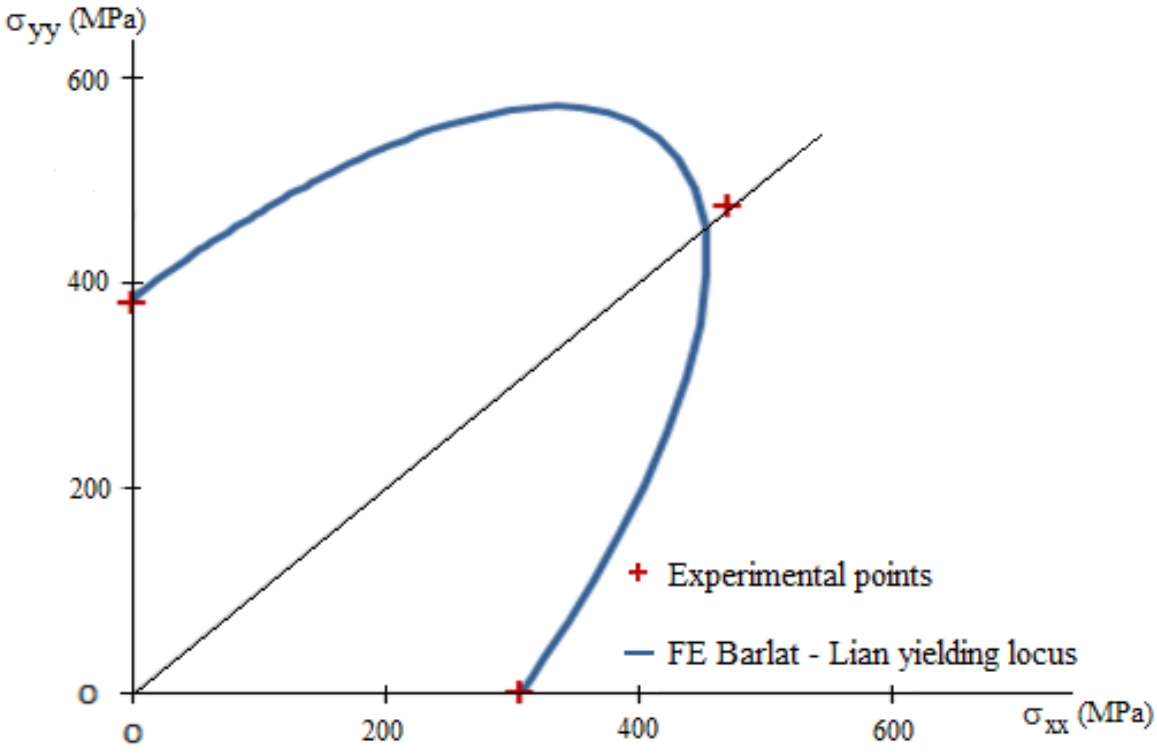

Fig. 5-22 – Comparison between experimental points and simulated yiels locus

Fig. 5-22 shows the comparison between experimental points and simulated yield locus for Ti-Al-Si-Nb alloy. The simulated yield locus (obtained using flow exponent m=2) is relatively similar to the yield locus obtained connecting the experimental data, and considering that these points are average values, the approximation obtained with the Barlat and Lian equation can be considered quite accurate. The same type of behavior has been identified also for Ti-Fe-Si-O alloy.

A second approach which could be considered in profitable way for using the experimental data obtained by the bulge test is the inverse procedure of the one described above. In detail, equation 4.1 describing the Barlat & Lian yield criterion can be used for generating an ellipse which fits the three experimental points $R_{p\ 0°}$, $R_{p\ 90°}$, $R_{p\ bulge}$. After that, the independent material parameters *a, h, p* can be recalculated back as a function of true plastic strain, as well as the the three plastic strain ratio values

$R_{0°}$, $R_{45°}$, $R_{90°}$. In Fig. VV are shown different representation of Barlat & Lian criterion for different levels of strain (at yielding, at 10% and 30% of major strain) obtained by imposing to Eq. 4.1 to fit the experimental points previosly described.

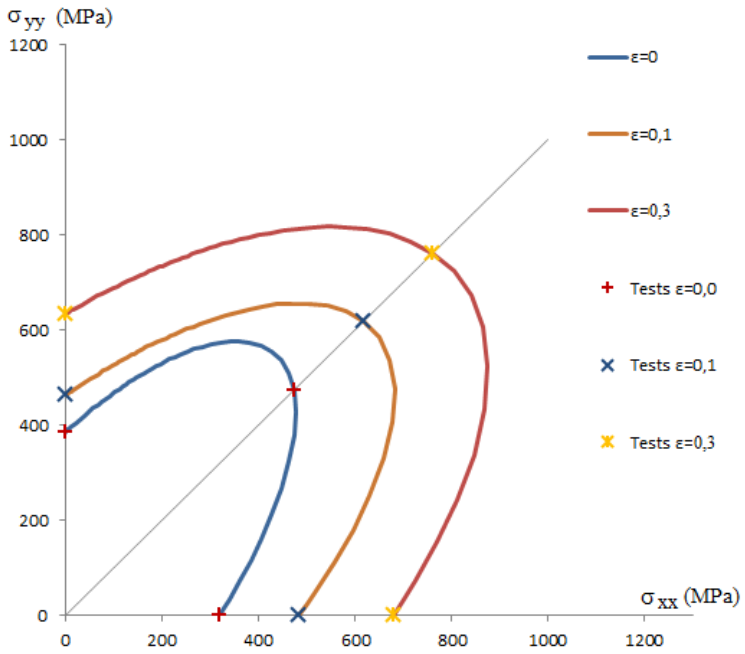

Fig. 5-23 - Barlat & Lian yield criterion fitting experimental data

With this procedure, the material parameters can be re-calculated back as a function of true plastic strain, as shown as example for coefficients a and p in Fig. 5-24.

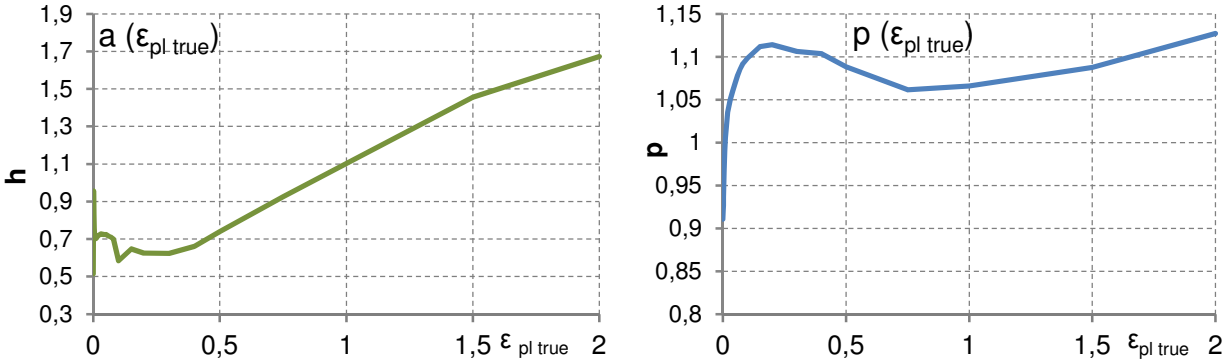

Fig. 5-24 – Parameters a and p trend with variation of true plastic strain (inverse calculation)

The two application examples shown in this paragraph demonstrate how useful can be the experimental data obtained by executing a bulge test on anisotropic materials, despite the difficulties which can occur when these laboratory trials are performed. Especially the comparison of the yield locus described using only experimental data with the simulated one gives an immediate perception about the quality of the material model which can be obtained with the Barlat & Lian criterion.

5.3 Determination of yield stress and necking by using an optical measuring method

As shown in previous chapter, tensile test is probably the most important mechanical characterization method for obtaining the material's parameters needed for the simulation.

Using standard strain gauges to measure the strain at chosen point, is not sufficient and does not provide the necessary information for the input parameters of the numerical simulation. Specifically, the standard measurement technique does not perform at the two most important sections of σ-ε curve:

- At yielding: an important characteristic for describing the material behavior during the forming process is the yield stress which indicates at what point the material passes from the elastic state to the stage of plasticity and deforms permanently. Several materials, included Ti-Fe-Si-O alloy, present a discontinuous yielding behavior where the strains distribution is totally unsettled. The σ–ε diagram in this portion shows a wavy trend, but no information is given about the strain distribution
- At necking: after the plastic field where the material is in uniform strain conditions, the local necking of the specimen starts. As soon as the necking starts, the deformation of the specimen concentrates more and more in this specific area; the portion of material further away from the necking region deforms less and less and just before breaking it does not deform additionally at all. From this point on, the strongly increased local strain values and their change in space and time are no longer captured adequately using conventional strain gauges. This happens because the elongation detected from the longitudinal one is averaged over the entire measuring length, while the width reduction is measured in a specific section of the specimen.

The use of an optical measuring system allows the evaluation of local deformations in both surface directions (longitudinal and transverse) at each surface point of the specimens under testing; consequently, assuming the volume constancy, the thickness reduction can be calculated as well. The accuracy of the measurements is really high, due created by the stochastic pattern created on the specimen's surface.

Due to the elevated number of measuring points and thanks to the specific digital correlation algorithm, the accuracy of strain measurement with optical measuring system is approximately 100 micro strain (με).

The most important benefit given from this measuring system is the capability to provide complete information in case of non-uniform strain field As such, it enables detailed study of the behavior of the material deformation in the yielding and necking zone, as it is possible identifying the local discontinuities in in the strain field and track the changes of the cross-section.

5.3.1 Measuring method

These trials have been performed of the same universal tensile machine (Instron 8033) which has been used for the tensile tests discussed in paragraph 3.2. The optical measuring system Aramis has been mounted in front of the tensile machine, as shown in Fig. 5-25 and Fig. 5-26.

Fig. 5-25 – Aramis equipment

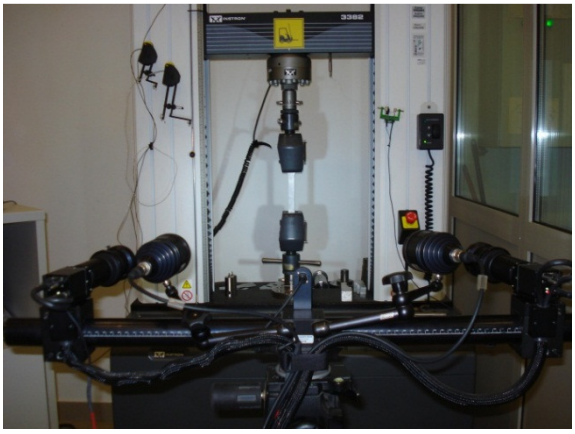

Fig. 5-26 – Optic system during measurments

The tensile tests have been performed using the strain control method; the strain rate was equal to 0,00012 1/s within the elastic field and equal to 0,0020 1/s in the plastic field until the specimen's break.

The grips were rotated 90° compared to the usual position, with the aim of having the flat surface of the specimen oriented towards the optic measuring system. The longitudinal clip-on extensiometer was still mounted on the specimen, to enable strain control and to provide a reference to the optical measurement system.

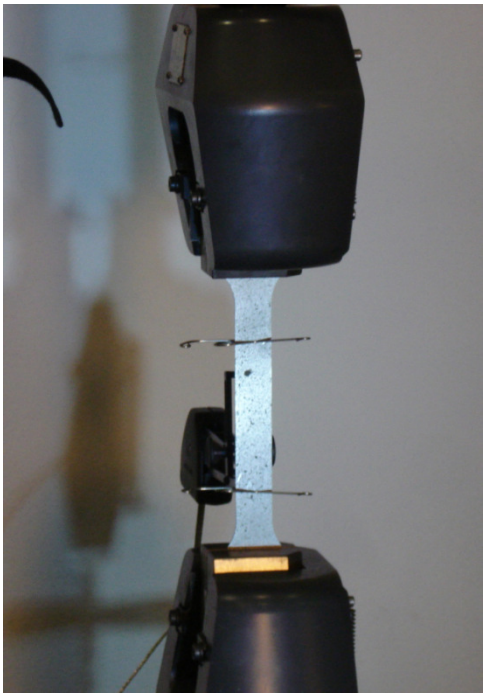

Fig. 5-27 – Specimen before testing

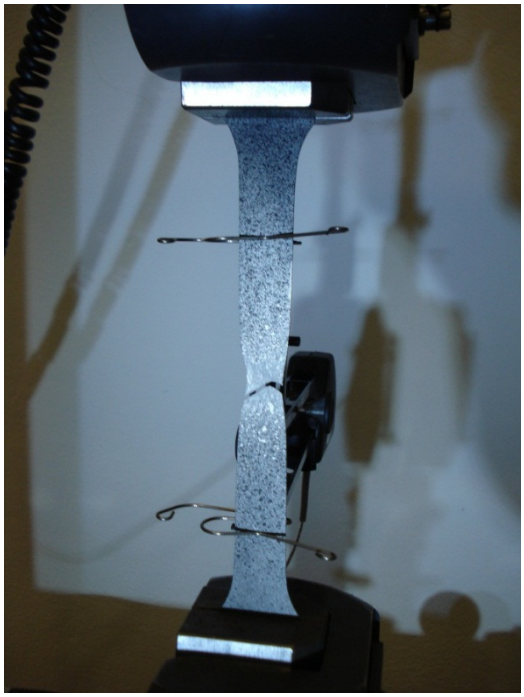

Fig. 5-28 – Specimen after testing

The frame rate used during the test was different depending on the position of the σ–ε curve; in correspondence to the yielding and necking area it was equal to 5 frames/s, while in other position less interesting for this specific analysis was kept equal to 2 frame/s.

5.3.1.1 Experimental Results

During a tensile test performed with the support of Aramis, a series of 500 – 600 frames was recorded by the optical measuring system. This data collection was synchronized with the strain data measured from the clip-on extensometer; in this way, a direct comparison of the specimen's deformation measured with two different techniques can be made. Besides that, the frames can be assembled into a continuous movie of the tensile test, where the strain distribution along the specimen surface is represented using a color coded scale.

In Fig. 5-29 and Fig. 5-30 is represented the strain distribution in the yielding area for Ti-Fe-Si-O alloy in longitudinal and transverse respectively.

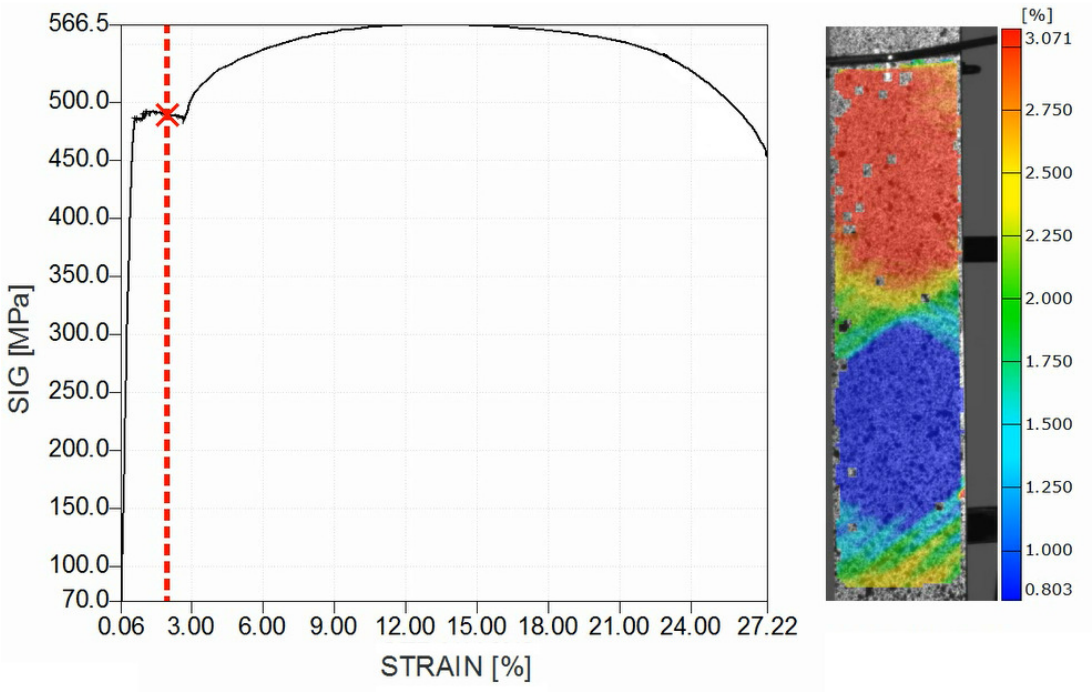

Fig. 5-29 – Ti-Fe-Si-O alloy in longitudinal direction; yielding behavior showing Lüders bands

In Fig. 5-30 a frame caught in the middle of the discontinuous yielding area is shown. The strain distribution recorded by the optical system clearly shows an inhomogeneous deformation due to the formation of the so called "Lüders bands". Lüders bands, also called "slip bands", are localized bands of plastic deformation which are sliding along the specimens during the tensile test[92]. These bands are a localized phenomenon and they are acting as boundaries between plastically deformed and undeformed material.

[92] J. W. Hutchinson – Shear bands formation in plane strain – Int. Journal of Solid Structures – Vol. 17, pp. 451-470 (1981)

Lüders propagation leads to lengthening perpendicular to the front, which is generally inclined at 50° - 55° to the loading direction. As can be easily seen in both Fig. 5-29 and Fig. 5-30 the portion of material located above the bands is deforming rapidly, while the strain below is significantly lower.

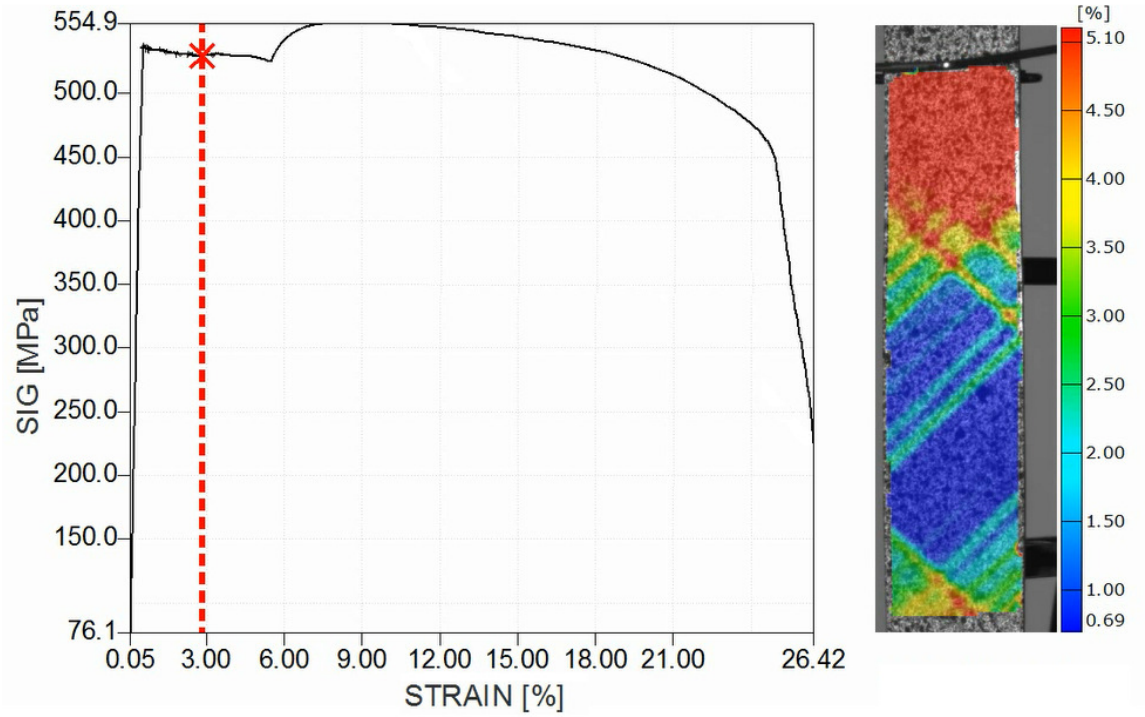

Fig. 5-30 – Ti-Fe-Si-O alloy in transverse direction; yielding behavior showing Lüders bands

As shown in Fig. 5-31, increasing the strain level the bands are propagating from the upper part of the specimen to the lower part. In transverse direction, where the tensile strength R_m is located approximately between 8-10% of elongation, the material is passing directly from the Lüders bands propagation to the necking conditions, while in longitudinal direction a portion of uniform plastic deformation exists between the two areas. This behavior is confirmed also from the plastic strain ratio trend (see Par. 3.2.6).

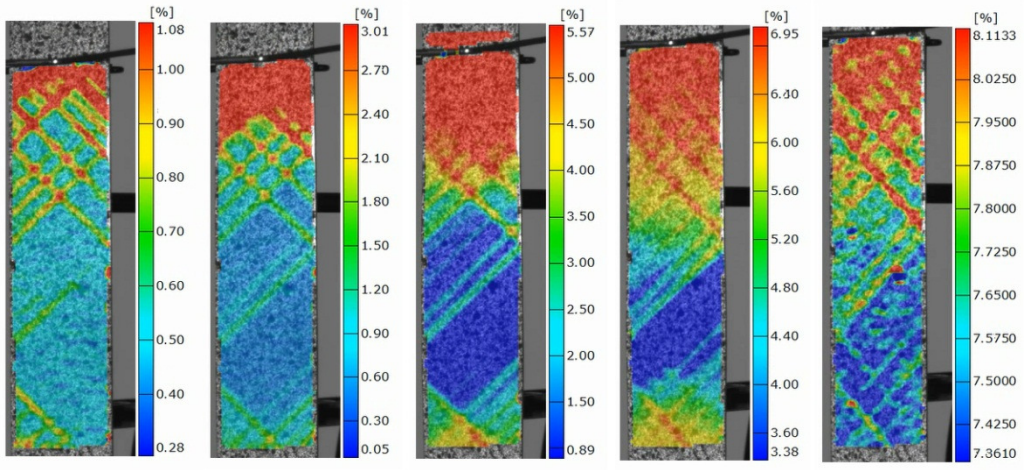

Fig. 5-31 – Lüders bands evolution during tensile test

With respect to Ti-Al-Si-Nb alloy, the yielding behavior shown from the material is entirely different from the one of Ti-Fe-Si-O material. The strain distribution is almost constant all along the specimen in both longitudinal and transverse directions.

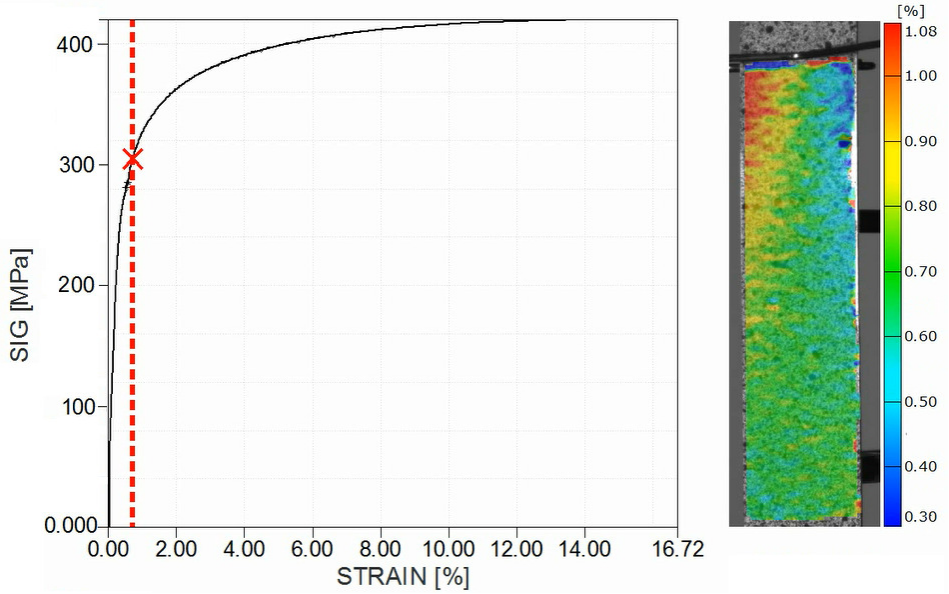

Fig. 5-32 – TI-AL-SI-NB-EX yielding behavior in longitudinal direction

The color scale suggesting a uneven strain distribution is definitely limited (0,3 – 0,4%), and is probably due to the influence of the upper clamp, which probably is not perfectly parallel to the fixed lower clamp.

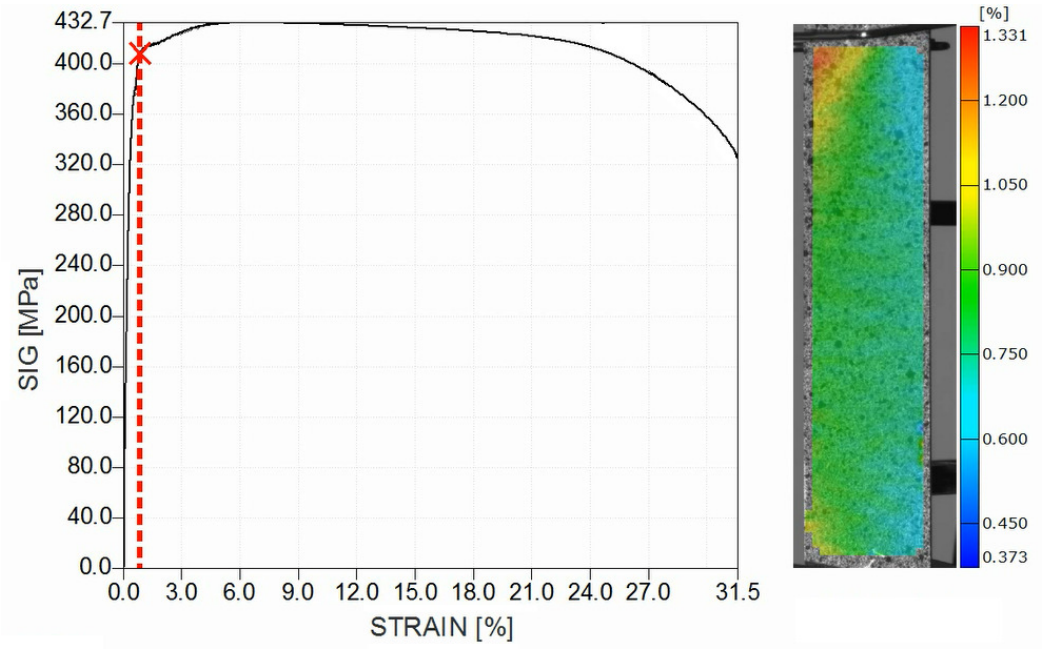

Fig. 5-33 – TI-AL-SI-NB-EX yielding behavior in transverse direction

Concerning necking, with the optical measuring system the strain distribution can be highlighted in every portion of the specimen. As can be seen in Fig. 5-34 and Fig. 5-35, both alloys show a similar behavior; the figures show the strain distribution five seconds before that break occurs.

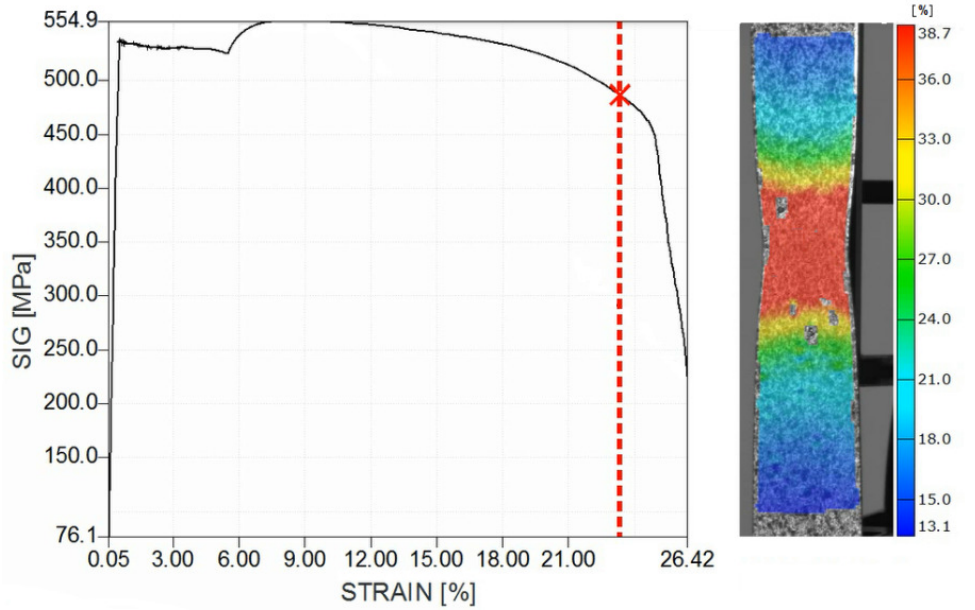

Fig. 5-34 – Necking behavior of Ti-Fe-Si-O

In both cases, the tensile test in transverse direction has been considered, because at this orientation the R_m peak is reached at lower level of elongation and the necking is prolonged through wider strain range. Observing in detail the proceeding of Ti-Fe-Si-O alloy, it can be seen that the volume of material subjected to section reduction is bigger than the one of Ti-Al-Si-Nb. However, it is necessary to underline the difference in terms of deformation between the area subjected to necking and the one presenting significantly smaller deformation. In case of Ti-Al-Si-Nb alloy, few seconds before the break, the core exhibits an elongation bigger than 50%, while the extremities of the specimen are subjected to a deformation between 20-25%. Instead, Ti-Fe-Si-O presents a nucleus with 37-38% elongation and the far ends where the elongation is limited to 15%.

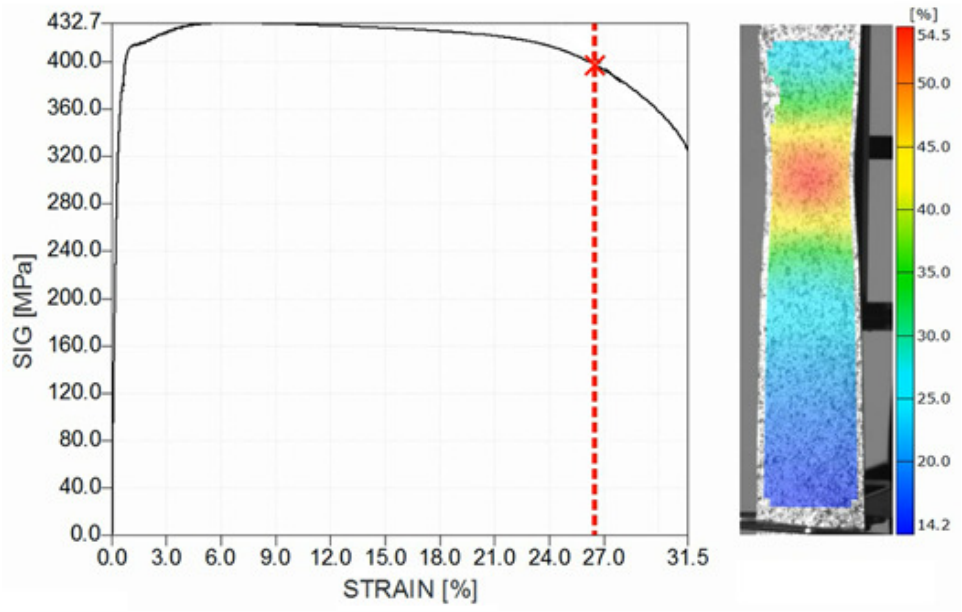

Fig. 5-35 – Necking behavior of Ti-Al-Si-Nb

5.3.2 Comparison between FEA simulation and experimental data

The optical stress/strain measurements performed using Aramis system can be very useful for supporting the full field verification of FE simulations. Determining material parameters with the optical measuring system helps to evaluate and improve existing material models, thus finite element simulations can be optimized and are getting more reliable.

As shown in Par. 5.3.1.1, a series of tensile tests on Ti-Fe-Si-O and Ti-Al-Si-Nb alloys in longitudinal and transverse direction have been performed using Aramis system. Due to this reason, the FE simulations of tensile test have been carried out in parallel, with the aim of executing an accurate comparison between the experimental data and those obtained through simulations. The most important target of this activity is identifying the accuracy of the material model in predicting the plastic behavior all across the considered deformation field.

In order to check the validity of this approach, Ti-Al-Si-Nb alloy has been chosen, due to its regular monotonic behaviour; the comparison has been carried out on the specimen with orientation coincident with rolling direction (L).

Concerning the simulation, for the mesh of tensile specimen quadrilateral four nodes shell elements have been used (element formation type 2 – Belytschko-Tsay). The specimen was constrained on one side with zero displacements and rotations in all directions as boundary conditions. The tensile load was applied on the other end of the specimen as a nodal displacement in a form of velocity and the direction of the movement.

Material model coordinates were oriented in such a way that the rolling direction was parallel to the specimen's loading axis and T direction was perpendicular to it. Both the directions belong to the same plane. Material model used in the simulation was 3-parameter Barlat & Lian model (1989): the input data were:

- Young modulus E
- Poisson ratio ν
- Experimental sigma-epsilon curves in three directions (L, D, T)
- Plastic strain ratio as functions of strain three direction (L, D, T)
- Flow exponent m=2

Running the simulation, the output data which can be obtained are stresses and strain displacements plotted with a time frame of 0,005 second.

In order to synchronize the simulation results with the experimental data, translational and rotational nodal displacements, and also velocities and accelerations for every single node have been exported as vectors and loaded by using Matlab software.

At each time step of the numerical simulation, nodal coordinates are taken as output as well as stresses and strains at selected integration points. The comparison with the experimental data is made with the use of projection of simulation results at the location of measurement points. The object of

comparison are strain components, which are computed at nodes of simulation mesh using nodal patch averaging (value at selected node is average value of values at integration points of adjacent elements).

Once the results of numerical simulations are projected to the measurement nodes, direct comparison can be made and difference of measured strain field and simulated field can be plotted. However, the location of the necking region in simulation does not match the actual location found in experiment. The longitudinal coordinate of simulation along the sample length is therefore adjusted such that the necking region coincides with the one obtained in the actual measurement.

As example of comparison between experimental and simulation data, three specific points taken from experimental measurements have been chosen as reference. In detail:

- Point 1 (Frame 272): true strain ε_l = 0,0476 (4,76%); true stress = 408,2MPa. This point is located in the plastic region
- Point 2 (Frame 308): true strain ε_l = 0,1390 (13,90%); true stress = 432,3 MPa. This point is located in correspondence of Rm peak
- Point 3 (Frame 411): true strain ε_l = 0,2683 (26,83%); true stress = 415,7 MPa. This point is located in the necking region, just five seconds before the break of the specimens. In this case, due to the different location of the necking region, just a qualitative comparison has been carried out.

In Fig. 5-36 the position of Frame 272 is visualized on the σ-ε diagrams, while in Fig. 5-37 and Fig. 5-38 are visualized the comparisons in terms of strains distributions in longitudinal and transverse direction.

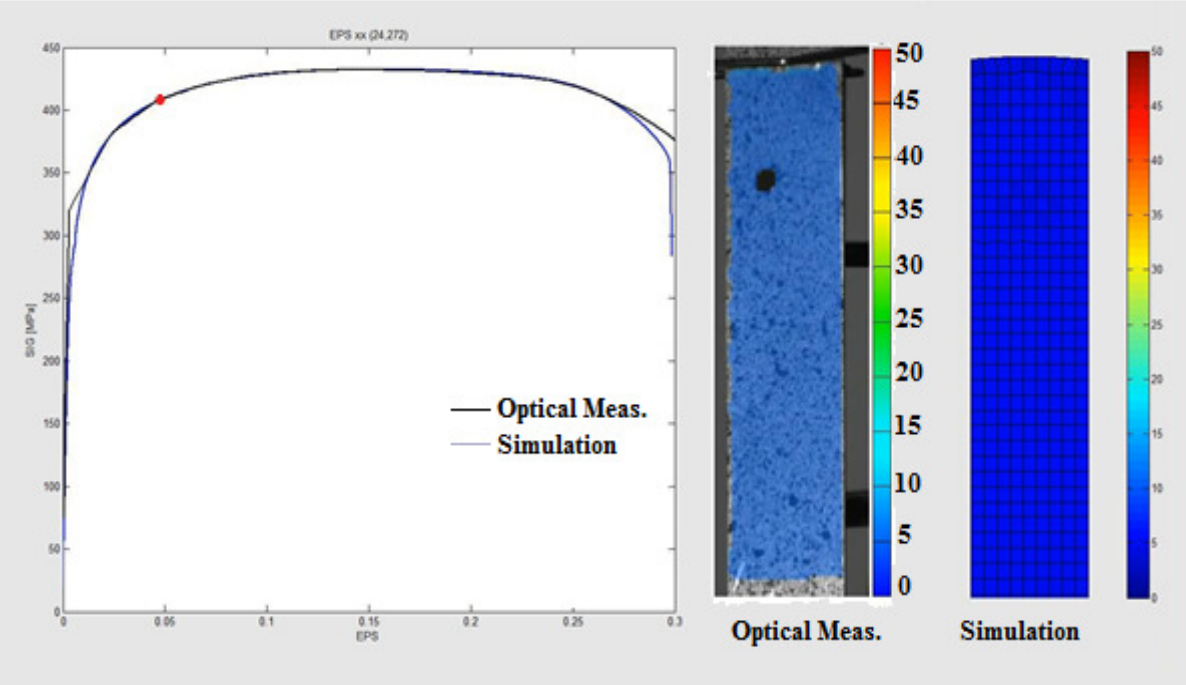

Fig. 5-36 – Frame 272: localization on σ-ε diagrams

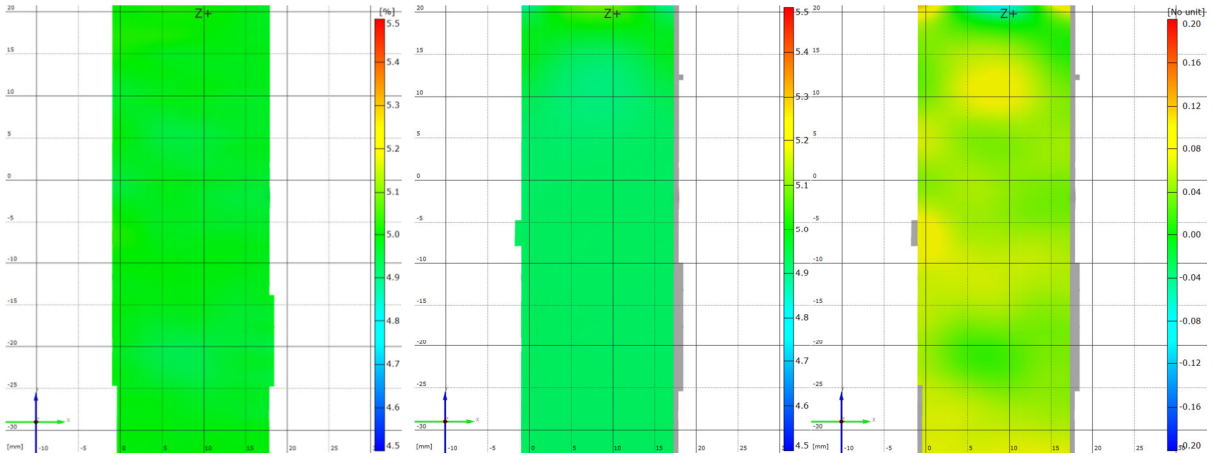

Fig. 5-37 – Frame 272: comparison of longitudinal strain ε_l from simulation and experiment (left experimental, center simulation and right difference)

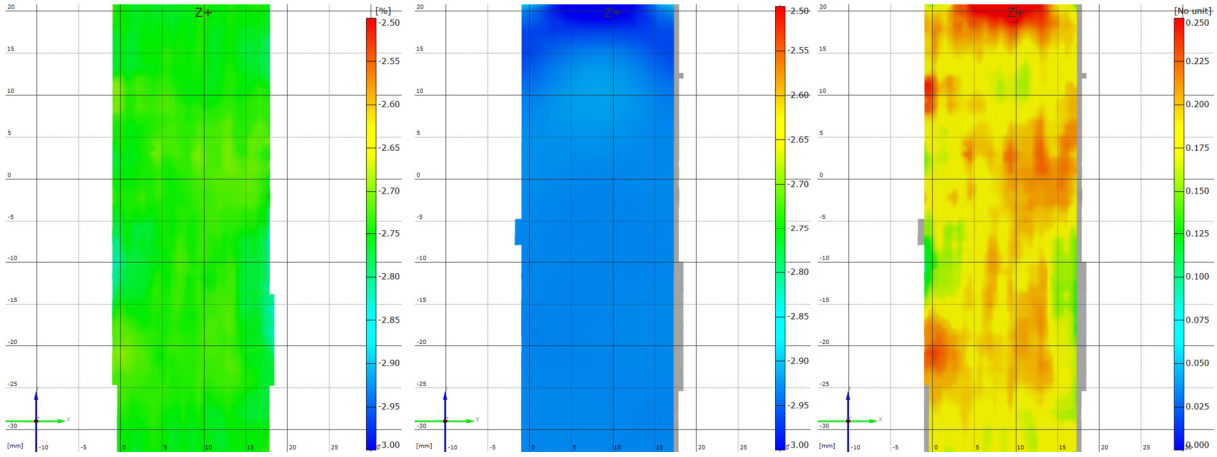

Fig. 5-38 – Frame 272: comparison of transversal strain ε_w between experimental measurements and simulation (left experimental, center simulation and right difference)

The comparison between experimental data and simulation in terms of strains (see Fig. 5-37 and Fig. 5-38) shows that in correspondance of frame 272 (located in the plastic field) the difference is less than 0,1% in longitudinal direction and between 0,1 – 0,25% in transverse direction. Generally speaking, the simulation is over-estimating the deformation occouring on the specimen.

In Fig. 5-39 the location of Frame 308 is visualized on the σ-ε diagrams. This specific point is particularly interesting because this specific position is defining the end of the plastic field and the beginning of the necking region, where the stress state will switch from uniaxial to triaxial. Due to this issue, it is considered extremely significant evaluating the level of approximation that the simulation can guarantee in this specific zone of the σ-ε curve.

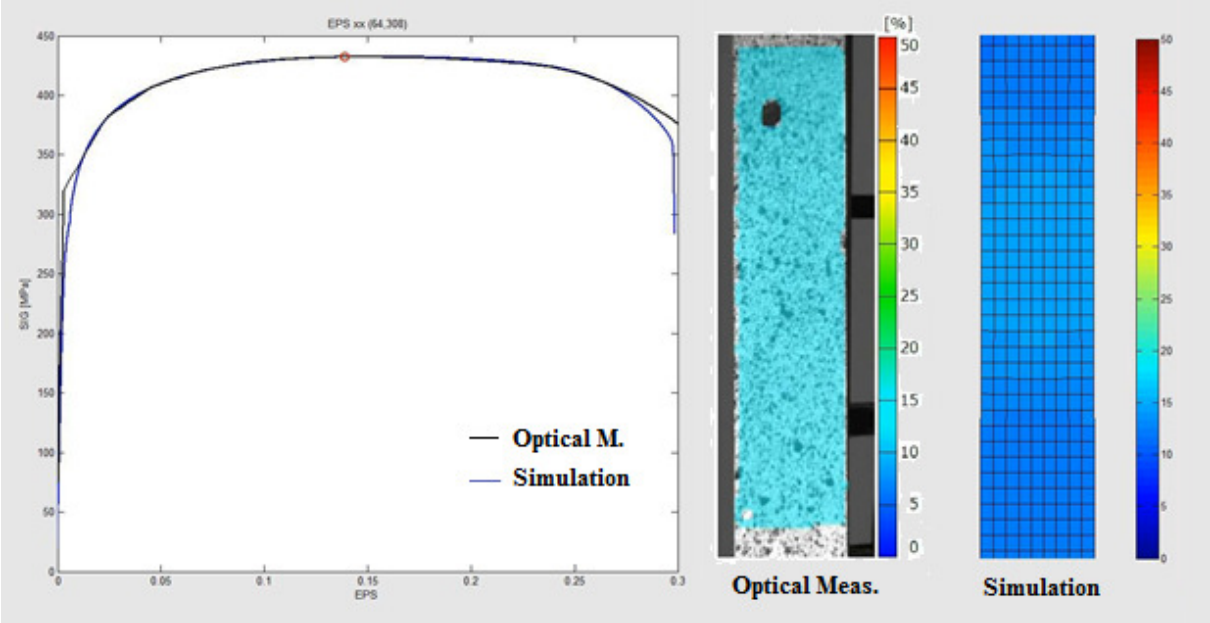

Fig. 5-39 – Frame 308: localization on σ-ε diagrams

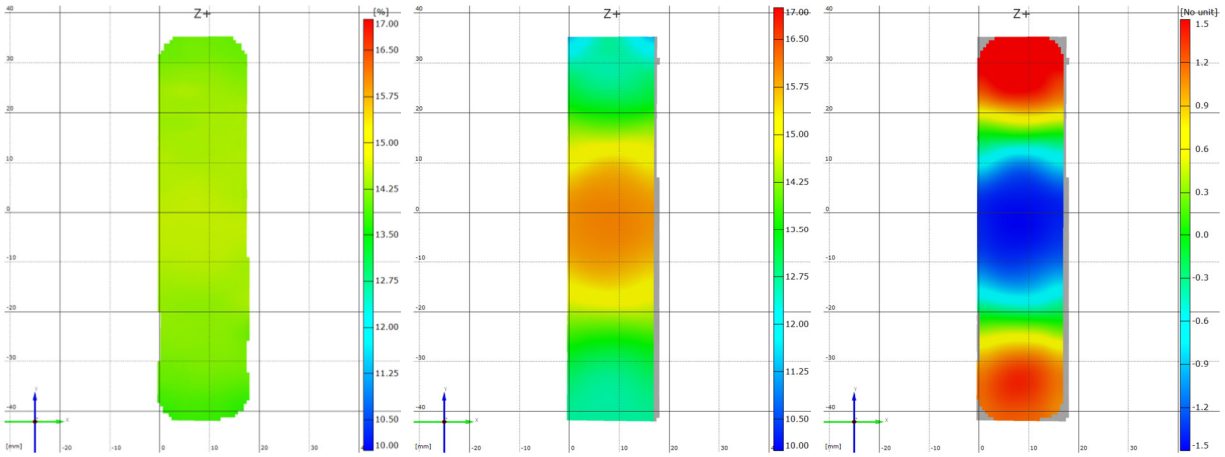

Fig. 5-40 – Frame 308: comparison of longitudinal strain ε_l from simulation and experiment (left experimental, center simulation and right difference)

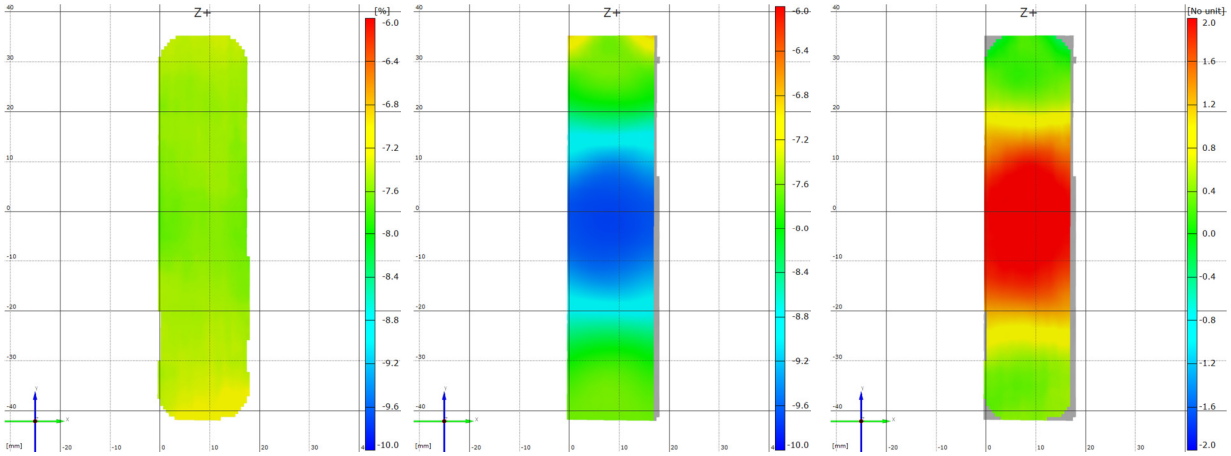

Fig. 5-41 – Frame 308: comparison of transversal strain ε_w between experimental measurements and simulation (left experimental, center simulation and right difference)

The comparison between experimental data and simulation in terms of strains (see Fig. 5-40 and Fig. 5-41) shows that in correspondance of frame 308 (located in correspondance of Rm peak) the difference is within ±1,15% in longitudinal direction while in transverse direction the discrepancy is varying from -0,2% up to 1,6%.

Overlapping the simulation to the experimental data allow showing that the deviation of longitudinal strain ε_l is underestimated from the model on the sides of the specimens, while it presents a tendency to be overestimated in the central area. Due to this reason, an additional analysis of the cross section reduction along the measuring length L_0=80 mm has been made (see Fig. 5-42).

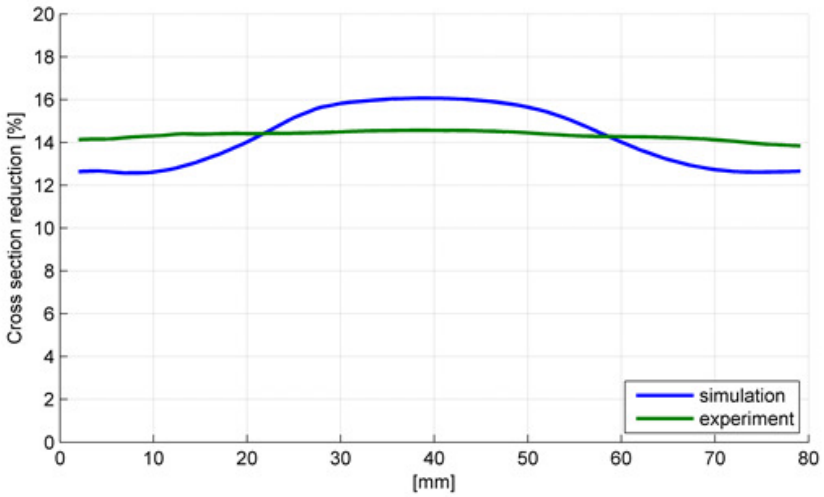

Fig. 5-42 – Frame 308: variation of cross section reduction along the specimen length L_0

In Fig. 5-43 the location of Frame 411 is visualized on the σ-ε diagrams. This comparison point is located on a position chosen just five seconds before that the break occurs. This point is significant, because looking at the σ-ε curves (experimental and simulation) it can be seen that up to this value the two diagrams coincide fairly well, while afterthat the discrepancies become evident. However, the necking phenomenon in the real specimen is not occurring exactly on the symmetry section and so a punctual comparison with numerical deviation in every node cannot be displayed. For frame 411 just a qualitative estimation can be done.

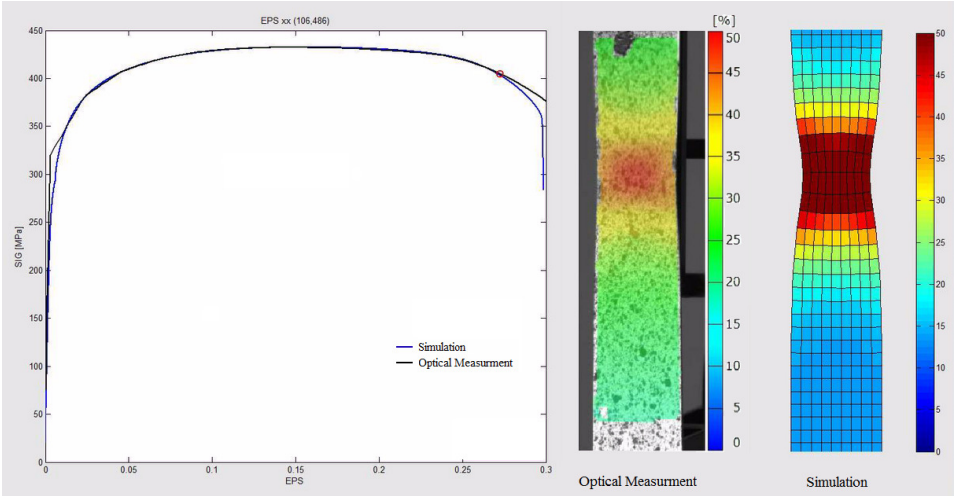

Fig. 5-43 – Frame 411: localization on σ-ε diagrams

5.4 Friction coefficient determination

During deep drawing operations, the friction conditions between the titanium alloy blank and the tooling (punch, matrix and blank holder) have a significant effect on the evolution of plastic deformation processes. For evaluating the appropriate values of the friction coefficient to be used during FE simulations, a series of wear tests have been performed using a CSM Instrument tribometer. The trials have been performed according to the ASTM G99-05[93] standard, which is describing the procedure for tribological test using pin on disc technique.

The tribometer consists of a fixed arm which supports the pin and a rotating base equipped with a sample holder where the titanium disk is fixed. In this way, the rotation of the disk causes the sliding pin on disk. The arm is supporting the pin and in addition to that, balances the weight of it and makes possible applying a known force, so that all the tests are carried with the same loading condition.

Using this procedure, a disc of the materials under testing (diameter 30 mm) rotates under a X100 Cr 6 steel pin with a hardness of 58 HRC. In this specific case, two different pin geometries were used: a spherical pin and a flat pin with a contact area of 1 mm^2. The linear pin speed was 15 cm/min, which is in the same order of magnitude as experienced under deep drawing, and the normal load applied to the specimen was 5 N.

During deep drawing operations, with titanium alloys is common praxis using a lubricated PVC foil on both sides of the blank, in order to reduce friction coefficient. Due to this reason, also some trials using PVC foils (lubricated and unlubricated) interposed between steel pin and titanium disk have been performed.

The duration of the tests was 30 min each, and the friction coefficient was calculated as average value of the entire test, excluding the initial discontinuities typical of this method.

Combinations of available lubrication conditions and pin geometries were examined and the results are presented in Table 5-IV.

Lubricant	Type of pin	μ
None	Spherical	0.45
None	Flat	0.50
Oil	Spherical	0.44
Oil	Flat	0.50
PVC foil unlubricated	Flat	0.38
PVC foil + oil	Flat	0.16
PVC foil + grease	Flat	0.17

Tab. 5-IV – Friction coefficients under different lubrication conditions

[93] ASTM G99 - 05(2010) - Standard Test Method for Wear Testing with a Pin-on-Disk Apparatus

CHAPTER 6
TEXTURE ANALYSES

A large number of polycrystalline metallic materials display preferred crystallographic orientation (texture). Such alignment has a strong effect on anisotropy of various mechanical and physical properties. Texture takes place during solidification, plastic deformation or is modified during recrystallization heat treatments or phase transformations.

Different methods are applied for characterizing orientation patterns and determining the orientation distribution; mainly these methods rely on diffraction[94]; the only requirement which must be fulfilled with diffraction techniques is that the wavelength of the incident radiation must be smaller than the lattice spacing, which for materials of interest is typically 10ths of a nanometer. Due to this reason, x-rays, electrons and neutrons can be used for this application because are diffracted by lattice planes, whereas light is not. The various kinds of radiation interact with the material in different ways. This manifests itself by substantial differences in the absorption of radiation by matter and, with regard to texture analysis, by the depth of penetration of radiation into the sample material[95].

The most consolidated method for performing texture analyses is x-ray diffraction with the use of Euler goniometer (or cradle). The principal disadvantage of this traditional approach is the lack of a direct connection between the study of microstructure and crystallography. Due to this reason, recently (since the early 1980s), electrons backscattered diffraction using scanning (SEM) or transmission (TEM) electron microscope are techniques which are becoming very popular, because allow correlating microstructures, neighbour relations and texture. For special applications, especially texture analyses at non-ambient conditions, neutron diffraction and synchrotron x-rays provide unique opportunities.

Speaking about texture analysis on metallic materials, two distinct approaces can be mainly used for measuring the crystal lattice orientations:

- Average the measurment over a large volume of polycrystal aggregate (x-ray technique)
- Measure the orientation of individual crystals (EBSD technique)

For studying the texture properties of Ti-Fe-Si-O and Ti-Al-Si-Nb alloys, both the aformentioned approeaches have been used. In the following paragraph the experimental procedure and the results obtained from these analyses will be presented, compared and discussed.

[94] H. R. Wenk, P. Van Houtte - Texture and Anisotropy – Reports on Progress in Physics 67, pp. 1367 – 1428 (2004)
[95] O. Engler, V. Randle – Introduction to texture analyses, 2nd edition – CRC press, pp. 51

6.1 Texture determination using x-ray diffraction technique

X-ray diffraction is the most established technique for texture measurement, and can be used for revealing the macro texture of material's volumes by measuring the intensities of diffraction peaks. This method became suitable for investigating preferential crystallographic orientation with the introduction of the Eulerian cradle in 1949[96], however a goniometer which using a precise mechanisms and by means of three rotation axes, allow samples to be brought to any orientation in space.

The radiation suited for diffraction experiments is commonly produced with x-ray tubes, and is a monochromatic beam. The x-rays diffraction techniques is based on the Bragg's law for reflection of radiation. The basic operational principle is simple: for determining the orientation of a given lattice plane (for example the basal plane of the HCP lattice), the x-ray source and the detector are positioned to the Bragg angle 2θ characteristic for the diffraction peak of interest. Setting the instrument according to this specific orientation is extremely important, because a reflected intensity is measured only if the corresponding lattice planes are arranged such that they lie parallel to the sample surface; for all the other orientation of the planes, the signal is zero.

For determining an unknown crystal orientation in practical applications, the sample is mounted on the Eulerian cradle and is systematically rotated about well-defined angles in such a way that all possible lattice planes are successively brought into the reflection condition and the reflected intensities are recorded as a function of these rotation angles. These systematic measurements can be used to produce a plot of the reflection intensity as a function of angular orientation of the specimen.

As we will see later (paragraph 6.2), this specific representation is called "pole figure".

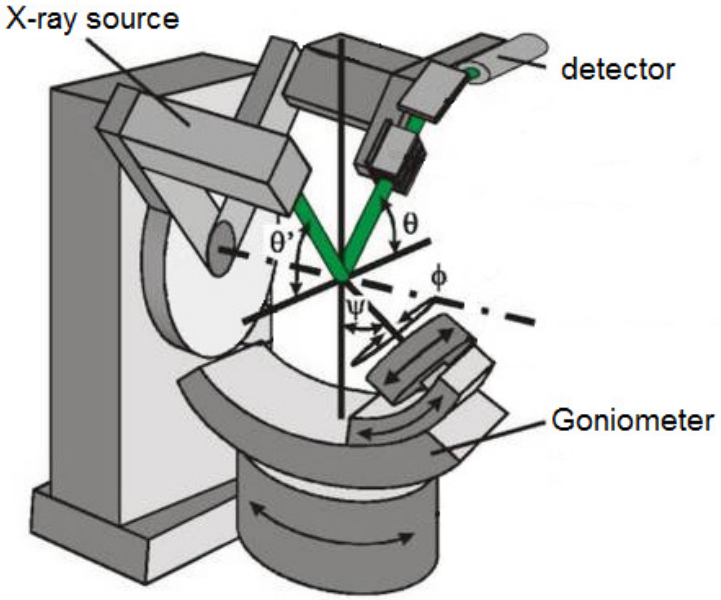

Fig. 6-1 – Eulerian cradle basic configuration

(Image courtesy of Helmhotz Zentrum, Berlin)

[96] G. Lloyd at al – Crystallographic Texture - Mineralogical Magazine, September 1991, Vol. 55, pp. 331-345

6.1.1 Pole figures representation

During measurements of crystal's orientations, often pole figures (or inverse-pole figures) are used to describe the orientations in a single plot. The direction of any vector characterizing the planes orientation in a crystal lattice can be described as a point on a unit reference sphere. The unit reference sphere is a sphere with unitary radius notionally residing the crystal. The point in which the normal of a plane intersects this sphere is called the "pole" of this plane. The poles distribution on the reference sphere is thus a description of the orientations of the planes. As shown in Fig. 6-2, the positions of the poles on the sphere can be described in a spherical coordinate system by using two angles, α (azimuthal angle) and β (polar angle).

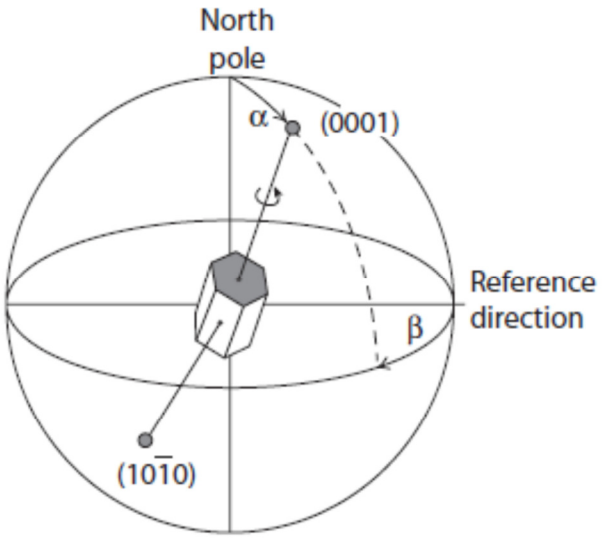

Fig. 6-2 – Chrystal plane orientation given in spherical coordinate system[97]

The angle α describes the azimuth of the pole, which means that α=0° represents the north pole of the unit sphere. Instead, the angle β is the rotation of the pole around the polar axis, in which β=0° is chosen from α reference direction.

For characterizing the crystal orientation, the pole angles need to be linked to the coordinate system of the sample. Conventionally, ND is chosen to be in the north pole of the reference sphere in which α=0°, and RD is chosen as the reference point in which β=0°. A pole figure can be created by realizing a stereographic projection of the poles located on the surface of the reference sphere on a two dimensional plane, usually the equator plane. In summary, a pole figure is a reference system that consists of the coordinates given by the specimen axes with the coordinates of the crystal axes projected into this reference system (direct pole figure). Vice versa, if instead of projecting the crystal axes in the specimen's reference system, the opposite is done, the result is an inverse pole figure.

For polycrystalline materials, a set of poles can be plotted for each individual grain to produce a pole figure. If the grains are randomly oriented, then we should expect to see the poles distributed evenly over the pole figure. More often the grains are not randomly oriented, but tend towards

[97] O. Engler, V. Randle – Introduction to texture analyses, 2nd edition – CRC press, pp. 31

particular orientations depending on the alloy composition and process history (texture). In this case the poles will be concentrated within certain areas of the pole figure.

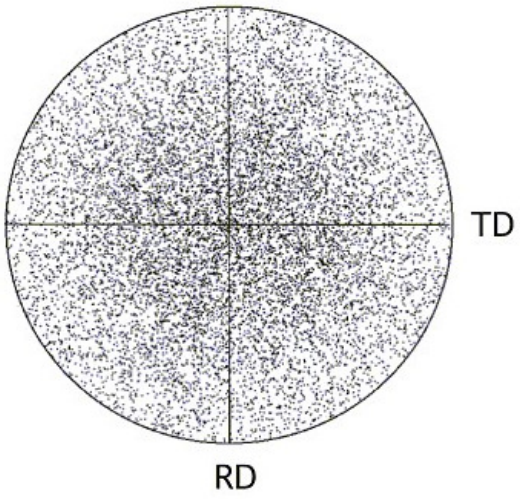

Fig. 6-3 – Random texture
(Source: http://www.doitpoms.ac.uk)

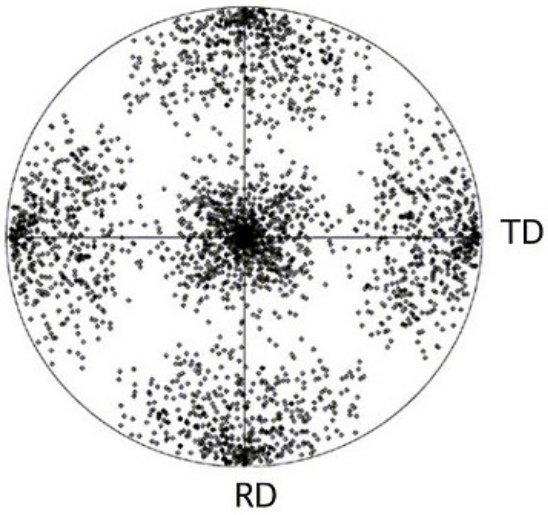

Fig. 6-4 – Preferred texture
(Source: http://www.doitpoms.ac.uk)

A single crystal can be plotted on the pole figure and there is no ambiguity regarding its orientation. However, as more crystallite poles are plotted onto the pole figure, the specific orientation of a particular crystallite can no longer be defined. For a large number of grains in a polycrystal, poles may overlap on the pole figure, so that the true orientation density is not clearly represented. In this case, contours tend to be used instead. Regions of high pole density have a high number of contours, while regions with low pole density have a few, greatly spaced contours

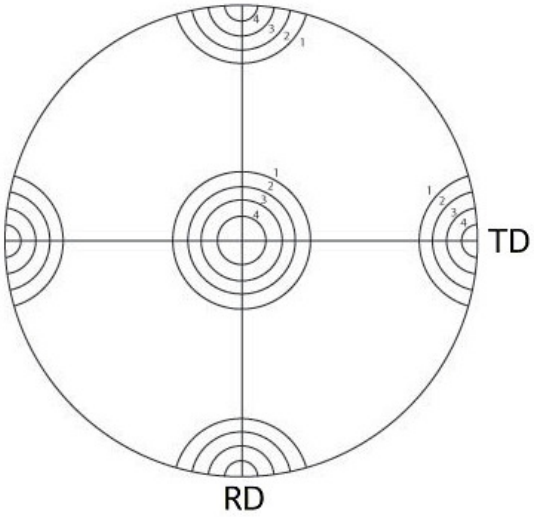

Fig. 6-5 - Texture and pole density represented using contours rather than discrete points
(Source: http://www.doitpoms.ac.uk)

6.1.2 X-rays diffraction measurements

In order to detect the preferential crystallographic orientation of the alloys under investigation in delivery conditions (annealed), a square sample 15x15 mm has been extracted from the coil. For the texture investigation, the crystallographic plane chosen as reference for the diffraction measurements is the basal plane (0002). For determining the spatial orientation of the preselected crystallographic planes, the emitting source of the diffractometer was positioned according to the specific Bragg's angle 2θ characteristic of the diffraction peak object of interest. This angle was determined with a preliminary analysis repeated for each sample under study.

For the measurements execution, the sample is stuck to the Eulerian cradle by using a double side scotch tape and orienting the rolling direction along a known reference. As previously mentioned, this device is capable of rotating the sample around the perpendicular axis to the irradiated surface, describing the angle Φ (full rotation of 360 °), and also tilting for achieving a lateral inclination of the sample holder of an angle Ψ between 0–90 °. In Fig. 6-7 is shown the conventional representation of angles Φ and Ψ used for plotting the direct pole figure, and also the orientation of the sample with respect to the sample holder.

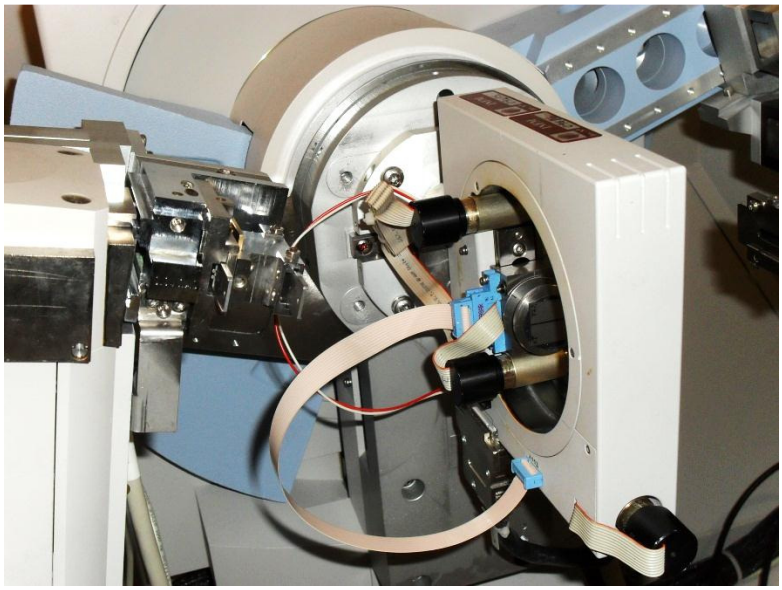

Fig. 6-6 – Eulerian cradle at the end of the measurement (Ψ=85°)

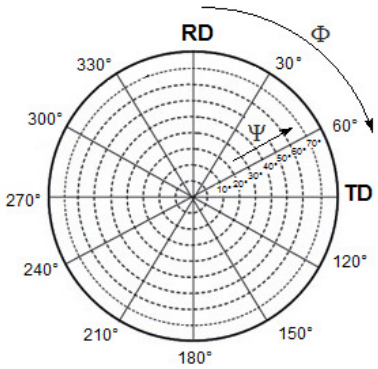

Fig. 6-7 – Angles in the pole diagram

The texture measurements in polycrystalline materials are carried out by detecting the intensity of the incident beam diffracted by the sample. In fact, the intensity of each diffraction peak is proportional to the fraction volume of the crystal lattices oriented according to a given configuration (Φ–Ψ). Therefore, if such measurement is performed by orienting the sample according to a wide range of combinations of the angles Φ and Ψ, a quantitative analysis of the crystallographic orientation can be made.

Before that the measurements obtained by recording the intensity of the diffraction peaks can be evaluated or used for pole figure determination, several corrections have to be applied.

The first error that has to be corrected is the "*background error"*. Background intensities are caused by incoherent scattering and fluorescence in the sample. Minor contributions may also result from interaction of the x-ray beam with any material in the path of the x-rays—collimator, beam stop, and air—as well as from electronic noise.

A second correction which needs to be made on the signal is the "*defocusing error*". In fact, by tilting a sample of reduced thickness to angles $\Psi >> 0°$ happen that half of the sample is behind and half of it is in front of its original plane. For those sample regions, however, the focusing condition is no longer exactly fulfilled, which leads to a decrease in intensity simultaneously with a broadening of the reflected peaks. Accordingly, this effect is called the defocusing error[98]. Both the aforementioned errors can be corrected by the software of the diffractometer by performing a specific scan of the sample.

Concerning the texture measurements on Ti-Fe-Si-O and Ti-Al-Si-Nb alloys, the diffractometer used for the trial was a Panalytical X'Pert Pro MRD XL; the x-rays source is using a Cu-α filament with a wavelength λ=1.5405980 Å. The analyses on the two alloys were performed positioning the source in a configuration with 2θ angle between 38 °, 30 ± 0.6 °. In this interval falls precisely the diffraction peak of the basal plane (0002) for both alloys object of study. The dimensions of the measuring area were equal to 5x1 mm.

As previously mentioned, the square test samples extracted from the cold rolled sheet metal have not been subjected to any type of surface preparation. For both the alloys, a preliminary analysis has been made performing a scan of the samples and varying the angle Φ between 0° and 360° (angular pitch = 10°), while the angle Ψ range was between 0° and 85° (angular pitch = 5°). The obtained results were corrected by subtracting the diffraction peaks the background and the defocusing errors previously mentioned.

The execution of these preliminary measuring steps, as well as the examination of the pole figures obtained therefrom, allowed identifying the values of angles Φ and Ψ for which the intensity of the diffraction peaks of the basal plane is higher, and then consequently run measures with better sensitivity in the closeness of these values. In detail, for both materials, the measuring range during the second attempt was limited, in case of angle Ψ, in the range 15 °–45° (angular pitch = 1°), while for angle Φ was still 360° but with angular pitch equal to 2°.

[98] O. Engler, V. Randle – Introduction to texture analyses, 2nd edition – CRC press, pp. 87

6.1.2.1 Experimental Results

As previously mentioned, on both the samples in unstrained condition, a preliminary measurement has been performed for detecting the qualitative pole figure. In Fig. 6-8 the simplified pole figure (2D and 3D representation) for Ti-Fe-Si-O is shown as example. In this diagram the corrections of background and defocusing errors are still not applied.

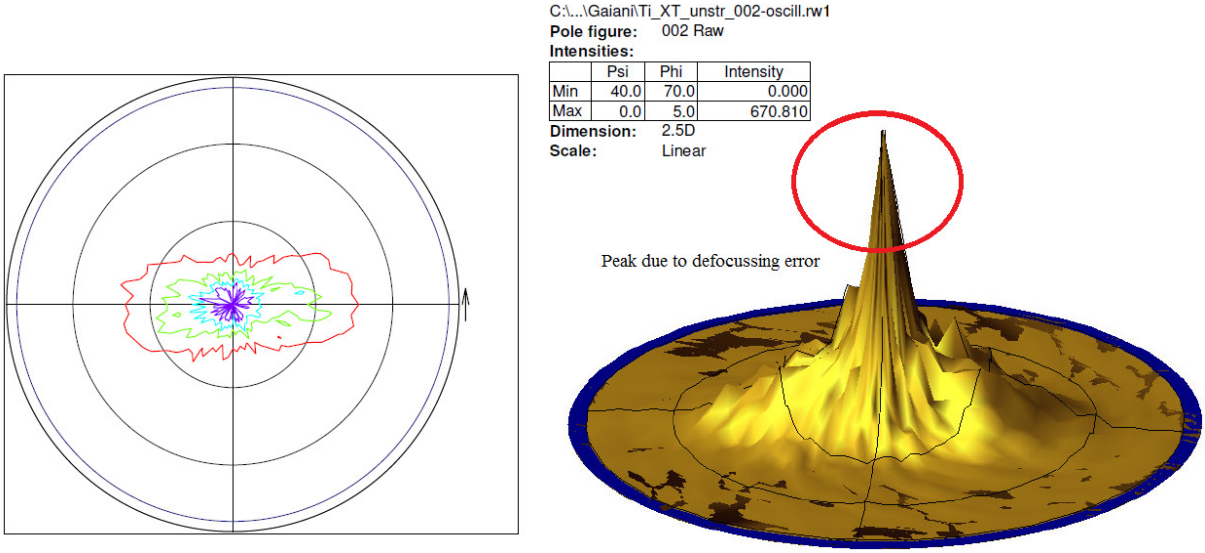

Fig. 6-8 – Example of simplified pole figure (uncorrected) for Ti-Fe-Si-O

After applying the correction functions for reducing the impact of defocussing and background errors, the pole figure is modified as shown in Fig. 6-9. The scale of the 3D representation in terms of peaks intensity is not equal before and after correction.

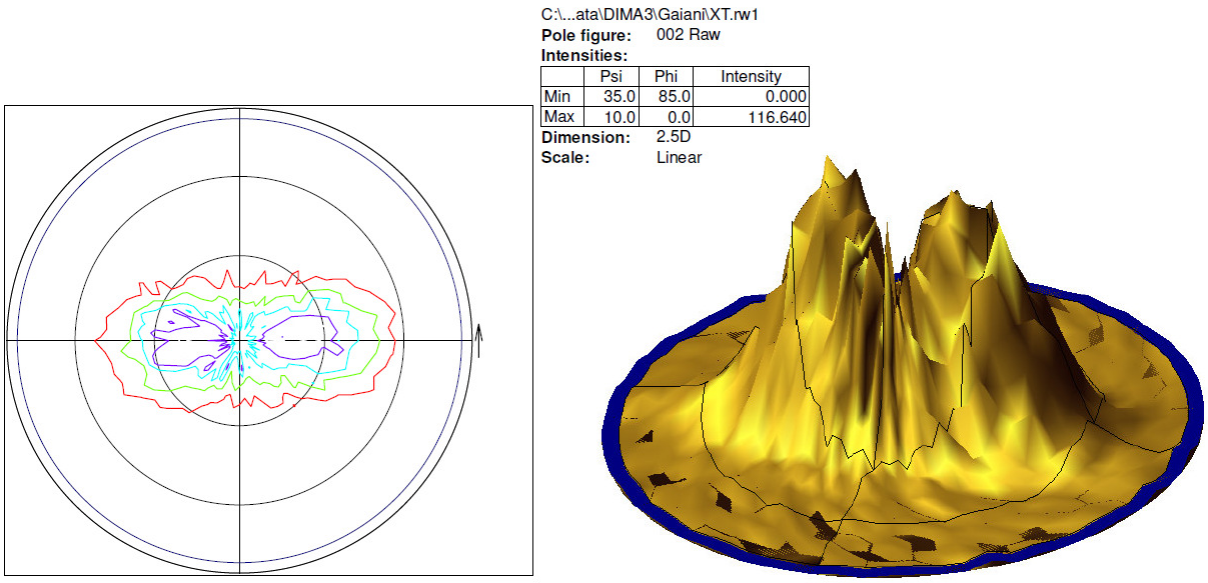

Fig. 6-9 – Example of simplified pole figure (corrected) for Ti-Fe-Si-O

The execution of a preliminary round of measurements allows understanding that Ti-Fe-Si-O and Ti-Al-Si-Nb alloys present similar preferential crystallographic orientation. Specifically, the main distribution occurs along transverse direction and for Ψ included in a range between 20° - 40°. Due to these results, for a more precise texture determination, measurements with higher resolution have been repeated on the same cold rolled samples (unstrained conditions).

As mentioned before, in case of Ψ is varying in the range 15 °–45° (angular pitch = 1°), while angle Φ was still describing 360° but with angular pitch equal to 2°.

The experimental pole figures obtained are shown in Fig. 6-10 and Fig. 6-11.

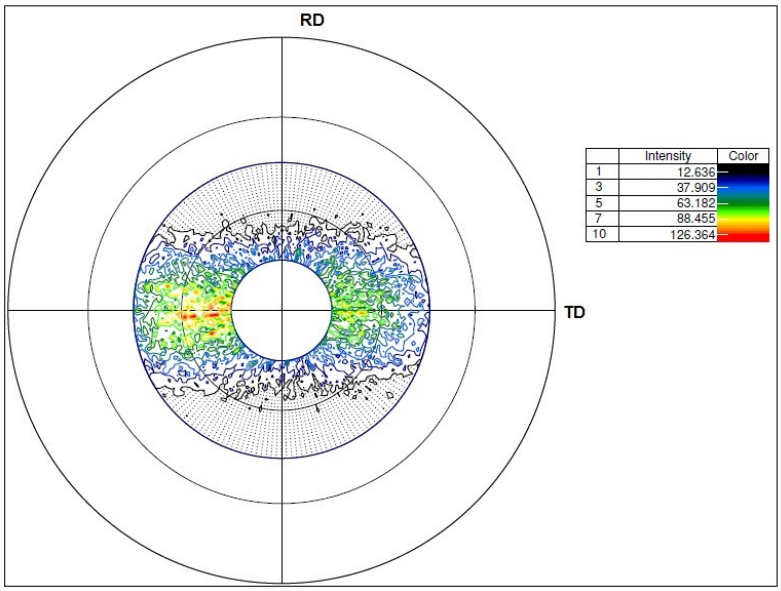

Fig. 6-10 – Ti-Fe-Si-O alloy pole figure for basal plane (0002) orientation

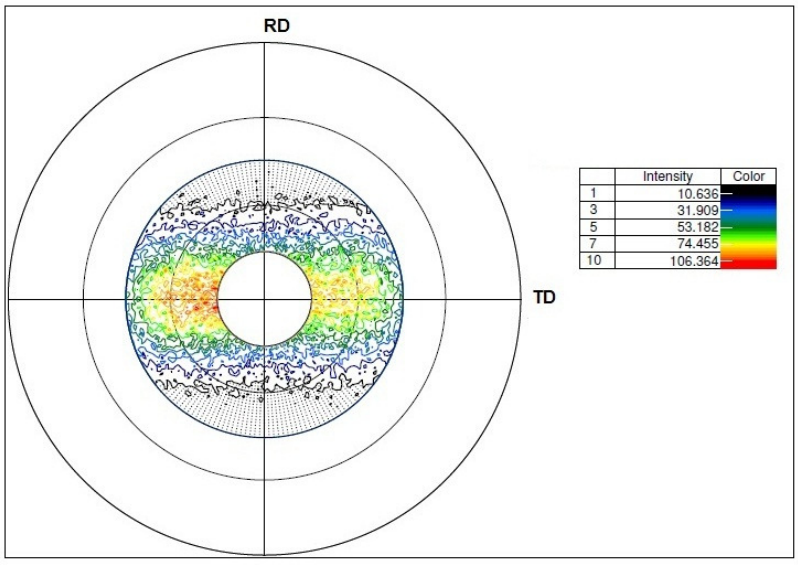

Fig. 6-11 – Ti-Al-Si-Nb alloy pole figure for basal plane (0002) orientation

It is important to underline how both the alloys, but especially Ti-Fe-Si-O, present asymmetric pole figures. This aspect is often due to some re-sizing operation performed on the final product after rolling for achieving the dimensional tolerances requested for this kind of flat products.

6.2 Texture determination using EBSD (Electron BackScatter Diffraction) technique

Electron backscatter diffraction (EBSD) is a measuring technique used for examining the crystallographic orientation of many materials, which can be used to evaluate texture or preferred orientation of any crystalline or polycrystalline material.

The EBSD technique is based on the use of a scanning electron microscope (SEM); an EBSD installation consists of a video camera coupled to a phosphor screen, a camera control and diffraction processor unit and a computer with data processing and analysis software. A schematic illustration of an EBSD installation is given in Fig. 6-12.

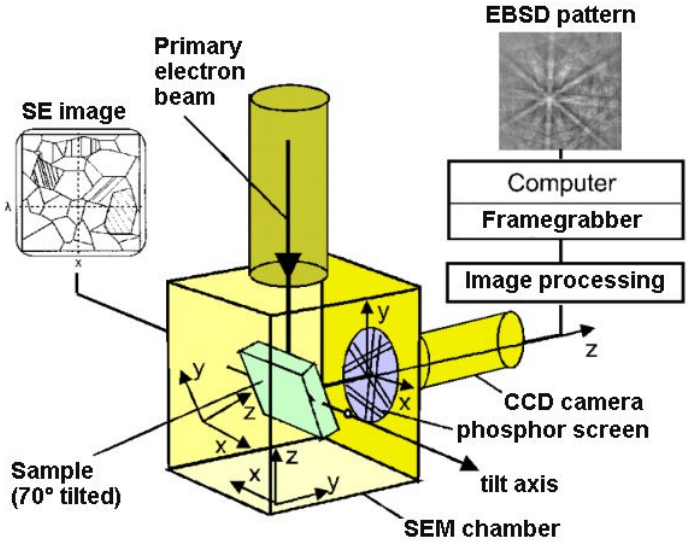

Fig. 6-12 – Schematic illustration of EBSD installation

During EBSD measurements, an electron beam is directed on the specimen, which diffracts the electrons. The specimen is tilted, usually over 70°, to increase the number of diffracted electrons. The diffracted electrons hit the phosphor screen and form a diffraction pattern (also known as "*Kikuchi lines*)", which is captured by the camera. The diffraction data is subsequently processed by the computer, which is comparing the acquired image with a standard database containing the theoretical crystallographic parameters of the lattice under investigation[99].

In recent years, the automation of this method has allowed developing a reliable technique for the quantitative characterization of plastic formability of crystalline materials. This is possible because, in addition to the grain and subgrains structures determination, it is possible to obtain important microstructural parameters which are not obtainable with traditional metallographic methods, in particular those related to quantitative crystallographic orientation and grain boundaries distribution. Moreover, this measuring technique allows the analysis of samples with dimensions which can vary from the order of magnitude of centimeters up to those of nanometers, typical example of thin films.

[99] Arjen Kamp - Investigation of Titanium a Plates by EBSD Analysis – Master Thesis (2007) Delft University of Technology

6.2.1 Hexagonal axes conventions for Euler angles

The typical output which is obtained performing an EBSD analysis is the three Euler angles which identify the crystal orientation in relation to the sample orientation. The Euler angles (named conventionally φ_1, Φ, φ_2) refer to three rotations that, when performed in the correct sequence, transform the specimen coordinate system onto the crystal coordinate system: in other words, they specify the orientation of the unit cell with respect of the material volume[100]. The convention most commonly used for expressing the Euler angles is the one formulated by Bunge, which is represented in Fig. 6-13.

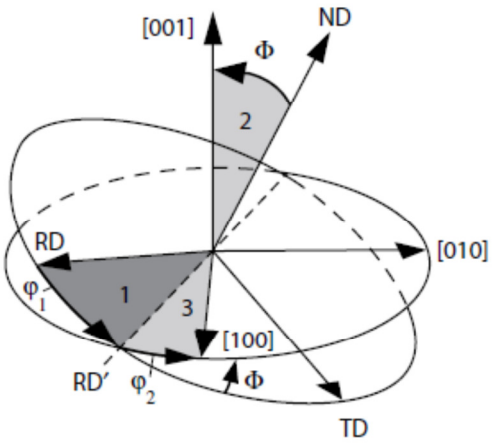

The rotations are as follows:

- Angle φ1: about the normal direction ND, transforming the transverse direction TD into TD' and the rolling direction RD into RD'
- Angle Φ: about the axis RD′ (in its new orientation)
- Angle φ2: about ND″ (in its new orientation)

Fig. 6-13 – Rotation between specimens and crystal axes

With these premises, in order to properly interpret the results obtained by EBSD analysis, it is also important to consider the basic condition for which the three Euler angles are all equal to zero. In our specific case, this aspect becomes even more important since the two titanium alloys under investigation present HCP crystal lattice. This unit cell, being asymmetrical, could allow different basic orientations; the one chosen for the texture analyses on Ti-Fe-Si-O and Ti-Al-Si-Nb samples is shown in Fig. 6-14.

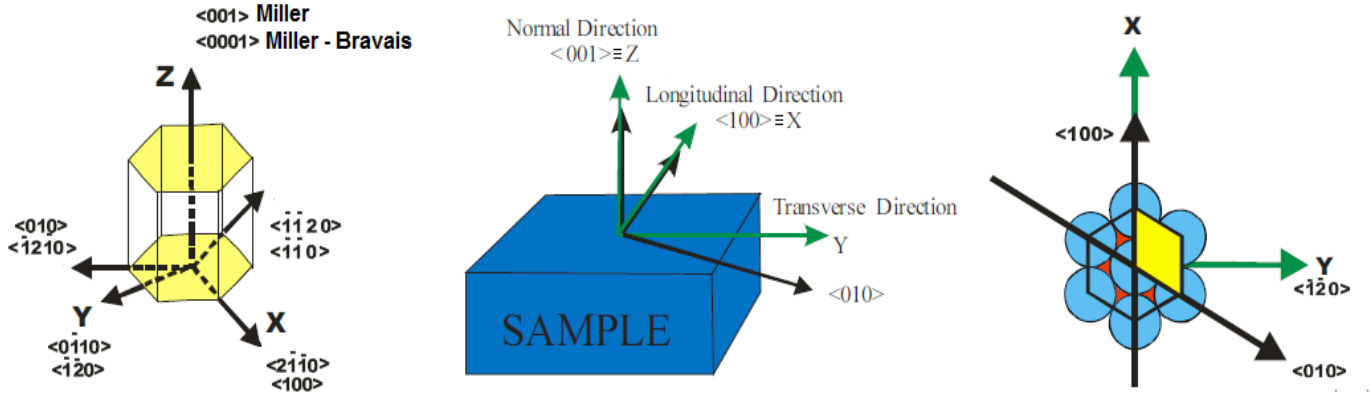

Fig. 6-14 – Sample axis configuration for $\varphi_1 = 0$, $\Phi=0$, $\varphi_2 = 0$
(Image courtesy of Labosoft Inc.)

[100] O. Engler, V. Randle – Introduction to texture analyses, 2nd edition – CRC press, pp. 34

6.2.2 EBSD diffraction measurements

The texture measurements on Ti-Fe-Si-O and Ti-Al-Si-Nb alloys were carried out using the probe Nordly EBSD Oxford Instruments mounted on a scanning electron microscope JEOL JSM-7600 and operating at 20 kV and a working distance of 20 mm.

As previously stated, with this technique, for the measurements execution, the sample must be inclined 70° from the horizontal, in order to increase the image contrast resulting from the diffraction of the electron beam on the crystallographic planes. The electron diffraction images which are obtained when the electron beam strikes the planes of the crystal lattice (Kikuchi bands) are impressed on a phosphor screen and acquired through the use of a video camera with CCD technology. These lines correspond to each plane of the diffracting lattice, and for the measurement are indexed from the software by assigning to all of them their specific Miller index.

During EBSD measuring, some practical difficulties may have to be overcome for achieving good results, especially if the measurements are carried out using the automatic indexing mode. The two main aspects which can negatively affect the analyses are:

- Samples presenting a microstructure with a lot of dislocations, twinning and residual stresses. These microstructures, which are typical for cold rolled materials like the two titanium alloys under investigation, are difficult to be identified by EBSD; the automatic indexing is decreasing with the increase of the rolling ratio
- Pseudosymmetry phenomenon, however images of the Kikuchi lines which are difficult to be distinguished one from each other within the resolution of the imaging system

From an operational point of view, when the aforementioned phenomena occur, an extremely accurate sample preparation must be applied. In this specific case, the samples representative of both alloys have been extracted from a cold rolled sheet metal and then were put in epoxy resin; first polishing step was done with the standard method used for the metallographic inspection (see par. 3.1). Afterthat, an additional polishing step for duration of 60 minutes using as abrasive material colloidal silica with the addition of 10 ml of H2O2 at 30% was made. At the end of these preparation phases, the samples have been extracted from the resin and then mounted directly on the sample holder of the microscope; this choice has been made with the aim of improving the sample's electrical conductivity during the measuring phase.

The texture analyses were performed using the automatic indexing mode; the reference database used for Kikuchi bands identification was the one named Ti-Hex, typical for titanium alloys presenting HCP crystal lattice. For the instrument at our disposal, the biggest working area was a rectangle with dimension 510x405 μm, while the measuring steps, chosen taking into consideration the average grain size, were equal to 3 μm. By using these operating conditions, the measuring grid was constituted approximately by 23,000 points (170x135 steps); the time required for data acquisition was equal to 205 minutes.

6.2.2.1 Experimental Results

By using the automatic indexing mode for performing EBSD texture analysis, the points which have been successfully acquired on the rectangle grid with dimension 510x405 µm were:

- 20.105 points for the alloy Ti-Fe-Si-O (equivalent to 87.6% of the total)
- 20.623 points for Ti-Al-Si-Nb alloy (equivalent to 89.9% of the total)

For each point acquired during the measurement, the set of three Euler angles is determined by the software; this large amount of data can be processed for obtaining different type of informations all connected to the quantitative texture analyses. In detail:

a) Crystals orientation map
b) Euler angles distribution functions
c) Pole figure

In the following sections the results obtained from EBSD texture analyses of Ti-Fe-Si-O and Ti-Al-Si-Nb alloys will be presented.

A) Grain orientation distribution map

In Fig. 6-15 and Fig. 6-116 are shown the crystals orientation map for the two alloys under investigation.

In these analyses, the primary scope was detecting the macro texture of the alloys; due to this reason, has been decided to keep a relatively large measuring step (3 µm) but performing the EBSD measurments on a bigger volume of material (over 20.000 points have been automatically indexed). Because of that, the grain boundaries are not perfectly defined, and the resolution of the output data appears relatively poor.

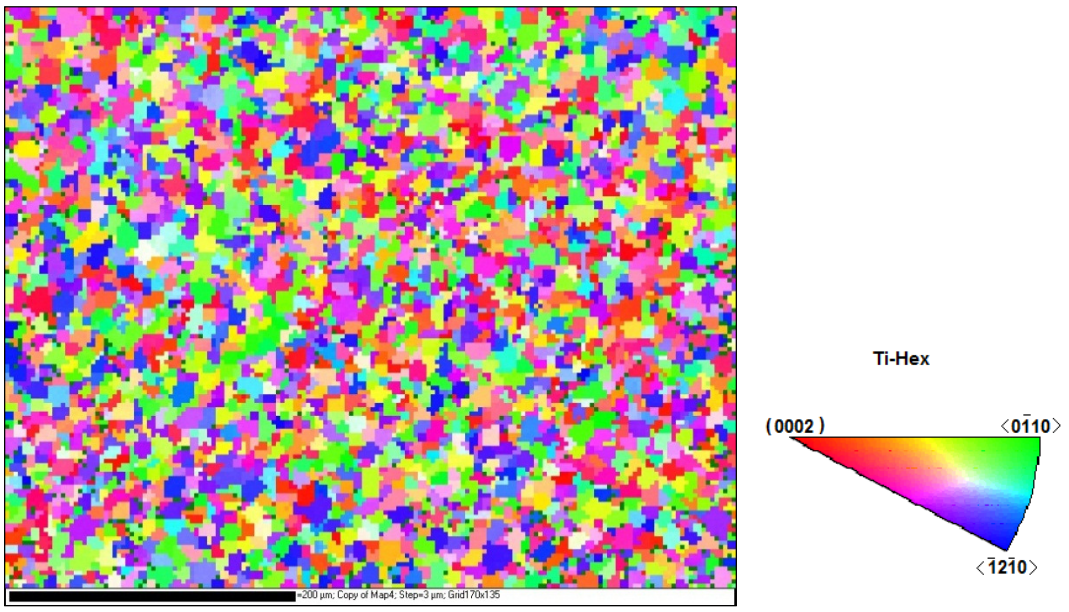

Fig. 6-15 – Crystals orientation map fot Ti-Fe-Si-O alloy

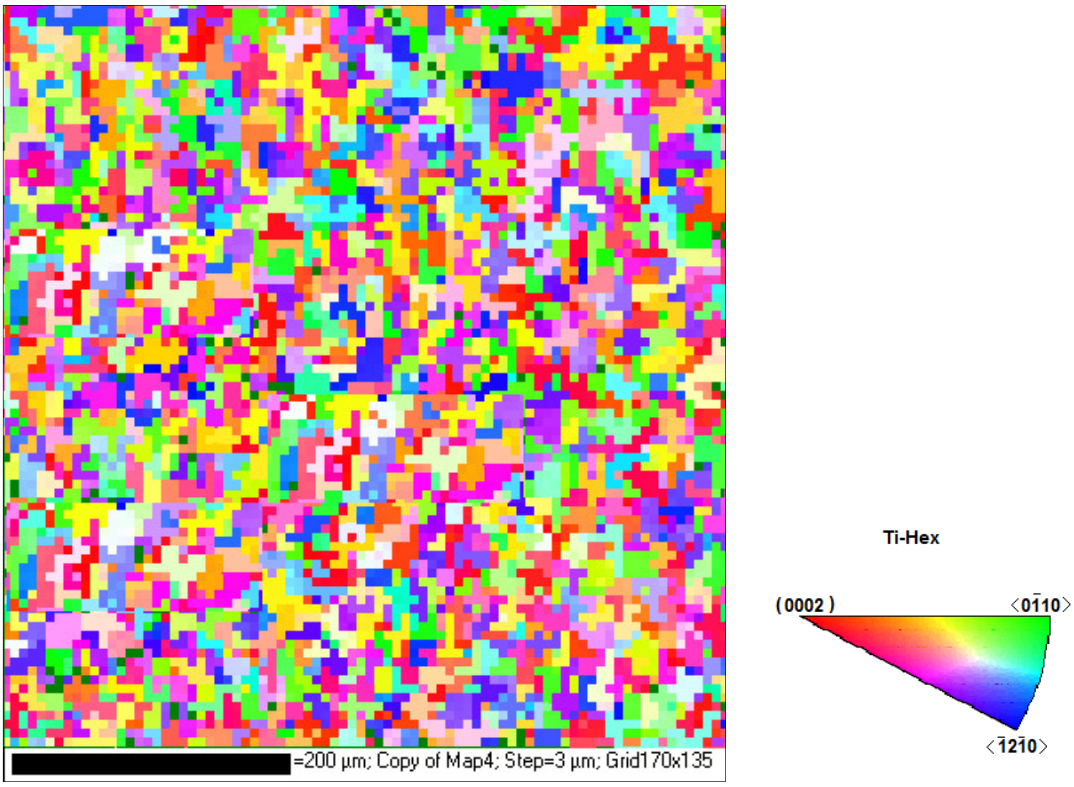

Fig. 6-16 - Crystals orientation map fot Ti-Al-Si-Nb alloy

B) Euler angles distribution functions

As previously mentioned, the main output of the EBSD analyses are sets of three Euler angles providing the orientation of the crystal lattice with respect of the sample. These data series have been analyzed and filtred in order to evaluate the quantity of crystal lattices oriented according to specific angular intervals of 5° each. With this procedure is possible to create some graphs, one specific for every Euler angle, which summarize the orientation distribution of the crystals as function of the angles themselves.

For better understanding the information present in the following diagrams, in Fig. 6-17 a schematic view concerning the disposal of Euler angles towars the specimens is shown.

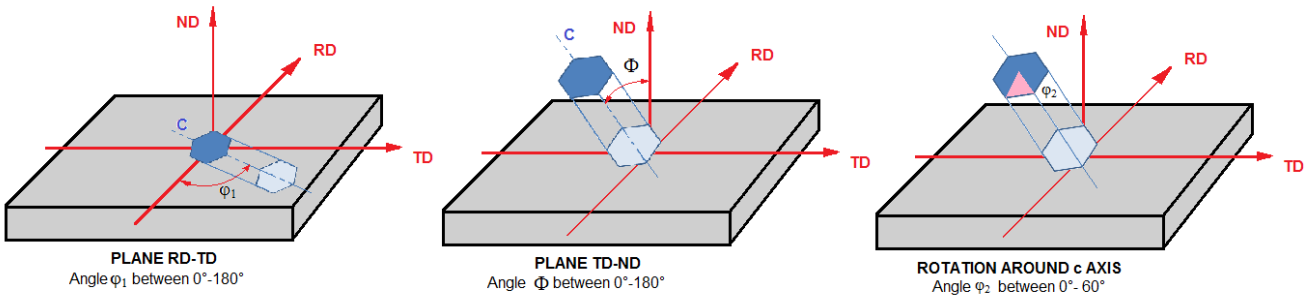

Fig. 6-17 – Euler angles representation with respect to the sample's directions

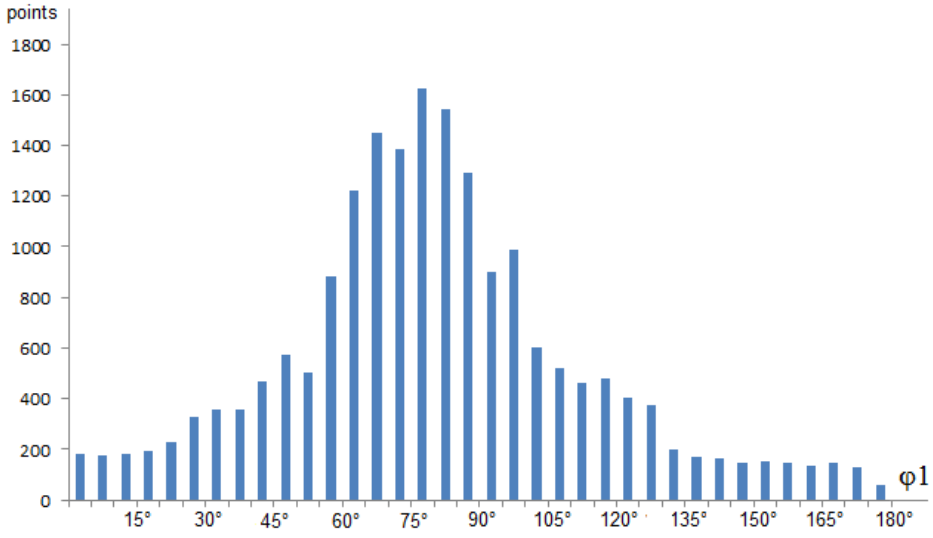

Fig. 6-18 – Angle φ_1 distribution of for Ti-Fe-Si-O alloy

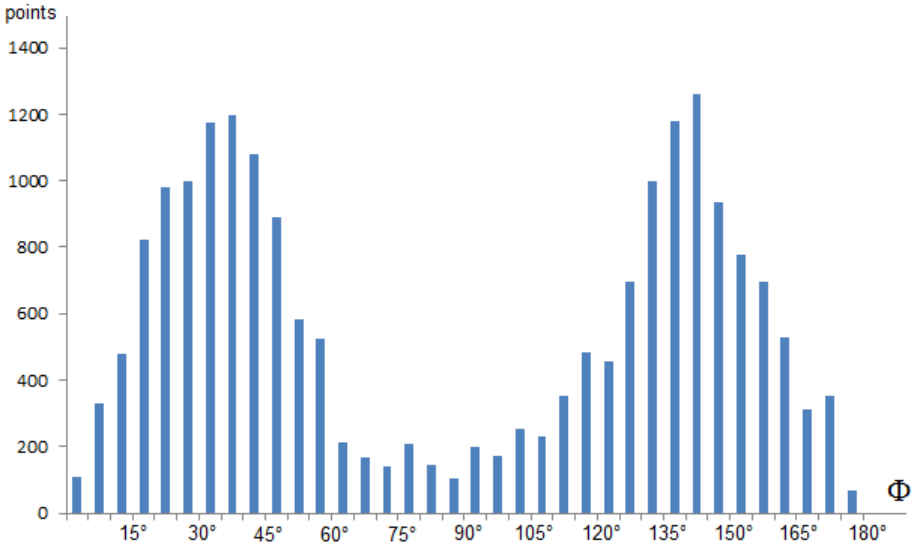

Fig. 6-19 – Angle Φ distribution of for Ti-Fe-Si-O alloy

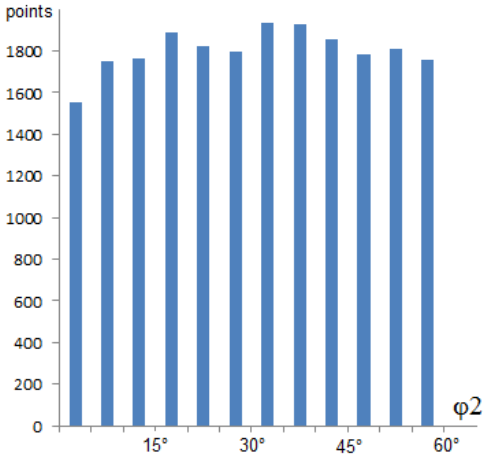

Fig. 6-20 - Angle φ_2 distribution of for Ti-Fe-Si-O alloy

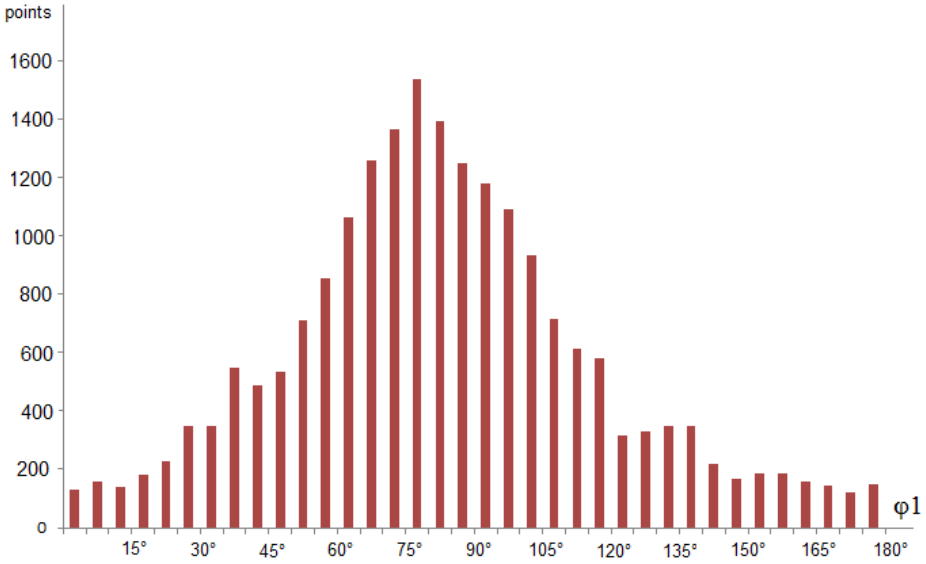

Fig. 6-21 – Angle φ_1 distribution of for Ti-Al-Si-Nb alloy

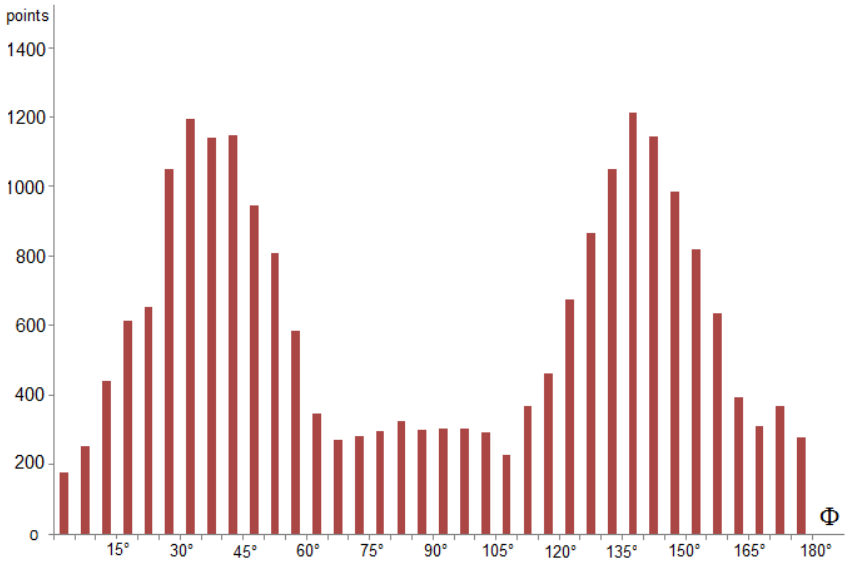

Fig. 6-22 – Angle Φ distribution of for Ti-Al-Si-Nb alloy

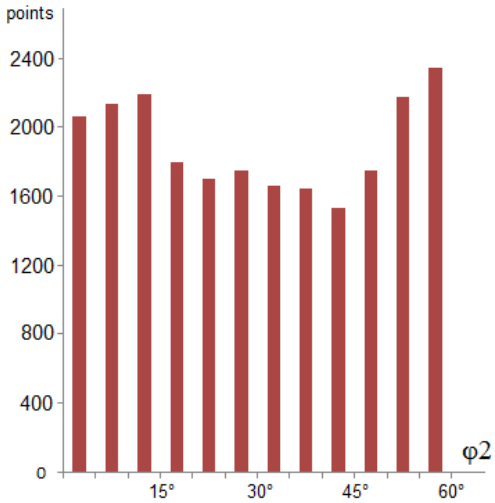

Fig. 6-23 – Angle φ_2 distribution of for Ti-Al-Si-Nb alloy

C) Pole figures

In Fig. 6-24 and Fig. 6-25 are shown the pole figure representing the typical texture of Ti-Fe-Si-O and Ti-Al-Si-Nb alloys. On the left side, the black and white images represent all the indexed point displayed on the pole figure. On the right side, for better understanding, the same data are visualized using a color coded scale which helps detecting the peaks position.

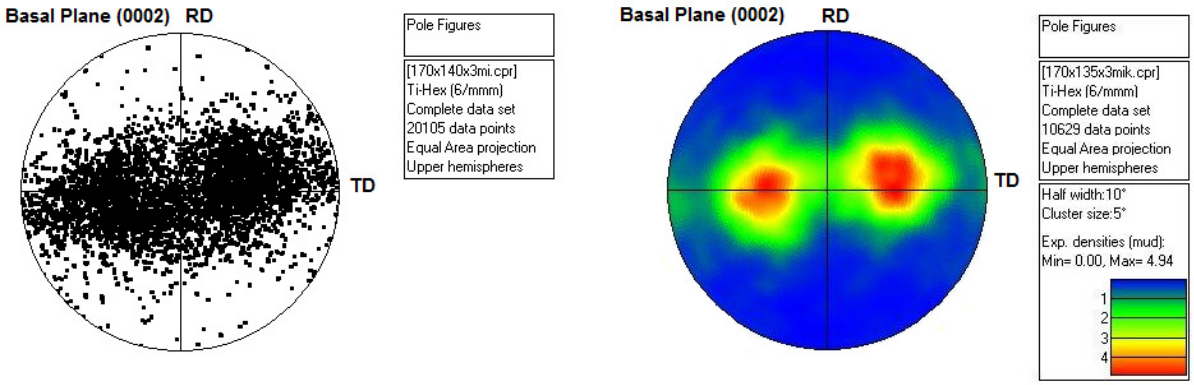

Fig. 6-24 – Ti-Fe-Si-O alloy pole figure for basal plane (0002) orientation

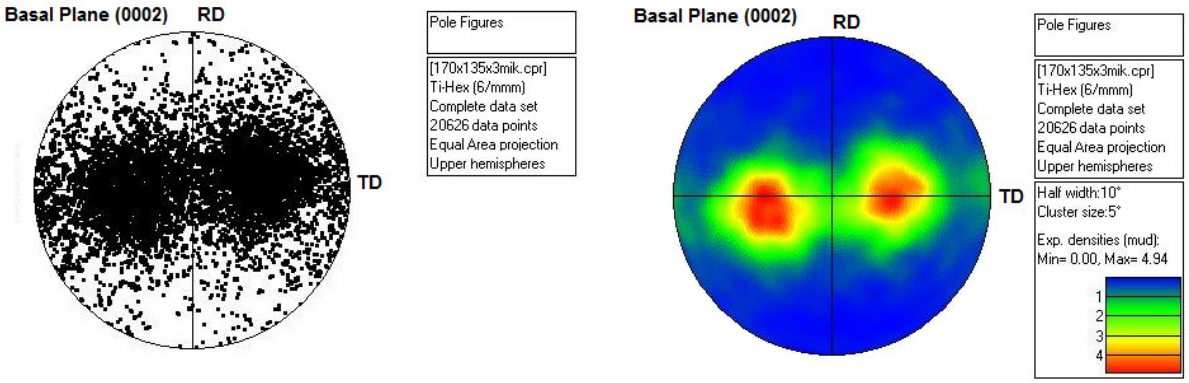

Fig. 6-25 – Ti-Al-Si-Nb alloy pole figure for basal plane (0002) orientation

Comparing the pole figures obtained with EBDS technique with the ones obtained with XRD technique presented in paragraph 6.1.2.1 it can be easily seen that the results obtained are fully comparable, even if the Ti-Fe-Si-O samples has been tested in a position rotated 180° with respect to the XRD measurements. Anyway, it can be stated that EBSD technique is preferable when the evaluation of quantitative data regarding texture properties of the materials under investigation is requested; the method is also more flexible because allows different representation of the experimental data.

6.3 Texture evolution during plastic deformation

The mechanical characterization campaign performed on Ti-Fe-Si-O and Ti-Al-Si-Nb alloys highlighted a substantially different behaviour between these material during plastic deformation. However, the two titanium alpha alloys under investigation present many similar characteristics in the delivery state. In detail:

- Same alpha based microstructure with similar grain size
- Equivalent production cycle by cold rolling with final annealing treatment
- Similar crystallographic orientation

For evaluating if during plastic deformation a different texture evolution can explain the different characteristics in terms of plasticity, some standard tensile specimens have been pulled using a universal laboratory machine to different predetermined levels of strains: 4%, 7% and 10%. The trials have been performed using strain rate control. The strain rate in the elastic field was equal to 0,00012 1/s trough 0,2% offset of yielding, while in the plastic field was increased up to 0,0017 1/s. For both the alloys the tensile specimens have been extracted both in longitudinal and transverse direction.

In Fig. 6-26 an example of the loading cycles executed on the specimens is shown.

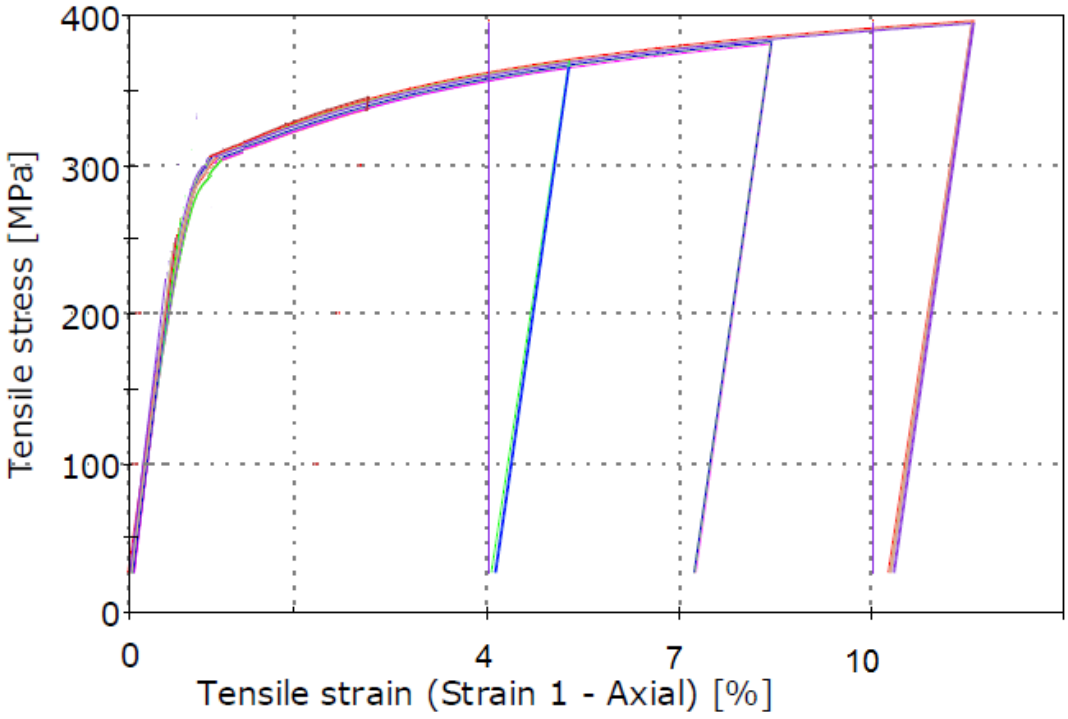

Fig. 6-26 – Pre-straining cycle performed on the specimens

After that a known preloading has been given, from the central area of every specimen a square sample 15x15 mm have been extracted. On these samples some texture measurements using XRD technique have been realized, using the same methodology illustrated in Paragraph 6.1.2. The aim of this activity is assessing if, for increasing deformation levels, a different texture evolution can be observed between the two titanium alloys under investigation.

6.3.1 Experimental results

The pole figures obtained measuring the textures on the pre-strained Ti-Fe-Si-O specimens are shown below.

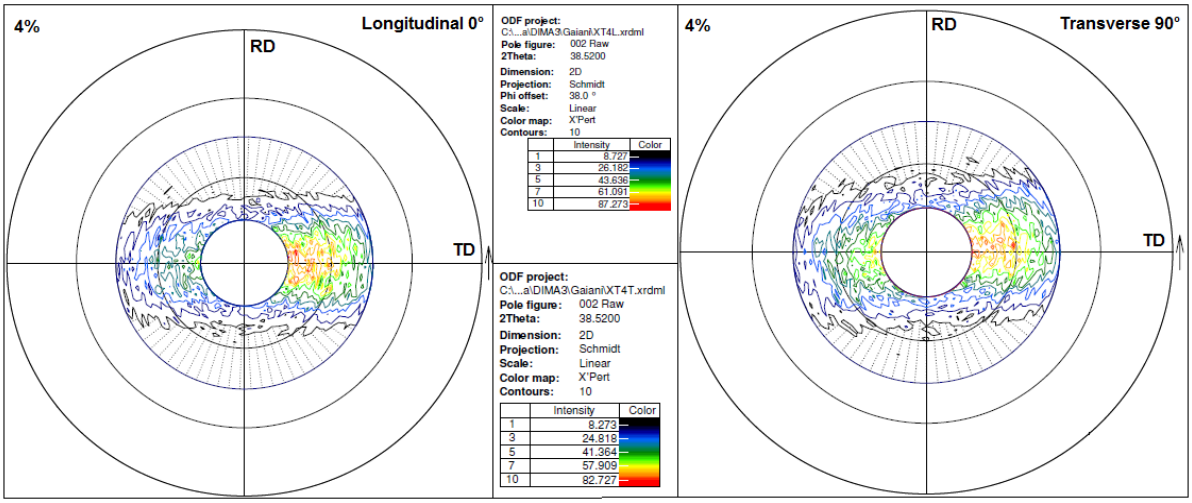

Fig. 6-27 – Pole figures for Ti-Fe-Si-O alloy (L+T directions, 4%)

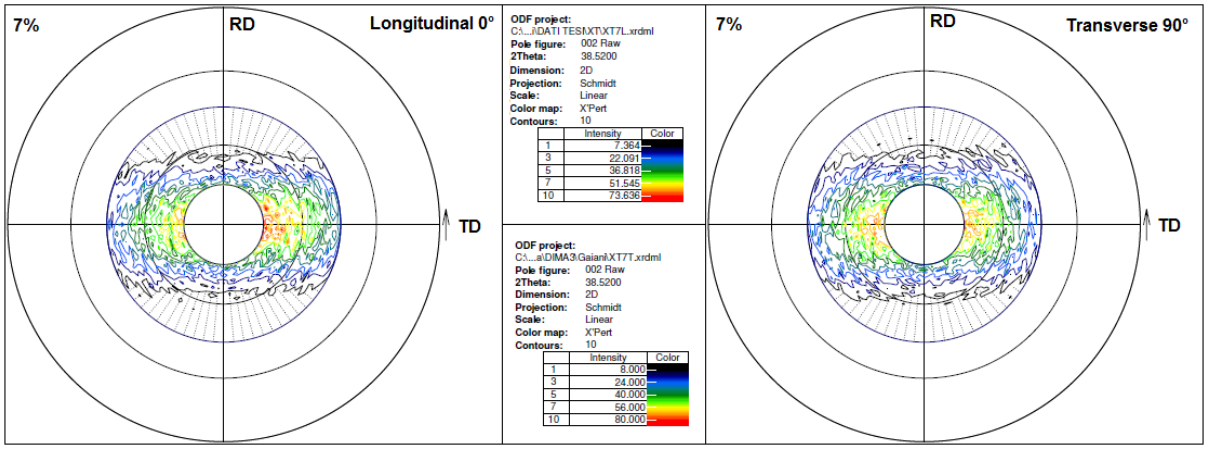

Fig. 6-28 – Pole figures for Ti-Fe-Si-O alloy (L+T directions, 7%)

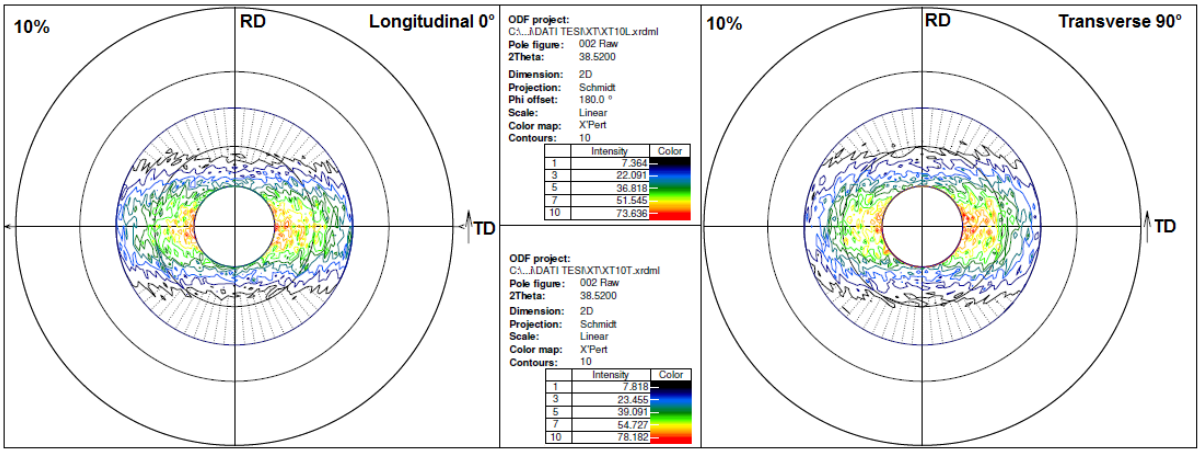

Fig. 6-29 – Pole figures for Ti-Fe-Si-O alloy (L+T directions, 10%)

The pole figures obtained measuring the textures on the pre-strained Ti-Al-Si-Nb specimens are shown below.

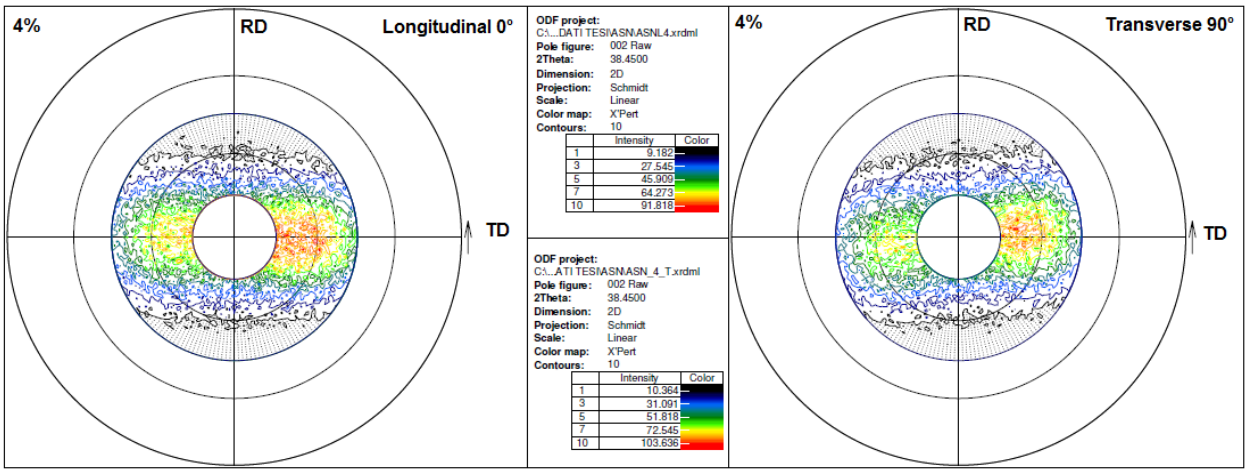

Fig. 6-30 – Pole figures for Ti-Al-Si-Nb alloy (L+T directions, 4%)

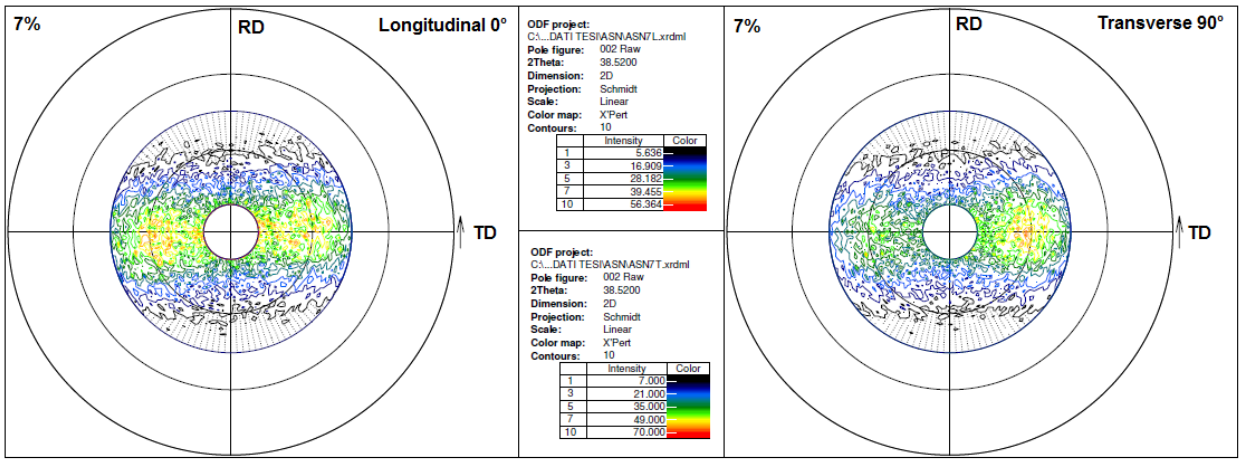

Fig. 6-31 – Pole figures for Ti-Al-Si-Nb alloy (L+T directions, 7%)

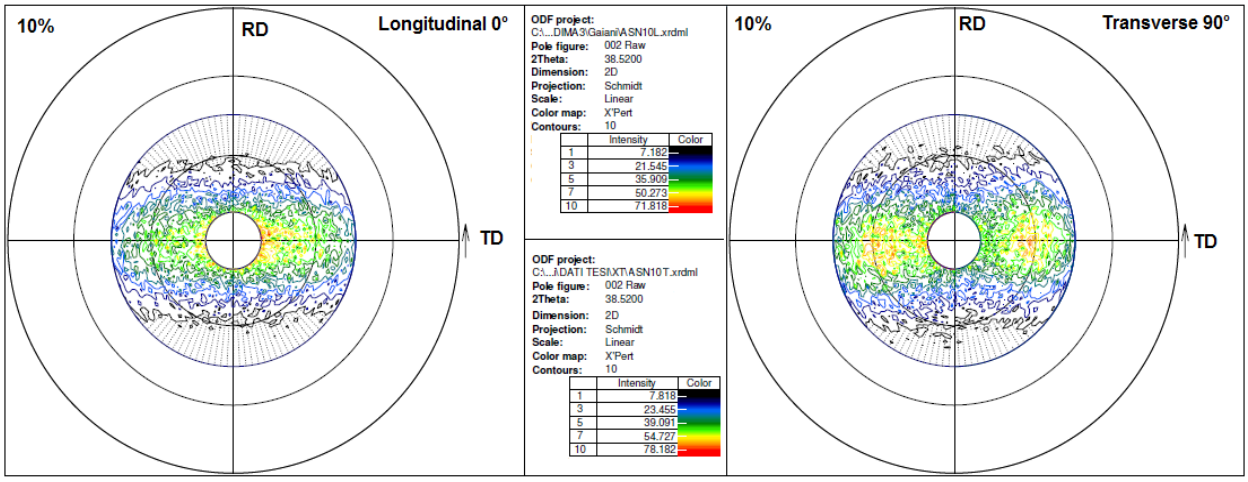

Fig. 6-32 – Pole figures for Ti-Al-Si-Nb alloy (L+T directions, 10%)

Performing qualitative analyses on the pole diagrams of the pre-strained specimens, some consideration can be made:

- The basic behavior of the two alloys is similar, and both the alloys keep presenting a marked preferential texture along transverse direction ($\Phi \in [345° - 15°]$ and $\in [165° - 195°]$) which is staying also for the higher strain levels
- Concerning the peak orientation along Ψ axis, for lower strain levels, the asymmetry of the pole figure detected on the unstrained specimens is still visible, and in transverse direction seems to be also enhanced
- For higher strain levels, both alloys show the tendency to present a basal type of texture

CHAPTER 7
CONCLUSIONS

The research activity performed on titanium alpha alloys Ti-Fe-Si-O and Ti-Al-Si-Nb has allowed investigating a consistent number of specific properties of these materials. It is important to highlight the fact that these alloys, specifically developed for heat resistant applications, despite their interesting mechanical properties and remarkable oxidation resistance, are still rarely used for large scale industrial applications, mainly because of their limited cold formability. To this end, all the characterization activities described in present work have been performed with the main target of better understanding the peculiar plastic deformation mechanisms of the alloys mentioned above, in order to use these informations as input data for numerical simulation of cold forming operations of sheet metal.

In agreement with these premises, the most significant results obtained thanks to this research activity are outlined and discussed below.

a) Mechanical Characterization

The experiments carried out by performing a relevant number of tensile tests on specimens extracted from cold rolled alpha titanium sheets delivered in annealed condition, had as main target to obtain data about the plastic properties of the alloys under investigation. The first important result which is reached performing these trials is that, for this type of characterization, is always necessary to operate using two clip-on extensometers (which detect respectively the axial deformation and the transversal deformation of the specimen). In addition to this, tests should be performed using the strain control method to increase the level of quality of results. It can be stated indeed that setting a constant strain rate allows obtaining $\sigma - \varepsilon$ curves which present a more regular trend in the large plastic deformations field; these curves can be used more profitably as input data for the numerical simulation.

Special attention needs to be paid when the plastic strain ratio values (R values) are determined. This experience has shown that for materials presenting σ - ε curves with monotonic growing trend, as Ti-Al-Si-Nb alloy, the anisotropy coefficients calculation carried out according to the ISO 10113 standard procedure allows obtaining acceptable results. Vice versa, for materials presenting a discontinuous yielding behavior as Ti-Fe-Si-O alloy, the standards calculation approach can lead to overestimate the real value of the anisotropy coefficient. As discussed in Par. 3.2.6.1 point e), with this type of alloy, the best results are obtained by expressing the anisotropy coefficient as a function of the longitudinal strain R(ε). For better understanding the intrinsic behavior of this alloy, extremely

meaningful is to superimpose the graph of R (ε) function with the σ – ε diagram, as shown in Fig 3-25. From this comparison can be easily seen that, in the second half of the discontinuous yielding region, a peak of plastic strain ratio value is detected. However, at the end of the discontinuous yielding, this peak is disappearing and the plastic stain ratio function becomes linear and with a tendency to a constant value.

The peak of R(ε) function occurs when the true strain signal in longitudinal direction ε_l becomes almost equal to the one read in the transverse direction ε_w; in this particular condition, the true strain along the specimen's thickness ε_t (obtained calculating the difference between ε_l and ε_w) tends to zero, and consequently the value of the anisotropy coefficient is increasing, generating a local maximum.

An aspect which needs to be emphasized is that, especially for specimens extracted along transverse direction, the discontinuous yielding area extends over 6% of strain, while the maximum tensile strength R_m is reached already around 8% of elongation. Because of this reason, when the plastic strain ratios are calculated according to ISO 10113 method, or rather by considering linearization intervals extended only up to R_m, their value is usually overestimated due to the presence of the local peak in these intervals.

It's undeniable that the use of a transversal clip-on extensometer induces few limitations related to the correct reading of the deformation along this direction. In fact, being the extensometer applied in correspondence of a specific specimen's section (generally close to the median one), when the maximum tensile strength is reached and the onset of localized necking takes place, the reading performed by this type of instrument becomes poorly reliable, because indicative only of the contraction occurring along the specific section where it is clamped. It's proved that optical systems can solve this problem.

A similar problem occurs, in case of Ti-Fe-Si-O alloy, even during the discontinuous yielding phase, since the optical deformation measurements performed using Aramis system have shown the occurrence of Lüders bands phenomenon . In this specific case, as shown in Fig 5-31, the material deformation in the area located above to the bands is almost twice larger than the one detected in the lower zone. This aspect cannot be properly appreciated by the clip-on extensometer, and therefore the transverse strain value detected by this type of strain gauge represents formally an average value.

Particularly effective, for a better understanding the influence of the intrinsic anisotropy of these materials on their mechanical and plastics characteristics, have been the results of the tensile tests performed on specimens extracted from the sheet metal at intervals of θ=10° orientation. This characterization (see Par. 3.2.6), performed at constant strain rate, allowed

understanding the basic trends of all the most significant parameters (R_p, R_m, E) as a function of the θ angle formed by the specimen's axis with the rolling direction.

Particular attention needs to be paid in observing the trend of plastic strain ratio R_θ which, for this specific evaluation, was calculated as punctual value at different levels of true strain ε_l, belonging to the range 1 – 15%. In Fig. 7-1 and Fig. 7-2 is shown the variation of the plastic strain ratio value as

function of angle θ; for this evaluation, two different strain levels of the specimen (5% and 10%) have been chosen.

It is significant to stress that for Ti-Al-Si-Nb alloy the plastic stain ratio values are substantially increasing moving from rolling direction (0 °) to transverse direction (90 °); it can be also seen that these values remain almost unchanged when the deformation is increasing from 5% to 10%. Vice versa, Ti-Fe-Si-O alloy presents a strongly discontinuous trend at 5% of elongation (due to the discontinuous yielding behavior which presents variable extension depending on the specimen orientation). However, the material tends to homogenize the R values when the deformation is increased up to 10%, showing a tendency to reach higher peaks between 60° - 90° specimen orientation.

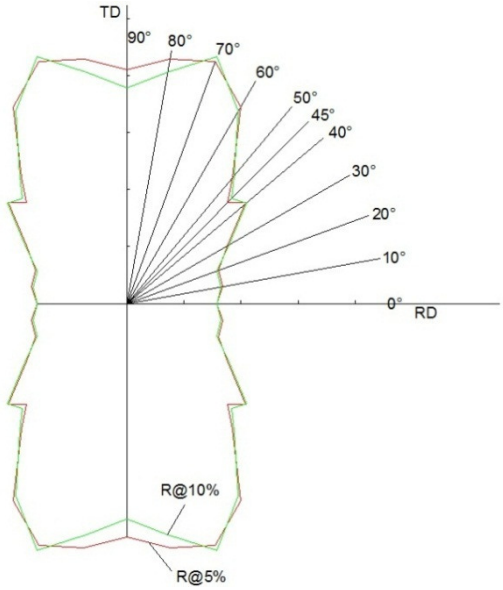

Fig. 7-1 – TI-AL-SI-NB-EX R(θ) variation

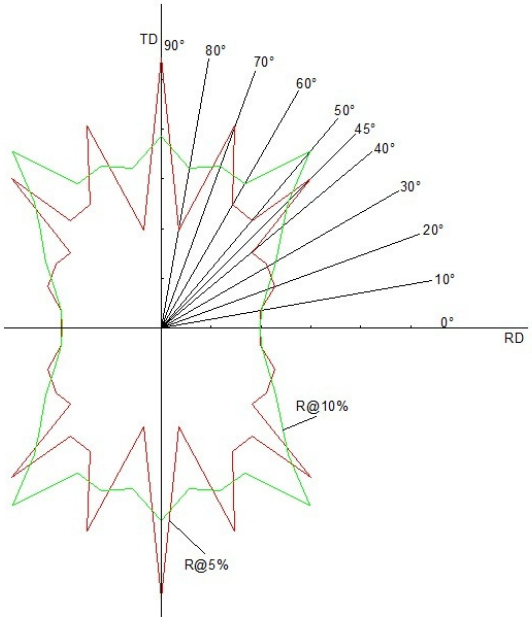

F ig. 7-2 – Ti-Fe-Si-O R(θ) variation

The angle θ formed between the rolling direction and the specimen longitudinal axis is basically representing the angle Φ introduced in Par. 6.1.1 concerning texture measurments. The basic pole figures for both alloys under investigation show that on the sheet metal plane (RD-TD) the crystal lattice presenting a c axis belonging to that plane are mainly oriented in the proximity of transverse direction to rolling. This aspect is clearly connected to the higher value of plastic strain ratio detected within the range θ = 60° - 90°, Anyway, further studies should be carried out in order to identify an analytical correlation between the results obtained from the mechanical characterization with those achieved performing texture analyses on unstrained or pre-strained samples. However, for this approach, the texture measurements need to be performed using EBSD technique rather than XRD technique, due to the higher number of quantitative information which can be obtained exploiting this specific procedure.

b) Ti-Fe-Si-O alloy and Lüders Band phenomenon

The application of an optical measurement technique for stresses and strains determination proved to be extremely useful also for clarifying the nature of the discontinuous yielding highlighted in the σ–ε diagram of the Ti-Fe-Si-O alloy. This phenomenon, also known as "*Portevin Le Chatelier effect*" or as "*dynamic strain hardening*" is somewhat unusual in case of titanium alpha alloys and, as previously discussed, strongly complicates the formability intensifying the anisotropic behavior of these materials.

The use of Aramis system has allowed distinctly to highlight the Lüders bands formation and propagation, and to measure the level of strain in areas located respectively upstream and downstream of this region of inhomogeneous deformation.

According to Barat and Sarkar[101] this effect can be described as dynamical interaction of the mobile dislocations and the diffusing solute atoms. In detail, dislocations which are the carrier of the plastic strain, move jerkily between the obstacles provided by the other dislocations. Solute atoms diffuse in the stress field generated by the mobile dislocations and pin them further while they are arrested at the obstacles. This effect leads to negative strain rate sensitivity of the flow stress for certain ranges of applied strain rate and temperature when the mobile dislocations and the solute atoms have comparable mobility. The type of Lüders bands detected in Ti-Fe-Si-O alloy, which exhibit an oscillatory or intermittent propagation are classified as "type B" bands.

In titanium alloys, the dynamic strain hardening is attributed to interstitial atoms, and is increased in magnitude by the presence of silicon, probably due to lattice distortions resulting from silicon-interstitial atom pairs; the temperature of dynamic strain ageing is reduced (up to room temperature) by increases in silicon or oxygen content[102]. Considering that Ti-Fe-Si-O alloy is using as alloying elements mainly Si and O (in the material under testing Si = 0,45% and O=0,14%), the presence of dynamic strain hardening can be so explained.

c) FE Analysis

The simulation activities performed for predicting the formability of deep-drawn components in titanium alpha alloy belonging to motorbike exhaust systems has shown that the use of Barlat & Lian 1989 material model is able to provide meaningful results, which are entirely adequate for forming simulations on industrial scale. With this method is possible to identify the presence of critical areas in the components under investigation and also verifying the tools geometry (especially in terms of radiuses) before starting their manufacturing.

[101] P. Barat, A. Sarkar, A. Barat - Portevin-Le Chatelier Effect: a Poisson Process - Variable Energy Cyclotron Centre, 1/AF Bidhan Nagar, Kolkata

[102] M. R. Winstone, R. D. Rawlings, D. R. F. West - Dynamic strain ageing in some titanium-silicon alloys - Journal of Less Common Metals, 31 (1973) 143 150

The simulation results correlate reasonably well with experimental data, however, the simulation is somewhat conservative. The material model obtained applying the Barlat & Lian 1989 criterion is working in the best conditions possible using as input data the following characteristics:

- Experimental true σ- true ε curve along rolling direction
- Plastic strain ratio expressed as function of strain R(ε)
- Flow exponent m= 2
- Experimental friction coefficient between tool and material surfaces

In order to use the FE analysis for the simulation of real components, the knowledge of the Forming Limit Curves is also essential, because these diagrams can provide the upper usage limit for the alloys. Observing also the principal strains distribution on the component, it is also possible to collect important information about blank orientation and its initial geometry.

To further study the deformation mechanisms of these alloys, the contribution provided by optical measuring instruments is essential, since it allows experimental evaluation of the of stress and strain distributions in components presenting complex geometry and also to study their performance in the large deformations field. In present work, this approach has been used realizing measures of deformation during a Bulge tests and a uniaxial tensile tests. However, this type of optical measurements is also equally applicable to real components and represents an innovative technique to further deepen the study of plastic deformation processes on industrial scale.

d) Texture Analyses

The approach of analyzing the preferential crystallographic orientation of Ti-Fe-Si-O and Ti-Al-Si-Nb alloys was born from the need to check if this feature might justify the anisotropic behavior of these materials. For texture determination, first were analyzed unstrained samples in delivering conditions (annealed) by using two different measurement techniques: EBSD and XRD. The first indicative result which has been obtained from these analyses is that both methods lead to reach the same result in terms of preferential crystallographic orientation. The pole diagrams obtained for Ti-Fe-Si-O and Ti-Al-Si-Nb alloys in unstrained condition show that both materials present the typical texture expected for cold rolled alpha titanium alloys with reduction ratios <50%. In detail, the basal plane (0002) is rotated approximately 35°–40° with respect to the normal of the sheet surface, while the plane [1010] is arranged parallel to the transverse direction. The fact that the crystallographic orientation is found to be the typical one of cold-rolled Ti sheet, shows that the annealing treatment performed in line (5–8 min duration) on both the materials is not carried out for a sufficient time which allows erasing the original texture induced in the materials during rolling.

A peculiarity highlighted from the texture measurements is that both alloys, but mostly Ti-Fe-Si-O, show slightly asymmetric polar diagrams. Deepening this aspect with the raw material manufacturers, a possible explanation arises from the fact that, at the end of the production process, coils are often submitted to a "*resizing*" operation, done pulling the sheet metal. This phase is performed in order to fulfill the dimensional requirements stated in ASTM B 265 standard.

Commenting the quality of the results obtained by the application of two different measuring methods, using the working conditions discussed in Par. 6.1.2 and Par. 6.2.2, it can be stated that EBSD technique allows obtaining more accurate experimental data, which can be processed in different ways to provide quantitative results with higher accuracy than those obtainable with XRD technique. The availability of the three Euler angles for each measuring point allows performing detailed distribution analyses across the entire area under investigation; these data can provide reliable informations about the crystallographic orientation of the sample. The only detrimental aspect which can be ascribed to EBSD technique is the complex procedure requested for surface preparation of the sample, especially if automatic indexing measurements need to be realized on an extended portion of material. In this specific case, the identification of the correct polishing cycle required the execution of few attempts, using various abrasive products and different preparation times.

Concerning the XRD technique, the results obtained with this method are basically comparable with those previously discussed. However, the conclusions which can be drawn from these data about the texture of the titanium alloys are mainly qualitative. This is because the samples present limited thickness, and with this conditions the defocusing error generated by tilting the Euler cradle around Ψ angle is not negligible. When the diffraction profiles are processed for obtaining the experimental pole figure, some correction algorithms built in the diffractometer software are rectifying the signals considering the influence of defocusing and background as well. However, this correction procedure is practically performed by cutting the peak intensities of the diffraction profile detected during the measurements and basically the pole figure processed automatically is in fact ghost corrected diagram. Due to this reason, if accurate evaluations of crystal orientation are needed, the EBDS technique should be chosen instead of XRD method.

List of References (alphabetical order)

S. Aleksandrović, M. Stefanović, D. Adamović, V. Lazić – Variation of Normal Anisotropy Ratio "*r*" during Plastic Forming – Strojniški vestnik (Journal of Mechanical Engineering) (2009) – Vol. 55pp. 392-399 **[Ref. 78]**

T. Altan, H. Palaniswamy, P. Bortot, M. Mirtsch, W. Heidl – Determination of sheet material properties using biaxial bulge tests – *Proceedings of the 2nd Int. Conference on Accuracy in Forming Technology, Nov. 13-15, 2006, Chemnitz, Germany* **[Ref. 87]**

P. Barat, A. Sarkar, A. Barat – Portevin-Le Chatelier Effect: a Poisson Process – *Variable Energy Cyclotron Centre, 1/AF Bidhan Nagar, Kolkata* **[Ref. 101]**

F. Barlat, K. Lian – Plastic behavior and stretchability of sheet metals. Part I: A yield function for orthotropic sheets under plane stress conditions – *International Journal of Plasticity (1989)* – Vol. 5, pp. 51-66 **[Ref. 68]**

F. Barlat, J. Liu – Precipitate induced anisotropy in binary Al-Cu alloys – *Materials Science (*1998*)* – Vol. A 257(1), pp. 47-61. **[Ref. 69]**

P. J. Bania – Beta Titanium Alloys and Their Role in the Titanium Industry – *Journal of Material*s – July 1994, Vol. 46, Issue 7, pp. 16-19 **[Ref. 22]**

I. J. Beyerlein, C. N. Tomé – Probabilistic twin nucleation model for HCP polycrystalline metals – *Proc. R. Soc. A* (2010) pp. 2517–2544 **[Ref. 36]**

H. K. D. H. Bhadeshia – *Titanium & its Alloys - Materials Science & Metallurgy* - Part II, Course C9, pp. 4-5 **[Ref. 18]**

H. K. D. H. Bhadeshia – *Titanium & its Alloys - Materials Science & Metallurgy* - Part II, Course C9, pp.7 **[Ref. 20]**

T.R. Bieler, R.M. Trevino, L. Zeng – Alloys: Titanium – *Encyclopedia of Condensed Matter Physics* (2005) – pp. 67-69 **[Ref. 27]**

N. Bozzolo, N. Dewobroto, F. Wagner – Recrystallization in cold rolled titanium: mechanism of texture and microstructure evolution – *Materials Science Forum* – Vol. 467, pp. 453-558 **[Ref. 47]**

H.J. Bunge, K. Pöhlandt, A.E. Tekkaya D. Banabic – Formability of Metallic Materials: Plastic Anisotropy, Formability Testing, Forming Limits – *Ed. Springer* – pp.144 **[Ref. 79]**

F. C. Campbell – Elements of metallurgy and engineering alloys – *Ed. ASM international (2008),* pp. 530 **[Ref. 21]**

O. Cazacu, F. Barlat, B. Plunket – Anisotropic yield function of hexagonal materials taking into account texture development and anisotropic hardening – *Acta Materialia (2006)* – Vol. 54, pp. 4159-4169 **[Ref. 70]**

M. Chaze, C. Codett – *Journal of Less Common Metals* – Vol. 157, pp. 55 (1990) **[Ref. 26]**

J. W. Christian, S. Mahajan – Deformation Twinning – *Progress in Materials Science* – Vol. 39, Issue 1, 2 (1995), pp. 1-157 **[Ref. 40]**

M. J. Donachie Jr. – Titanium: a technical guide 2nd Ed. – *Ed. ASM International (2000)* – pp. 27-28 **[Ref. 12]**

O. Engler, V. Randle – Introduction to texture analyses, 2nd edition – *CRC press* – pp. 51 **[Ref. 95]**

O. Engler, V. Randle – Introduction to texture analyses, 2nd edition – *CRC press* – pp. 31 **[Ref. 97]**

O. Engler, V. Randle – Introduction to texture analyses, 2nd edition – *CRC press* – pp. 87 **[Ref. 98]**

O. Engler, V. Randle – Introduction to texture analyses, 2nd edition – *CRC press* – pp. 34 **[Ref. 100]**

D. Eylon – Titanium for energy and industrial applications – *Metallurgical Society AIME* (1987) **[Ref. 5]**

E. S. Fisher, C. J. Renken – Single-Crystal Elastic Moduli and the hcp-bcc Transformation in Ti, Zr, and Hf – *The Physical Review* – Vol. 135, no. 2A, July 1964, pp. 482-494. **[Ref. 61]**

J. W. Flowers, K. C. O'Brien Jr., P. C. Mc Eleney – Elastic Constant of Alpha Titanium Single Crystals at 25°C – *Journal of Less Common Metals* – Vol. 7, no. 5, November 1964, pp. 393-395 **[Ref. 62]**

M. Freemantle – Titanium Extracted Directly from TiO2 – *Chemical and Engineering News,* 25 September 2000 **[Ref. 10]**

F.H. Froes – How to market titanium: lower the costs – *Journal of metals (2004)* – Vol. 56, N°1, pp. 39 **[Ref. 11]**

G. Goodwin – Application of strain analysis to sheet metal forming problems – Metallurgia Italiana (1968) – Vol. 60, pp. 767-771 **[Ref. 81]**

B.M. Hance – Influence of Discontinuous Yielding on Normal Anisotropy (R-Value) Measurements – Journal of Materials Engineering and Performance – Vol. 14(5) October 2005, pp. 616-622 **[Ref. 56]**

R. F. S., Hearmon – An Introduction to Applied Anisotropic Elasticity – *Acta Crystallographica* (1962) – Vol. 15, pp. 625-626 **[Ref. 60]**

A. V. Hershey – The plasticity of an isotropic aggregate of anisotropic face centered cubic crystals – *Journal Of Applied Mechanics, (1954)* – Vol. 21, pp.241– 249 **[Ref. 72]**

D. S. Hickton – Global Commercial Aerospace – *Proceeding of the 25th ITA Conference, Orlando (FL, USA)* – October 3-6, 2010 **[Ref. 1]**

R. Hill – The elastic behavior of a crystalline aggregate – *Proceedings of the Physics Soc. (1952) – Vol. A 65* – pp. 349-354 **[Ref. 7]**

R. Hill – A theory of the yielding and plastic flow of anisotropic metals – *Proceedings of the Royal Society of London (1948)* – Vol. 193, pp. 281–297 **[Ref. 64]**

W. F. Hosford – A generalized isotropic yield criterion – *Journal of Applied Mechanics* (1972) – Vol. 39, pp. 607–609 **[Ref. 67]**

H. Hu – Texture of Metals – *Texture (1974)* – Vol. 1, pp. 233-258. **[Ref. 45]**

J. W. Hutchinson – Shear bands formation in plane strain – *Int. Journal of Solid Structures* – Vol. 17, pp. 451-470 (1981) **[Ref. 92]**

S. Jurendić, S. Gaiani – Deep drawing simulation of α-titanium alloys using LS-Dyna – *Proceedings of 8th European LS-Dyna Conference (2011)* **[Ref. 77]**

A. Kamp – Investigation of Titanium Plates by EBSD Analysis – *Master Thesis (2007) Delft University of Technology* **[Ref. 99]**

S. Keller – Circular grid system: a valuable aid for evaluation sheet forming – *Sheet Metal Industries Journal (1969)* – Vol. 45, pp. 633-640 **[Ref. 82]**

P. Koc, B. Štok – Computer aided identification of the yield curve of a sheet metal after onset of necking – *Computational Materials Science (2004)* – Vol. 31, pp. 155–168 **[Ref. 75]**

P. Koc, B. Štok – Usage of the yield curve in numerical simulations – *Journal of Mechanical Engineering (2008)* – Vol. 54, pp. 821-829 **[Ref. 76]**

U. F. Kocks, C. N. Tome, H. R. Wenk – Texture and Anisotropy - Preferred Orientations in Polycrystals and their Effect on Materials Properties – Cambridge University Press, UK (1998) – pp. 203-204 **[Ref. 43]**

Y. Kosaka, S. P. Fox, K. Faller – Newly Developed Titanium Alloy Sheets for the Exhaust Systems of Motorcycles and Automobiles – *Journal of Materials, November 2004* **[Ref. 30]**

E. Kraft – Summary of emerging titanium cost reduction technologies - 2004, EHK Technologies for ORNL: Vancouver, WA. pp. 1-59 **[Ref. 16]**

A.A. Kruglov, F.U. Enikeev, R.Y. Lutfullin – Superplastic forming of a spherical shell out a welded envelope – Materials Science and Engineering (2002) – Vol. 323, pp. 416–426 **[Ref. 90]**

O. G. Lademo, O. Hopperstad, M. Langseth – An evaluation of yield criteria and flow rules for aluminum alloys – *International Journal of Plasticity* (1999) – Vol. 15, pp. 191-208 **[Ref. 66]**

L. Lazarescu, D. S. Comsa, D. Banabic – Determination of stress-strain curves of sheet metals by hydraulic bulge test – *Journal of Materials Process Technologies (2001)* – Vol. 115, pp. 83-86 **[Ref. 89]**

C. Leyens, M. Peters – Titanium and Titanium Alloys – *Ed. DLR (German Aerospace Center)*, pp.6 **[Ref. 32]**

G. Lloyd at all – Crystallographic Texture – Mineralogical Magazine (1991) – Vol. 55, pp. 331-345 **[Ref. 96]**

R. W. Logan, W. F. Hosford – Upper bound anisotropic yield locus calculations assuming pencil glide – *International Journal of Mechanical Science, (1980)* – Vol. 22, pp. 419– 430 **[Ref. 73]**

A. C. Lovell, J. A. Clegg, C. D. Ellyett – Mechanism of Twinning in Metals – *Nature* 123, 262-263 (9/03/1946) **[Ref. 34]**

G. Lutjering, J.C. Williams – Titanium 2nd Edition – *Ed. Springer (2007)* – pp. 22 **[Ref. 38]**

G. Lutjering, J. C. Williams – Titanium 2nd Edition – *Ed. Springer (2007)* – pp. 65-66 **[Ref. 13]**
G. Lutjering, J. C. Williams – Titanium 2nd Edition – *Ed. Springer (2007)* – pp. 76 **[Ref. 14]**

Z. Marciniak, K. Kuczynzky – Limit strains in the process of stretch- forming sheet metal - *International Journal of Mechanical Sciences (1967)* – Vol. 9, pp. 609-62 **[Ref. 85]**

L. Meekisho, X. Yao, G. E. Totten – Quenching Theory and Technology, 2nd Edition – *Ed. Taylor and Francis Group LLC,* pp. 86-87 **[Ref. 23]**

M. L. Meier, A. K. Mukherjee – The onset of tensile instability – Department of Chemical Engineering and Materials Science University of California – Course note **[Ref. 58]**

S. Mesarovic – Dynamic Strain Aging and Plastic Instabilities – *Journal of Mechanical Physic of Solids* – Vol. 43, pp. 671-701 No. 5 **[Ref. 51]**

K. Nakazima, T. Kikuma, K. Asaku – Study on formability of steel sheet –*Yawata Technical report 264 (1968)* **[Ref. 84]**

R. Penelle, T.Baudin, C. Quesne – Relationships between texture, microstructure and properties in titanium and some titanium alloys – *Proceedings of the 10th World Conference on Titanium, Hamburg, Germany* – July 13-18, 2003 **[Ref. 3]**

B. Plunkett, R.A. Lebensohn, O. Cazacu, F. Barlat – Anisotropic yield function of hexagonal materials taking into account texture development and anisotropic hardening – *Acta Materialia (2006)* – Vol. 54, pp. 4159–4169 **[Ref. 65]**

P. Perez, V. A. C. Haanappel, M. F. Stroosnijder – The Effect of Niobium on the Oxidation Behavior of Titanium in Ar/20% O2 Atmospheres – *Oxidation of Metals, Vol. 53, Nos. 5/6, 2000* **[Ref. 29]**

M. J. Philippe, C. Eslingt, B. Hocheid – Role of Twinning in Texture Development and in Plastic Deformation of Hexagonal Materials – *Textures and Microstructures* – 1988, Vol. 7, pp. 265-301 **[Ref. 42]**

A. A. Salem, S. R. Kalidindi, R. D. Doherty, S.L. Semiatin – Strain Hardening Due to Deformation Twinning in α-Titanium: Mechanisms – *Metallurgical and materials transactions* – Vol. 37a, January 2006, pp. 259 **[Ref. 41]**

S. L. Semiatin, T. R. Bieler – Effect of texture and slip mode on the anisotropy of plastic flow and flow softening during hot working of Ti-6Al-4V – *Metallurgical and materials transactions* – Volume 32a, July 2001: pp. 1787 **[Ref. 2]**

S.L. Semiatin, S.V. Shevchenko, O.M. Ivasishin, M.G. Glavicic, Y.B. Chun, S.K. Hwang – Modeling and simulation of texture evolution during the thermomechanical processing of titanium alloys **–** *ASM Handbook, Vol. 22– Modeling and Simulation: Processing of Metallic Materials* **[Ref. 37]**

A. D. Santos, P. Teixeira, A. Barata da Rocha, F. Barlat – On the Determination of Flow Stress Using Bulge Test and Mechanical Measurement – *Proceedings of the 10th International Conference on Numerical Methods in Industrial Forming Processes, pp. 845-852* **[Ref. 88]**

S. Seong, O. Younossi, B. W. Goldsmith – Titanium: industrial base, price trends, and technology initiatives – *Rand Corporation (2009)* – pp. 15 – 16 **[Ref. 17]**

J. Slota, E. Spižák – Comparison of the Forming Limit Diagram (FLD) Models for Drawing Quality (DQ) – *Steel Sheets Metallurgy (2005)* – Vol. 44 pp. 249 - 253. **[Ref. 91]**

K. Tada, Y. Itsumi – Characteristics of Low-cost Heat-resistant Titanium Alloy for Automobile Exhaust Systems, KS Ti-0.9SA – *Kobe Steel Engineering Reports, Vol. 60 No. 2, Aug. 2010* **[Ref. 31]**

M. Tisza – Physical Metallurgy for Engineers – *Ed. ASM International, 2nd Edition (2002)* – pp. 142 **[Ref. 35]**

M. Tisza, Z. P. Kovács – New methods for predicting the formability of sheet metals – *Production Processes and Systems (2012) - Volume 5, No. 1, pp. 45-54* **[Ref. 83]**

A. Tuncer – The role of texture evolution and strain hardening on the anisotropic response of polycrystalline metals – Master's Thesis (2009), pp. 3-4 - Master of Science (M.S.) **[Ref. 33]**

P. C. Turner, J. S. Hansen – An assessment of existing Titanium Technologies – *Albany Research Center, Department of Energy* – July 28th (1999) **[Ref. 15]**

D. Vojtěch, M. Mort'aniková, P. Novák – Kinetic and Thermodynamic Aspects of High-Temperature Oxidation of Selected Ti-Based Alloys – *Defect and Diffusion Forum* – Vol. 263, pp. 123-128 (2006) **[Ref. 25]**

D. Vojtěch, T.Kubatík, H. Čížová – Application of Silicon for a Protection of Titanium against High Temperature Oxidation – *Materials Science Forum* – Vol. 482, pp. 243 – 246 **[Ref. 28]**

Y.N. Wang, J.C. Huang – Texture analysis in hexagonal materials – *Materials Chemistry and Physics* – Vol. 81 (2003), pp. 11-26 **[Ref. 44]**

H. R. Wenk, P. Van Houtte – Texture and Anisotropy – *Reports on Progress in Physics* – Vol. 67, pp. 1367 – 1428 (2004) **[Ref. 94]**

M. R. Winstone, R. D. Rawlings, D. R. F. West – Dynamic strain ageing in some titanium-silicon alloys – *Journal of Less Common Metals (1973)* – Vol. 31, pp. 143 150 **[Ref. 102]**

S. L. Wong – Deformation Twinning: Mechanisms and Their Role in Crystal Plasticity Models – Graduate Diploma (May 2006) **[Ref. 39]**

Z. S. Zhu, J. L. Cu., N. P. Chen – On the texture controlling methods and mechanical property anisotropy in commercially pure titanium sheet – *Materials for Mechanical Engineering* (1994) – Vol. 18(6): 8–1 **[Ref. 46]**

VV.AA. – Ansys LS-Dyna user's guide – *Ansys Inc., Release 12.0, April 2009* – pp. 77 **[Ref. 71]**

VV.AA. – Ansys LS-Dyna user's guide – *Ansys Inc., Release 12.0, April 2009* – pp. 78 **[Ref. 74]**

VV.AA. – History of titanium – Titanium Industries Inc.; Internet web site **[Ref. 8]**

VV.AA. – Titanium alloy guide – RMI International Company – pp.3 **[Ref. 4]**

VV.AA. – Titanium alloys guide – RMI Titanium Company pp. 4 **[Ref. 19]**

VV.AA. – Titanium alloys guide – RMI International Company – pp. 5 **[Ref. 19]**

VV.AA. – Titanium processing – Encyclopedia Britannica On Line **[Ref. 9]**

VV.AA. – Titanium, the infinite choice – Brochure published from International Titanium Association Education Committee **[Ref. 6]**

VV.AA. – Welding Titanium: a designers and users handbook – Titanium Information Group (1999) pp.2 **[Ref. 24]**

ASTM B265 (2011-e1) – Standard Specification for Titanium and Titanium Alloy Strip, Sheet, and Plate **[Ref. 80]**

ASTM E8 (2011) – Standard Test Methods for Tension Testing of Metallic Materials **[Ref. 53]**

ASTM E111 – 04 (2010) – Standard Test Method for Young's Modulus, Tangent Modulus, and Chord Modulus **[Ref. 52]**

ASTM E132 – 04 (2010) – Standard Test Method for Poisson's Ratio at Room Temperature **[Ref. 54]**

ASTM E517 – 00 (2010) – Standard Test Method for Plastic Strain Ratio r for Sheet Metal **[Ref. 57]**

ASTM E1409 (2008) – Standard Test Method for Determination of Oxygen and Nitrogen in Titanium and Titanium Alloys by the Inert Gas Fusion Technique **[Ref. 48]**

ASTM E1447 (2009) – Standard Test Method for Determination of Hydrogen in Titanium and Titanium Alloys by the Inert Gas Fusion Thermal Conductivity/Infrared Detection Method **[Ref. 49]**

ASTM G99 – 05(2010) – Standard Test Method for Wear Testing with a Pin-on-Disk Apparatus **[Ref. 93]**

EN ISO 6892-1 (2009) – Metallic materials - Tensile testing - Part 1: Method of test at room temperature **[Ref. 50]**

ISO 10113 (2006) – Metallic materials - Sheet and strip - Determination of plastic strain ratio **[Ref. 55]**

ISO 10275 (2007) – Metallic materials - Sheet and strip - Determination of tensile strain hardening exponent **[Ref. 59]**

ISO 12004-2 (2008) – Metallic materials - Sheet and strip - Determination of forming-limit curves - Part 2: Determination of forming-limit curves in the laboratory **[Ref. 86]**

ISO 20482 (2003) - Metallic materials - Sheet and strip - Erichsen cupping test **[Ref. 63]**

List of Tables

List of Figures

List of Publications

S. Gaiani – "Mechanical characterization of heat resistant titanium alloys for automotive applications"
Proceeding of 24th ITA Conference, 16th - 18th September 2008, Las Vegas (Nevada, USA)

S. Gaiani, P. Veronesi, B. Juriševic – "Characterization of titanium alloys cast from recycled materials"
Proceeding of 25th ITA Conference, 1st- 5th October 2009, Kona (Hawaii, USA)

S. Gaiani, P. Veronesi, S. Jurendic – "Plastic deformation of α-Ti Alloys Sheets"
Proceeding of 26th ITA Conference, 1st- 5th October 2010, Orlando (Florida, USA)

S. Gaiani, P. Veronesi, R. Sola, G. Poli, B. Juriševic - "Caratterizzazione di leghe di titanio alfa ottenute da riciclo di scrap tecnologico"
Proceeding of 33rd Convegno Nazionale AIM, 10th – 12th November 2010, Brescia (Italy)

S. Jurendic, **S. Gaiani**, P. Veronesi - "Deep drawing simulation of alpha titanium alloys using LS-Dyna"
Proceeding of 8th European LS-Dyna Conference, 23rd - 25th May 2011, Strasburg (France)

S. Gaiani, B. Juriševic, P. Veronesi - "Oxidation behavior of cast alpha-titanium scraps blends for exhaust system applications"
Proceeding of 12th Titanium World Conference, 19 – 24 June 2011, Beijing (China)

J. Medved, **S. Gaiani**, M. Voncina, P. Mrvar, R. Tisu - "Visokotemperaturna oksidacija Ti materialov"
Proceeding of 51st International Foundry Conference Portorož 2011, 14th – 16th September 2011

S. Gaiani, E. Colombini, P. Veronesi, F. Mantovani - "Comparisons between different arc welding technologies for titanium exhaust systems manufacturing**."**
Proceeding of 27th ITA Conference, 3rd - 6th October 2011, San Diego (CA, USA)

Colombini E., **Gaiani S**., Veronesi P. - Surface treatments for increasing wear resistance on α-Ti alloys
Proceeding of 27th ITA Conference, 3rd - 6th October 2011, San Diego (CA, USA)

S. Gaiani, E. Colombini, P. Veronesi, U. Rosa – "Optimization of the chemical milling of investment cast titanium alloys"
Proceeding of 28th ITA Conference, 5th - 8th October 2012, Atlanta (GA, USA)

S. Gaiani, P. Veronesi, E. Colombini, G. Poli – "Evoluzione della tessitura cristallografica durante la deformazione plastica di leghe di titanio alfa laminate a freddo"
Proceeding of 34th Convegno Nazionale AIM, 6th – 8th November 2012, Trento (Italy)

S. Gaiani, S. Jurendic - Numerical Simulation of Cold Forming of α-Titanium Alloy Sheets
"Strojniški Vestnik" (Journal of Mechanical Engineering)
State: Accepted for publication, Issue of March 2013

S. Gaiani, E. Colombini, P. Veronesi, G. Poli, I. Pribošic – "Studio della tessitura cristallografica e delle proprietà di anisotropia di leghe di titanio alfa laminate a freddo"
La Metallurgia Italiana
State: Accepted for publication, Issue of May 2013

P. Veronesi, **S. Gaiani**, E. Colombini, G. Poli – "Recycling of alpha titanium technological scrap for exhaust system part manufacturing"
Journal of cleaner production
State: submitted for publication, III reviews on going